Title

Annual Report FY 1995 Analog Site for Fracture Rock Characterization

Authors

Long, Jane C S
Doughty, Christine
Aydin, Atilla
et al.

Publication Date

1995-10-01

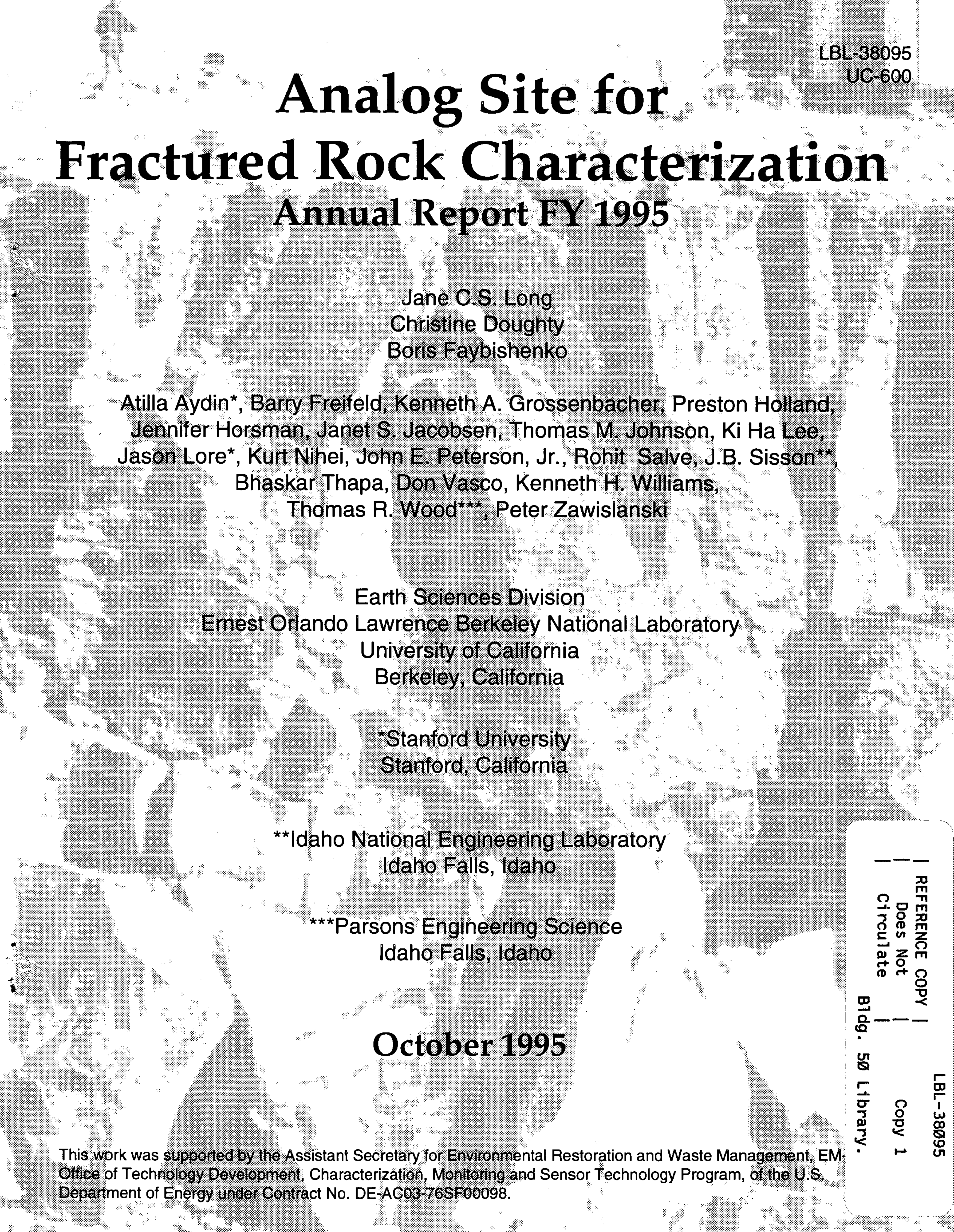

LBL-38095
UC-600

Analog Site for Fractured Rock Characterization

Annual Report FY 1995

Jane C.S. Long
Christine Doughty
Boris Faybishenko

Atilla Aydin*, Barry Freifeld, Kenneth A. Grossenbacher, Preston Holland, Jennifer Horsman, Janet S. Jacobsen, Thomas M. Johnson, Ki Ha Lee, Jason Lore*, Kurt Nihei, John E. Peterson, Jr., Rohit Salve, J.B. Sisson**, Bhaskar Thapa, Don Vasco, Kenneth H. Williams, Thomas R. Wood***, Peter Zawislanski

Earth Sciences Division
Ernest Orlando Lawrence Berkeley National Laboratory
University of California
Berkeley, California

*Stanford University
Stanford, California

**Idaho National Engineering Laboratory
Idaho Falls, Idaho

***Parsons Engineering Science
Idaho Falls, Idaho

October 1995

This work was supported by the Assistant Secretary for Environmental Restoration and Waste Management, EM-Office of Technology Development, Characterization, Monitoring and Sensor Technology Program, of the U.S. Department of Energy under Contract No. DE-AC03-76SF00098.

Annual Report FY 1995

Analog Site for Fracture Rock Characterization

Jane C.S. Long, Christine Doughty,
Atilla Aydin*, Boris Faybishenko, Barry Freifeld,
Kenneth A. Grossenbacher, Preston Holland, Jennifer Horsman,
Janet S. Jacobsen, Thomas M. Johnson, Ki Ha Lee, Jason Lore*,
Kurt Nihei, John E. Peterson, Jr., Rohit Salve,
J.B. Sisson**, Bhaskar Thapa, Don Vasco, Kenneth H. Williams,
Thomas R. Wood***, Peter Zawislanski

Earth Sciences Division
Ernest Orlando Lawrence Berkeley National Laboratory
University of California
Berkeley, California

*Stanford University
Stanford, California

**Idaho National Engineering Laboratory
Idaho Falls, Idaho

***Parsons Engineering Science
Idaho Falls, Idaho

October 1995

This work was supported by the Assistant Secretary for Environmental Restoration and Waste Management, EM-50, Office of Technology Development, Characterization, Monitoring and Sensor Technology Program, of the U.S. Department of Energy under Contract No. DE-AC03-76SF00098.

Table of Contents

Abstract

This report describes the accomplishments of the Analog Site for Fracture Rock Characterization Project during fiscal year 1995. This project is designed to address the problem of characterizing contaminated fractured rock. In order to locate contaminant plumes, develop monitoring schemes, and predict future fate and transport, the project will address the following questions:

- What parts of the system control flow-geometry of a fracture network?
- What physical processes control flow and transport?
- What are the limits on measurements to determine the above?
- What instrumentation should be used? How should it be designed and implemented?
- How can field tests be designed to provide information for predicting behavior?
- What numerical models are good predictors of the behavior of the system?

The answers to these question can be used to help plan drilling programs that are likely to intersect plumes and provide effective monitoring of plume movement. We will develop a conceptual model and technology that will be useful in characterizing a contaminated site in order to predict future behavior and design effective remediation schemes.

The work is done at an "analogue" site, *i.e.*, a site that is not contaminated, but has similar geology to sites that are contaminated, in order to develop tools and techniques without the financial, time and legal burdens of a contaminated site. The idea is to develop conceptual models and investigations tools and methodology that will apply to the contaminated sites in the same geologic regimes. The Box Canyon site, chosen for most of this work represents a unique opportunity because the Canyon walls allow us to see a vertical plane through the rock.

The work represents a collaboration between the Lawrence Berkeley National Laboratory (LBL), Stanford University (Stanford), Idaho National Engineering Laboratory (INEL) and Parsons Environmental Engineering (Parsons). LBL and Stanford bring extensive experience in research in fractured rock systems. INEL and Parsons bring significant experience with the contamination problem at INEL.

This project was initially designed to address characterization of behavior in both the saturated and vadose zones in fractured rock. A series of interdisciplinary efforts (geology, geophysics, isotope geochemistry and hydrology) were proposed. These tasks built on previous experience with fracture hydrology at LBL and FY 94 efforts conducted by INEL, namely the Large Scale Infiltration Test and the Aquifer Stress Test. The results of these two tests are used in this project as a starting point. However, given the funding limitations, a decision was made to conduct only pilot studies for the saturated zone studies and conclude theses tasks in FY 95. Thus, this report represents a final report for this work. The remaining tasks are ongoing and will focus on issues associated with contamination in the vadose zone.

The project is organized into 7 tasks. Task 1 is the geologic investigation that sets the stage for the remaining tasks. The pattern of fractures formed in Snake River basalts will be quantified and analyzed in order to predict the nature of fluid flow in these rocks. Task 2 brings geophysics into the program to help us image important features and processes in the rocks. A variety of electrical, radar and seismic methods are being evaluated. Task 3 is a pilot application of inverse analysis to the aquifer stress test conducted by INEL in FY 94. The inverse method attempts to identify connected fracture networks that explain all of the well test data simultaneously. This task is now completed. Task 4 was a pilot study of the use of isotopic data in conjunction with hydrologic data

to identify fast flow paths on the aquifer scale. (This task was completed as a pilot study and is now the subject of the new proposal to DOE Energy Research Basic Energy Sciences in collaboration with DOE Environmental Restoration Waste Management.)

The purpose of Task 5 is to understand contamination transport in the vadose zone of fractured basalt. This topic will be the focus of the outyears and will continue to be supported by Tasks 1 and 2. The first efforts of the task were to learn from the experience of the Large Scale Infiltration Test conducted by INEL in FY 94. Then we chose a site at Box Canyon where the fracture system is exposed on the surface and in vertical cliffs along a river. Because of the excellent exposures, this site has been used in the past to test characterization techniques. In addition, an array of vertical and slant holes have been drilled back from the face of the cliff. A series of tests are being conducted at Box Canyon in the boreholes and from the surface and cliff face to determine how water moves downward.

Task 6 provides the project with database management and visualization systems and Task 7 provides coordination. The primary focus of these tasks in the outyears also will be on the vadose zone studies.

The major accomplishments of each of the tasks in FY 95 are as follows:
- Task 1: Collection of fracture data and qualitative analysis.
- Task 2: Field testing of CSAMT and radar methods, evaluation of channel wave methods.
- Task 3: Completed inverse analysis of the Aquifer Stress Test data showing patterns of fracture connectivity in the vicinity.
- Task 4: Completed pilot study of the use of a combination of Sr isotope ratio data and hydraulic measurements to determine fast paths in the Snake River Aquifer.
- Task 5: Evaluation of the Large Scale Infiltration test, establishment of the Box Canyon analogue site including well installation, conduction of a hot air injection test, evaluation of the air injection method with numerical modeling, development of instrumentation for Box Canyon.
- Task 6: Development of a data base management system and visualization of data from the Large Scale Infiltration Test.
- Task 7: Held coordination meetings, responsed to ERWM reviews, and coordinated project communication.

Tasks 3 and 4 have now been completed. The remaining tasks will focus on infiltration in fractured basalt. The focus of FY96 will be an infiltration test to be conducted at Box Canyon. This test will be designed and predicted based on the FY95 and early FY96 data collection and analysis efforts of Tasks 1, 2, 5 and 6. The test is scheduled for the summer of 1996.

List of Figures Captions

lower transmissivity. The arrangement of the plots on the page mimics the well field pattern shown in Figure 3.1.

Figure 3.11. Drawdown as a function of time calculated using a two-layer (single continuum) model with a variable pumping rate, including wellbore storage and a skin around the test well. The arrangement of the plots on the page mimics the well field pattern shown in Figure 3.1.

Figure 3.12. Orders of magnitude of T (m^2/s) and S used to produce the drawdowns shown in Figure 3.11

Figure 4.1. Sr isotope ratio plotted versus distance, illustrating a greater value of L, the distance over which isotope ratio varies, for a fast flow path; and contours of Sr isotope ratio showing a fast flow path.

Figure 4.2. The Snake River Plain and the surrounding highland regions, which provide recharge to the aquifer with a high Sr isotope ratio.

Figure 4.3. Sr isotope ratios plotted versus distance along a flow path through INEL.

Figure 4.4. A mixing model for Sr isotope ratios in the Snake River Plain Aquifer.

Figure 4.5 The synthetic transmissivity distribution used to test the hydrologic inverse method for a regional-scale analysis, and the steady-state hydraulic head values obtained from it. T_0 is the average or background transmissivity. The black dots show the locations of the steady-state head values that were used in the inversion.

Figure 4.6. The transmissivity distribution returned by the hydrologic inversion, and the corresponding hydraulic head values.

Figure 5.1. Location of the Box Canyon site (about 9-1/2 miles northwest of the RWMC).

Figure 5.2. General aerial view of the Box Canyon site and its vicinity.

Figure 5.3. Photo of the mesh established at the site in June 1995 in order to survey the land surface.

Figure 5.4. Close-up view of the center of the site, June 1995.

Figure 5.5. Grid coordinates surveyed in June 1995.

Figure 5.6. Three-dimensional view of surface topography created using AVS.

Figure 5.7. Borehole layout at the Box Canyon site. The line identifies the lithological profile shown in Figure 5.14. Slant holes as show in red.

Figure 5.8. Example of gamma logging - well II-7.

Figure 5.9. Example of caliper measurements - well II-7.

Figure 5.10. Example of core logging - well II-5.

Figure 5.11. Example of core photos - well II-5.

Figure 5.27c. Changes in the TIR image between 2:20 am and 4:07 am on August 8, 1995.

Figure 5.27d. Changes in the TIR image between 2:20 am and 5:07 am on August 8, 1995.

Figure 5.28. Central portion of the axisymmetric grid used for the numerical simulation of the third hot air injection test. Shading: uniform diagonal stripes: vesicular zone; paired diagonal stripes: fracture; cross-hatching: rubble zone; solid black: injection interval. The first frame (a) shows the inner 2 m of the grid; (b) shows the inner 88 m of the grid. The entire grid extends to 4 km.

Figure 5.29a. Temperature distribution after 16 hours of hot air injection. The injection depth is 9-12 m; there is a fracture zone at 9 m depth and a rubble zone at 11-13 m.

Figure 5.29b. Gas saturation distributions after 16 hours of hot air injection (upper frame) and no injection (lower frame).

Figure 5.30. Temperature distribution after 16 hours of hot air injection into an initially dry medium.

Figure 5.31. Temperature distributions after 16 hours of air and water vapor injection (A) and dry air injection (B) into an initially partially-saturated medium. Note the different temperature color scale from the previous temperature distributions, to enable subtle temperature differences to be seen.

Figure 5.32. Scheme of deep tensiometer with two-cell transducer.

Figure 5.33. Tensiometer and barometer data measured at the IRC test site.

Figure 5.34. Regression between water tension and barometer pressure at the IRC test site.

Figure 6.1. Visualization of geological data of monitoring wells at the INEL Large-Scale Infiltration Test site.

Figure 6.2. Fence diagram of geological model of INEL Large-Scale Infiltration Test site.

Figure 6.3. Concentrations of selenium^{75} measured by lysimeters or from bottom hole, water sample measurements on August 14, 1994. The concentrations are shown on August 14, 1994.

Figure 6.4. Concentrations of selenium^{75} measured by lysimeters or from bottom hole, water sample measurements on August 24, 1994.

Figure 6.5. Shown are both far (1 Ci, labeled "F") and near (50 mCi, labeled "N") source neutron data collected on July 30, 1994. The neutron data have been normalized against background data collected before the LSIT began.

Figure 6.6. Shown are both far (1 Ci, labeled "F") and near (50 mCi, labeled "N") source neutron data collected on August 10, 1994. The neutron data have been normalized against background data collected before the LSIT began.

Figure 6.7. Water levels and selenium 75 concentration in open wells as measured on September 6, 1994. See text for explanation of water levels.

Figure 6.8. Shown are dialogue boxes that allow the user to query the Illustra database management system.

Figure 6.9. Shown are the results of the query shown in Fig. 6.8. See text for explanation.

List of Tables

Acknowledgments

This work was supported by DOE Contract No. DEAC03-76SF00098 from the DOE's Environmental Restoration and Waste Management Program, EM-50, Office of Technology Development, Characterization, Monitoring and Sensor Technology Program.

The authors of this report would like to thank Caroline Purdy of the OTD and Bill Haas of Ames Laboratory for their support of this project; Kenzi Karasaki and George Moridis for their careful and thorough review of this report; and Sherry Seybold for her attention to detail and careful typing of this report.

1.0 INTRODUCTION

This report describes the accomplishments of the Analog Site for Fracture Rock Characterization Project during fiscal year 1995. This project is designed to address the problem of characterizing contaminated fractured rock. In order to locate contaminant plumes, develop monitoring schemes and predict future fate and transport, the project will address the following questions:

- What parts of the system control flow-geometry of a fracture network?
- What physical processes control flow and transport?
- What are the limits on measurements to determine the above?
- What instrumentation should be used? How should it be designed and implemented?
- How can field tests be designed to provide information for predicting behavior?
- What numerical models are good predictors of the behavior of the system?

The answers to these question can be used to help plan drilling programs that are likely to intersect plumes and provide effective monitoring of plume movement. We will have developed a conceptual model and technology that will be useful in characterizing a contaminated site in order to predict future behavior and design effective remediation schemes.

Implementation of isolation technology also requires an understanding of the system. With this understanding, one can answer critical questions related to isolation:

- How can the containment scheme be tailored to active and connected flow paths?
- How can natural barriers be incorporated into the isolation scheme?
- How should grouting operations be staged?
- How can we effectively test for containment integrity?

The work to answer these questions is being done at an "analogue" site, *i.e.*, a site that is not contaminated, but has similar geology to sites that are contaminated, in order to develop tools and techniques without the financial, time and legal burdens of a contaminated site. The idea is to develop conceptual models and investigations tools and methodology that will apply to the contaminated sites in the same geologic regimes. The Box Canyon site, chosen for most of this work represents a unique opportunity because the Canyon walls allow us to see a vertical plane through the rock.

Similar projects have been conducted at fractured sites for the purpose of learning how to characterize potential high level nuclear waste repositories. Projects such as the Stripa Project in Sweden developed new methods and understanding that now enables good repository design in fractured granite. LBL was a major participant in several of these projects. No similar projects have yet been done to address enabling technology for the contamination problems in fractured rock faced by DOE.

The work represents a collaboration between the Lawrence Berkeley National Laboratory (LBL), Stanford University (Stanford), Idaho National Engineering Laboratory (INEL) and Parsons Environmental Engineering (Parsons). LBL and Stanford bring extensive experience in fractured rock. INEL and Parsons bring significant experience with the contamination problem at INEL. This report describes the work done by the Analog Site for Fractured Rock Characterization Project during fiscal year 1995.

This project was initially designed to address characterization of behavior in both the saturated and vadose zones in fractured rock. A series of interdisciplinary efforts (geology, geophysics, isotope geochemistry and hydrology) were proposed. These tasks built on previous experience with fracture hydrology at LBL and FY 94 efforts conducted by INEL, namely the Large Scale Infiltration Test and the Aquifer Stress Test. The results of these two tests are used in this project as a starting point. However, given the funding limitations, a decision was made to conduct only pilot studies for the saturated zone studies and conclude these tasks in FY 95. Thus, this report represents a final report for these tasks. The remaining tasks are ongoing and focus on issues associated with contamination in the vadose zone.

The project is organized into seven tasks. Task 1 is the geologic investigation that sets the stage for the remaining tasks. The pattern of fractures formed in Snake River basalts will be quantified and analyzed in order to predict the nature of fluid flow in these rocks. Task 2 brings geophysics into the program to help us image important features and processes in the rocks. A variety of electrical, radar and seismic methods are being evaluated. Task 3 is a pilot application of inverse analysis to the aquifer stress test conducted by INEL in FY 94. The inverse method attempts to identify connected fracture networks that explain all of the well test data simultaneously. This task is now completed. Task 4 is a pilot study of the use of isotopic data in conjunction with hydrologic data to identify fast flow paths on the aquifer scale. (This task was completed as a pilot study and is now the subject of the new proposal to DOE Energy Research Basic Energy Sciences in collaboration with DOE Environmental Restoration Waste Management.)

The purpose of Task 5 is to understand contaminant transport in the vadose zone of fractured basalt. This topic will be the focus of the outyears and will continue to be supported by Tasks 1 and 2. The first efforts of Task 5 were to learn from the experience of the Large Scale Infiltration Test conducted by INEL in FY 94. Then we chose a site at Box Canyon where the fracture system is exposed on the surface and in vertical cliffs along a river. Because of the excellent exposures, this site has been used in the past to test characterization techniques. In this project an array of vertical and slant holes have been drilled behind the face of the cliff. A series of tests are being conducted at Box Canyon in the boreholes and from the surface and cliff face to determine how water moves downward.

Task 6 provides the project with database management and visualization systems, and Task 7 provides coordination. The primary focus of these tasks in the outyears also will be on the vadose zone studies.

1.1 Statement of the Problem

A number of DOE contaminated sites are in fractured rock including sites at INEL, Hanford, Oak Ridge, and others. For example, sites at INEL contain radioactive material and volatile organic carbons (VOC's) stored at the surface some 600 feet (200 m) above the fractured basalts of the Snake River Plain Aquifer, and several plumes of contaminated ground water have been identified. For instance, the Test Area North Injection Well was used for twenty years to inject waste materials into the fractured basalts of the Snake River Plain Aquifer. These facilities have already resulted or potentially could result in significant contamination passing through the fracture system. Table 1.1 gives a preliminary assessment of needs throughout the DOE complex collected by the Plumes Focus Area plus several other estimated problems.

Table 1.1. Needs related to fractured geology.

DOE Field Office	Facility	Comments
Chicago	Princeton Plasma Physics Lab	a) Want to know flow and contaminant distribution in fractured bedrock (sandstone and shale) b) Want to potentially apply air sparging to the bedrock (possibly with hydrofracturing)
	Argonne National Lab	Do not know extent of contamination (probably DNAPL) in fractured dolomite
Idaho	INEL	Improved fate and transport models; better stochastic model parameters, better characterization tools
Nevada	Nevada Test Site	Need new transport modeling approaches
Berkeley	LBL	Difficulty in locating DNAPL in fractured bedrock (siltstone and shale)
Oak Ridge	ORNL	a) Need methods to overcome matrix diffusion during remediation b) Need methods for treating organics and radionuclides in fractured rock (shale) c) Need basic research to understand flow in complex geology
	Y-12	a) Need help in locating, containing, and remediating DNAPLs in fractured bedrock (shale, limestone) b) Need help on demonstrating technical unfeasibility
	ORNL	Some waste is stored above the water table. Waste could leach through unsaturated fractured rock.
Hanford	Hanford Reservation	Possible contamination below the water table in fractured basalt
Los Alamos		Waste disposed of on top of mesas in the Bandolier Tuff, a fractured rock far above the water table.

The first task of this project (completed in FY 94) was to choose an initial site for developing characterization methods in fractured rock. The INEL site was chosen because there is a significant contamination problem at INEL in the fractured rocks of the Snake River basalts. Waste is being stored at the surface (*e.g.*, at the Radioactive Waste Management Complex, RWMC) where it can leak down through the vadose zone to the Snake River Plain Aquifer below. Waste has also been injected into the rocks and the remediation of these sites poses significant problems. A further reason for choosing INEL was that the project was well received by EM40 project managers facing remediation of these sites. Finally, INEL conducted two major experiments in FY 94 to characterize the fracture hydrology: the Large Scale Infiltration Test and the Aquifer Stress Test. These tests provided an excellent foundation for this project. Consequently, INEL was chosen as the first site for this project.

The purpose of this project, as described below, is to develop a conceptual model for flow and transport in the Snake River basalts and to develop tools for characterizing fractured rock at this site. The question arises: how much of what is done in this project will apply to the other sites given in the above table? Technology transfer falls into two categories: know-how and specific technologies. The know-how aspects of work in fractured rock are extremely important. As a group of scientists and engineers learns how to build a conceptual model of one kind of fractured rock, they are better able to develop a conceptual model for the next type. Most fractured systems are examples of extreme heterogeneity and have strongly preferential flow geometries. Effective approaches for characterizing such systems are something that is learned from experience.

Of the specific technologies under development, many may be applicable to every contaminated site and some will have to be modified for use in different geologic conditions. For example, the geomechanical analysis of fractures at INEL might be almost directly applicable to fractures at Hanford. Some modifications might be necessary for application to the Bandolier Tuff and substantial revision might be needed to predict fracture patterns for the shales at ORNL. Other technologies are geared specifically for either the saturated zone or the vadose zone. Some of the geophysical methods are designed to sense a change in water content that takes place during infiltration in the vadose zone. Similar results can be obtained below the water table by changing the electrical conductance of the water or by injecting air. We are employing numerical inversion methods for interpreting well test data. These methods could be modified for interpreting infiltration data. Nearly every method or technology described below could be applied at one or more of the above sites or may be modified to be useful at another site. We are developing a “box of tools”, but we expect that these tools will always have to be modified to be applicable to a specific problem at a specific site.

1.2 Need for a Conceptual Model

A key issue in dealing with a contaminated site is the identification of an appropriate conceptual model. Having an incorrect conceptual model is responsible for many significant errors in making predictions and obtaining less than expected results in planned remediation efforts. A conceptual model describes the geometry and physics (and chemistry, etc.) that dominate the relevant behavior of the system. If this is wrong, you cannot create an appropriate numerical model to predict the behavior of the system. You cannot design a remediation system that will work in a cost-effective manner, or satisfy the remedial action objectives. Why is it so hard to determine an appropriate conceptual model in fractured rock? The reasons are as follows.

Contaminant migration in earth materials is largely controlled by heterogeneity. Fractures in rocks are one type of heterogeneity that is particularly difficult to deal with for four fundamental reasons. The first is that fracture systems are distinguished from most porous systems in that the contrasts in permeability are both extreme and localized. Fractures can be highly permeable conduits imbedded in a matrix rock that itself is practically impermeable. High contrasts in permeability between the fractures and the matrix mean that flow in a fracture network depends strongly on the interconnection or “connectivity” of the fractures. The second reason is that the design and interpretation of borehole tests in fractured media is complicated by the fact that the response in a well may be controlled by a single fracture. In a porous media, this would be equivalent to measuring the response in a single “pore.” The third reason is that in a given system, many, or (in some cases) nearly all, observable fractures (even those that appear to be interconnected) can be non-conductive and play no significant role in flow. The fourth is that fractured systems are created through chaotic processes that may result in features of many different scales that are related to each other in a complex manner.

For the case of multiphase and/or multicomponent flow in fractures there are additional complications due to hysteresis, flow instabilities and chaotic behavior. This means that the physics of the flow system is not the same as the physics underlying "standard" fluid flow laws (Darcy's law, Richard's equation, *etc.*). If the physics is not the same, then the usual, well known parameters such as relative permeability are not meaningful.

1.3 Need for Characterization Tools

Many of the tools designed to monitor and characterize porous media are inapplicable or problematic in fractured media. For example, tensiometers are commonly used in porous media to measure moisture tension. If such an instrument is placed in a fractured rock it could either be in contact with a relatively impermeable matrix and never see any response. If the tensiometer does intersect dripping water in a fracture, the tensiometer acts like a sponge underneath a leaky faucet. Moisture tension develops in the instrument, but it may have no relevance to the flow occurring in the fracture. Worse still, a tensiometer may be installed in a fracture where water is flowing, but the instrument may not be where the water is and thus never see the moisture. This is because infiltration in a fracture may look much like water dripping down a windshield where the water is dripping down one part of the windshield and not another. The design, emplacement and interpretation of vadose zone technology in fracture networks is a new field.

1.4 Solutions Sought

The fundamental needs of program managers responsible for contaminated sites in fractured rock that are relevant to this project fall under two categories. The first category is to locate, monitor and predict the future transport of existing plumes. The current trend is to evaluate risk before deciding on a remediation strategy. In low risk cases, the strategy may simply be monitoring. In higher risk cases isolation or remediation may be prescribed. In any case, the need to predict the future transport of contaminants is critical. The solutions offered by this project with respect to these needs are discussed below.

Contamination in fractured rock has been problematic because we do not understand how the systems work, and we do not have appropriate tools for measuring the behavior. Consequently, solutions to the problems require concurrent development of technology and scientific understanding. It is necessary to understand the system in order to know that we have relevant tools. Similarly, relevant tools are needed to make the measurements in fractured rock, which contributes to understanding. The only way we can target specific needs and issues is to couple understanding and technology to find *solutions*.

The theme of the project is that we are developing a "box of tools" that will increase our understanding of the flow and transport problem in Snake River basalts to be used at contaminated sites at INEL, and, possibly with some modification can be used at other sites in the DOE complex and other contaminated sites in fractured rock. Our project includes developing a conceptual model for how flow and transport occurs in the fracture system of the Snake River basalts because development of an accurate conceptual model is a prominent need identified by the INEL customer base. The conceptual model drives risk assessment and the selection of the remedy for corrective action. It also includes the development of some specific technologies useful for characterizing flow and transport in these rocks.

For example, in the saturated zone, we are testing technologies for identifying fast paths. These include inverse analysis of multiple well test records to get site scale heterogeneity and co-inversion of tracer and pressure data to find fast flow paths on the aquifer scale. We completed an evaluation of the large scale Aquifer Stress Test performed last year and a feasibility study for determining aquifer fast paths.

Vadose zone work includes geologic, geophysical and hydrologic methods. We will be evaluating different radar systems to flow monitor the progress of fluid flowing in the vadose zone. We have conceived of an air injection and gas tracer test to quickly determine the nature of connectivity in the near surface fracture system. We will use this as a design test for the infiltration experiment. If the gas transport provides a good estimate of the water pathways, we will have a tool that can be used to estimate infiltration pathways quickly, cheaply and safely. We are working on tensiometer installations, new TDR (time domain reflectometry) designs, and borehole linings for neutron probe surveys specifically for fractured rocks. We will develop models for vadose zone flow and transport that can predict the kind of behavior we observe. The evaluation should provide some information on connected pathways in the saturated zone. We are developing a database/visualization system that will allow data from a site to be entered into a database that can be queried and simultaneously visualized. These technologies are briefly discussed below.

1.5. Activities and Accomplishments for FY 94

The only task for FY 94 was to write the proposal and identify the location for the analog project experiments. We chose the INEL site because it has a significant contamination problem, the large scale infiltration and aquifer stress tests funded by EM40 were in progress at the time, and there were interested collaborators on the site. Interest was also expressed by ORNL as well as SNL and LANL for bringing the project to their sites.

2.0 ACTIVITIES AND ACCOMPLISHMENTS FOR FY 95-96

The following sections describe the work done over FY 95 in each of the seven tasks and present a brief description of planned FY 96 work. The major FY 95 accomplishments of each of the tasks are as follows:

- Task 1 : Collection of fracture data and qualitative analysis.
- Task 2: Field testing of CSAMT and radar methods, evaluation of channel wave methods.
- Task 3: Completed inverse analysis of the Aquifer Stress Test data showing patterns of fracture connectivity in the vicinity.
- Task 4. Completed pilot study of the use of a combination of Sr isotope ratio data and hydraulic measurements to determine fast paths in the Snake River Aquifer.
- Task 5: Evaluation of the Large Scale Infiltration test, establishment of the Box Canyon analog site including well installation, conduction of a hot air injection test, evaluation of the air injection method with numerical modeling, development of instrumentation for Box Canyon infiltration test.
- Task 6: Development of a database management system and visualization of data from the Large Scale Infiltration Test.
- Task 7: Held coordination meetings, responded to ERWM reviews, and coordinated project communication.

2.1 Task 1. Geomechanical Model of Fracture Spacing Distribution and Connectivity

2.1.1 Background

One of the promising approaches for identifying hydrogeologic units in fractured basalt flows systems is to infer these from the way fractures are formed. To understand hydrology, we have to go beyond the origin of single features to the evolution of fracture patterns. The key idea is that some of the recognizable patterns also have a definable role in the hydrology of the rock.

The Snake River Plain is primarily composed of fractured Quaternary basalts, interlayered with sedimentary deposits. Individual basalt flows are typically long finger-like structures, on the order of 10 m thick and 50 m wide, which show a chaotic distribution in plan view. Sedimentary interbeds range from zero to 15 m thick. Geophysical evidence suggests total basalt thickness may exceed one kilometer (*Garabedian*, 1992). In the vicinity of Box Canyon and the southwestern portion of INEL, the water table depth is about 200 m. In the saturated zone, permeability generally decreases with depth, and only the upper most 75 m below the water table are considered to comprise the active aquifer. In both the vadose zone and the saturated zone, horizontal permeability arises largely from rubble and clinker zones, which form at basalt flow tops during dolling while underlying lava moves, whereas cooling cracks (thermal fractures) provide important vertical high-permeability pathways. Other high-permeability paths are formed by lava tubes and possibly rift zones. The sedimentary interbeds are generally associated with low permeability. In the saturated zone they create locally confined regions of the aquifer, and in places separate the aquifer into distinct layers. In the vadose zone, perched water may form above the interbeds. Both the rubble zones and sedimentary interbeds are largely horizontal structures; to predict and control contaminant transport through the vadose zone to the water table, an understanding of the nature and connectivity of the vertical fractures is critical.

The purpose of this particular task is to develop a methodology by which the geometry of thermal fractures and their distribution in basaltic lava flows at INEL can be estimated. The bases of the methodology are the documentation of field data from the study site, integration of these data with those from other sites, and development of a computer-based geomechanical model for the spacing, distribution and connectivity of the fractures.

The technical basis of the model is two-fold: the classification of the fractures into one-, two-, or multi-tiered domains and identification of each domain with characteristic fracture attributes. One of these attributes is fracture spacing, which is also related to fracture height as illustrated by field data from various environments, experimental results, and model studies. It is expected that fracture spacing will increase from the top surface and the base of a flow towards the interior. The nature of this increase, however, is different for fractures forming at the flow top than for those forming at the flow base as evidenced by the data from various locations including Hell's Half Acre near the investigation site. The technology will provide a method for estimating spacing, height, distribution, and connectivity characteristics of fractures given the thickness of a flow unit. In particular, the proposed technology addresses:

1. the relationship between changes in thickness in a flow unit with a lenticular geometry on the tier types and the spacing-height relationships,
2. the geometry and distribution of horizontal fractures,
3. the interaction between fractures forming at the flow top and the base and the connectivity between these two domains of fracture systems,
4. the influence of post-genetic deformation on the modification of the fracture system.

This work builds on previous studies conducted in the Stanford Fracture Research Project for a consortium of oil companies as well as a large body of research done at Stanford. Similar work has been done at LBL for fractures in granite. This task will take expertise developed from other projects on fracture genesis to develop technology applicable to the Snake River basalts. Agreement with subsequent field observations will attest to the success of this technology.

2.1.2 Performer

The work is being done by Atilla Aydin at Stanford and his graduate student Jason Lore. Carroll Knutson (INEL) and Tom Wood (Parsons) will work with Atilla Aydin to incorporate previous measurements of Snake River Plain Basalts. The current database includes several thousand measurements from across the INEL and Hell's Half Acre.

2.1.3 FY 95 Activities

2.1.3.1 Field Work

In the following sections, we first describe the field work conducted at Box Canyon. We then outline the data reduction procedure used, and finally discuss two features of the geology that play a key role in controlling subsurface fluid flow and transport.

We began our investigation in June 1995 with an examination of previous work at the Box Canyon site, and a survey of the fractured basalt exposures. This included initial photogrammetry of the surface exposures at a location where prior drilling had been conducted and a search of the canyon for other potential sites for future investigation. To be considered as a potential mapping location, a site needed to be close to the canyon, lie over a discrete flow unit with well-defined boundaries, and be accessible to heavy equipment. Additionally, a site needed to have adequate exposure of typical fracture geometry on the vertical canyon face and horizontal surface to facilitate mapping and characterizing the fractures. A site meeting these criteria was identified. At this location, we defined a 1 m spaced grid (40 m E-W x 50 m N-S) over the horizontal surface to allow precise mapping of the surface fractures and exposed geology. Photographs of the individual 1 m elements were combined with laser location data. The basalt flow structure chosen as the experimental site measures approximately 45 m wide (E-W) and 9 m thick, has a single entablature and colonnade set, well-defined lateral boundaries, and overlies a partially-exposed older flow unit of apparently similar geometry (Figure 1.1).

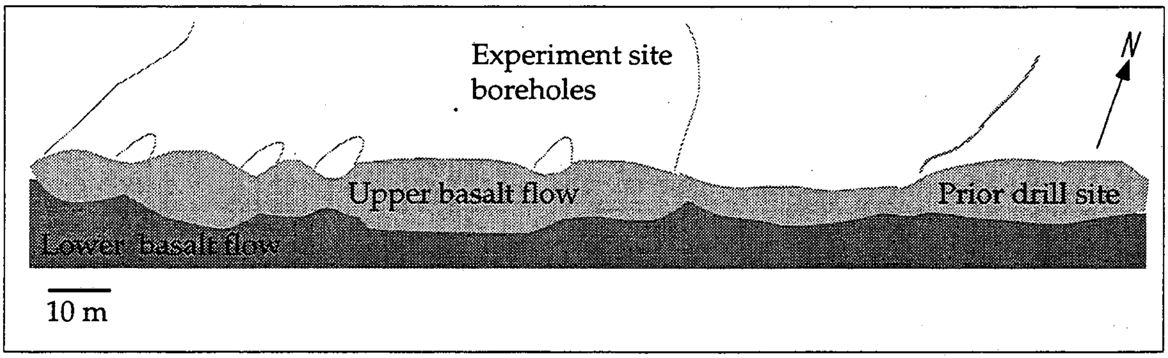

Figure 1.1. Schematic oblique view of the investigation site in relation to the boundary and extent of the underlying basalt flows.

Work in July 1995, widened the database of fracture information available to the project and carefully documented the fracture characteristics of the particular flow unit at the investigation site. We accomplished this in several ways. First, we recorded a photomosaic of the fracture exposures on the vertical canyon wall adjacent to the experiment site. This information is critical, as it forms the basis for an accurate scaled map (Figure 1.2) of the fracture exposures and correlation with sub-surface data from core, wells, and radar images. Second, we examined and recorded fracture geometries at the previous Box Canyon drill site so that existing data could be integrated into the present investigation. Additionally, two other representative flow unit exposures were examined, measured, and recorded using similar techniques. Together, these scaled fracture images provide the foundation for a database of fracture variation among several flow units. This

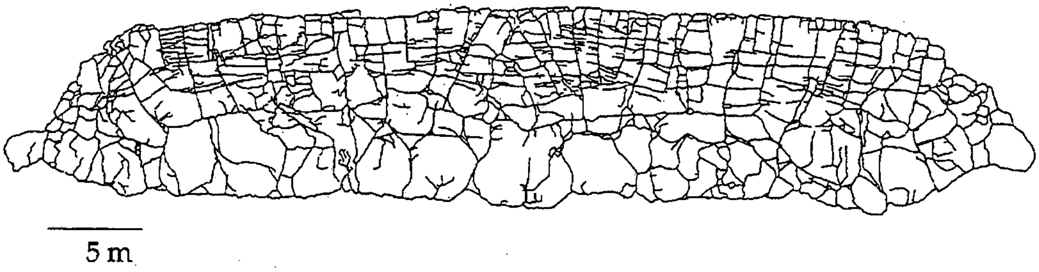

Figure 1.2. Fracture map of the canyon wall exposure at the Box Canyon investigation site. Orientation of exposure is ~ N70W and nearly vertical. The map has been compiled from digital photo-mosaic of 8 ground photographs and verified in the field.

breadth of data is important in developing a representative model of fracture geometry that is accurate for this investigation, yet not site-specific.

We also began an examination of the column-bounding and column-normal fracture connections that form a system of conduits for potential fluid flow (Figure 1.3). During this examination, we noticed connectivity and interaction between basalt vesiculation and fractures. We will use these physical attributes in conjunction with large-scale fracture maps to characterize the fracture system connectivity on the scale of the entire basalt flow.

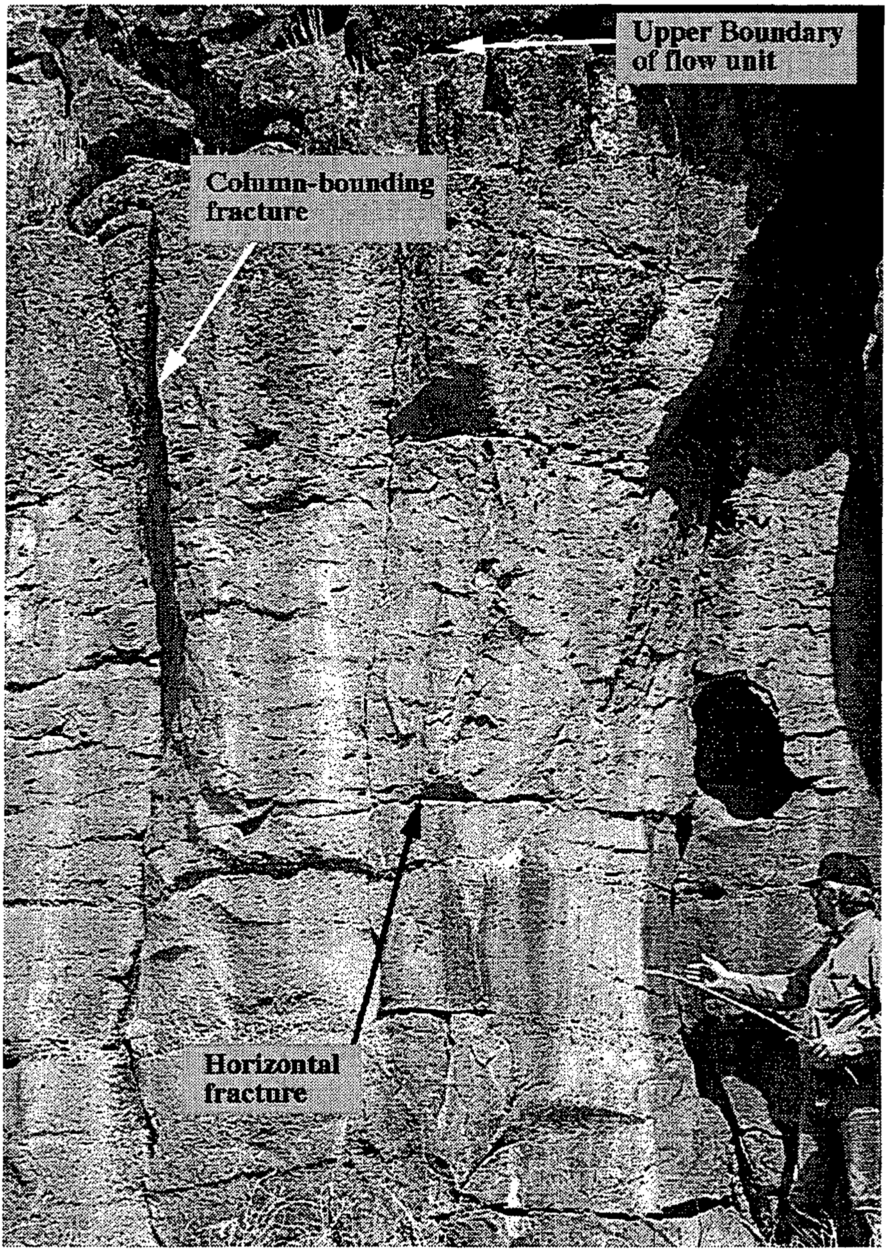

Figure 1.3. Close-up of a canyon exposure showing the upper boundary of the flow unit and typical column spacing of the entablature section of the flow. Note that column diameter varies with position relative to the upper boundary. A column-normal fracture also is identified.

2.1.3.2 Digital Analysis of Field Data

In August and September, 1995 we prepared photomosaic images from the July field work by converting all photographic data into a digital format. This allowed us to remove primary distortion induced by non-orthonormal camera positioning in the field. We digitally amalgamated the corrected images to form a complete scaled image of the fractures exposed at the investigation site as well as for three other sites. In doing so, we were able to map the fracture geometry within the complete flow unit. This is an important step in the analysis of the gas injection and tracer testing at the investigation site.

2.1.3.3 Discussion of the Basalt Flow Boundary

The boundary zone of the basalt flow is defined as the outermost few centimeters of fragmented material, as well as any interbed material such as soils or clays. This zone appears to form a strongly preferred flow path, based on observations of secondary mineral alteration on the canyon walls. Coring techniques do not allow for recovery of the boundary material (also referred to as the rubble zone) in an undisturbed state; thus, we must characterize this feature *in situ* where exposure allows. The boundary at the base of the flow unit tends to be sharply-defined over a thickness of millimeters to centimeters, and is often identified by a lack of vesicularity and lack of closely-spaced fractures compared to the entablature of the unit below. The upper boundary is correlated with the presence of significant vesicularity, the smallest-diameter columns, and pahoehoe texture at the outermost surface.

At depth, a sub-horizontal clay interface may be an indicator of a paleo-soil horizon between adjacent flow boundaries. The presence or lack of a paleo-soil surface is controlled by the climatic conditions and time span between flow events. Thus, the clay layer thickness varies between mm and cm depending on the history of the unit. The presence of a soil horizon (or clay layer) indicates a possible flow boundary, but the lack of a recognizable soil interface cannot be taken to rule out a flow boundary. In general, it is reasonable to expect that boundary interfaces can be traced laterally to the full extent of the flow, as breaks are not usually seen except at the physical edge of the flow. One caveat is that the flow geometry tends to be less systematic in areas near the origination vent and final termination of the lava flow. This is likely due to the unusual concentration of collapsed lava tubes and general complexity of the flow geometry.

2.1.3.4 Fracture Characterization

Three distinctive types of fractures have been identified and studied: column-bounding fractures, column-normal fractures, and fracture zones.

Column-bounding fractures (Figures 1.2 and 1.3) form as a direct result of stresses from the cooling and resulting shrinkage of the basalt flow. Thus, their orientation is controlled by the orientation of the local thermal gradient and the local stress field (*DeGraff and Aydin*, 1993). Our observations of the orientation and spacing of the column-bounding fractures agree with previous work that identifies column diameter and height of the vertical fractures as being a function of the cooling rate and thus the geometry of the basalt flow. The upper portion of the flow unit, called the entablature, generally consists of columns of a smaller diameter, due to the rapid cooling from the effect of the convective upper boundary condition. The lower portion of the basalt flow, called the colonnade, generally consists of more widely-spaced columns forming as a result of the slower rate of cooling from the conductive boundary condition (*DeGraff et. al.*, 1989). The relative thicknesses of the entablature and colonnade is a measure of the comparative efficiency of cooling from the flow top and flow bottom. The lateral edges of the basalt flow feel the effect of both the upper and lower boundaries, and thus often contain smaller columns of inclined orientation (Figure 1.2) in response to the rapid cooling and resulting thermal gradient.

Column-bounding fracture continuity is an important consideration in identifying hydrological units for analysis. In the case of the investigation site, column-bounding fractures forming upward from the base of the colonnade meet and connect to downward propagating fractures from the entablature (Figure 1.2). In general, the nature of the connection between the upper and lower boundaries varies, and is not well characterized because of the two-dimensional exposure of the three-dimensional fracture surfaces. Upcoming analysis of collected data will address this issue. This connection is critical for understanding infiltration.

Column-normal fractures (Figures 1.2 and 1.3) are observed in the Box Canyon site along the vertical canyon walls. These fractures tend to be concentrated in the upper portion of the flow unit — mainly within the entablature — although they also are seen in the colonnade to a lesser extent. Two types of column-normal fractures appear to exist: one in which the lateral extent is less than the width of a single column; and another type, which may cut across several column-bounding fractures. Column-normal fracture spacing is roughly correlated with the column diameter, and upcoming detailed analysis of fracture spacing will seek to model and explain this observation. These fractures may connect vertical fractures and also play an important role in infiltration.

We investigated two exposures of fracture zones that were found between the upper part of a colonnade and the lower part of a flow unit in the canyon. The fracture zone illustrated in Figure 1.4 consists of an anastomosing series of apparent Mode I fractures which show little or no fracture-parallel displacement. The internal structure, lateral extent, and continuity of fracture zones will be an important criteria in the correlation of any core data with canyon exposure and in interpreting their role in fluid flow. Our analysis of the interaction of the fracture zones, the column-normal fractures, and the column-bounding fractures will be based on the data collected during FY 95.

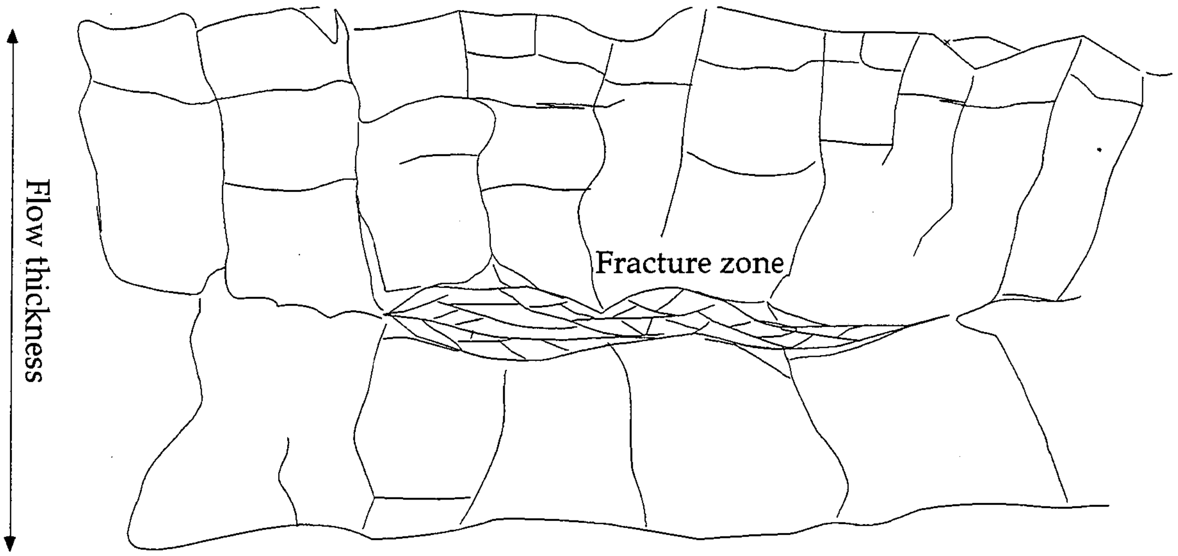

Figure 1.4. A schematic map of a fracture zone located between the entablature and colonnade of a flow unit at Box Canyon.

2.1.4 FY 96 Work

Analysis of fracture geometry will be based on the fracture mapping and characterization that will continue through 1995 and in part through 1996. An important goal is preparation of a complete fracture survey, which includes characterization of fracture orientation, spacing, and connectivity. From this, we will develop a model to predict fracture characteristics given information about the material parameters, basalt flow geometry, and boundary conditions. The output of this model will aid LBL in determining the hydrological characteristics of the Box Canyon experiment site and other unknown basalt units.

2.1.5 Significance

If this work is successful, one should be able to understand how the fracture geometry in basalt flows connects to conduct vertical flow. In addition, we may be able to use basalt flow unit thicknesses obtained from borehole data to estimate the fracture density and consequently the hydrologic properties of the flow units. The flow thickness/fracture density relationship is important because boreholes are generally vertical or near-vertical, so basalt flow thickness is readily observable, whereas vertical fractures are likely to be missed. Knowledge of hydrologic properties will be enormously useful for constructing flow and transport models of the rock beneath INEL. For instance, most Waste Area Groups (WAGS) are modeling subsurface flow and transport for risk assessment, and this study will provide valuable information for quantifying the rock matrix. Ultimately, for remedial design purposes, this detailed knowledge about the basalts will be needed to perform a mass balance, select and design the final remedy, and monitor clean-up and operate the system in a cost-effective manner.

2.2 Task 2. Remote Sensing Methods for Seeing Fracture System Geometry and Methods for Seeing the Location of Water in the Vadose Zone

2.2.1 Background

Geophysical methods can help to see the fluids moving through the opaque fractured medium and to locate important features that can have a large effect on fluid flows. To detect fluids, we are focusing on electromagnetic (EM) methods because water changes the electromagnetic properties of the medium. The key problem is to get sufficient sensitivity and resolution given the small amounts of water that may be involved. For determining the location of major structural features such as rubble zones or distinct basalt columns, we are looking at seismic interface waves as a possible imaging tool.

In FY 94, INEL conducted dc resistivity measurements in conjunction with the Large Scale Infiltration Test (LSIT). The dc resistivity method applied in a mode called "geometrical sounding" provides resistivity information at depths proportional to the transmitter-receiver (Tx-Rx) separation. The wider the Tx-Rx separation, the deeper the penetration we achieve. Electrical resistivity calculated using the measured data is attributed to a depth equal to one half of the Tx-Rx separation and is called the 'apparent' resistivity.

Another EM method called CSAMT is considered to be a promising geophysical technique to compare with dc resistivity. CSAMT is an audio-frequency magnetotelluric (MT) wave EM technique in which subsurface resistivity can easily be calculated using the ratio of the electric field to magnetic field. The method uses a high-frequency controlled source to generate waves which simulate plane waves a short distance away from the source. The plane wave approximation of the controlled-source field requires that the source-receiver separation be no less than 3 to 4 skin depths. The skin depth is 500 times the square root of the ratio of the resistivity to the frequency. So, if the average resistivity is 100 ohm-m and the frequency used is 1 kHz, the skin depth is about 170 m. For the plane wave assumption to be valid in this case, the source-receiver separation needs to be at least 500 m. The software used to interpret CSAMT data, assuming that waves are plane waves, is the same as that used for MT data. This code has been developed at LBL under other DOE projects, in particular one within the geothermal program.

Unlike the dc resistivity method, which varies Tx-Rx separation to vary the depth being investigated, the CSAMT method is based on frequency sounding. Apparent resistivity underneath the surface can be calculated using the plane wave impedance as a function of frequency. As we lower the frequency the attenuation is decreased, and therefore, the impedance tends to contain resistivity information from deeper regions. Based on the sounding mechanisms and other considerations it is commonly acknowledged that the dc resistivity method should be sensitive to resistive layering, and more affected by lateral resistivity variations. In general, CSAMT has a greater depth of penetration than the traditional high resolution ground penetrating radar (GPR) techniques, but provides lower resolution.

In the infiltration experiments planned for Box Canyon, one of the key issues we face is to image the flow of water with very high resolution (< 1m). Monitoring will involve measurements at all phases of an infiltration test. The first set of data will be collected before the infiltration begins. This data will yield information about the baseline geologic structure. Subsequent data sets will be collected during the infiltration experiment in order to monitor the infiltration process through changes in the electrical properties created by water. A final set of measurements will be made some time after the completion of infiltration to determine if the site has returned to its original state.

The resolution provided by CSAMT may not be adequate for this site, so we need to investigate the use of high frequencies, *i.e.,* radar. Radar is used widely in ground water applications primarily though GPR. This method works well because water has a high velocity contrast and high reflectivity coefficient for radar waves. The higher the frequency we use, the higher the resolution, but the greater the attenuation. Therefore we need to look for radar systems that are powerful enough to overcome attenuation at high enough frequencies. Success with seeing the water in the rock will be seen by comparing surveys done before, during and after the application of water to the system. Changes in the response will be due to the presence of water. Reflection methods are expected to be better suited to this problem than transmission methods (*e.g.*, tomography) because the amount of water is small. The delay in travel time through a small amount of water may not be noticeable, but even a small amount of water may be a good reflector.

In order to detect major features, such as regions of strong vertical fracturing or horizontal fractures connecting wells, we are looking at some promising new seismic techniques for seeing connected features, which act as a wave guides that channel seismic energy. These may be able to image subsurface fracture structures and evaluate the continuity of interbeds in three dimensions. Hydrologic modeling requires more data than is easily obtainable from drill holes. Features of particular importance are fractures and faults that may provide highly conductive pathways and the distribution of interbed structures, which may act as hydrologic barriers. The coal mining industry has used this technology to locate faults in coal seams. More recently, it is being developed to determine the continuity of thin flow units on the kilometer scale for gas and oil production. This technology may have application to the remediation of the TSF-05 injection well hotspot. This remediation will require detailed knowledge of the fracture connections between wells less than 30 m apart. These fractures are filled with mixed waste sludges and possible DNAPL's, which must be removed or stabilized. Delineation of these waste flow paths is critical and will be accomplished using a combination of hydrologic tests, geophysical logging and tracer testing.

2.2.2 Performer

The data acquisition and initial analysis of CSAMT, borehole radar, and laboratory feasibility study for seismic channel waves were done by LBL and funded by EM50. Related work is being done at LBL in interpretational technology for EM data. This includes high-resolution imaging funded by BES and development of a high-frequency capability, which is funded by another EM50 project. Results of the CSAMT survey at the Large Scale Infiltration Test site were compared with results of INEL's FY 94 dc resistivity survey conducted there.

2.2.3 FY 95 Activities

2.2.3.1 CSAMT

The CSAMT Experiment Design

CSAMT data was collected subsequent to the 1994 Large Scale Infiltration Test to yield information about changes in resistivity due to drainage. This method was chosen to complement information obtained from previous dc resistivity surveys conducted by INEL before and during the infiltration test. The hope is that the dc resistivity survey and CSAMT survey, in conjunction with the hydrologic and tracer data, can help determine large-scale subsurface transport structures by providing useful information about fracture characteristics and the location of perched water table. This will help to predict which fractures are likely to be responsible for fast flow.

We used the field system STRATAGEM (subcontract to EMI) for this purpose. The system can digitize and process two orthogonal sets of electric and magnetic fields at a rate of up to 192,000 samples/sec simultaneously. It is capable of 10 channel (6-electric/4-magnetic) data acquisition with a 20 Hz ~ 88 kHz bandwidth. Short orthogonal electric dipoles were used to measure the electric fields and two horizontal magnetic sensors for the magnetic fields. Vertical loops, instead of a conventional long grounded electric dipole, were used as the source. Two traverses, NS and EW (see Figure 2.1), each 405 m long, were covered with a fixed dipole length of 15 m.

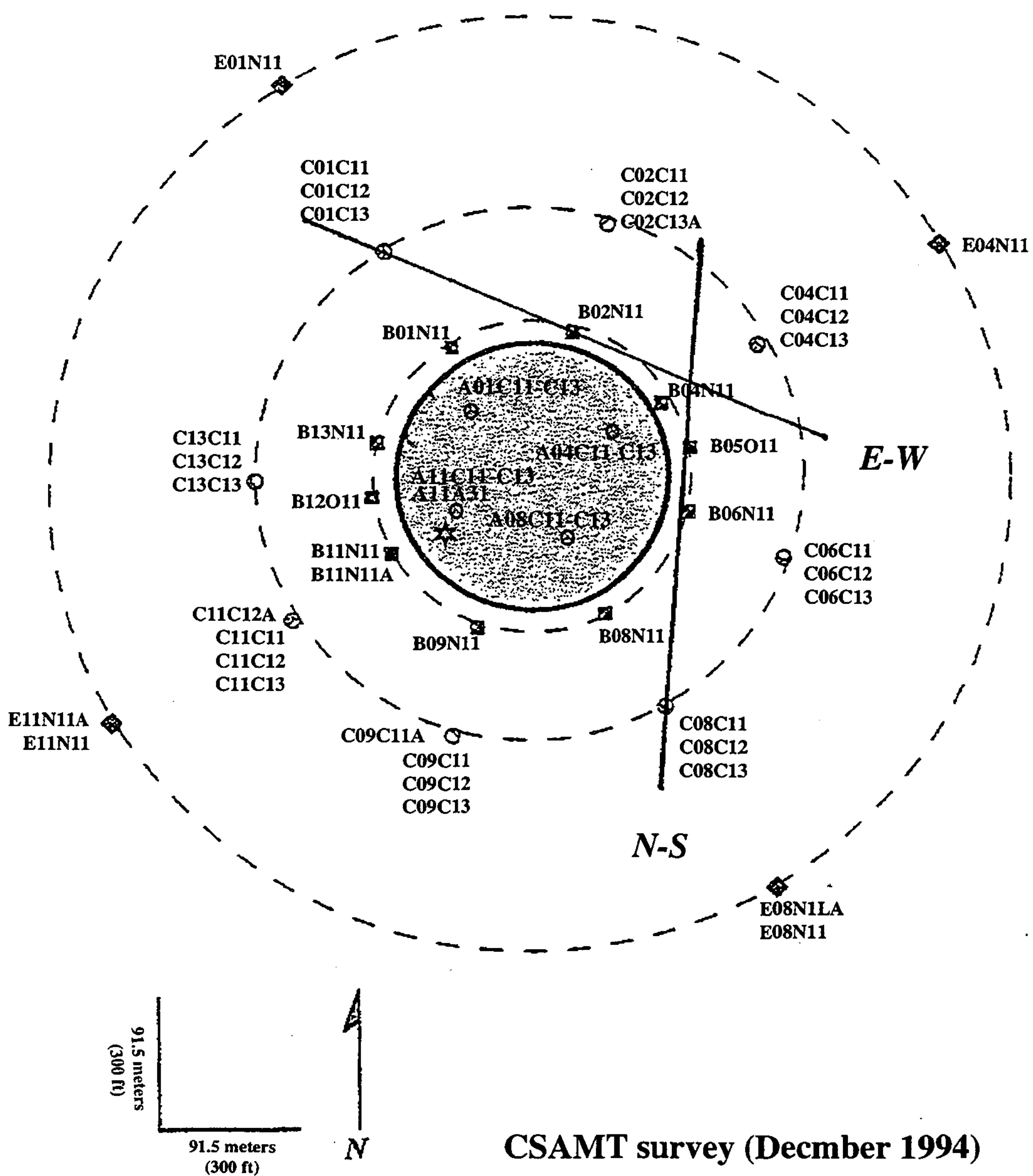

CSAMT survey (Decmber 1994)
at the Large Sale Infiltration Test site

Figure 2.1 Schematic view of the LSIT site showing the two CSAMT survey lines.

The magnetic sensors used in this survey were two of EMI's high frequency BF-6 coils which have a minimum noise level of 1 μgamma/$\sqrt{\text{Hz}}$ and the electric field sensors used in this survey have only 40 nanovolts/$\sqrt{\text{Hz}}$ noise over the entire measured frequency range, which was from 100 Hz to 96 kHz. An orthogonal horizontal loop transmitter was set 300 m away from each profile to boost the signal level. The eight transmitted frequencies include 1, 2, 3, 6, 10, 20, 30, and 70 kHz.

Twenty-seven stations consisting of 15 m electric field dipoles were measured along the two survey lines which trend approximately north-south and east-west. Along the 405 m long traverses, the orthogonal electric field (Ey) was shared between two neighboring Ex dipoles oriented along the survey line. Figure 2.2 shows the typical field set up used for the measurement.

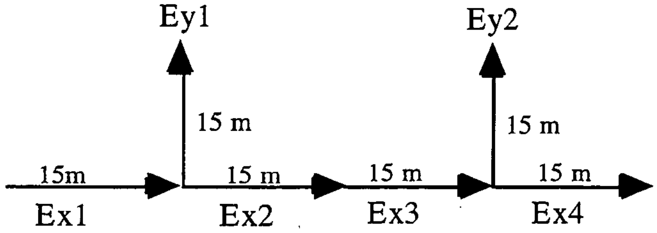

Figure 2.2. Field configuration where each arrow represents direction of E fields.

In addition to electric dipoles (Ex and Ey), an orthogonal pair of magnetic sensors for Hx and Hy are located at the junctures of three electrodes.

Single-polarization of the naturally occurring very low frequency (VLF) signal and thunderstorm activity, along with a mechanical problem with the small EMI transmitter, resulted in some difficulties in calculating the impedance tensor above 1 kHz.

Data Interpretation

Data collected on these lines were first spatially filtered using 'EMAP' processing, and then 1D Bostic inversion was applied to the filtered impedance. The results are shown in Figures 2.3 and 2.4 for N-S and E-W profiles.

A further analysis was made by inverting the original impedance data using the 2D MT inversion algorithm developed at LBL. The final resistivity-imaging cross sections are shown in Figures 2.5 and 2.6. INEL's dc resistivity survey also indicates that there is a strong resistivity anomaly at positions marked by 300m near the surface in both Figures 2.5 and 2.6, confirming that both dc and CSAMT surveys result in similar interpretations at this site.

It was suggested that the CSAMT could have provided a higher-resolution image than those shown by Figures 2.5 and 2.6. The effective highest frequency from the survey was about 20 kHz, and at this frequency the spatial resolution is on the order of 10 m. A preliminary analysis shows that the maximum frequency should have been higher than the one achieved during this survey. The high-frequency portion of the STRATEGEM did not work in the field test.

At frequencies below 3 kHz the 300 m separation was not wide enough to meet the requirement for a plane wave. Since the depth of investigation at the infiltration site is much shallower than, say 170m, the source effect at low frequencies should not affect the outcome of the investigation. Nevertheless, the source effect on the impedance needs to be further investigated for future work.

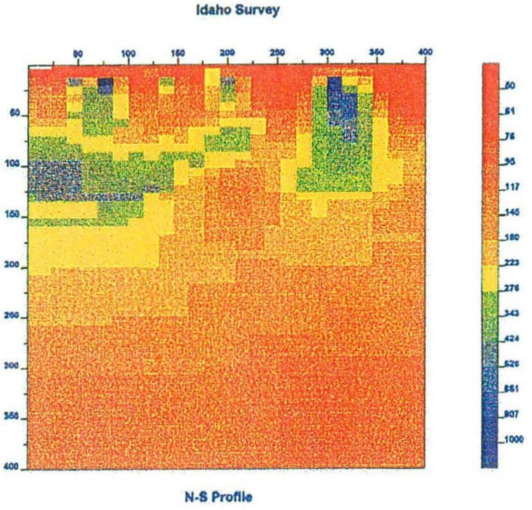

Figure 2.3. Resistivity tomogram (in ohm-meters) for a north-south vertical cross-section through the LSIT site, obtained from a one-dimensional Bostic inversion of the filtered CSAMT impedance data.

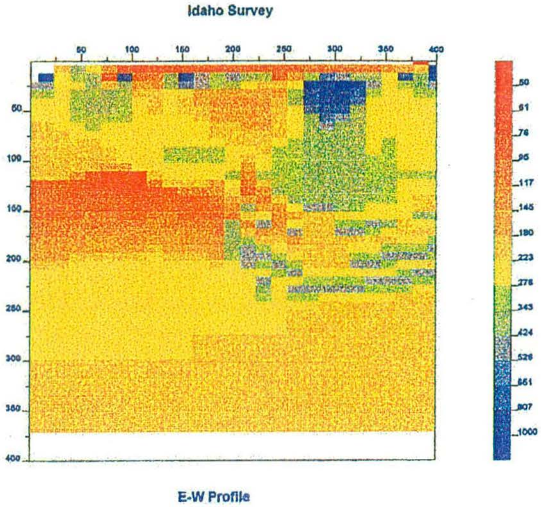

Figure 2.4. Resistivity tomogram (in ohm-meters) for an east-west vertical cross-section through the LSIT site, obtained from a one-dimensional Bostic inversion of the filtered CSAMT impedance data.

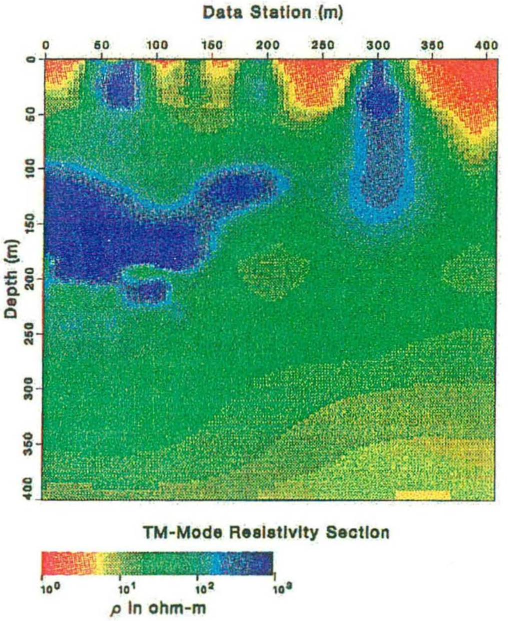

Figure 2.5. Resistivity tomogram for a north-south vertical cross-section through the LSIT site, obtained from a two-dimensional MT inversion of the CSAMT impedance data.

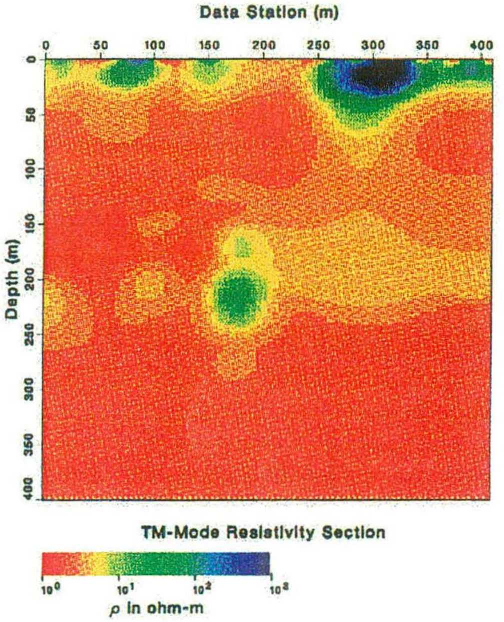

Figure 2.6. Resistivity tomogram for an east-west vertical cross-section through the LSIT site, obtained from a two-dimensional MT inversion of the CSAMT impedance data.

The success of this technology was assessed by comparison with results of the dc-resistivity surveys and data gained through vadose zone monitoring. These two surveys each found similar anomalies in the regions where they overlapped. However, the resolution of the method was not adequate for locating specific fractures or fracture zones which contained the majority of the infiltrating water. To achieve a one-meter resolution in a medium of 50 ohm-m resistivity, which is typical for the infiltration site, the skin depth should be on the order of 4 to 5 m. The frequency of the CSAMT system should be close to 1 MHz to get this resolution. Consequently, the current evaluation is that borehole radar may be a promising technology for the detection of infiltrating water.

Conclusions

The electrical conductivity at the Box Canyon site, especially at near surface, is much lower than that of the LSIT site. Because of this the frequency requirement for the CSAMT survey at the Box Canyon site will be much higher than that at the LSIT site. Since the existing system (EMI's STRATAGEM) can only operate at frequencies up to 100 kHz, we do not expect desirable results with a CSAMT survey at the Box Canyon site. Unfortunately, no high-frequency (above 100 kHz) system is available for this purpose in the market. With this in mind, we propose to investigate the feasibility of developing a high-frequency (100 kHz to 30 MHz) surface based EM system. The high-frequency system expected from the Very Early Time Electromagnetic (VETEM) project (funded by EM50) may be an excellent candidate for this application. The penetration depth range with this system will be up to 20 m in a typical Box Canyon type of environment whose electrical conductivity is around 0.001 to 0.01 S/m.

2.2.3.2 Test of High Frequency Radar Systems

A proof-of-concept geophysical study was conducted at the Box Canyon and RWMC Cold Test Pit sites by *Knutson and Wood* (1994) using seismic, GPR and borehole radar. Our task this year consisted of reviewing borehole radar data obtained at Box Canyon, and based on the outcome of this analysis, conducting a preliminary test to evaluate commercially available radar systems, and finally developing a survey design for the future work at Box Canyon in support of our hydrologic investigation.

We reviewed the data obtained by INEL in FY 94 at Box Canyon. The wellbore radar experiment appears to have been reasonably successful in imaging basalt flow units at the Box Canyon site. A rubble zone between upper and lower units had been identified from exposure on the cliff face and information from borehole H1, and was inferred to be horizontal (Figure 2.7a). In the tomogram (Figure 2.7b), the rubble zone is seen to be dipping down away from the cliff face, demonstrating the additional two-dimensional information obtained from the radar survey. Based on the limited information derived from INEL's radar experiment, and in collaboration with LBL's on-going hydrologic characterization experiments, we have conducted a preliminary radar survey at Box Canyon described below.

The intent of this task is to design and conduct a high-resolution borehole radar investigation at the INEL Box Canyon test site and to determine its ability to characterize the vadose zone at the site, by determining the location and extent of subsurface physical structures such as high angle fractures and interflow rubble zones. The principal research site is on the northern margin of Box Canyon, approximately 6 miles southeast of Arco, Idaho. The primary medium under investigation is the fractured vadose zone basalt.

Previous research work with ground penetrating radar systems suggested that the Sensors and Software Pulse Ekko 100 was the most technically capable and cost-effective commercially available radar system. This system has been used by LBL for multiple sight characterization surveys in conjunction with DOE's Subsurface Science program. The results obtained using this system are superior in both data resolution and signal-to-noise ratio to those obtained during earlier surveys using another radar system, the GSSI SIR system. In many cases, subsurface features imaged successfully by the Pulse Ekko 100 were either not observed or were obscured by noise in data collected by the SIR system. The Sensors and Software Pulse Ekko and the GSSI SIR systems are the primary radar systems being used today and are therefore the most readily available for use by LBL researchers. Other radar systems, such as RAMAC designed by ABEM, have been developed, but their availability and cost make them unsuitable. Additionally, not all companies manufacturing ground penetrating radar systems have designed equipment suitable for downhole use.

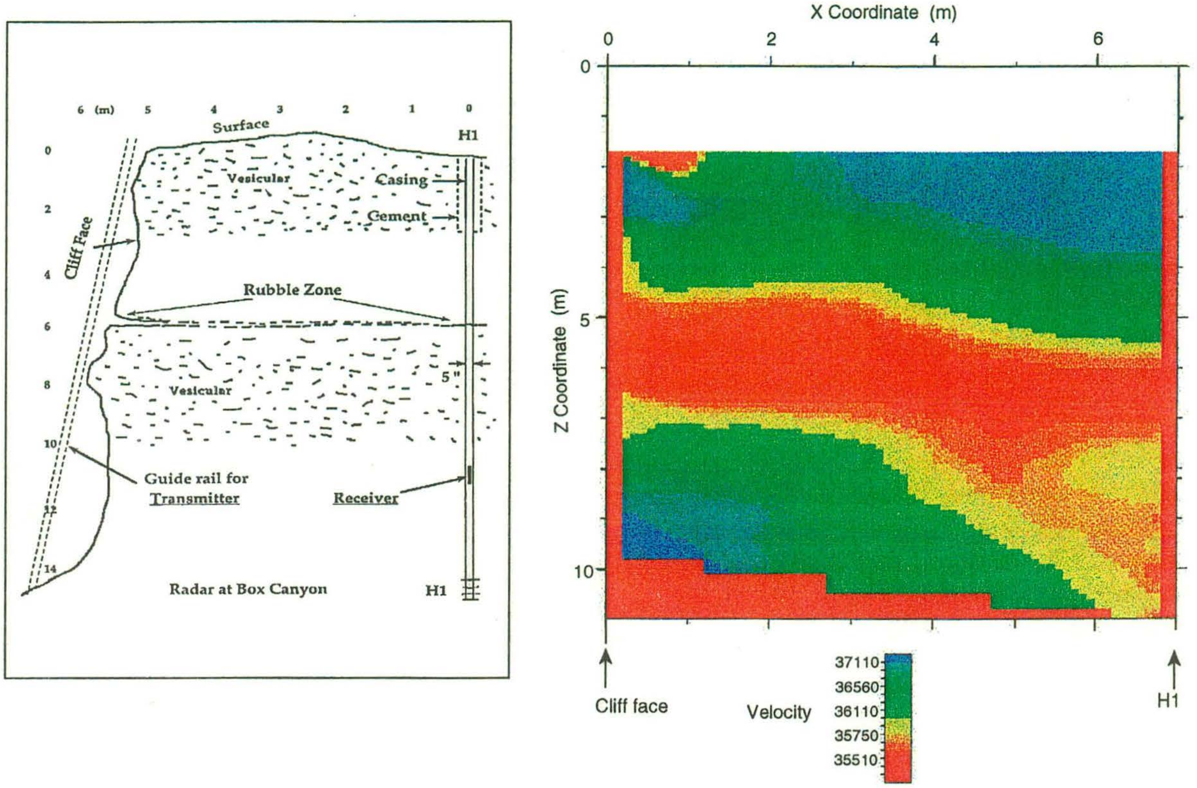

Figure A

Figure B

Figure 2.7. Results of a previous wellbore radar experiment conducted at Box Canyon (*Knutson and Wood*, 1994). a) Sketch based on cliff-face and information from borehole H1 suggested a horizontal rubble zone at a depth of 6 m; b) velocity tomogram revealed that the rubble zone actually dipped away from the cliff face.

Based on conversations with experts in the field of radar investigation (Gary Olehoff of the Colorado School of Mines, Dave Wright of the USGS-Denver, Randy Kath of the University of Georgia) and with LBL's past research work, the decision was made to utilize the Sensors and Software Pulse Ekko 100 equipped with downhole antennas. The experience of the aforementioned researchers was uniform and suggested that the GSSI borehole radar system needed substantial improvements and modifications before being a field-worthy system. Attempts were made to utilize the modified GSSI systems owned by the USGS and the School of Mines, however both systems were in steady use and were unavailable at the time of the Box Canyon experiment. Additionally, previous research work at INEL (*Knutson and Wood*, 1994) utilized a downhole system designed by the Swedish company ABEM. Although highly regarded, this system is very expensive and unavailable for use by most commercial geophysical surveying companies. The system used by *Knutson and Wood* (1994) is owned Raytheon Nevada and was not available at the time of the experiment.

Sensors and Software, Inc. of Canada supplied the borehole radar antennas and an operator. North American Exploration of Virginia supplied the radar electronics and recording system and an operator. Personnel from LBL supplied technical expertise and field assistance. The data collection effort was conducted during a seven-day period from September 23 to 29. Preliminary processing and interpretation began thereafter and is continuing. A variety of datasets were collected using the borehole radar system. These included borehole-to-borehole transillumination, surface-to-borehole transillumination and single borehole reflection. Through the use of such complementary datasets, the borehole radar technique successfully provided interpretable subsurface characterization at the test site.

Field Design and Development

The borehole radar investigation was confined to the 17 wells already drilled at the Box Canyon test site (see section 2.5.3.2 for a complete description of the borehole layout). These wells varied both in inside diameter (ID) and in total depth (TD); specifically the five wells designated 'I-x' have TD of 12 meters, the eight wells designated 'II-x' have TD of 18 meters, and the four slant wells designated 'S-x' have variable depths from 3 to 20 meters. Datasets were collected in wells designated 'II-x' and 'S-x' in order to image as deeply as possible. All wells were measured prior to data collection in order to determine if well depths were accurate and whether collapse had occurred. Several wells, including II-1, II-4, and II-6, showed significant collapse at depths ranging from 10 to 16 meters. The well layout was designed according to the requirements of hydrologic investigations being conducted and is shown in Figure 2.8. (A table of well data is given in Section 2.5 where the design of the Box Canyon facility is discussed.)

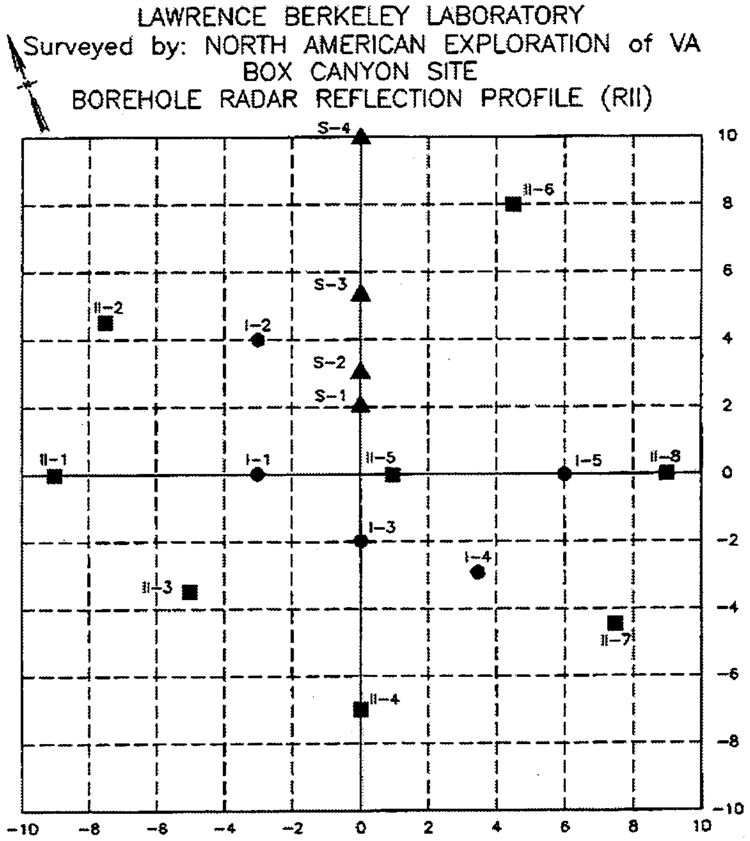

Figure 2.8. The Box Canyon well field layout.

Borehole Radar Design and Evaluation

The borehole radar system used in the investigation is the multicomponent Pulse Ekko 100 system manufactured by Sensors and Software, Inc. The system consists of two 100 MHz borehole antennas powered by batteries located at the surface. All components are driven by software that transfers operator-defined parameters (sampling interval, number of samples, *etc.*) to the transmitter/receiver electronics. The transmitter antenna transmits a set number of radar pulses to be received, averaged and stored by the receiver antenna, receiver electronics and computer recording system.

The Box Canyon radar investigation comprised several data collection methods, including borehole-to-borehole, surface-to-borehole, and single hole. The borehole-to-borehole transillumination method was conducted entirely within the boreholes and consisted of two profile collection styles. A multiple offset profile (MOP) was done where the transmitting radar antenna was held fixed while the receiving radar antenna was moved through its full range of positions within the hole. Once this was completed, the transmitting antenna was lowered and the cycle was repeated, continuing this way until all positions within the hole were used. A total of 4 well pairs were completed in this fashion and are shown in Figure 2.9. Alternatively, as a zero offset profile (ZOP), the transmitting and receiving antennas were moved simultaneously and at equal spacing down the boreholes. A total of nineteen well pairs were completed in this fashion and are shown in Figure 2.10.

The surface-to-borehole transillumination method was similar to the borehole-to-borehole method, with the exception that the transmitting antenna was located at the surface and the receiving antenna moved down the hole. This data was collected as an MOP with the locations shown in Figure 2.11.

The single hole reflection method was purely experimental in technique, as it had not been field tested prior to the Box Canyon investigation. In this method, the two antennas were fixed with a one meter spacing and lowered down the same borehole. Data from a total of five boreholes was collected using this method.

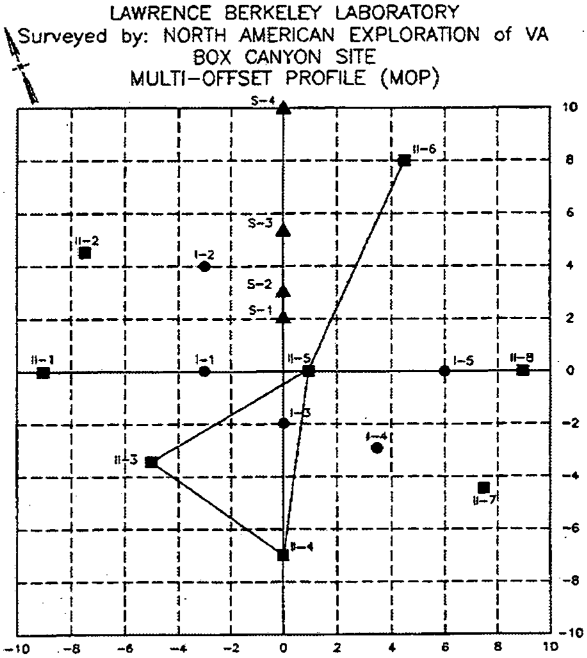

Figure 2.9. Map showing the location of MOP well pairs

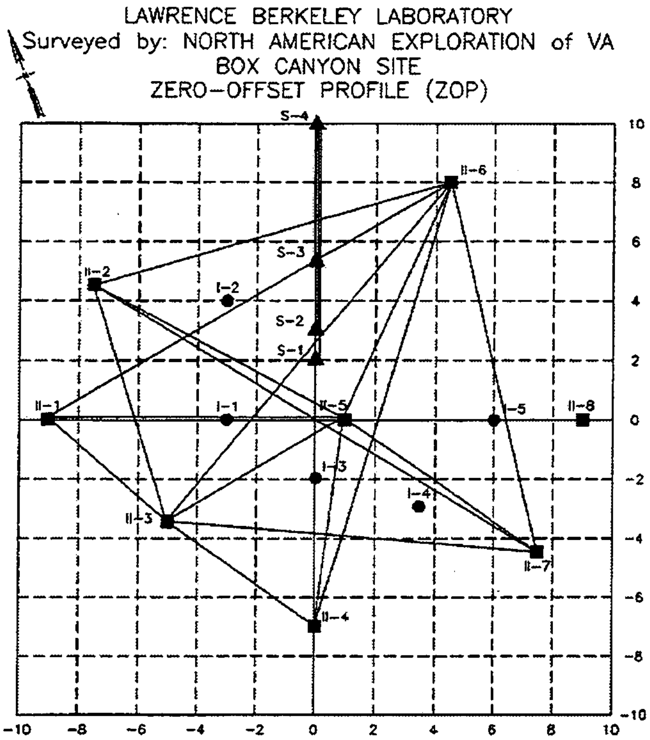

Figure 2.10. Map showing the locations of ZOP well pairs.

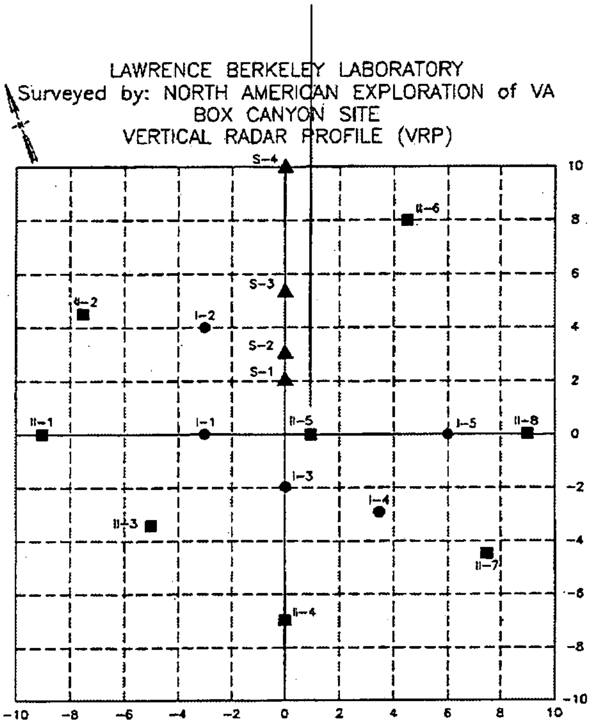

Figure 2.11. Map showing the location of the surface borehole survey.

Preliminary Results of Borehole-to-Borehole Transillumination

Preliminary processing of the borehole-to-borehole transillumination datasets suggests that radar is a promising tool for the purpose of characterizing fractures in basalt. The construction of tomograms and the careful analysis of crosswell signal travel times illustrate the ability of high frequency radar data to characterize both vertical fractures and the lateral extent of zones of interest (zones of high fracture and vesicle content, interflow rubble zones, *etc.*)

Predictive modeling was undertaken before the tomographic processing was completed. The analysis is based on simple 1D models. Both the source and receiver are electric dipoles simulating antennae adapted by the Sensors and Software's tool. The full waveform electromagnetic field cannot be computed directly in the time domain. To obtain the solution in the time domain, we first compute the solution in the frequency domain and then use a Fourier transform to invert it to the time domain. The frequency-domain solution of the electromagnetic field is symbolically written in the form of the Sommerfeld integral.

$$\tilde{E}(r,r_s,\omega)=\int_0^{\infty} f(z,z_s,\lambda,\omega)J_0(\lambda\rho)d\lambda \qquad (2.1)$$

$f(\cdot)$ is the spectrum of the electric field in the horizontal wave number domain. The subscript s indicates source position, ρ the azimuthal distance between source and receiver antennae, and ω the angular frequency of the electromagnetic field. The original code computing the 1D frequency-domain solution, EM1D, was developed at LBL for mining exploration and crustal studies using low frequencies (dc to 1 MHz). At these frequencies the electromagnetic field is dominated by induction which is basically governed by a diffusion equation. To investigate environmental problems at shallow depths, however, it is necessary to use high frequencies for enhanced resolution. The high-frequency version of EM1D was subsequently developed under the VETEM project. When the frequency is increased to a few MHz and above, the electromagnetic field is now governed by a wave equation. The propagating wave is still subject to attenuation due to the electrical conductivity of the medium. So the high-frequency electromagnetic field (radar is one example) needs to be powerful enough to propagate through a lossy (electrically conductive) medium.

The voltage in the transmitting antenna has its own waveform. The resulting electromagnetic field measured with the receiving antenna will have the following expression in the time domain.

$$E(r,r_s,t)=\frac{1}{2\pi}\int_{-\infty}^{\infty}\tilde{g}(\omega)\tilde{E}(r,r_s,\omega)e^{i\omega t}d\omega \qquad (2.2)$$

Here, the term $\tilde{g}(\omega)$ represents the frequency spectrum of the waveform of the transmitter voltage. In the inverse Fourier transform, the highest frequency necessary to achieve 1 nanosecond sampling in the time domain is 500 MHz.

The model used for prediction is described in Figure 2.12. The fracture is simulated by a thin layer filled up with saturated soil. The conductivity of the saturated soil used is 0.2 S/m and the dielectric constant is assumed to be 40. The wavelengths at 100 MHz in the basalt (background) and in the fracture are about 10m and 5m, respectively. The source voltage waveform used is a Gaussian pulse with its half-amplitude pulse width of 8 nanoseconds. The center frequency of this waveform is a little over 100 MHz. Both the y- and z-components of electric fields at the receiver are shown in Figure 2.13. Because of the dispersive nature of the conductive medium (0.002 S/m), the waveform of the electric field at the receiving antenna becomes distorted. Based on a

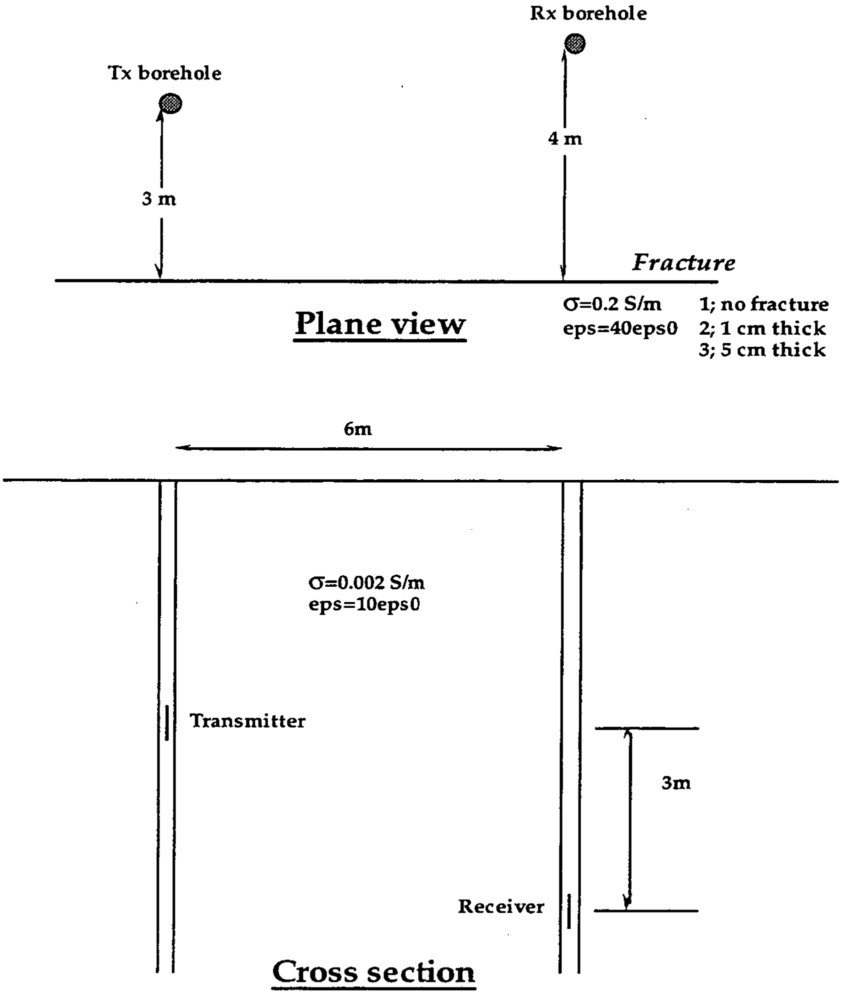

Figure 2.12. The model used for predictive modeling of borehole-to-borehole transillumination.

comparison of the fracture thickness and the wavelength, we did not expect a measurable reflection off the fracture if the thickness were much less than 1 meter. The modeling result, however, shows that the reflection can be still significant even when the fracture thickness is only 1 cm (a 7% anomaly in the reflection). The percent anomaly of the reflection is increased to 35% if the thickness is 5 cm. This is a very positive finding in terms of the utility of the borehole electromagnetics (*i.e.*, radar) for detecting and characterizing fractures in the vadose zone.

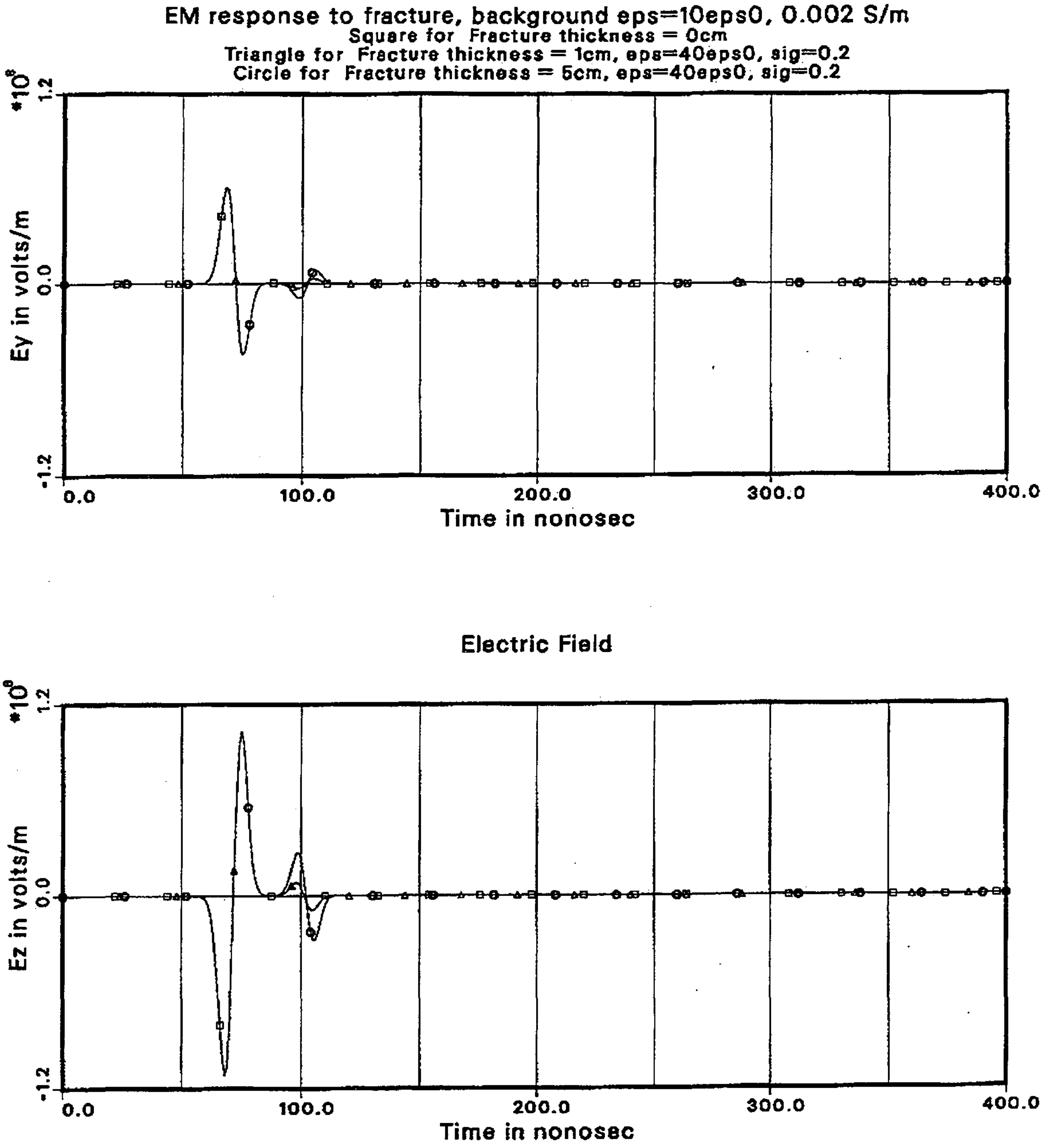

Figure 2.13. Theoretical EM responses to a fracture.

2.2.3.3. Crosswell EM

Careful examination of the crosswell (MOP) data sets, as shown in Figure 2.14, does not show much evidence of secondary arrivals that would identify reflections off vertical fractures. The strong secondary arrival shown in Figure 2.14a between receiver depths of 6 and 10 m is probably a reflection off a horizontal layer at a depth of about 6 m. The later weaker secondary arrival visible between receiver depths of 1 and 14 m closely parallels the first arrival, and probably is a part of the source signal. Similar conclusions can be made about Figure 2.14b. Therefore, velocity and amplitude tomograms, which make use of first arrivals, were created to see if the presence of vertical fractures can be inferred from this information.

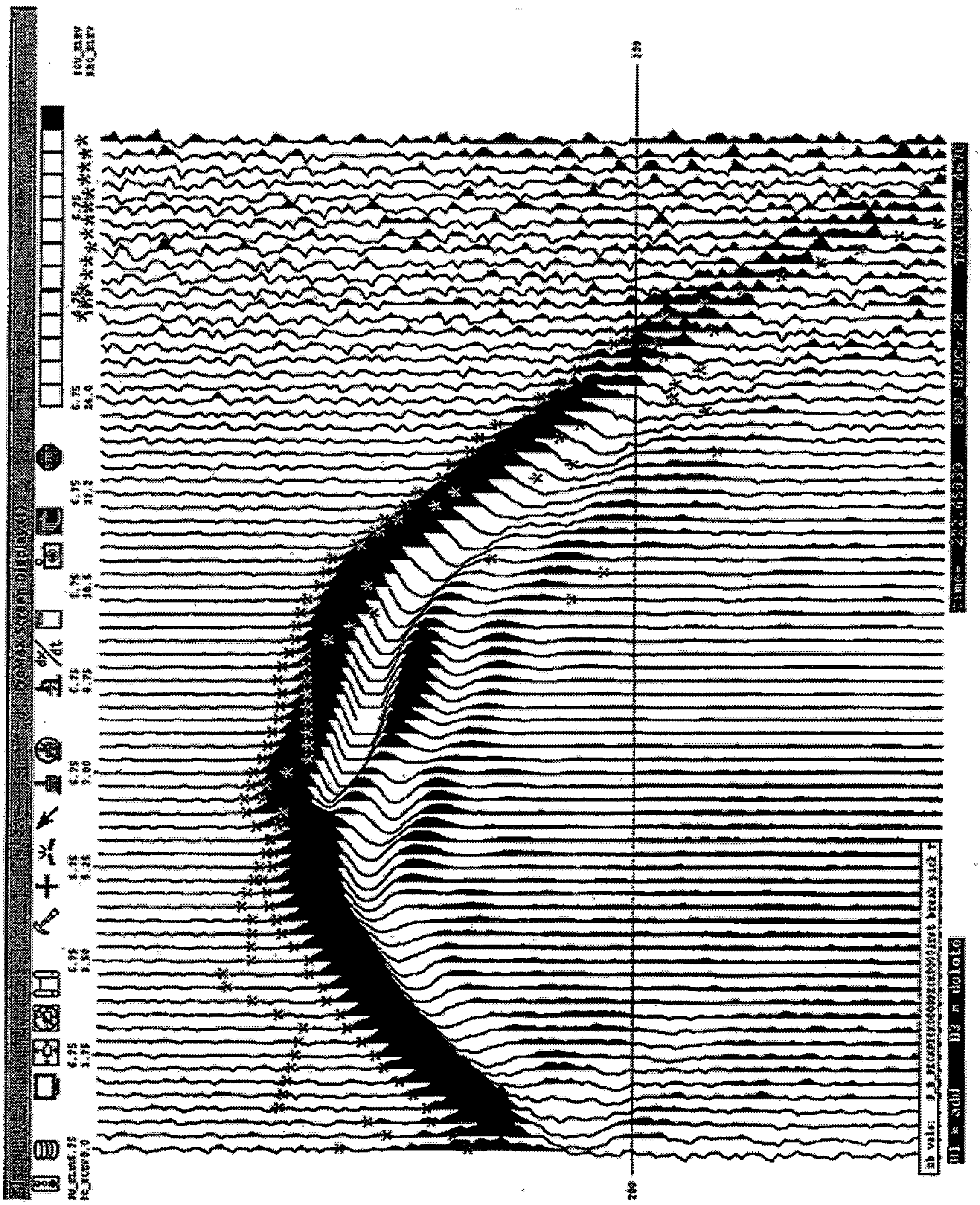

Figure 2.14a.

Figure 2.14a. Waveforms for the MOP well pair II-3/II-5. In (a) the source depth is held fixed at 6.75 m, while the receiver depth varies between 0 and 16 m.

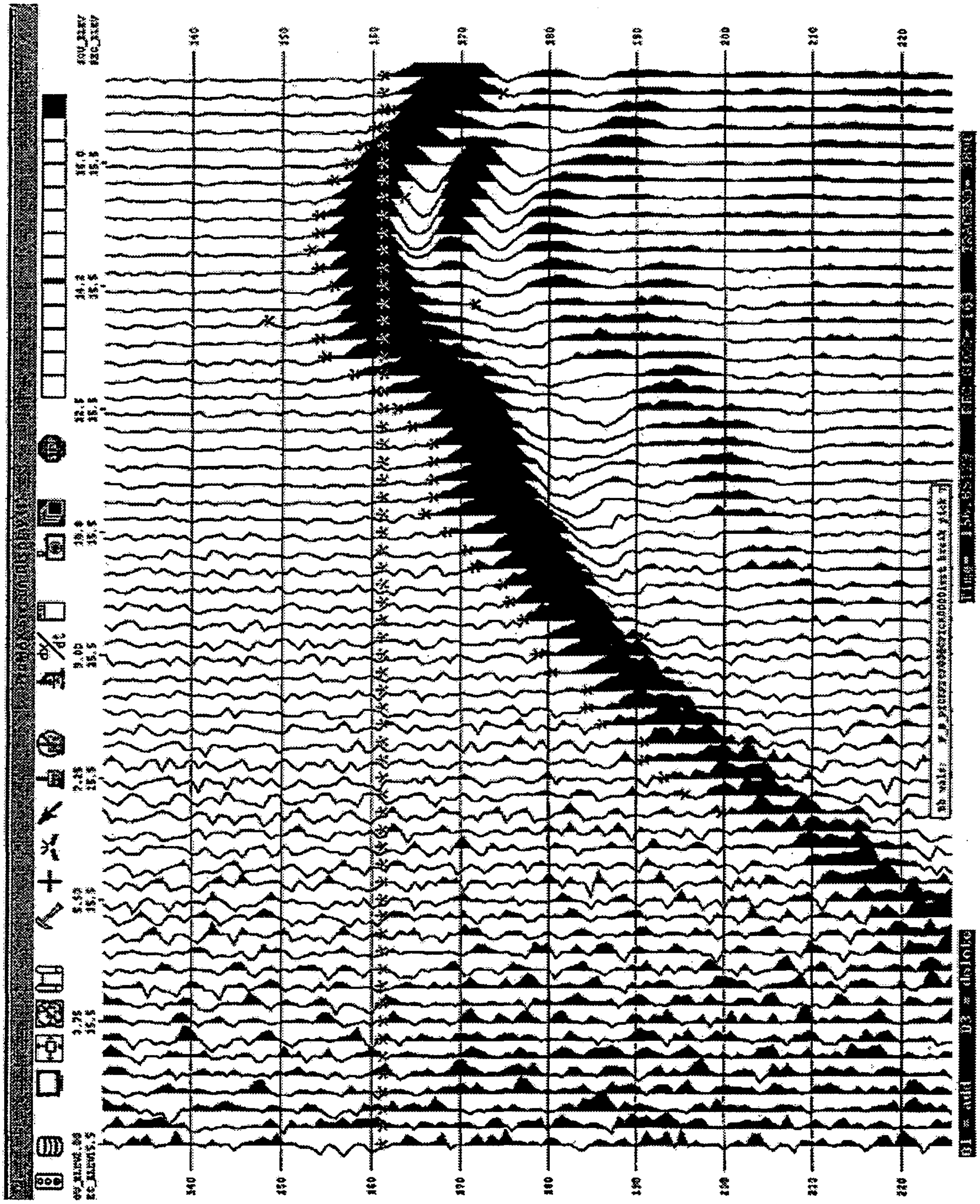

Figure 2.14b.

Figure 2.14b. Waveforms for the MOP well pair II-3/II-5. In (b) The receiver depth is held fixed at 15.5 m, while the source depth varies between 2 and 17 m.

The travel times from all four cross well pairs; II-3 to II-5, II-4 to II-5, II-6 to II-5, and II-3 to II-4 were inverted to produce preliminary velocity tomograms. Some difficulty was encountered in determining the zero time for each survey. Ultimately, we determined this value by calculating the travel time at various depths using the zero offset profile (ZOP) data sets for corresponding well pairs. The zero time for these data sets is determined accurately since calibration data was taken with the source and receiver antennas held together. These times were then compared to the times picked for the corresponding MOP well pair data and the zero time calculated.

Scatter plots of travel time versus source-receiver offset and velocity versus source-receiver angle for individual ray paths may be used to get an indication of the amount of heterogeneity and anisotropy present in the medium between the source and receiver. As shown in Figure 2.15, there is significant scatter in the travel time versus source-receiver offset plot, indicating substantial heterogeneity. In a homogeneous medium, this data would plot as a single straight line. For an isotropic medium, velocity would be independent of source-receiver angle, however, Figure 2.15 shows that this is not the case between wells II-3 and II-5.

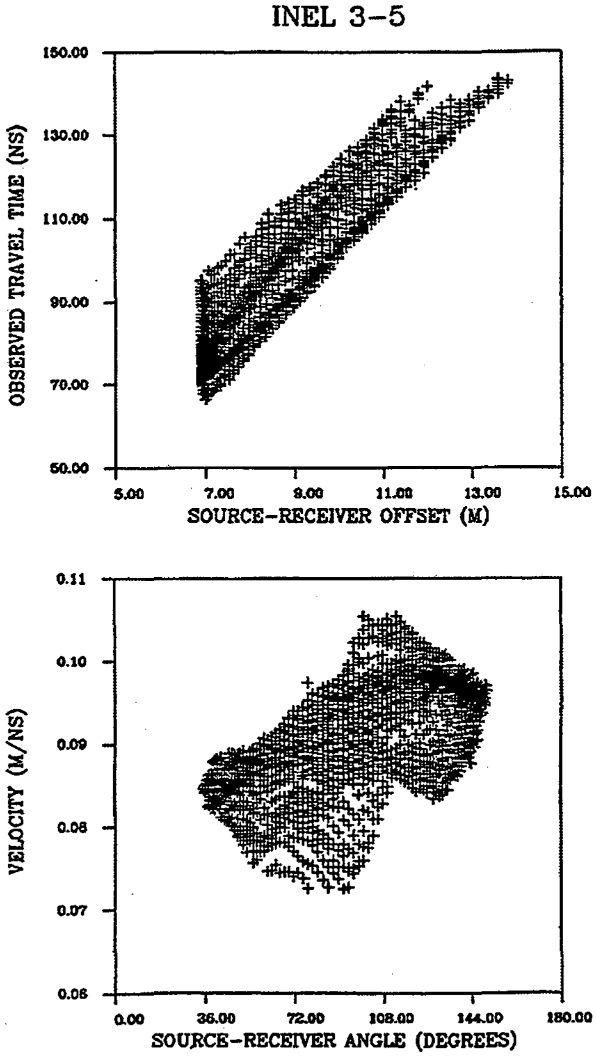

Figure 2.15. Travel time of individual rays as a function of source receiver offset and velocity of individual rays as a function of the angle between the ray and the vertical for MOP well pair II-3 to II-5.

The inversion algorithm we are using solves for an anisotropic velocity field, and the resulting tomogram shows the average velocity at each point. Comparable tomograms are obtained using an isotropic model, suggesting that anisotropy does not have a dominant effect. The velocity tomograms were produced using pixel sizes of about 0.5 meters in both the vertical and horizontal directions.

The velocity tomograms (Figure 2.16) are dominated by a horizontal feature at about 12 to 15 meter depth corresponding to a rubble zone - known from core data to be located at such a depth. (Depths assume a common zero at 5250 foot elevation.) The horizontal zone has a low velocity corresponding to a high dielectric constant. The dielectric constant is expected to increase with water content, so a low velocity zone could represent a vesicular zone, a fracture zone, or a rubble zone, all of which contain more void space than does the massive basalt, and under the wet conditions of the field experiments, have a higher water content. Another weaker zone is observed at about a 6 to 8 meter depth. The thickness of this zone appears to be highly variable. Well pair II-6 to II-5 shown in both 2.16a and 2.16b contains a well defined low velocity tenure extending horizontally across the image. This may correspond to a rubble zone. The line segments indicate the direction of maximum velocity. Figure 2.16c is an unfolding of the three surveys II-3 to II-4, II-4 to II-5, and II-3 to II-5. There is considerable continuity between the survey results. The cross well data will not resolve vertical or very high angle fractures which do not intersect both boreholes, though they may be resolved in single well or ZOP data as reflections. Note that the data from well II-6 stops at about a 10 meter depth. Data below this level could not be acquired because of obstructions in the borehole. This level also corresponds to the top of the low velocity, high attenuation zone. Both these observation suggest a rubble zone at this depth. Similar obstructions were also found in II-3 and II-4, at a somewhat lower depth, but still within the rubble zone.

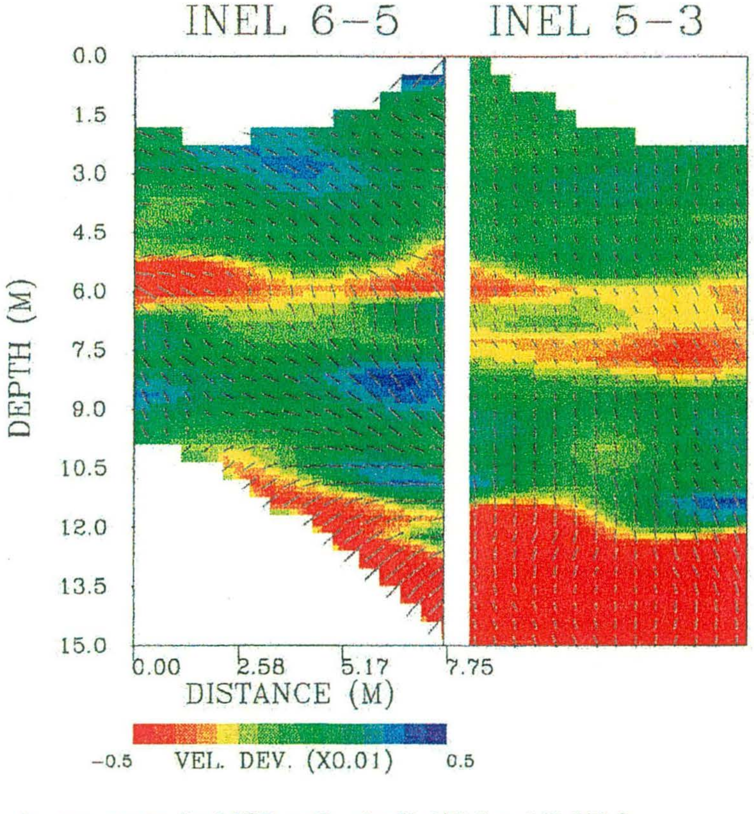

Figure 2.16a Velocity tomogram for MOP well pairs II-6/II-5 and II-5/II-3.

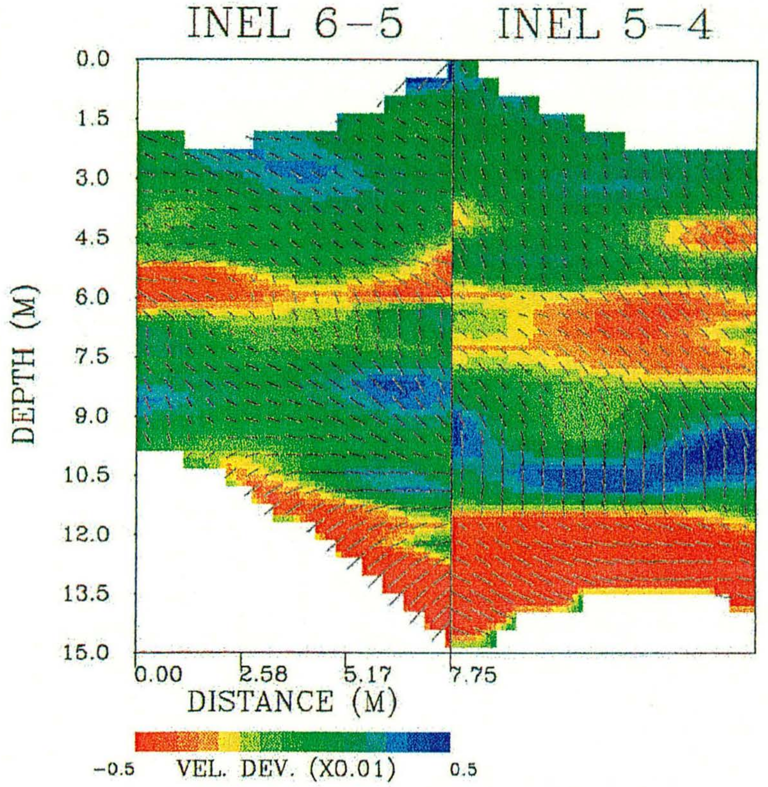

Figure 2.16b. Velocity tomograms for MOP well pairs II-6/II-5 and II-5/II-4.

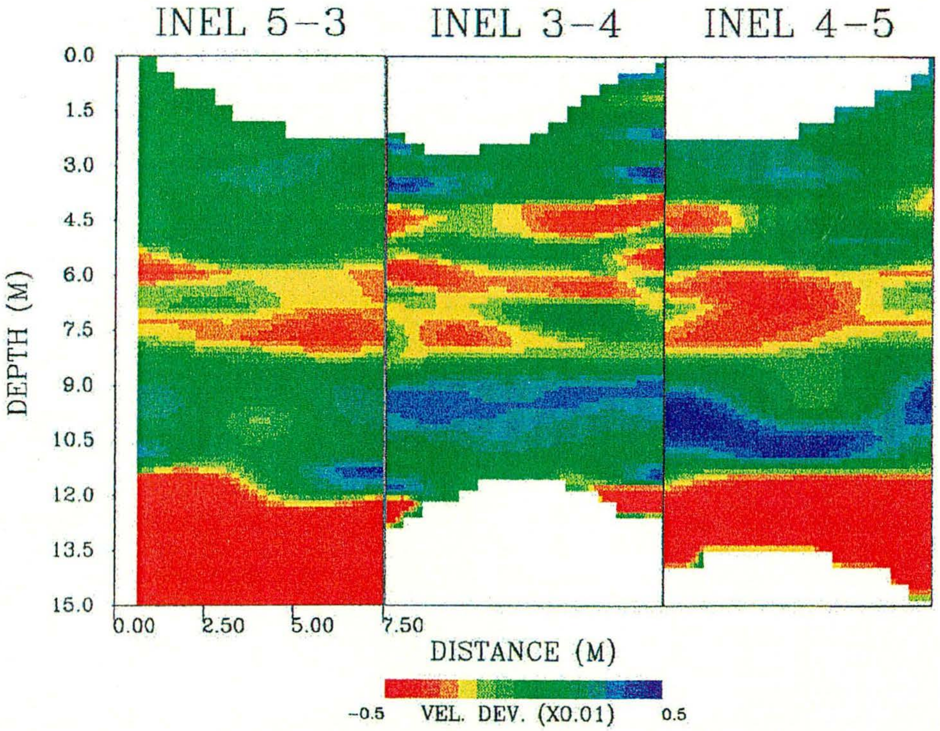

Figure 2.16c. Velocity tomograms for MOP well pairs II-3/II-5, II-3/II-4, and II-4/II-5.

In general, the various velocity tomograms correlate at coincident boreholes.

The Zero Offset Profile (ZOP) datasets are most useful in determining the lateral extent of zones of interest. Comparison of the ZOP well pairs shows consistent signal response when correlated with the known depths of such zones. For example, core data indicates the presence of a highly fractured zone bounding the upper region of a flow underlying the test site. This zone appears at different depths throughout the site varying from 7.5 to 8.5 meters. Close examination of the records reveal that signal arrival times are decreased upon reaching depths that correspond with this zone. This can be seen in Figure 2.17. This zone may act to focus the radar signal, thereby decreasing travel times. Air-filled fractures may represent regions of higher velocity, again decreasing travel times. A velocity tomogram based on ZOP arrival time data between wells II-3 and II-5 is illustrated in Figure 2.18. It is particularly useful in illustrating vertical change between the two wells and appears to correlate well with available core data. As with the MOP tomograms, areas of low velocity give some indication of fracture content and areas of high velocity some indication of massive or competent basalt.

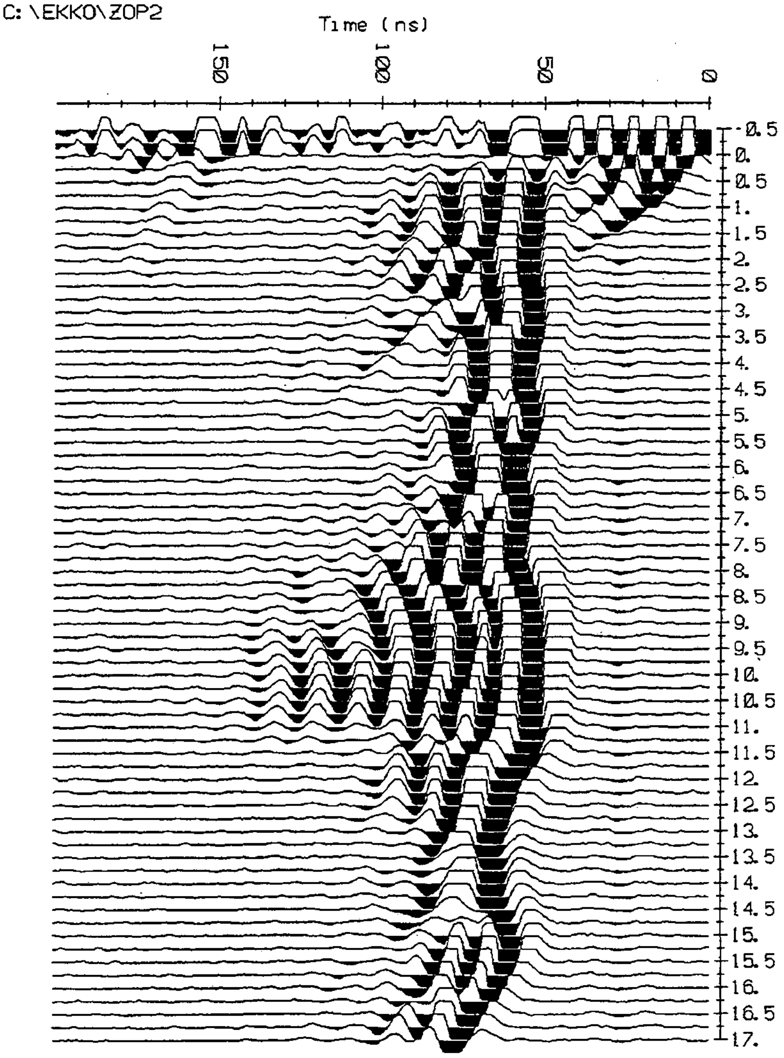

Figure 2.17. Waveforms for the ZOP well pair II-3/II-5. Note the arrival time decrease at depths between 8.5 and 11.5 m.

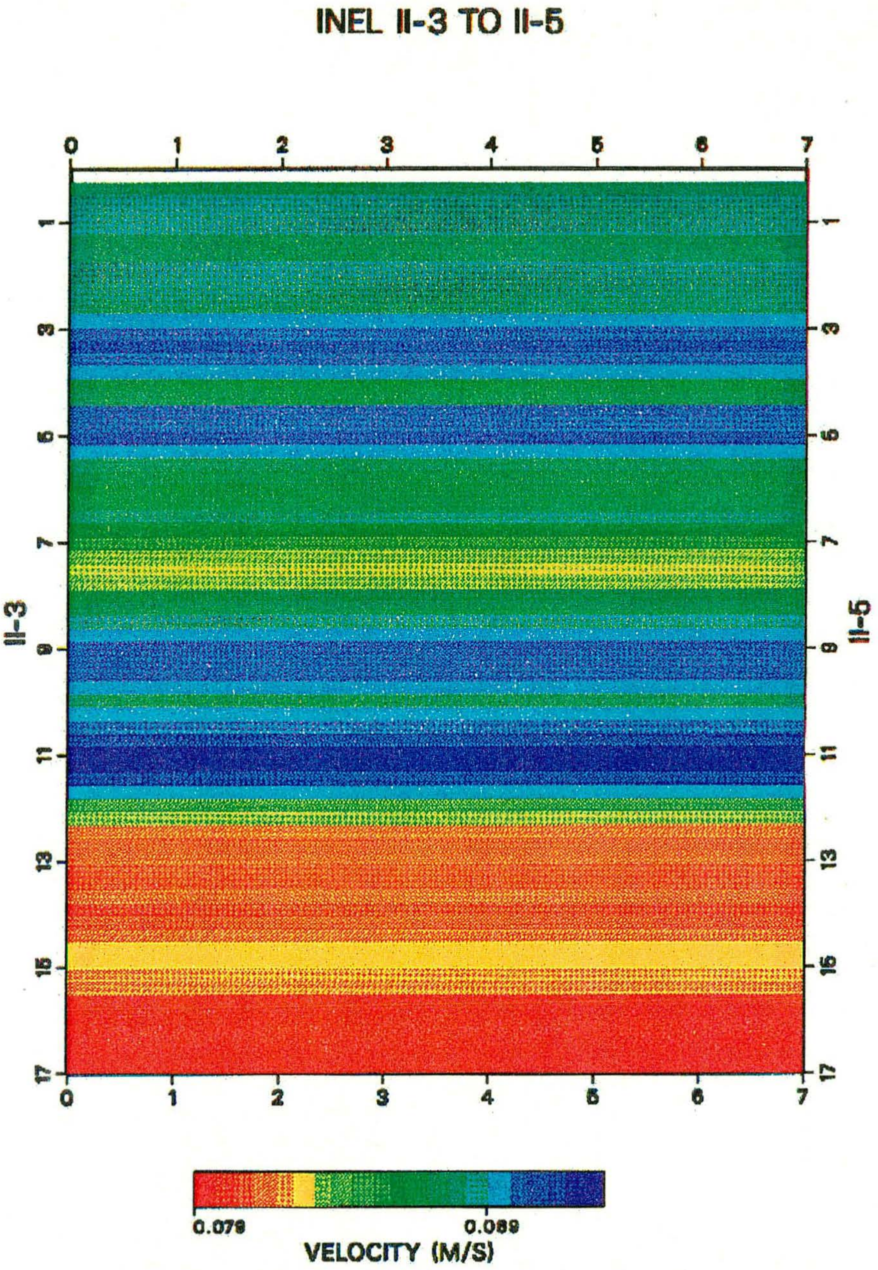

Figure 2.18. Velocity tomogram for ZOP well pair II-3/II-5. Low velocity zones correlate well with fracture or rubbles zones noted in the core data.

Preliminary Results of Surface-to-borehole Transillumination

Processing of the surface-to-borehole transillumination dataset is being deliberately delayed to FY 96. The dataset will be processed as a vertical radar profile and will be used to generate a triangular tomogram assisting in the overall characterization of the area's flow regime.

Preliminary Results of Single Hole Reflection

As mentioned above, the single hole reflection datasets were found to be useful at Stripa (*Olson,* 1992). Careful examination of the single hole records from Box Canyon indicates the presence of features of interest. These features are represented by diffractions and secondary arrivals that appear to correlate with known interflow rubble zones. This is illustrated in Figure 2.19.

Although not present in all records, core data analysis suggests that these signal effects are the likely result of subsurface features. Further analysis and modeling are planned for in FY 96.

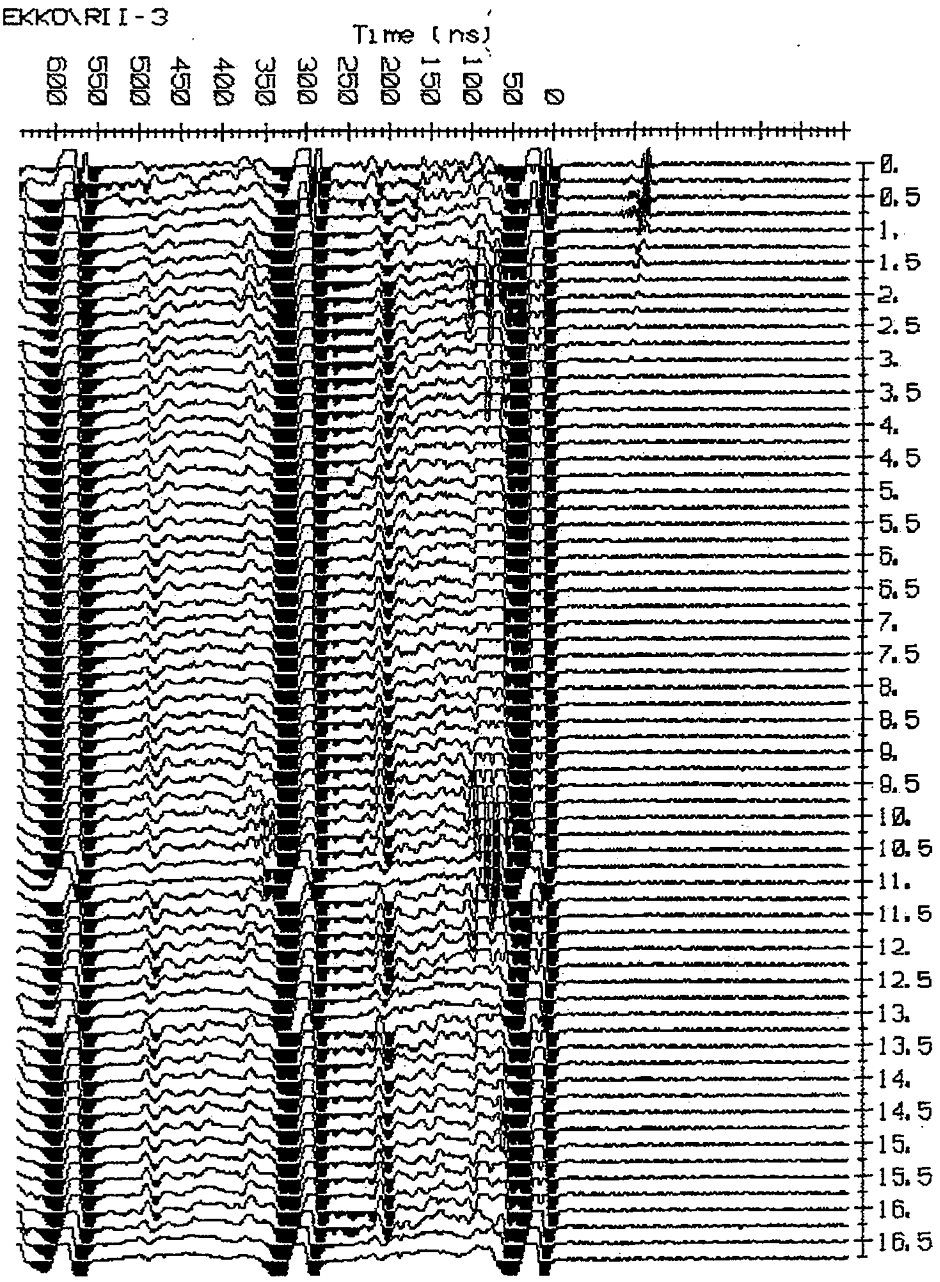

Figure 2.19. Waveforms for single-hole reflection.

Conclusions

The borehole radar survey methods utilized at Box Canyon produced interpretable results and appear to represent an effective means of vadose zone characterization. Velocity tomograms were derived from the MOP datasets collected during the borehole-to-borehole surveys. Amplitude tomograms for the borehole-to-borehole surveys as well as a triangular tomogram are planned for the surface-to-borehole configuration. Predictive forward modeling was used to establish the threshold of detection for vertical fractures in the investigation. The ability of high frequency borehole radar to assist in the characterization of flow regime appears to be very promising with further efforts being directed primarily toward increased fracture resolution.

2.2.3.4 Seismic Detection of Channels

The objective of this study is to examine the feasibility of using guided waves to determine continuity of the basalt flows at the INEL site. If the basalt flows can support guided waves, these waves can be launched between boreholes to provide information about the lateral discontinuity within the basalt flows. Since guided waves can propagate over much larger distances than body waves, the use of guided waves may provide a valuable supplement to conventional crosshole seismic tomography, particularly when the well separations are large. Seismic properties of INEL basalt obtained from the upper, lower and middle parts of a flow were measured on cores in the laboratory. Estimates of typical flow unit thicknesses were obtained from core logs. An analysis of guided wave modes was performed for a basalt waveguide using these properties. The results of this analysis suggest that it will be possible to generate and detect guided waves at crosshole seismic frequencies in INEL basalt and that these waves may prove useful in determining the extent of vertical fracturing within the flow.

2.2.3.5 Laboratory Measurements

Two cylindrical cores of basalt from INEL well #B07N21 were obtained from the INEL Lithologic Core Storage Library. The first core is a vesicular basalt from the upper element of the flow cored from a depth of 3.17 m. Two samples A and B were prepared from this core. The second core is from the central core of the flow from a depth of 12 m. Two samples D and E were prepared from this core. The physical dimensions of the four samples are given in Table 2.1. All samples were prepared for seismic testing by grinding the ends flat and parallel to within 13 μm.

The density of samples A and B from the upper vesicular element is approximately 10% lower than the density of samples D and E from the central core element reflecting the higher porosity of the former. Samples D and E contain millimeter size pores embedded in a non-porous matrix, while samples A and B contain centimeter size pores embedded in a non-porous matrix. The pore spacings in both rock types are on the order of the pore diameter.

Table 2.1. Physical dimensions and densities of the basalt samples.

sample	diameter (cm)	length (cm)	density (kg/m^3)
A	6.096	5.080	2.52
B	6.088	30.480	2.52
D	6.104	5.080	2.80
E	6.104	30.480	2.80

Ultrasonic P-wave and S-wave velocities were measured using the pulse-transmission method with 1 MHz piezoelectric transducers. To test the stress-dependence of the basalts, the sample was loaded along its axis in uniaxial compression between two cylindrical piezoelectric transducers. The measured P-wave and S-wave velocities are given in Table 2.2. The P-wave and S-wave velocities in both elements increase with increasing compressive stress, indicating the likely presence of compliant intergranular grain boundaries, particularly in the sample D from the central core element. After one loading cycle, the velocities at zero stress were higher than that which was measured before the samples were loaded indicating that irreversible compaction of the samples had occurred.

The zero stress ultrasonic velocities of the sample A from the upper vesicular element (c_p=3953 m/s) are over 25% higher than the velocities of the sample D taken from the central core element (c_p=2632 m/s). The lower velocity of sample D is partly due to the higher density of the central core basalt (since velocity=[modulus/density]$^{1/2}$), but also due to the higher compliance of the central core basalt, presumably due to the presence of compliant intergranular grain boundaries as was evidenced by the stress-dependent velocities noted above.

Table 2.2. Ultrasonic velocities of the basalt samples.

sample	uniaxial stress (MPa)	P-wave velocity (m/s)	S-wave velocity (m/s)
A (upper vesicular)	0	3953	---
	12.3	4170	2375
	19.4	4240	2375
B (upper vesicular)	0	3054	---
D (central core)	0	2632	---
	12.3	3338	1734
	19.4	3533	1783
E (central core)	0	2568	---

The velocities of central core basalt are within several percent for the short sample D (c_p=2632 m/s) and the long sample E (c_p=2568 m/s), indicating a degree of homogeneity over the 36 cm core. However, for the upper vesicular basalt , the velocities for the short sample A (c_p=3953 m/s) are over 25% higher than the long sample B (c_p=3054 m/s). This large velocity dispersion was unexpected and visual inspection of sample B was performed which revealed the presence of a band of coplanar porosity, running along the circumference of the sample roughly perpendicular to the axis of the sample, which is presently being interpreted as a vesicle train.

Resonance bar tests were performed on the two 0.30 m long samples (B and E) to determine the velocities and attenuation of upper vesicular and central core basalt in the kilohertz (*i.e.*, crosshole) frequency range. To generate standing waves in the rock samples, a small expansion mode piezoelectric crystal was bonded on one end of the sample. The extensional mode free-vibrations were detected by a miniature accelerometer that was bonded on the opposite end. The amplitude and phase spectra were measured using a swept sine frequency analyzer.

The center frequency and widths of the resonance peaks of the fundamental extensional mode observed in samples B and E were used to estimate the extensional wave velocity and attenuation computed (Table 2.3).

Table 2.3. Extensional wave velocities and attenuation of the basalt samples.

sample	resonance frequency (Hz)	c_e (m/s)	c_p † (m/s)	Q_E
B(upper vesicular)	1411	860	942	188
E(central core)	3964	2416	2646	496

†computed using $c_p = c_e[(1-2\nu)(1+\nu)/(1-\nu)]^{1/2}$ assuming $\nu = 0.25$.

The P-wave velocity computed from the measured extensional wave velocity for sample E (c_p= 2646 m/s) is in close agreement with the P-wave velocity of sample D (c_p=2632 m/s). However, for sample B, the P-wave velocity obtained from the resonance bar test is over three times lower than the P-wave velocity of sample A. The low velocity of sample B is due to the presence of the planar vesicle train identified above. An estimate of the stiffness of this feature required to produce the observed low velocity can be obtained from the equation for the free-vibrations of a one-dimensional bar containing a single nonwelded interface,

$$\sin(kL) - \frac{\omega Z}{\kappa}\sin(kR)\sin[k(L-R)] = 0, \qquad (2.3)$$

where k is the wavenumber, Z is the acoustic impedance, ω is the angular frequency, and L and R are the length of the bar and the distance to the vesicle train, respectively. The roots of this equation are the resonance frequencies of the modes of free-vibration of a bar for a given value of the fracture stiffness κ. From Eq. 2.3, the sample B resonance frequency of 1411 Hz corresponds to a vesicle train stiffness of $\kappa = 10^{10}$ Pa/m.

2.2.3.6 Model Analysis

The frequency-dependent velocities and displacements of the various propagating guided wave modes that can exist in a low velocity layer can be obtained by numerically solving the Rayleigh channel wave determinant. As a first-order analysis of guided wave propagation in an INEL basalt flow, the geometry of the basalt flow was assumed to consist of a 2 m thick low velocity layer (central core) with plane-parallel boundaries imbedded between two higher velocity halfspaces (upper and lower vesicular elements). Using the laboratory measured velocities (Table 2.2) and densities (Table 2.1) and the simplified flow geometry, the Rayleigh channel wave determinant predicts a family of symmetric (extensional) and antisymmetric (flexural) guided waves with frequency-dependent velocities (Figure 2.20). For a piezoelectric bender source, it should be possible to excite the fundamental extensional mode most strongly in the 100 to 600 Hz frequency range. Higher order symmetric and antisymmetric modes exist in the higher frequency range, but these modes may not be strongly excited by a simple bender source.

To first order, the effects of waveguide attenuation (Q^{-1}) and vertical fractures on the fundamental mode guided wave can be estimated, ignoring mode conversions, from the following equation,

$$u \propto T\,\frac{e^{-\pi f/(QL)}}{L^{1/2}}. \qquad (2.4)$$

In Eq. 2.4, u is particle displacement, f is the frequency of the wave, L is the distance between the source and receiver, Q^{-1} is the intrinsic attenuation of the basalt, and T is the transmission coefficient of the vertical fracture. T can be computed from,

$$T = \left[1 + \left(\frac{\pi f \rho c}{k}\right)^2\right]^{-1/2}, \qquad (2.5)$$

where ρ and c are the density and velocity of the basalt, respectively, and κ is the stiffness of the fracture in units of [Pa/m]. For f=5 kHz, Q=496, L=200m and T=1, Eq. 2.3 predicts that only a 15% reduction in amplitude will result from intrinsic attenuation losses (*i.e.*, ignoring the $L^{-1/2}$ geometric decay). However, if the fracture is completely open, then κ=0 Pa/m and T=0, resulting in zero transmission. Finite values of fracture stiffness in the range $0 < \kappa < 5 \times 10^{10}$ Pa/m will result in transmission coefficients in the range $0 < T < 0.53$. For this range of stiffness, a single fracture can have a strong effect on the amplitude of the transmitted guided wave (Eq. 2.5 that can be used in crosshole transmission measurements to infer the presence of fractures in basalt flows.

2.2.3.7 Conclusions

Laboratory measurements of the seismic properties of INEL basalt from well #B07N21 indicate that the central core basalt may act as a low velocity, low (intrinsic) attenuation waveguide. Guided wave analysis performed under the assumption of a planar waveguide in which seismic properties of the lower vesicular element are the same as the upper vesicular element predicted that a family of guided waves will propagate in the central core. The fundamental guided wave mode should be most strongly generated in the 100 to 600 Hz range.

Based on the measured values of attenuation, in the absence of open vertical fractures, it should be possible to propagate seismic waves at crosswell frequencies in the kilohertz range over distances in excess of a hundred meters.

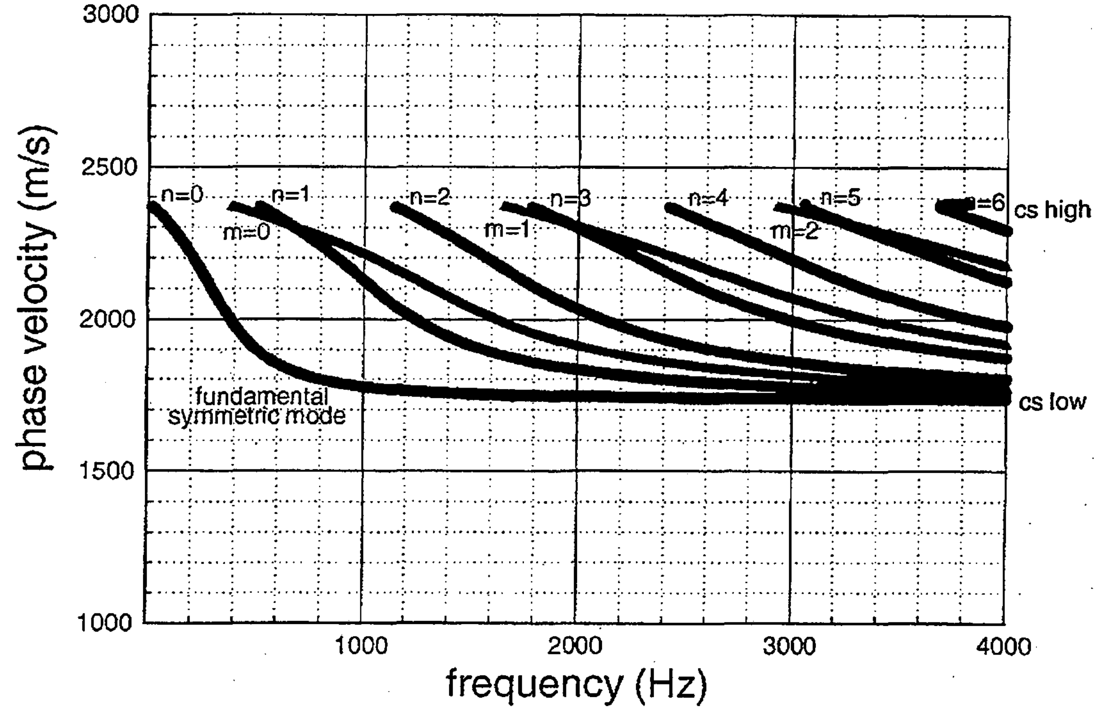

Figure 2.20. Phase velocity dispersion curve for guided waves in a low velocity layer (central core) imbedded between two higher velocity halfspaces (upper and lower vesicular elements)..

2.2.4 FY 96 Activities

Radar surveys will be done before, during and after the infiltration test (see Task 5). Development of high frequency CSAMT will be explored as well. Cross-correlations will be made with hydrologic infiltration measurements.

Future work on guided seismic waves will examine the effects of more realistic basalt flow architectures that include the finite thickness of the vesicular elements, the presence of rubble zones and vertical fractures, and variability in flow unit geometry using a numerical boundary element code. The feasibility of doing a seismic cross-hole survey will be assessed, based on the modeling results of FY 95 and conducted if possible, to test the results of the laboratory studies.

2.2.5 Significance

CSAMT has been shown to be effective at seeing large-scale variations in fluid content at depths of 50 m, and if the high frequency capability is developed, it should be able to have resolution as fine as 10 m.

If we can find an appropriate radar system and demonstrate that we can see fluid flow with this system, it will be used by landfill sites such as RWMC to detect small-scale infiltration in the vicinity of the site. The state of Idaho has criticized the lack of monitoring beneath the RWMC. Quarterly radar surveys could be used to monitor for the expected migration of leachate, track perched water zones, and identify fast flow paths during wetting events.

The guided wave study may provide a technique for determining the inter-well continuity and the degree of vertical fracturing of flow units. This could be used in conjunction with the geomechanical model described above to predict the variation of hydrologic properties beneath INEL contaminated sites. Channel wave surveys have the potential to delineate fast flow paths between the TAN injection well and nearby wells (as close as 25 feet). Connectivity to the TSF-05 well bore is important for operation of the pump and treat system currently at TAN and for design of the remedy currently under consideration by the agencies. This technology will provide useful information for the operation of the OCVZ vapor vacuum extraction project.

2.3 Task 3. Aquifer Stress Test Analysis

2.3.1 Background

Hydrologic inverse modeling can be used to infer spatial distributions of hydrologic and transport properties from interference well test and tracer data and can be conditioned on other types of information such as data on fracture genesis and geophysical imaging. LBL has designed a number of inverse methods specifically for identifying fast flow paths and fracture networks (*e.g.*, *Datta-Gupta et al.*, 1994; *Doughty et al.*, 1994). The primary purpose for using this technology is that it results in an interpretation of the fracture flow paths that is consistent with all the data available.

The general framework of the LBL inverse methods is to create a numerical model of the fracture network and use this model to simulate the tests that were performed in the field. In general, the model is a lattice of conductors that represent fracture flow paths. The simulated test results are compared to the actual well test data and the degree of mismatch is calculated. Then the lattice is changed to see if a better fit can be achieved. If the change improves the fit, the change is kept. If not, the decision to keep the change is made randomly with a probability determined by the degree of increased misfit. This iterative process, known as "simulated annealing" continues until a good match is found. The resulting network of conductors can be said to reflect a possible pattern of fracture conductance in the field.

The particular inverse method used for the Aquifer Stress Test analysis is known as the Iterated Function System (IFS) inverse method (*Doughty et al.*, 1994; *Doughty*, 1995). In contrast to the basic application of simulated annealing, known as lattice annealing, in which the lattice of conductors is changed one lattice element at a time, with the element chosen at random, in the IFS inverse method, many elements of the lattice are changed at each iteration, with the pattern of changed elements constructed in a special way to have a fractal (self-similar) geometry. Since variability is repeated at multiple scales in a self-similar medium, far fewer parameters are needed to describe it, improving the efficiency and robustness of the inversion.

The success of inverse modeling can be assessed by comparing the inferred property distributions with results of geological, geophysical, and geochemical measurements. However, the method is most usefully assessed by seeing whether the resulting models can be used to predict new hydrologic behavior. Success in this case can best be judged by using the inferred fracture patterns to predict the results of subsequent aquifer stress tests and comparing the prediction to actual performance.

2.3.2 Performer

INEL collected the data from the Aquifer Stress Test and performed a standard analysis in work funded by EM40 (*Wylie et al.,* 1995). This included a significant effort to filter out the noise in the data. The filtered data were transferred to LBL to perform the analysis described below. This analysis was funded by EM50 in FY 95. The scope of work on this task has been curtailed due to budget limitations and will be closed out as part of the EM50 project this year as a completed feasibility project.

2.3.3 FY 95 Activities

The Aquifer Stress Test conducted by INEL during FY 94 was analyzed using inverse modeling techniques developed at LBL to identify fluid flow properties in the saturated zone of the Snake River Plain aquifer and to see if preferential flow paths could be identified. The goal of the analysis is to understand the fluid flow behavior of the Snake River Plain aquifer at the well-field scale (tens to hundreds of meters). This information has been compared with results of both smaller-scale (Box Canyon) and comparable-scale (Large Scale Infiltration Test) vadose zone studies (Section 2.5.3) and will be compared to larger-scale studies of regional aquifer behavior (Section 2.4).

2.3.3.1 The Aquifer Stress Test

Beginning on July 25, 1994, INEL conducted a large-scale pumping test near the Radioactive Waste Management Complex (RWMC), located near the southwestern corner of INEL, to obtain water for an infiltration test being conducted nearby and to obtain hydrologic parameters for the Snake River Plain aquifer. Figure 3.1 shows a plan view of the well field. At this location the water table is about 185 m (600 ft) below the ground surface. The productive portion of the aquifer is thought to be limited to the upper 75 m of the saturated zone. The test well was pumped at 3000 gpm (0.19 m^3/s) for 36 days, and drawdowns were monitored at the test well and at well USGS-120, and at two levels in wells OW1 and OW2, which were separated by packers. INEL completed a standard analysis of this data (*Wylie et al.*, 1995). LBL reviewed both the raw data and the analysis provided by INEL. The INEL work included a significant effort to filter out the noise in the data. The filtered data was transferred to LBL and used as the starting point for the LBL analysis.

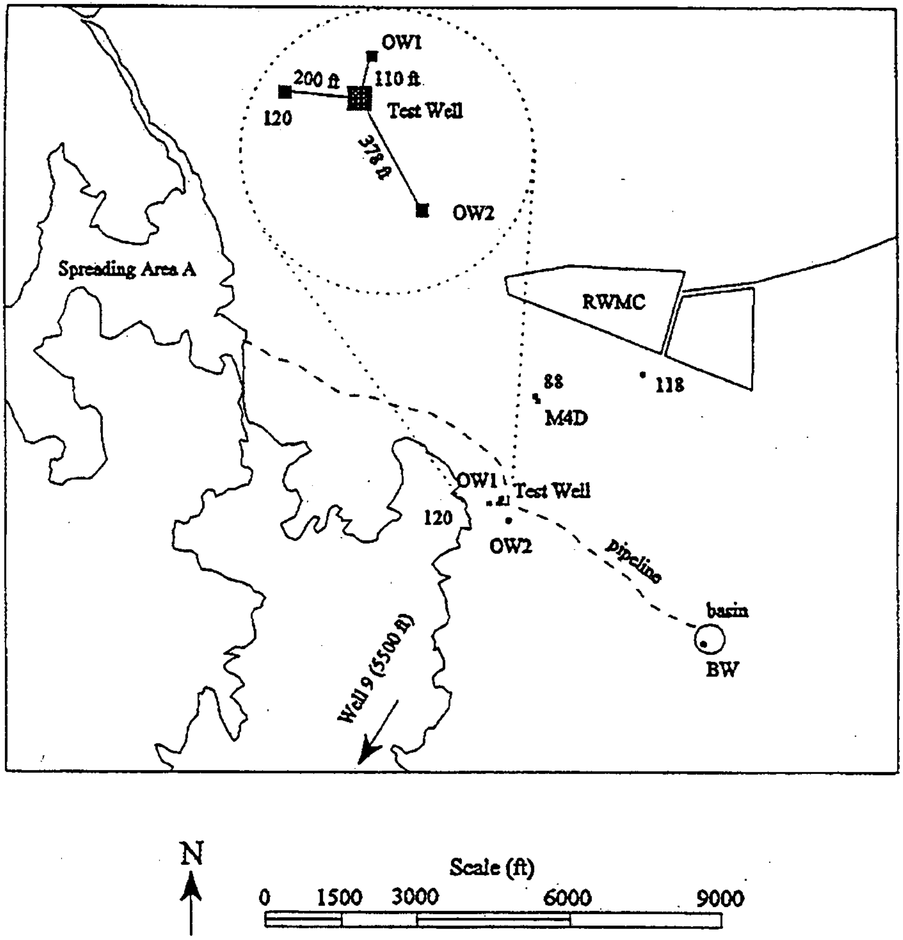

Figure 3.1. The well field for the 1994 aquifer stress test (*Wylie et al.*, 1995). The circle marked 'basin' is the site of the site of the Large Scale Infiltration Test. -

2.3.3.2 The Observed Data

Figure 3.2 shows drawdown as a function of time for each of the five intervals that responded to the well test (the lower level of well OW2 did not respond). It is apparent that well USGS-120 and the upper interval of well OW1 (OW1U) respond similarly to each other, and that the lower interval of well OW1 (OW1L) and the upper interval of well OW2 (OW2U) respond similarly to each other, but that the two pairs of drawdowns show a significant difference in response.

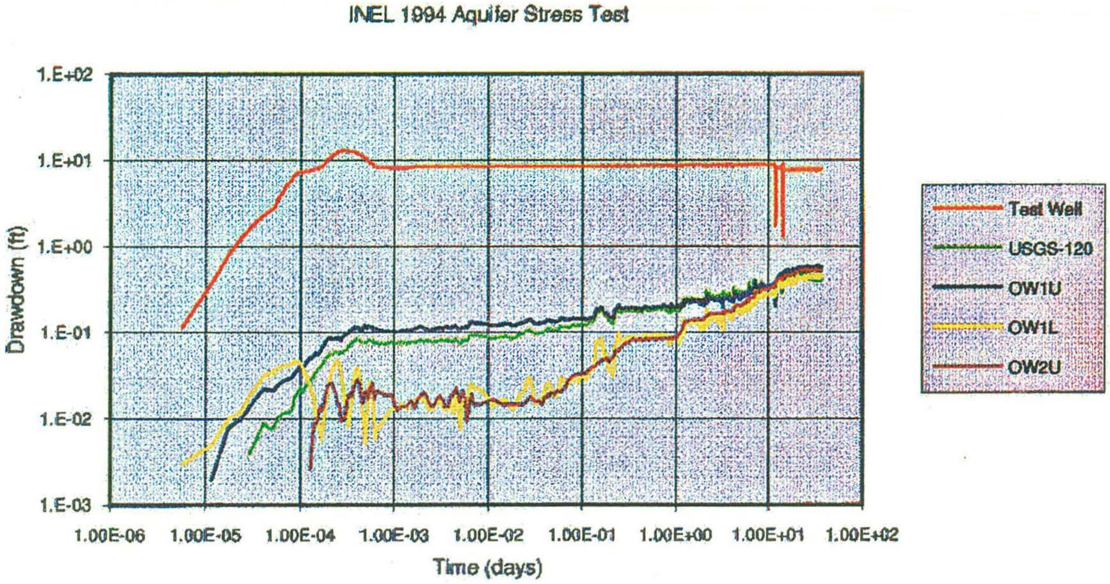

Figure 3.2. Drawdown as a function of time in the pumping well and observation wells for the 1994 aquifer stress test.

The following suite of well logs for the Aquifer Stress Test wells were provided by the USGS (*D. Boyce*, personal communication, 1995).

Well	Logs
Test	Gamma, caliper
USGS-120	Gamma, caliper
OW1	Gamma, caliper, flow-profiles, resistivity, self-potential, temperature
OW2	Gamma, caliper, flow-profiles, resistivity, self-potential, temperature

Table 3.1. Available well logs for the Aquifer Stress Test.

We found the gamma, caliper, and flow-profile logs provided the most information on geological features that are relevant for fluid flow. The gamma log is sensitive to the chemical elements potassium, thorium, and uranium. Potassium is abundant in the clays, which comprise the sedimentary interbeds found between some basalt flows, so the interbeds show up as strong spikes in the gamma log. The caliper log shows increased wellbore diameter at breakouts. If these breakouts are coincident with the gamma spikes they are inferred to represent the sedimentary interbeds, which are much softer than the basalts, so tend to break out. If the breakouts are not coincident with the gamma spikes, they are inferred to represent the rubble zones which may form at the boundaries between basalt flows, during cooling of the basalt flow. The flow-profile logs show jumps where there is a large flow into or out of the wellbore, which occurs at highly permeable intervals. These intervals are inferred to be rubble zones by correlation to the caliper breakouts. The result of combining all these interpretations is shown in Figure 3.3.

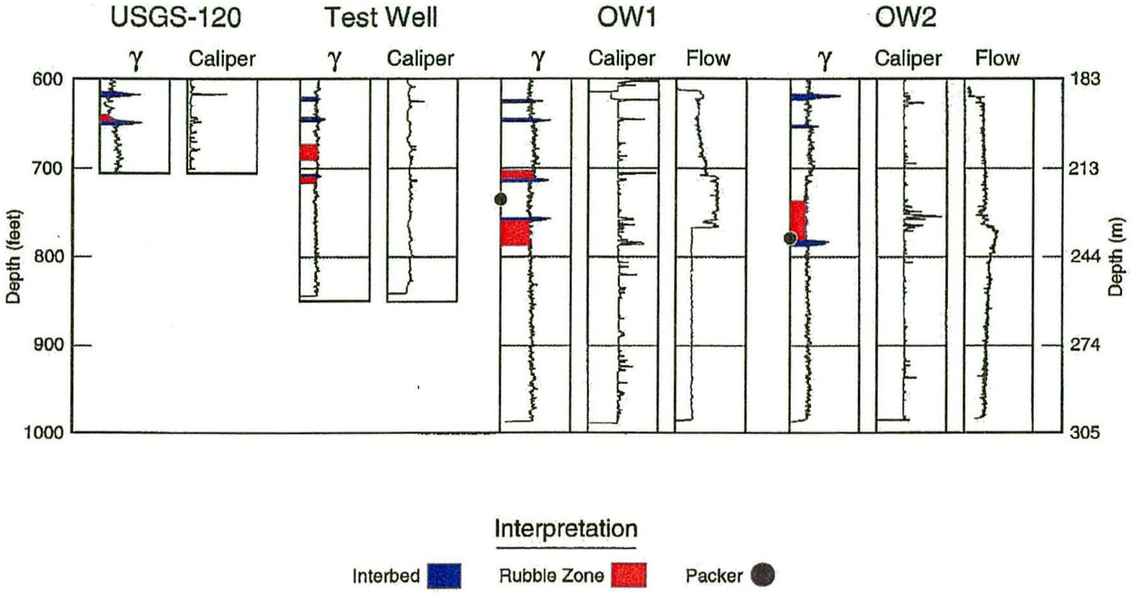

Figure 3.3. The well logs that were used to develop a conceptual model of saturated-zone fluid flow during the Aquifer Stress Test.

Figure 3.3 suggests that there is a high-permeability rubble zone just below the packer in well OW1 and just above the packer in well OW2, which could be providing the characteristic response of OW1L and OW2U. Furthermore, well USGS-120 and the upper interval of well OW1 occur at similar depths and the lithologies show similar features, consistent with the similar response of these two intervals. The sedimentary interbeds in the Snake River Plain basalts are generally associated with decreased permeability, although it is an open question as to whether the interbed material itself has low permeability, or the presence of an interbed causes changes in the overlying or underlying fractured basalt, decreasing its permeability. Taken as a whole, Figures 3.2 and 3.3 suggest that there is good lateral continuity of flow features, but incomplete vertical communication between layers, allowing distinct pressure responses at different depths, and therefore, requiring a multi-layer model for analysis.

2.3.3.3 The Numerical Model

The inverse analysis consists of simulating the well test repeatedly, using different distributions of fluid flow properties, until the observed drawdowns are adequately matched by the simulated values. During the inversion, the well test is simulated numerically using a finite element program for flow and transport called TRINET (*Karasaki*, 1987). TRINET discretizes the flow domain by constructing a lattice of one-dimensional finite elements, which schematically represent a porous medium or fracture network.

The present model of the Snake River Plain aquifer consists of a three-layer lattice with vertical elements connecting the layers, as shown schematically in Figure 3.4. The test well is open in all three layers of the lattice, whereas the shallower well USGS-120 is open only in the upper layer. The upper interval of well OW1 is open in the upper layer of the lattice and the lower interval of well OW1 and the upper interval of well OW2 are open in the lower layer of the lattice. The lower non-responding interval of well OW2 is not included explicitly in the model, but may be considered to exist below the lowermost layer of the lattice, which has a no-flow boundary condition at the bottom, prohibiting communication with that interval.

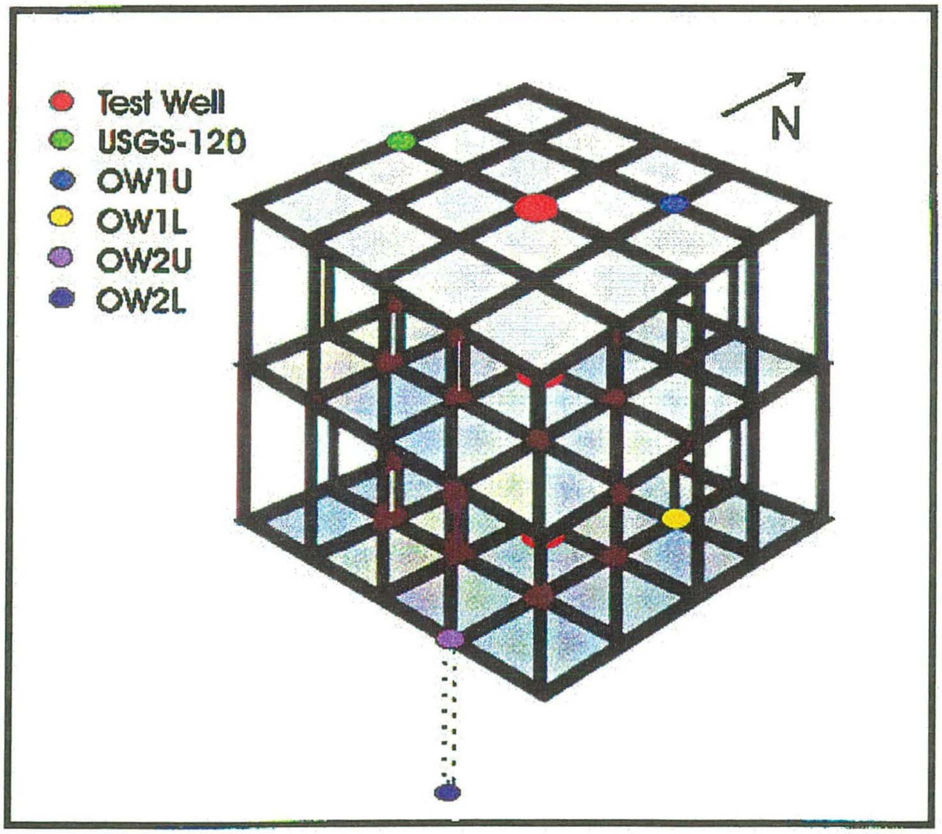

Figure 3.4. Schematic diagram of the numerical model used to analyze the aquifer stress test. The gray shading of the various layers is merely to aid visualization, flow occurs through the black line elements.

Figure 3.5 shows a plan view of the actual lattice used for each of the layers. The lattice must extend far beyond the well field in order to not impose spurious far-field boundary conditions on the problem. In the outermost regions of the lattice, the aspect ratio of the lattice is vary large (horizontal element lengths of up to 16 km, with vertical element lengths of about 35 m), which causes TRINET to run very inefficiently if realistic vertical permeability values are used. Because the vertical communication between different layers of the lattice is not important at great distances from the well field, vertical permeability was greatly decreased for elements more than 8 km from the well field, effectively isolating the individual layers at these distances, enabling the code to run efficiently.

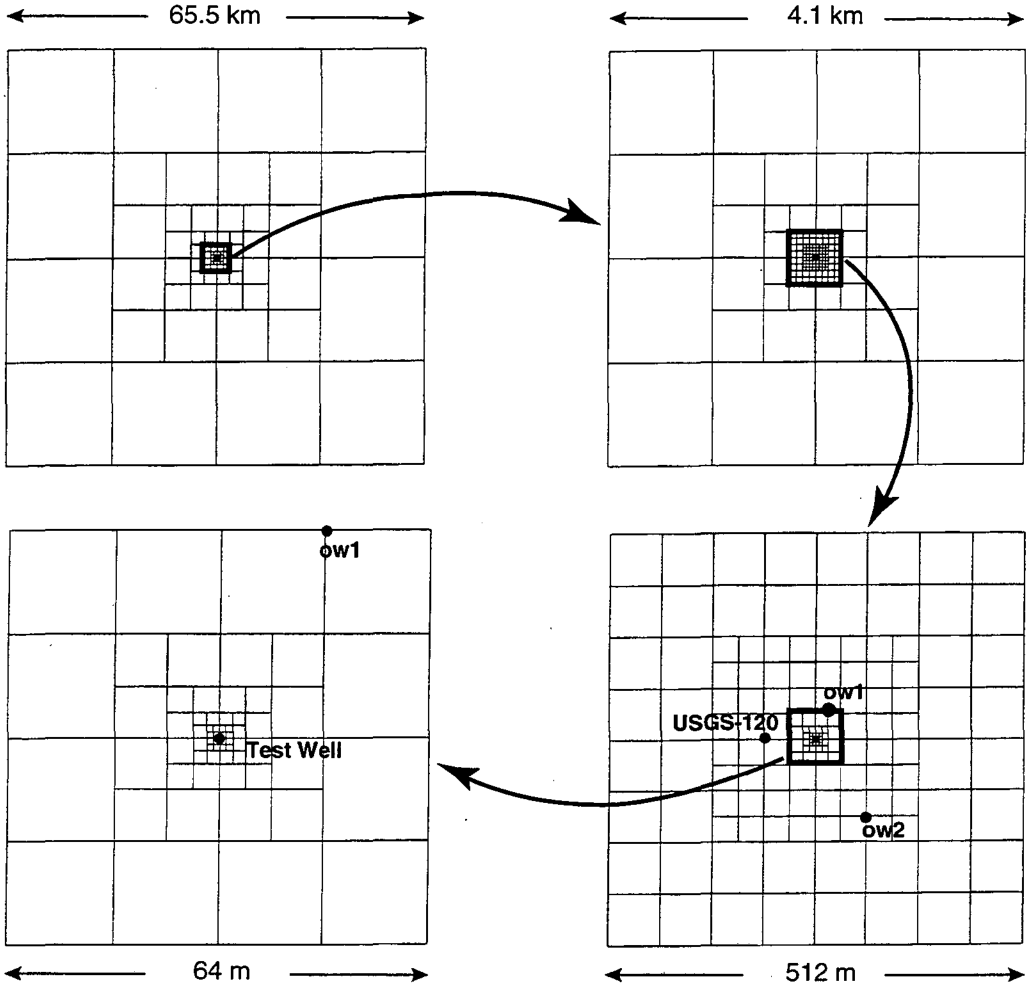

Figure 3.5. Plan views showing one of three identical layers of the lattice used to model the aquifer stress test at 4 different scales.

2.3.3.4 Preliminary One-Layer Calculation

A preliminary calculation was done using just one layer of the lattice, a constant pumping rate, and uniform values of transmissivity, T = 2.8 m^2/s (2.6 x 10^6 ft^2/day), and storativity, S = $7x10^{-3}$, which were determined by matching the observed drawdown curves to the *Theis* (1935) analytical solution. The resulting drawdowns are shown in Figure 3.6, along with the observed data and (for purposes of comparison) the Theis solution. The slightly imperfect match between the Theis solution and the numerical solution is probably due to the rapid coarsening of the lattice around the test well (Figure 3.5). The large misfit between the calculated and observed data quantified by the parameter E indicates the need for a heterogeneous model of the aquifer. Note that T=2.8 m^2/s is a huge value of transmissivity (corresponding to a permeability of 3500 darcies for a 76 m (250 ft) thick aquifer), which probably represents a rubble zone.

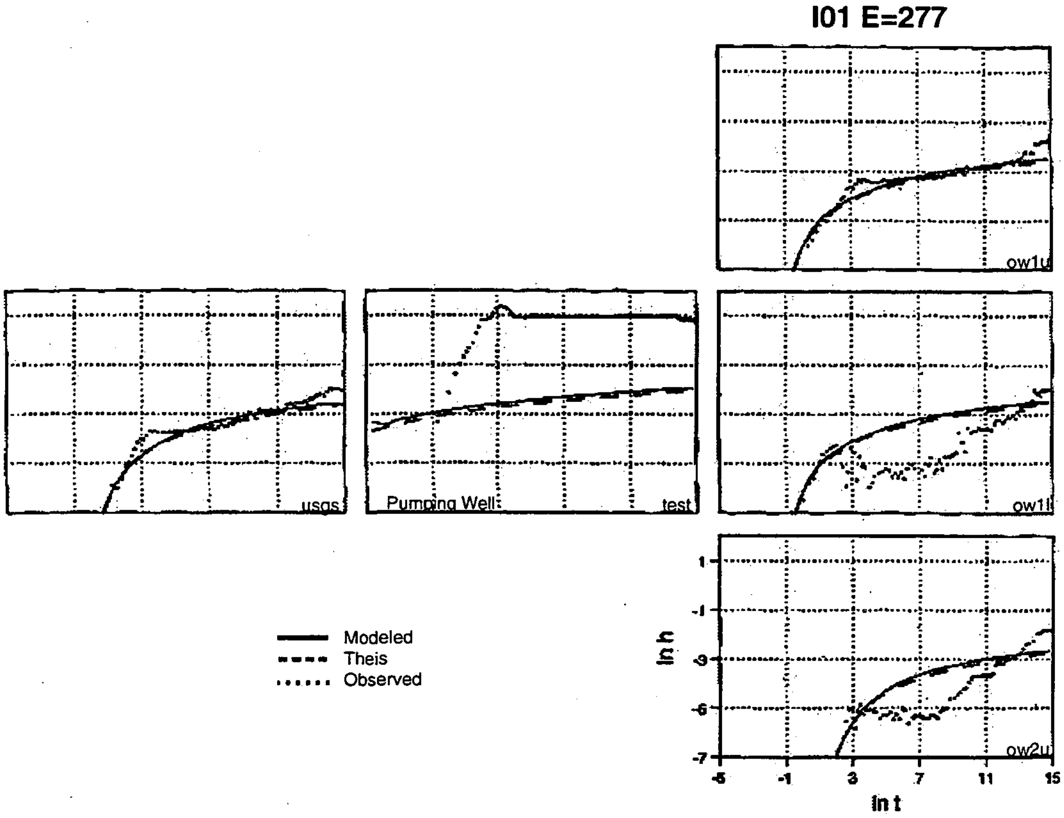

Figure 3.6. Drawdown as a function of time calculated using a uniform single-layer model with a constant pumping rate. The arrangement of the plots on the page mimics the well field pattern shown in Figure 3.1.

2.3.3.5 Multi-Layer Calculations

As described above, the distinct responses between the upper and lower intervals of wells OW1 and OW2 must be addressed by using a multi-layer model. Additionally, the pumping well pressure response (Figure 3.2) shows the effects of wellbore storage (unit-slope increase on a log-log plot of drawdown versus time) and a variable pumping rate (non-monotonic variation in drawdown versus time). Wellbore storage can be included in the model explicitly, by using vertical elements to represent the well, and assigning the appropriate storage value based on wellbore volume.

The early-time variable pumping rate can be approximated using pump performance-curve data. The pump performance curve shown in the upper frame of Figure 3.7 (*T. Wood*, personal communication, 1995) gives $q(h)$, the variation of pumping rate q with the hydraulic head difference h across the impellers of the pump. When the pump is first turned on, the wellbore above the water table is empty, so $h=0$ (there is no water column for the pump to lift) and the pumping rate is at its maximum, 5800 gpm (0.63 m^3/s, extrapolated from measured values). Under steady-state conditions (the wellbore is filled with water from the water table to the ground surface), the pumping rate is 3000 gpm. Under steady conditions, h (720 ft or 220 m) is greater than the depth of the water table (about 600 ft or 185 m) because additional power is required to pump the water from the test well to the infiltration basin about one mile away.

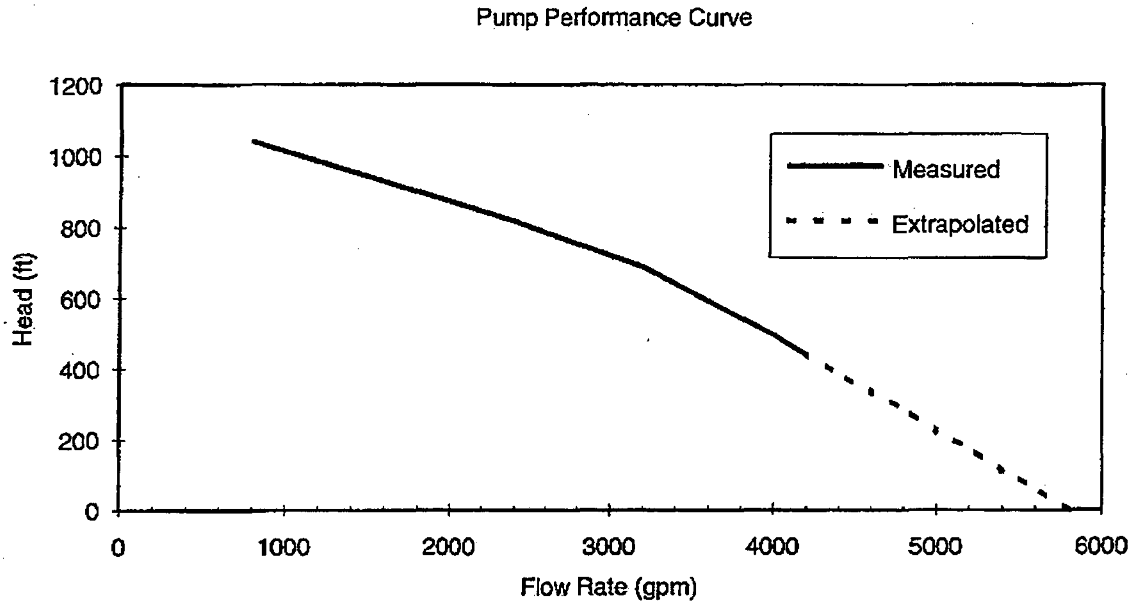

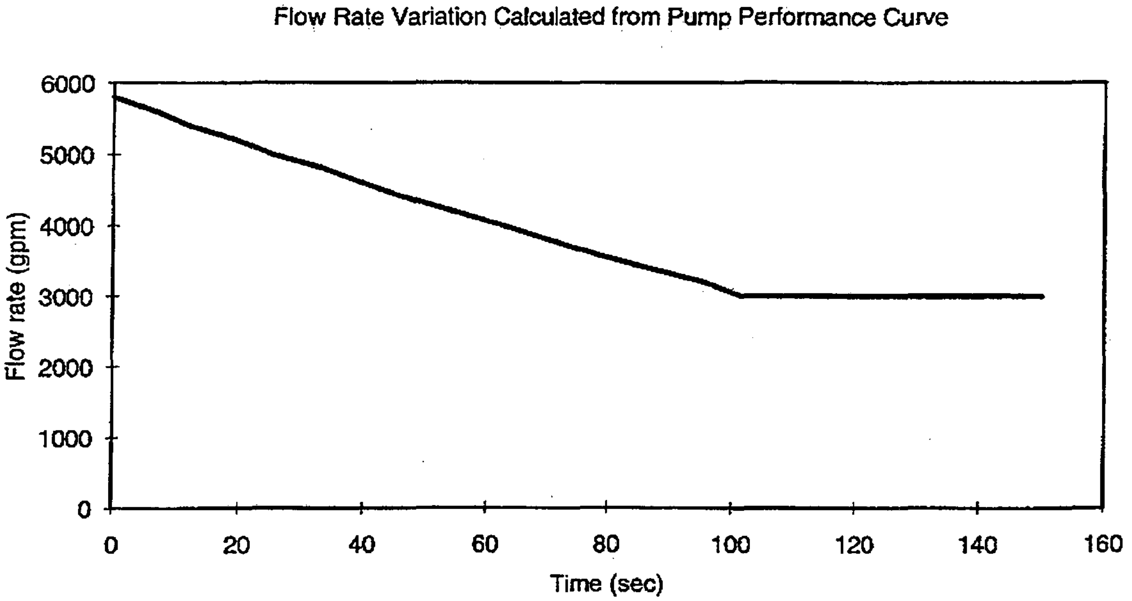

Figure 3.7. Pump performance curve (upper frame) and the variable pumping rate as a function of time inferred from it (lower frame).

Because the total drawdown due to pumping (10 ft or 3 m) is very small compared to the total change in h (720 ft or 220 m), we assume that the depth of the water table does not change, and therefore that changes in h are all due to the growing height of the water column in the wellbore above the water table. Under these conditions, a change in the height of the water column may be written as *dh*. For a value of *dh* which occurs in a time period *dt*, we may write

$$dh = vdt, \tag{3.1}$$

where v is the upward velocity of the water column. Furthermore, the water-column velocity is related to pumping rate by

$$v = q/A, \tag{3.2}$$

where A is the cross-sectional area of the wellbore through which fluid flows. For a well of radius r_w containing a riser pipe of radius r_r,

$$A = \pi r_r^2. \tag{3.3}$$

The expressions for *dh* and v can be combined to give

$$dh = v\,dt = q(h)/A\,dt. \tag{3.4}$$

This expression can be numerically integrated, using tabulated values of $q(h)$ taken from the pump performance curve, to obtain a table of values of $h(t)$. With this information, the tabulated values of $q(h)$ may readily be converted to tabulated values of $q(t)$, as required for the numerical simulation of the well test and shown in the lower frame of Figure 3.7. The variable pumping rate shown in Figure 3.7 is averaged into 15 constant flow-rate steps for the TRINET simulation of the Aquifer Stress Test.

A narrow zone around the production well with distinct values of T and S also is included to represent skin effects, which could include turbulent flow near the well or the fact that most flow enters the well through a few dominant fractures. An inversion was done in which the T and S values of each layer, the T and S values of the production-well skin, and the wellbore T values were all allowed to vary independently, without constraints. Because T and S were not allowed to vary spatially within each layer, the fractal-geometry aspect of the IFS inverse method was not invoked. The resulting drawdowns, shown in Figure 3.8, show a much improved match to the observed values, and a corresponding decrease in E, compared to Figure 3.6. Figure 3.9 shows the T and S values used to obtain the match.

One possible interpretation of the hydrologic property distribution shown in Figure 3.9 is that the large transmissivity and small storativity values of the upper and lower layers represent the primary flow network, composed of large fractures and rubble zones. The much smaller transmissivity and larger storativity values of the middle layer represent smaller fractures, dead-end fractures, and matrix permeability and provide a source of delayed storage typical of dual porosity, dual permeability fractured/porous media. The interaction between the upper and middle layers also could represent gravity drainage from the vadose zone into the upper layer of the aquifer (gravity is not included in the present model, so the existence of the middle layer below the upper one does not preclude this interpretation). It is of interest to note that the vertical permeabilities connecting the three layers of the model are all smaller than the permeabilities of the layers themselves, explaining the limited vertical communication that gives the distinct responses for different depth intervals seen in the drawdown versus time plot (Figure 3.2).

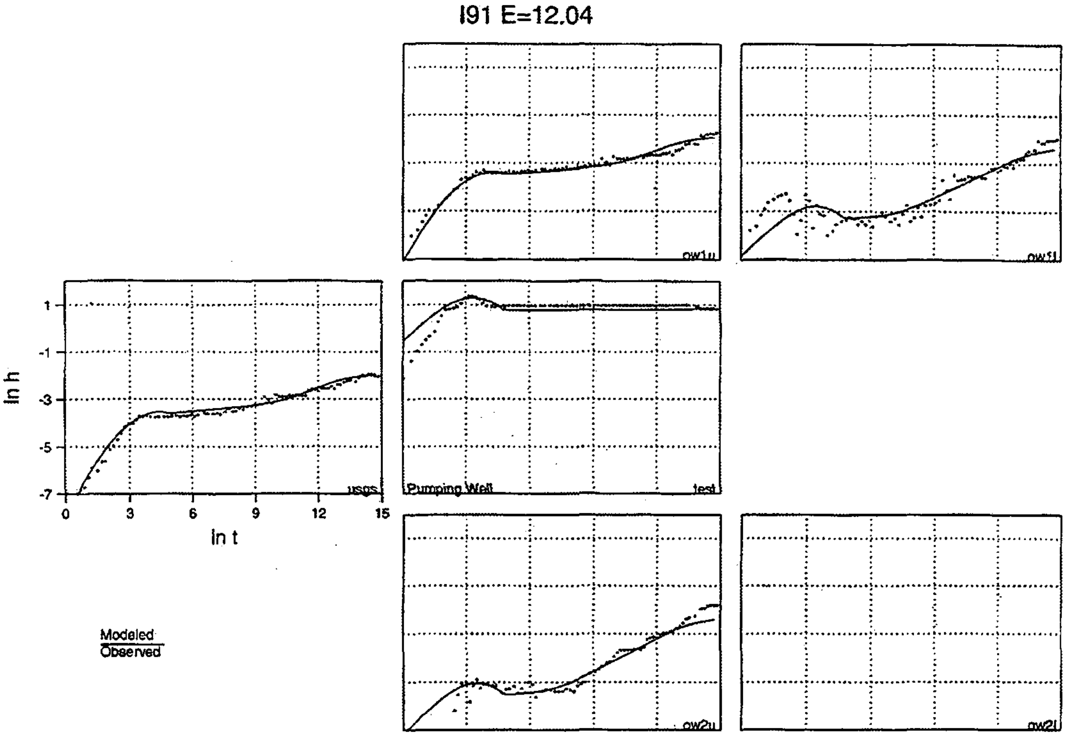

Figure 3.8. Drawdown as a function of time calculated using a three-layer model with a variable pumping rate, including wellbore storage and a skin around the test well. The arrangement of the plots on the page mimics the well field pattern shown in Figure 3.1.

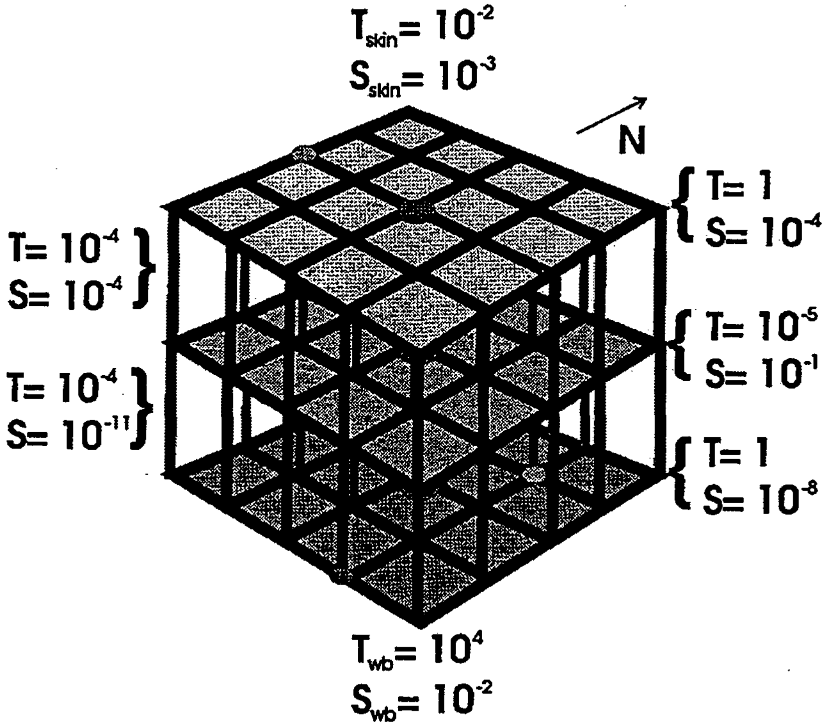

Figure 3.9. Orders of magnitude of T (m^2/s) and S used to produce the drawdowns shown in Figure 3.8.

With the large number of unknowns involved (17), the parameters returned by the inversion cannot be considered to provide a unique solution to the problem. However, a number of inversions were done, employing different starting guesses for properties, using different random seeds, and holding different combinations of parameters fixed. All the inversions yielded similar results and all the T and S values are consistent with the conceptual model of the flow system.

The remaining discrepancies are the early-time behavior at the test well and OW1L, and the late-time behavior at all the observation intervals, in which the calculated drawdowns are all too small. The late-time mismatch was addressed by dividing each layer into an inner and outer zone, and doing an inversion in which the T and S values of each zone vary independently. The boundary between zones is about 8 km from the test well, so the outer zone represents extremely far-field conditions, and may even be representative of the boundary of the Snake River Plain aquifer. The resulting drawdowns, shown in Figure 3.10, no longer consistently underpredict the late-time drawdown trend, as do the drawdowns shown in Figure 3.8. The far-field transmissivities of the upper and lower layers are decreased by a factor of about 10^4, compared to the corresponding inner-zone transmissivities. Other properties are only changed slightly from the values shown in Figure 3.9.

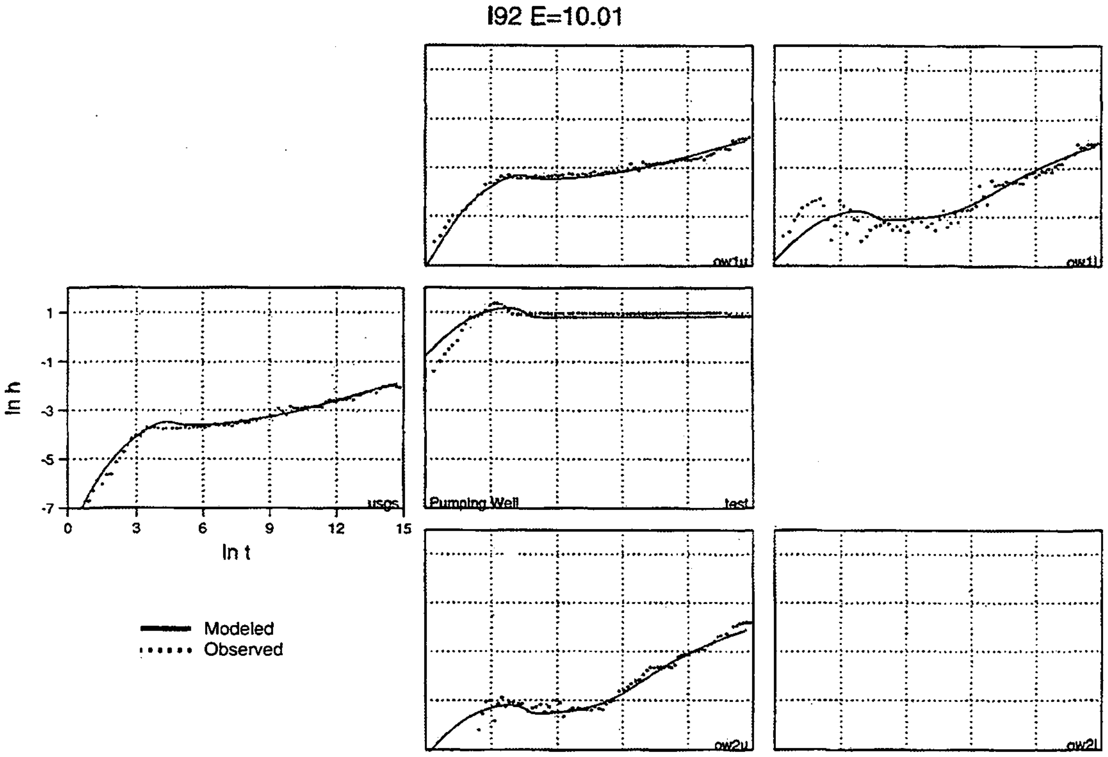

Figure 3.10. Drawdown as a function of time calculated using a three-layer model with a variable pumping rate, including wellbore storage and a skin around the test well, and a far-field zone with lower transmissivity. The arrangement of the plots on the page mimics the well field pattern shown in Figure 3.1.

A series of inversions was done looking for near-field lateral heterogeneities (*i.e.*, T and S were allowed to vary within each layer, in the vicinity of the well-field, using the fractal-geometry feature of the IFS inverse method), but none significantly improved the match shown in Figure 3.10. This non-result reinforces the interpretation of the drawdown versus time plot shown in Figure 3.2, that vertical heterogeneity (*i.e.*, layering) is more significant than lateral heterogeneity at the well-field scale.

Several additional inversions were done that did not allow a distinct matrix-type layer between the upper and lower fracture layers, to see if the variability observed in the pressure transients could be modeled without invoking the dual continuum (fracture/matrix) assumption. Both models with and without lateral heterogeneities were developed. None of the models yielded as good a match to the observed pressure transients as those obtained with models containing a layer with low T and large S. An example of the pressure response obtained for a single-continuum model is shown in Figure 3.11. Figure 3.12 shows the T and S values used to obtain the match. As in the previous case, far-field transmissivities are about 10^{-4} smaller than the corresponding inner-zone values. Unlike the previous calculations, in which a large-storativity region provided recharge and delayed propagation of the pressure pulse, in this case the pressure signal propagates to the boundary of the model during the 36 day duration of the Aquifer Stress Test. The closed boundary there causes the late-time up-turns in the drawdown versus time plots shown in Figure 3.11.

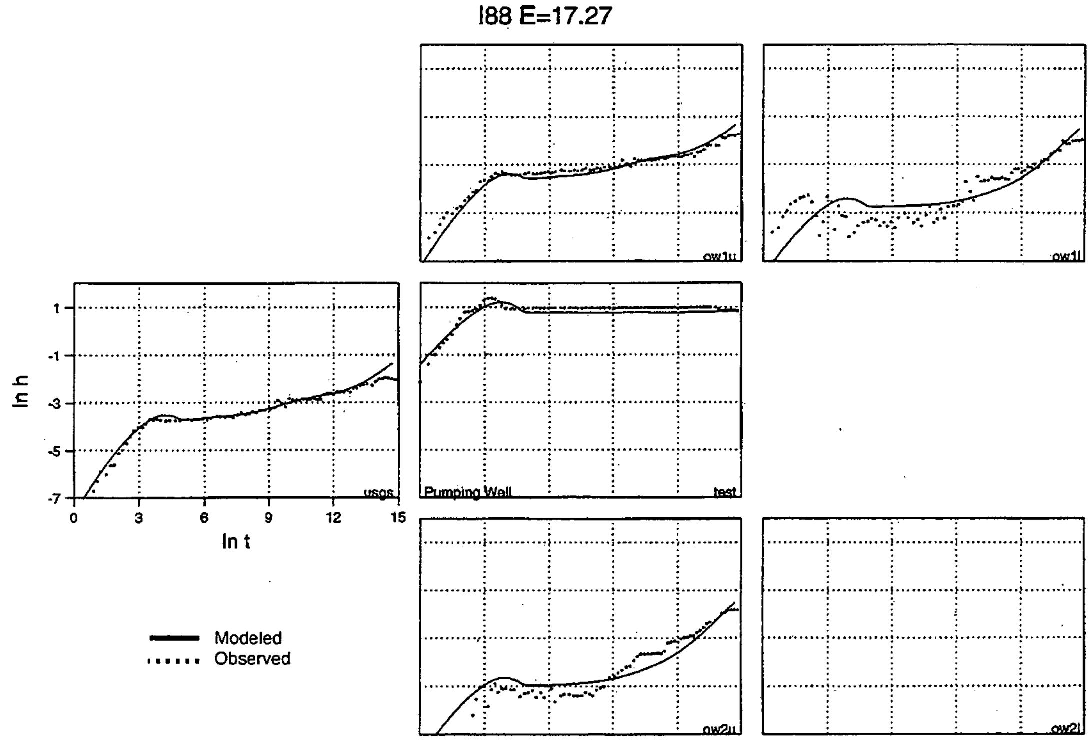

Figure 3.11 Drawdown as a function of time calculated using a two-layer (single continuum) model with a variable pumping rate, including wellbore storage and a skin around the test well. The arrangement of the plots on the page mimics the well field pattern shown in Figure 3.1.

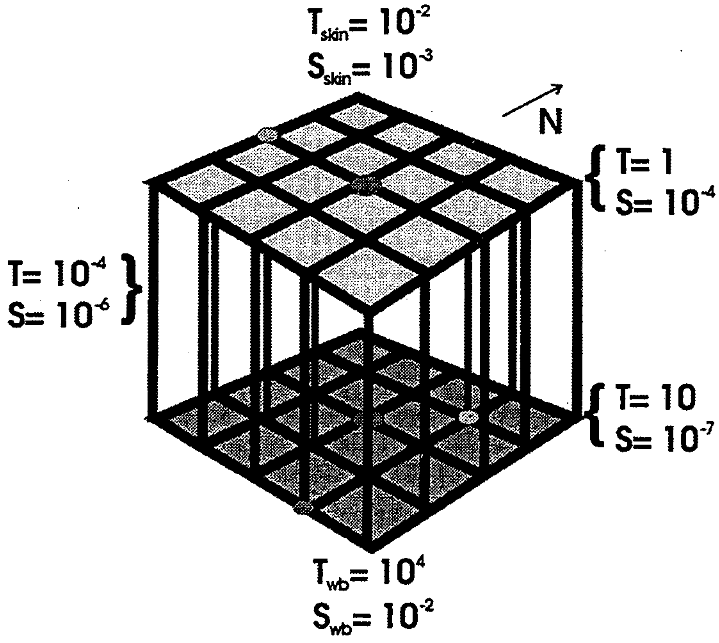

Figure 3.12. Orders of magnitude of T (m^2/s) and S used to produce the drawdowns shown in Figure 3.11.

2.3.3.6 Discussion and Conclusions

A significant effort was made to include in the model physical effects such as wellbore storage and variable pumping rate that affect early-time drawdowns. Often in well-test analysis this is not done and the early-time drawdown data is simply omitted from the analysis. When searching for a single average value of transmissivity and storativity to represent an aquifer, this approach makes sense, because late-time drawdown data reflects an average of aquifer properties over a large area. However, when using interference test analysis to look for heterogeneities at the well-field scale, early-time data is of great importance, particularly for understanding the near field properties. Therefore, it is worthwhile to try to design a numerical model that can account for early-time effects, so early-time data can be used in the analysis.

Two primary findings have come out of the present analysis. First, at the well-field scale (about 100 meters), vertical heterogeneity appears to be more significant than lateral heterogeneity. This conclusion arises from the fact that matching the drawdowns observed during the Aquifer Stress Test requires a model with very different transmissivities at different depths, but uniform transmissivities within a given layer (at least in the vicinity of the well field). Therefore, we infer that the scale of lateral heterogeneity is large compared to the size of the well field, whereas the scale of vertical heterogeneity is small compared to the length of the wells. This pattern of heterogeneity is consistent with the conceptual geological model, in which major high-permeability structures (rubble zones) and major low-permeability structures (sedimentary interbeds and massive basalt flow cores) have much greater areal extent than thickness. However, the conceptual model also includes vertical fractures, an important lateral heterogeneity that may provide fast paths from the surface to the water table. In fact, the low permeabilities and storativities for vertical elements shown in Figure 3.9 probably reflect a spatial average over moderately-permeable vertical fractures, and a nearly impermeable basalt matrix.

The exact locations of individual vertical fractures are difficult to identify through analysis of interference well-test data because their permeability is probably much smaller than that of rubble zones. Hence rubble-zone permeability controls most of the pressure response of observation wells, with vertical-fracture permeability providing a secondary effect. High-permeability vertical fractures have the best chance of being identified by interference test analysis. If multiple observation wells are packed off to isolate different depth intervals within the aquifer, then similar or identical responses in a given well at different intervals suggests a nearby vertical fracture providing good communication between layers. Conversely, strongly different responses in a given well at different intervals suggests poor communication between layers, and the absence of a high-permeability vertical fracture. Such an approach has been successfully taken in a fluvial sand-clay sequence, in which gaps in clay layers were searched for using interference test data (*Doughty*, 1995). However, in that case the gaps in the clay layers were filled with sand, which had a permeability about equal to that of the sand channels themselves. In the present case, vertical fractures are expected to have a permeability many times lower than that of rubble zones. However, if the method proves useful only for the most permeable vertical fractures, it may be worthwhile, precisely because it is the highest-permeability vertical fractures that may provide the biggest potential for fast paths. This multi-well, multi-interval testing approach also may be applied to pneumatic testing for air permeability in the vadose zone, as is planned as part of the Box Canyon studies (Section 2.5.4).

The second general finding of the Aquifer Stress Test analysis is that a dual continuum (fractured/matrix) medium matches the well-test data better than does a single-continuum model. A dual continuum model is consistent with observations made during the Large Scale Infiltration Test, in which tracer breakthrough curves at many observation points showed no clean water arriving before traced water, although clean water was ponded for about a week before tracers were added. This finding suggests the existence of a significant storage capacity (dead-end fractures or pore spaces), within a primary flow network, which also fits the conceptual geological model.

In summary, the analysis of the Aquifer Stress Test has been a successful application of a hydrologic inverse method designed to simultaneously match observation data from multiple wells at multiple levels. However, the unique feature of the IFS inverse method, to examine spatial variability using a fractal geometry, was not brought into play because the locations of all the heterogeneities that were included in the model (multiple horizontal layers, skin zone around the pumping well, far-field contrasting permeability zone), were specified a priori, and no further structural detail resulted from the inverse process itself. In order to make use of this feature, well-test data including observations from more wells is necessary, so the data has a chance to resolve heterogeneous features, rather than simply averaging over them, as occurs with only a few observation wells. An example of the use of the IFS inverse method in which this is possible is given in Section 2.4.3.2.

2.3.4 FY 96 Activities

This analysis was funded by EM50 in FY95. The scope of work on this task has been curtailed due to budget limitations and will be closed out as part of the EM50 project this year as a completed feasibility project. We recommend that this work be continued by EM40 to provide a more complete characterization of important parts of the Snake River Plain aquifer and conducted primarily by INEL. LBL essentially has a relatively complete technology for inverse analysis of multiple-observation-well test data that yields the distribution of permeability throughout a well field, including high-permeability flow paths or barriers to flow between wells. We recommend that future well-test data be subjected to this analysis.

2.3.5 Significance

LBL has an established reputation for using inverse modeling to determine aquifer properties in fractured rock. Transfer of these methodologies to the basalts of Eastern Idaho and, eventually, Eastern Washington, will enable hydrologists to better predict the fate and transport of contaminants in these subsurface environments. Many data sets from pumping tests exist for these sites that are virtually uninterpretable because standard well test analyses cannot address site specific, fracture-dominated flow. Therefore, modelers are forced to make many over-simplifying assumptions about the properties that control ground water flow. These assumptions are often based on "gut-feelings" and bracketed by worst and best case scenarios. The ultimate disposition of buried waste at many sites depends on our ability to make accurate and defensible predictions on future risks caused by migration of contaminants from these sites. In the end, regulators and DOE program managers compromise using conservative estimates of flow and transport. Accurate testing and interpretation technologies are required to provide DOE with data needed to make informed environmental decisions.

Proper analysis of hydraulic test data provides the framework for the design and operation of any pump-and-treat system. Inverse modeling holds the potential for an accurate interpretation of numerous pumping test conducted at the INEL to date. Obviously, this method has a direct applicability to the Idaho Chemical Processing Plant, the OCVZ vapor vacuum extraction, and any other INEL remedial action requiring pumping of ground water or subsurface vapors. This methodology may be useful for delineation of aquifer storage as part of the Snake River Plain adjudication.

The completed feasibility project demonstrates how advanced well test analysis could be used in a more comprehensive program to identify fast flow paths beneath the INEL complex in areas where there is particular concern. Such a program would require relatively extensive drilling, which is why we recommend continuation as a EM40 project.

2.4 Task 4. Regional Flow System

2.4.1 Background

Connected zones of high permeability are likely to exist in fractured aquifers such as the Snake River Plain aquifer, providing fast flow paths that may conduct contamination. Tracer tests can provide local information about groundwater flow, but these are impossible on a regional scale. Large scale assessments of fast flow paths are critical for management of many threatened aquifers including DOE sites at Hanford, INEL and ORNL.

The goal of this task is to use geochemical and hydrologic data to extract information about regional flow patterns. The geochemical part focuses on using strontium (Sr) stable isotope ratios as an indicator of flow patterns. $^{87}Sr/^{86}Sr$ ratios in groundwater evolve over time toward the ratio of Sr acquired from the matrix rock. In areas where flow is unusually fast, changes in the isotope ratio are drawn out over longer distances (Figure 4.1). Unless there is significant mixing of different types of water, contours of Sr ratios should be orthogonal to the flow paths. Methods recently developed at LBL enable inversion of isotope ratios to yield flow path information (*Johnson and DePaolo*, 1994).

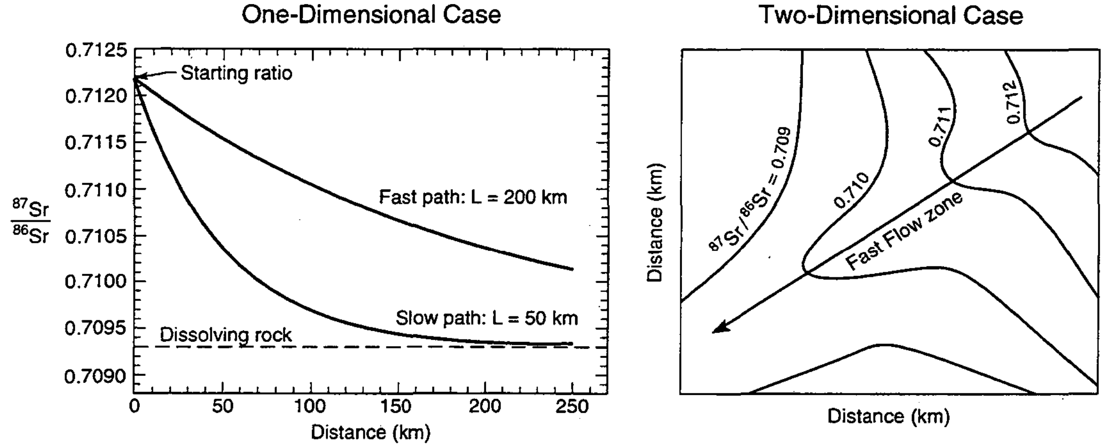

Figure 4.1. Sr isotope ratio plotted versus distance, illustrating a greater value of L, the distance over which isotope ratio varies, for a fast flow path; and contours of Sr isotope ratio showing a fast flow path.

Natural geochemical variations have been used in this way before, but the isotope ratios are generally more reliable indicators of flow than concentration data because they are influenced by fewer processes. Minerals precipitated by groundwater have the same $^{87}Sr/^{86}Sr$ ratio as the parent water, and thus the water ratio is not affected by the precipitation. In contrast, concentrations are affected by both dissolution and precipitation, and interpreting concentration data involves dealing with the net effect, *i.e.* the difference between dissolution and precipitation. Typically, clay minerals are precipitated and are chemically very complex, sensitive to small temperature and chemical variations. In contrast, in the Snake River Plain aquifer, the isotope ratios of the rocks are well characterized, leading to relatively uncomplicated interpretation. Figure 4.2 shows the Snake River Plain, which for the most part has a restricted range of Sr isotope ratios, and the surrounding highland areas, which have higher values.

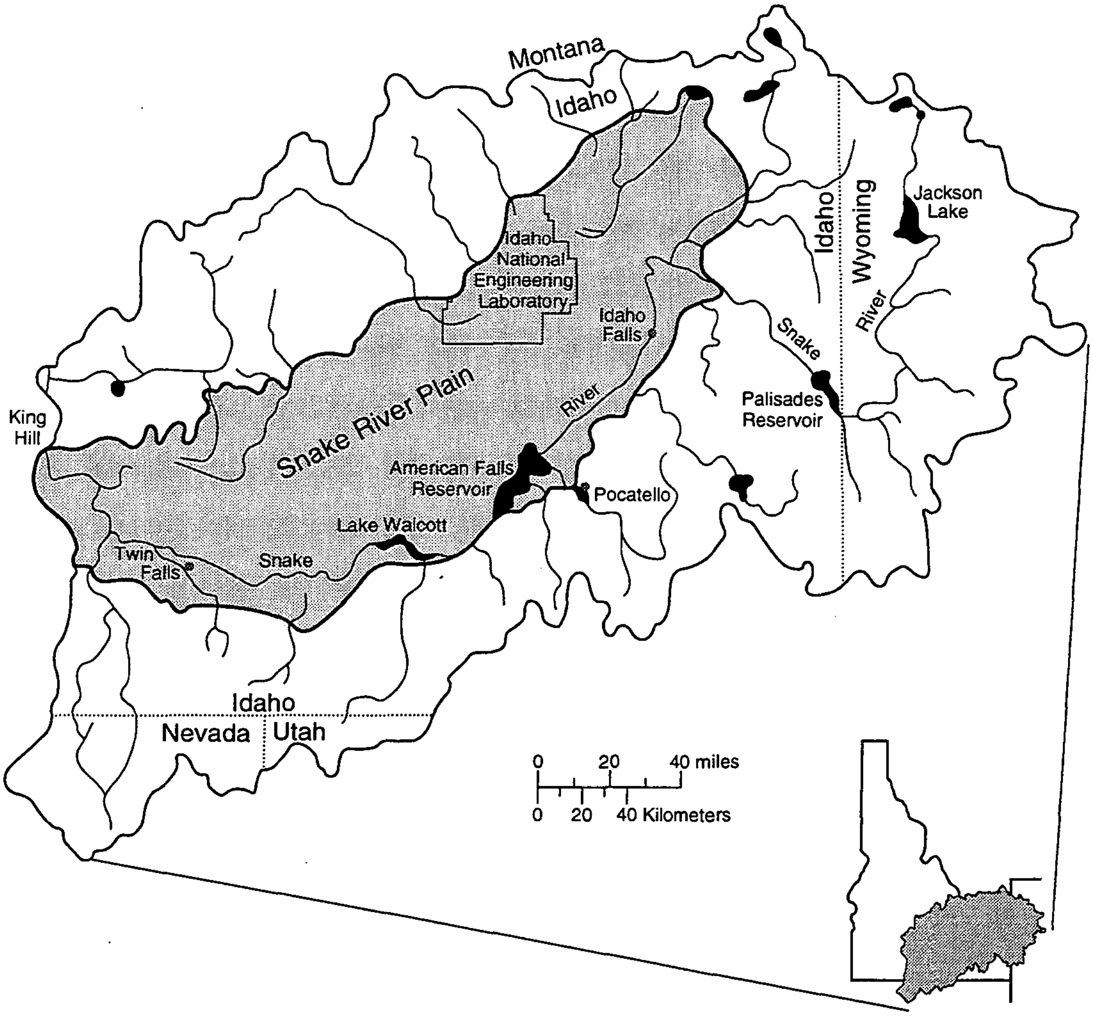

Figure 4.2. The Snake River Plain and the surrounding highland regions, which provide recharge to the aquifer with a high Sr isotope ratio.

The second facet of this task deals with inversion of hydraulic head data. We have developed a state-of-the-art inversion technique that processes fields of hydraulic head data and identifies zones of especially low or high permeability (*Doughty et al.*, 1994). This unique inverse method, known as the Iterated Function System (IFS) inverse method, has been used to analyze transient well-test data, but should be applicable to quasi-steady hydrologic head distributions on a regional scale. The IFS inverse method incorporates concepts of fractal geometry, which enables changes in the scale of application to be made easily. The method will be adapted and expanded to integrate isotope, chemical and hydraulic head data in a single inverse analysis.

If fast flow zones through and away from INEL exist, they should be reflected in both the hydraulic head and Sr isotope data. This task involves development of techniques for inverting the data, analysis of existing data, assessment of feasibility, and preliminary modeling of the INEL region. Ultimately, the goal is to define flow directions, identify any fast paths and possibly estimate their flow velocities relative to surrounding areas.

2.4.2 Performer

The interpretation of isotope and head data is being conducted by LBL under EM50 funding. Tom Bullen at the USGS provided the isotope ratio data. Travis McLing at Idaho State completed a related masters thesis at INEL on chemical analysis that was used as background material.

2.4.3 FY 95 Activities

Although the ultimate goal of this task is to integrate the analysis of isotope-ratio and hydraulic head data, preliminary separate studies addressing the geochemistry and the hydrology of the Snake River Plain aquifer were necessary to ascertain that the conceptual models and technologies to be integrated are appropriate for this setting. This work is described below. Section 2.4.4 then outlines the plan to integrate the geochemical and hydrological analysis technologies.

2.4.3.1 Geochemical Studies

We found that the USGS has already collected some Sr isotope data, and that solute concentrations are being studied by workers at INEL. These data provide a small database with which the feasibility of the Sr isotope study was evaluated. The Sr carried by rivers and groundwater from the valleys to the north of INEL has relatively high $^{87}Sr/^{86}Sr$ ratios. As the groundwater flows through INEL, the ratios fall, as is illustrated in Figure 4.3. Some of this change is due to dissolution of low-$^{87}Sr/^{86}Sr$ basalt rock beneath INEL, and some is due to mixing with a low-$^{87}Sr/^{86}Sr$ water mass to the southeast (Figure 4.4). The first feasibility condition was the need to have a clear trend observed in the data. The USGS Sr isotope data provided this. However, it also provided a somewhat complicated picture, because of the need to separate mixing effects from dissolution effects. A preliminary model for the data was constructed, and at present is ambiguous with regard to the amount of mixing.

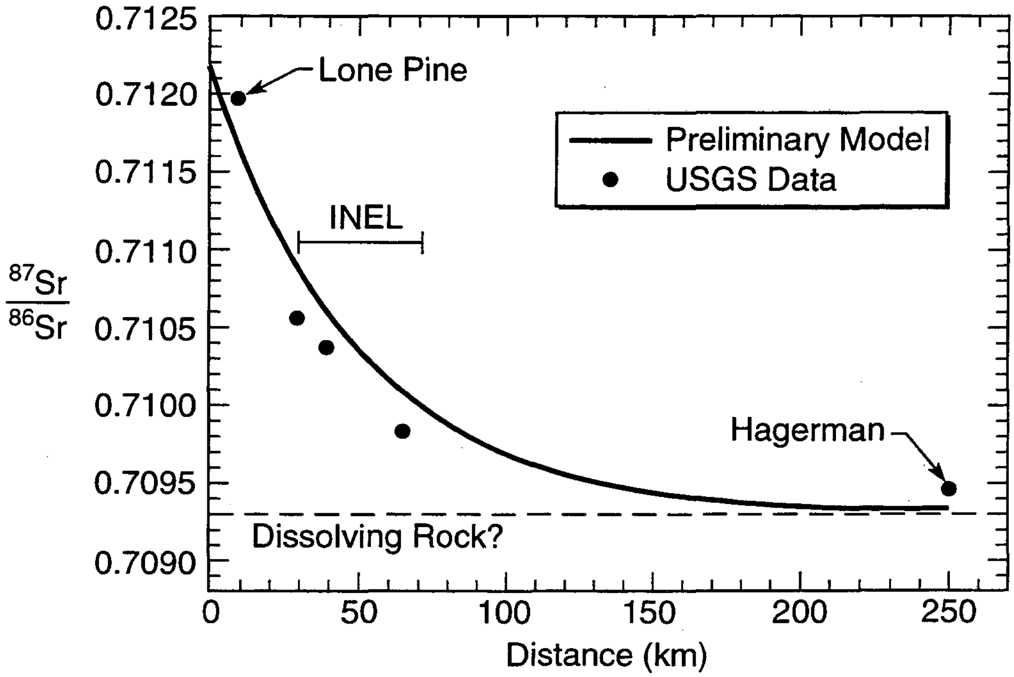

Figure 4.3. Sr isotope ratios plotted versus distance along a flow path through INEL.

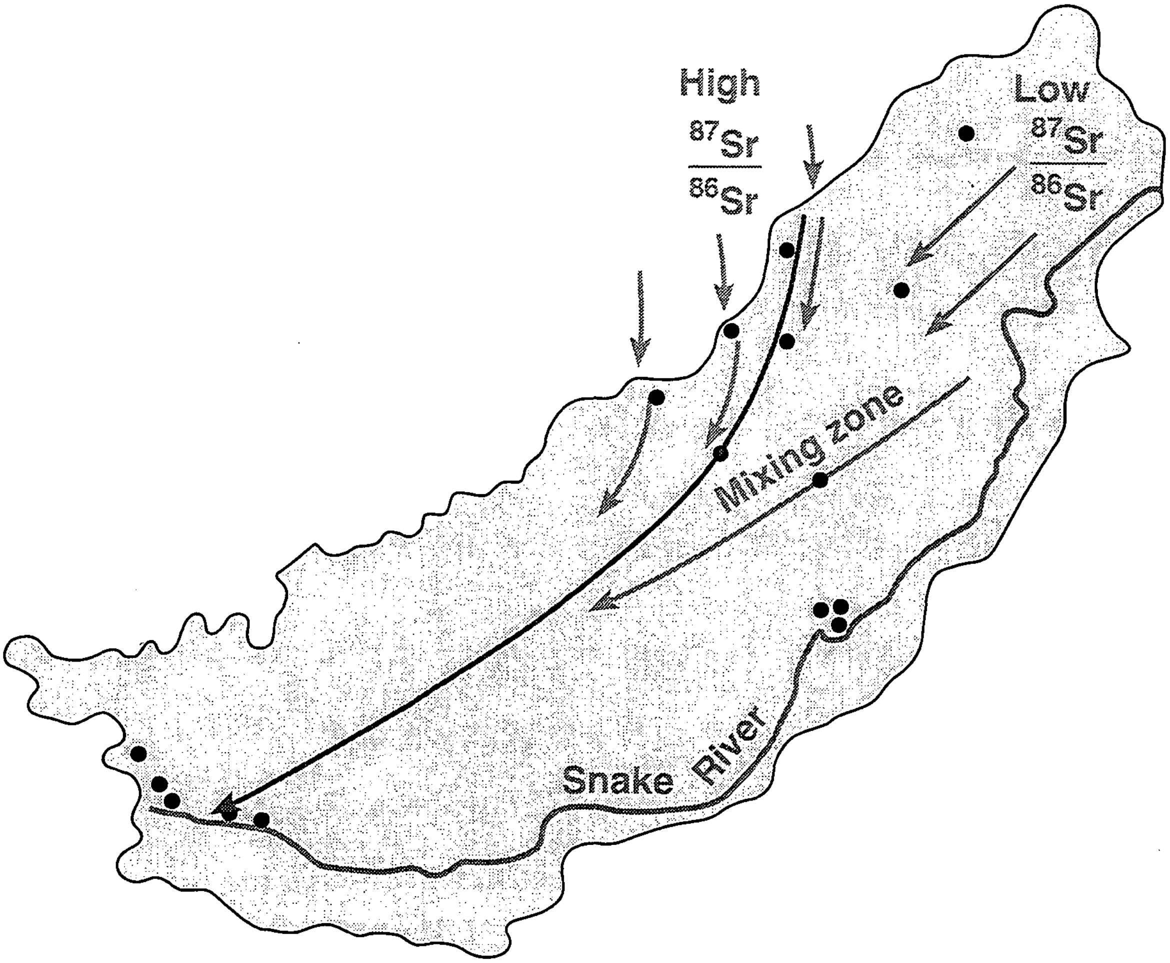

Figure 4.4. A mixing model for Sr isotope ratios in the Snake River Plain Aquifer.

We also found that oxygen isotope data, also provided by the USGS, show a small but significant difference between samples from the northwest areas of INEL and those from further to the southeast. Oxygen isotope ratios are much less susceptible to water-rock interaction effects and could possibly be used to deconvolve the mixing from the travel time effects on the strontium ratios.

There are not enough Sr isotope data points currently available to create diagrams like Figure 4.1, in which multiple flow paths can be compared. Since this is how fast paths are most readily identified, further Sr isotope data collection will be necessary.

2.4.3.2 Hydrological Studies

Section 2.3 described the use of the IFS inverse method to study the Snake River Plain aquifer at the scale of a few hundred meters, by constructing a model that could match the transient drawdowns at four wells during the Aquifer Stress Test. In contrast, in the present task we are interested in characterizing the aquifer at a much larger scale (several hundred kilometers), by building a model that can match quasi-static hydraulic head data from several hundred wells located throughout the aquifer. Because the IFS inverse method has not been applied to this sort of problem before, a synthetic problem designed to very roughly mimic the Snake River Plain aquifer was constructed to test the code. The model represents the aquifer as a single layer containing zones of high and low transmissivity. Figure 4.5 shows the model and the corresponding steady-state hydraulic head distribution. The lower boundary of the rectangular model is held at a constant head value of 0.60 km, and the upper boundary is held at a constant head value of 0, resulting in a regional groundwater flow from bottom to top. The side boundaries are closed. The locations of high and low transmissivity regions are arbitrary and not meant to represent any actual features of the Snake River Plain aquifer. The dimensions of the model and the overall hydraulic head gradient are representative of the Snake River Plain aquifer. The results of a hydrologic inversion, which used a uniform transmissivity distribution as a starting point, are shown in Figure 4.6. The inversion is successful in matching both the steady-state head distribution and transmissivity variation.

An obvious difference between the transmissivity distribution returned by the IFS inversion (Figure 4.6) and the one originally specified (Figure 4.5) lies in the nature of the high and low transmissivity regions. Although the inversion locates them in the right place, and assigns about the right magnitude transmissivity, they are much less regular than in the synthetic data. This rough, more random character, which is probably more representative of natural aquifers than the sharp boundaries of Figure 4.5, arises naturally from the IFS inverse method. Rather than requiring the user to divide the model into zones and then letting the inverse method search for the values of transmissivity for each zone, as is commonly done in hydrologic inversion, the IFS inverse method uses concepts from fractal geometry to identify both locations and values of transmissivity variations (*Doughty et al.,* 1994). This greatly enhances the flexibility of the method, enabling it to more readily identify fast paths or barriers. Furthermore, the self-similar nature of fractals allows multiple scales of heterogeneity to be incorporated in the model easily.

The creation of a realistic model of the Snake River Plain aquifer will need to incorporate an accurate water budget, including recharge from irrigation and precipitation, tributary drainage-basin under flow, interactions with the Snake River and other surface waters, and groundwater pumping. This data has been compiled for previous studies of the Snake River Plain aquifer (*e.g. Garabedian,* 1992; *McCarthy et al.,* 1995). The computer model by *McCarthy et al.* (1995), which focused on the INEL region, but examined the aquifer as a whole well, has been made available to LBL and will provide the starting point for our IFS inverse analyses.

2.4.4 FY 96 Activities

With the completion of the feasibility studies and preliminary modeling, this task will be separated from the remainder of the project. We plan to submit it to ER for funding as a basic research project. The project will then focus on developing methods for deconvolving mixing and reaction effects and inverting hydraulic head and geochemical data together with application to a variety of sites. A brief outline of the planned work follows.

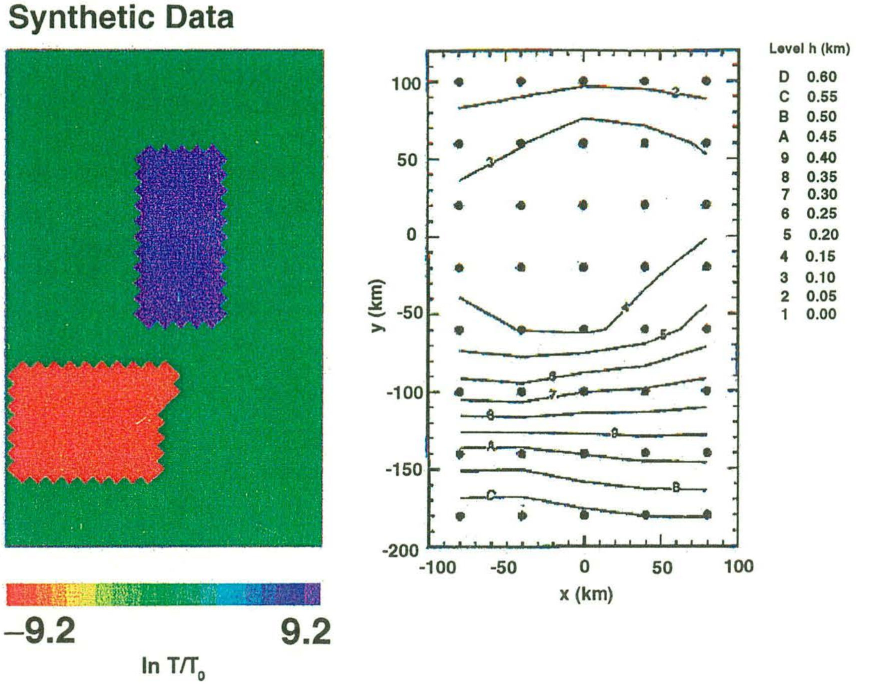

Figure 4.5. The synthetic transmissivity distribution used to test the hydrologic inverse method for a regional-scale analysis, and the steady-state hydraulic head values obtained from it. T_0 is the average or background transmissivity. The black dots show the locations of the steady-state head values that were used in the inversion.

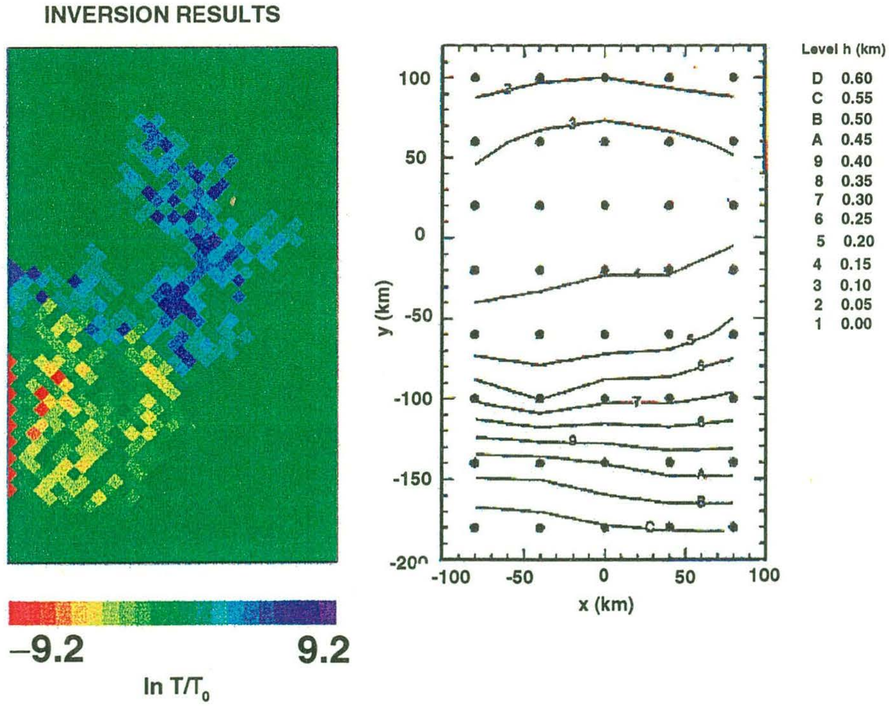

Figure 4.6. The transmissivity distribution returned by the hydrologic inversion, and the corresponding hydraulic head values.

Activity	**Purpose**
Phase I	
Collection and analysis of Sr isotope data	Need more complete database to identify fast paths
Collection and analysis of other isotopic and chemical data	Use non-reactive species to deconvolve mixing and rock-water interactions
IFS inversion of hydraulic head data, using a modified version of MODFLOW	Previous Snake River Plain modeling studies use MODFLOW, forward model is ready to go; technique should be straightforward
Phase 2	
Graphical display of full Sr isotope data set in the form of Figure 4.1, and initial one-dimensional flow and transport modeling	Look for trends, verify conceptual model
IFS inversion of hydraulic head data, using TRINET for forward model instead of MODFLOW	TRINET can calculate both flow and transport, and it has been used extensively with IFS inverse method; anticipate co-inversion of both isotope and head data
Combine hydrologic and geochemical inversions iteratively	Simplest way of jointly analyzing geochemical and hydrologic data; enables judging value of different data sets
Examine sensitivity of results to observed data	Determine whether additional data needs to be collected
Phase 3	
Combine hydrologic and geochemical inversions directly	Most elegant way of jointly analyzing geochemical and hydrologic data; eliminates bias that may arise from iterative inversions
Apply technology to other sites	Characterize fast flow paths for other problem areas

Table 4.1. Outline of proposed work to extend feasibility and modeling studies of the Snake River Plain aquifer (to be submitted to ER).

2.4.5 Significance

If this method can be made to work it will provide a very powerful new approach to defining hydrologic regimes. This will have application to a broad variety of waste problems including nuclear waste storage and remediation. Down gradient water users and INEL Stakeholders from the Twin Falls-Thousand Springs have historically been the most vocal opponents to operations at the INEL. This opposition exists in large part because of a general lack of understanding on the actual flow pattern of water through the Snake River Plain aquifer. Delineation of these flow patterns may demonstrate that a relatively small portion of water discharging to Thousand Springs travels beneath the INEL and, therefore, concerns over radioactive contamination are overstated. Analysis of groundwater flow at a regional scale will provide boundary conditions for basin modeling needed for managing water rights in Eastern Idaho and calibrating the INEL-wide modeling.

2.5 Task 5. Vadose Zone Hydrology

2.5.1 Background

One of the major problems in understanding infiltration in fractured basalt is the complexity of the fracture system and fluid flow paths. Previous studies carried out at the RWMC, the Large Scale Infiltration Test (LSIT), and the Box Canyon sites have shown rapid local movement of percolating water with an average rate of 5-10 m/day from the land surface to the first interbed. Percolating water tends to perch above interbeds and on dense continuous basalt flows and then move laterally until vertical fractures or oblique rubble zones redirect the flow downward to the next interbed or unfractured basalt flow. Identifying and mapping the locations where rapid movement takes place will allow better design of monitoring systems as well as improved control of water migration and contaminant transport.

The issue under investigation in FY 95 is whether and how gas flow tests can be used to predict some aspects of the connectivity within the fracture system and fluid flow geometry under infiltration. Preliminary success of using hot air injection to identify connected fractures at the Box Canyon site (*Knutson et al.*, 1992) indicates that a similar method can be used to identify fractures connecting the injection well with monitoring wells and the land surface. The Box Canyon site is ideally suited for instrumentation evaluation because of excellent rock exposures, both on the ground surface and on the cliff face, and previous work conducted there.

2.5.2 Performer

The 1995 field work at the Box Canyon site has been conducted in a collaboration involving the following.

- LBL: surface survey; borehole scanning; test design; sensors and data acquisition system; analyses of test results and geological information from TV recording, gamma and caliper data.
- INEL and LBL: site characterization, hot air injection tests, and analysis of the site geology.
- INEL: borehole drilling; description of cores; IR imaging; analyses of test results.
- USGS: TV recording, gamma, and caliper logging.

The Bureau of Land Management provided the Box Canyon site and archeological survey.

2.5.3 FY 95 Activities

The 1995 activities included the following.

1. Review results of LSIT.
2. Establish experimental site, including site selection, archeological survey, site permitting, site preparation, well drilling, and logging.
3. Instrument and conduct hot air injection tests to establish a preliminary model of gas flow in fractured basalt.
4. Development and evaluation of sensors and instruments.

These activities are described below.

2.5.3.1 Review of Results of the Large Scale Infiltration Test

The LSIT was conducted at the INEL during the summer of 1994. The LSIT took place in a bermed basin approximately 600 ft (200 m) in diameter. The basin floor consisted of a thin veneer of soil and exposed basalt. Well water was ponded in the basin for approximately one week before the radiological tracers selenium-75, strontium-85, and terbium-160 were added and mixed into the ponded water. Results of the neutron probe monitoring indicated that the wetting front moved downward at an average rate of 5 ± 2.9 m/day. Using first arrival at lysimeters the rate was estimated at 4.8 ± 5.4 m/day. The average velocity estimated from tracer analysis indicated 1 m/day based on break through curves and the estimated dispersivities were found to range from

0.08 to 45.8 m. The infiltrating water wetted the cylindrical volume directly below the pond until the water reached an interbed at the 55 m depth. Once the water reached the interbed it ponded and spread laterally over a larger area.

In general the volume of fractured basalt beneath the infiltration basin was wetted in an irregular manner in that wetting was observed at deep depths before it was observed at shallow depths. Also some lysimeters indicated water, but no tracer was detected. Other lysimeters indicated tracer and initial wetting to take place at the same time although water was ponded for one week prior to tracer additions.

The Need for Hydrologic Understanding

Models based on curve fitting break through curves indicated that porous medium models worked as well as fractured/matrix medium models. These results are probably due to the flow in fractures taking place at such a high rate that the mass transfer into the basalt matrix was too slow to be significant in this test. The LSIT clearly indicated the need to better understand water and tracer transport into and through fractured basalt. While the LSIT demonstrated that water and solute were transported rapidly through fractured basalts, the mechanism for maintaining fracture flow was not evaluated. Current theory predicts that the basalt matrix should adsorb water out of the fractures and greatly reduce the velocity of the wetting front through the system. But the wetting was rapid through the entire volume below the ponded area. Thus, one must conclude that the basalt matrix is nearly saturated under arid conditions or that the rate of adsorption into the matrix is too slow to be important under conditions of rapid infiltration. Most of the hydrographs for the perched water displayed a bell shaped curve with the rising limb slightly steeper than the falling limb. This indicates that preferential flow and air entrapment are significant.

The sharp contrasts in tracer arrivals for nearby monitoring locations gives strong evidence for the concept of infiltration occurring through multiple high-permeability flow paths. The fact that some monitoring locations showed no clean water arrival prior to tracer arrival, and some monitoring locations showed the arrival of clean water only, suggests the existence of dead-end fractures, or lower-permeability pore space, into which infiltrating water may enter but not leave quickly. This is consistent with the conceptual geological model containing cooling cracks that do not fully penetrate basalt flows, and poorly-connected vesicular zones. It is also consistent with the finding that a dual-continuum model was better able to fit the Aquifer Stress Test data than a single-continuum model.

The infiltration rate remained constant throughout the test, despite the continual increase in subsurface moisture content. This suggests that the infiltration rate was predominantly controlled by the surface soils, because otherwise increasing moisture content in the fracture network would increase hydraulic conductivity and thus infiltration rate. This is consistent with the notion of the surface soil layer acting like an interbed, which is discussed below.

Site Instrumentation

The back fill material used to seal the well casings may have created direct conduits for water flow, interfered with water content measurements using neutron probes, and ruled out accurate mass balance computations. Thus, the amount of water that moved through the system undetected could not be evaluated. In addition, small fractures induced during the drilling of wells may have been a source of dead-end flow paths or may be connected to major fractures. Also the large size of the LSIT required large distances between wells creating a sparse sampling network that further complicated accurate mass balance calculations.

Implications for Future Studies

In order to better model and understand water movement into and through fractured basalts additional studies are needed. The studies need to be conducted at a scale applicable to the scale of observed fractures, *e.g.*, a scale of 1 to 5 m. The reduced scale of the study will allow a dense instrumentation network to be installed where the interaction between fractures and matrix can be observed. The LSIT needed instruments designed specifically for monitoring water and solute transport into and through fractured rock systems on a much larger scale.

The vertical hydraulic conductivity of the fractures at the LSIT was higher than expected, leading to predominantly downward flow below the infiltration pond. This finding is consistent with initial observations made at Box Canyon, that through-going vertical fractures — not included in the original conceptual flow model — are present. At the interbed, ponding of water and lateral flow did occur, as interbed conductivity was smaller than that of the basalts. Together, these observations suggest that the interbeds themselves, or the sediment-filled fractures below the interbeds, may provide the primary control on infiltration. If this is the case, then one must be cautious about attempting to solve the whole ground-surface-to-water-table problem by the Box Canyon studies, where no interbed exists between the basalt flows. Instead, these studies may provide a more detailed picture of the fracture flow, which can become part of a more comprehensive subsurface model. On the other hand, a possible interbed surrogate exists at the Box Canyon site: the surface soil layer. Sediments fill the fractures below the soil layer, and the soil layer has one major advantage over a subsurface interbed, namely ease of access.

To best make use of different types of monitoring data, including evaluating which provide the most information about infiltration processes, different types of data should be collected at the same time, over the same spatial region. Real-time analysis and visualization of field data could have been a big help in effective deployment of monitoring devices (for example, choosing where to send the neutron logging truck).

One must understand the connectivity of the fracture network before emplacing instruments to monitor infiltration, so that the instruments will be located where they will intercept liquid flow in fractures. Otherwise they will be likely to monitor matrix flow, a much slower process, which provides little information on critical fast paths.

2.5.3.2 The Box Canyon Site

Selection of Site

The Box Canyon site is located 4.2 km (2.5 miles) south of Butte City, Idaho, along a reach of the Big Lost River known locally as Box Canyon (Figure 5.1). The site Box Canyon "B" is located 500 ft (150 m) west of a previously studied area Box Canyon "A" and has a 15 m (50 ft) vertical exposure of fractured basalt. An experimental site, 40 m (east-west) by 50 m (south-north), has been selected at the top of Box Canyon within a typical basalt flow about 80 m wide at the cliff face. The center of the site is located about 30 m from the cliff face. A general aerial view of the Box Canyon site is shown in Figure 5.2. The surface of the site consists of exposed weathered basalt and soils (clays and silts). In some places, these soils cover the basalt and seal practically all surface fractures, as well as joints between basalt columns, which are typical features of the area surrounding the INEL. The surface is relatively flat. Two basalt flow fingers and a rubble zone between them can be seen on the cliff face.

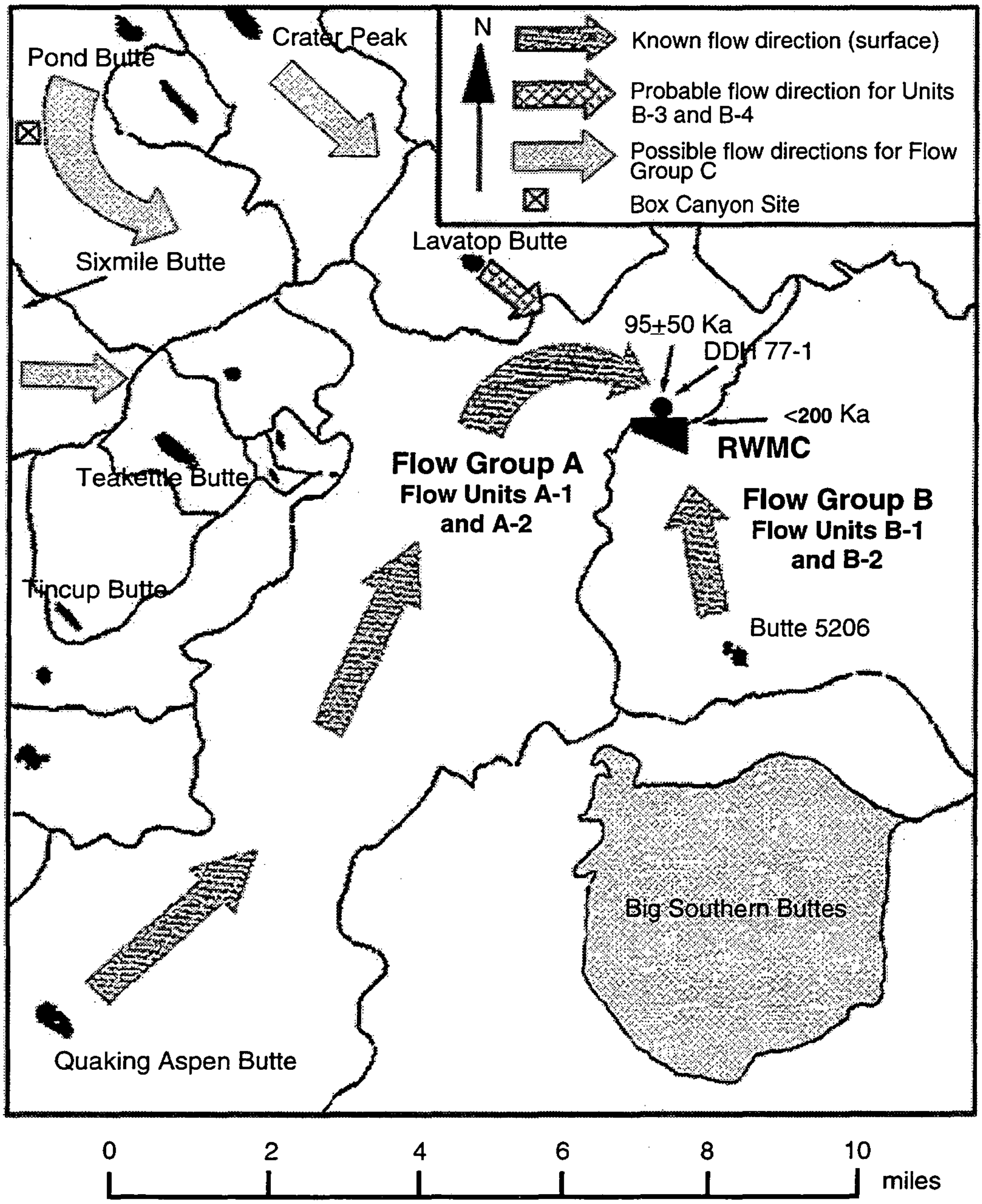

Figure 5.1. Location of the Box Canyon site (about 9-1/2 miles northwest of the RWMC).

Figure 5.2. General aerial view of the Box Canyon site and its vicinity.

Surface Survey and Topography

A surface survey of the site was conducted on June 13, 1995, using a laser survey system (Hewlett-Packard Model 3820 Electronic Total Station). In order to perform the survey, a mesh with cells of 1 m by 1 m was established (Figure 5.3). Photos of the surface exposure at each cell were taken in order to create a map of the surface fracture system. A close-up view of the cells at the center of the site is shown in Figure 5.4. Points that were surveyed are shown in Figure 5.5. A three-dimensional plot of the surface topography was created using visualization software (AVS) and is shown in Figure 5.6. These data will be used for three-dimensional computer visualization of the site geology.

Figure 5.3. Photo of the mesh established at the site in June 1995 in order to survey the land surface.

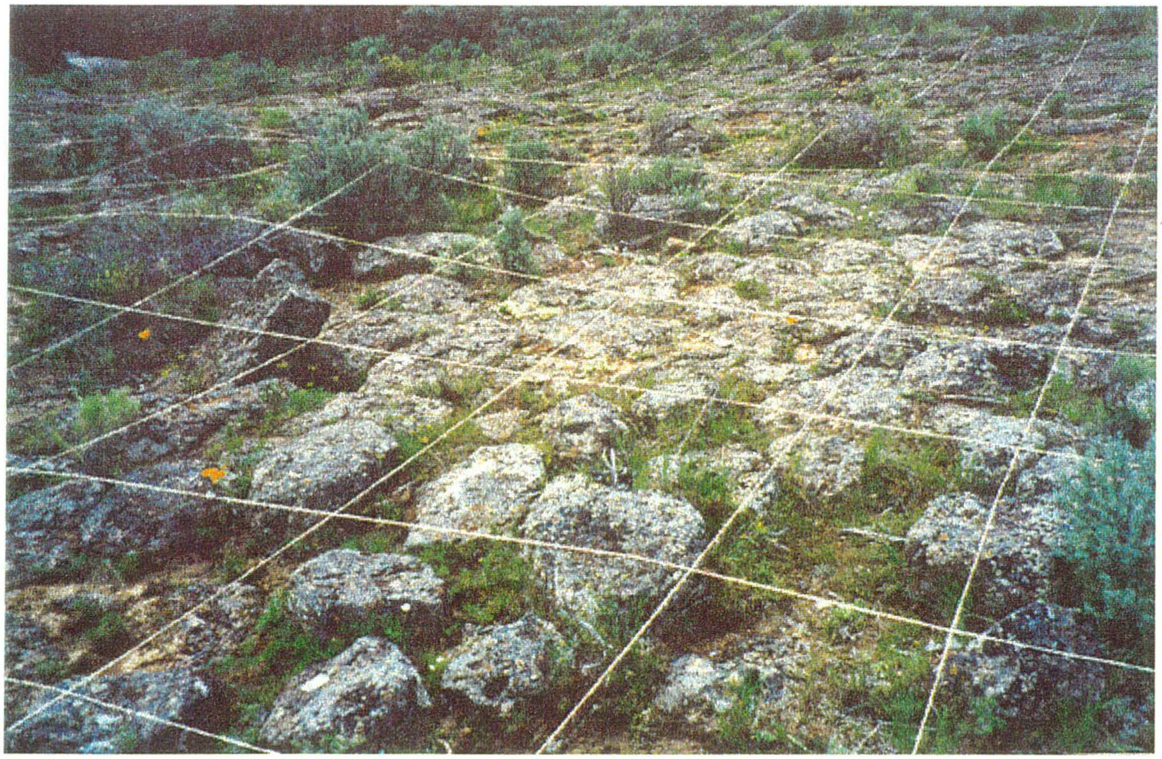

Figure 5.4. Close-up view of the center of the site, June 1995.

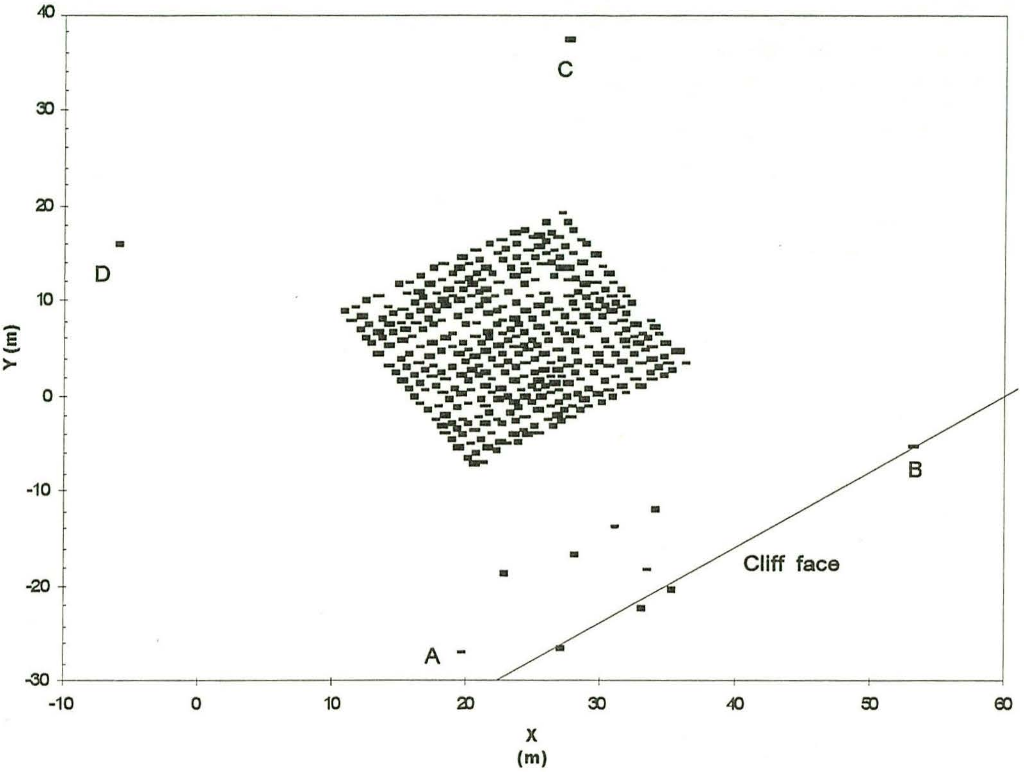

Figure 5.5. Grid coordinates surveyed in June 1995.

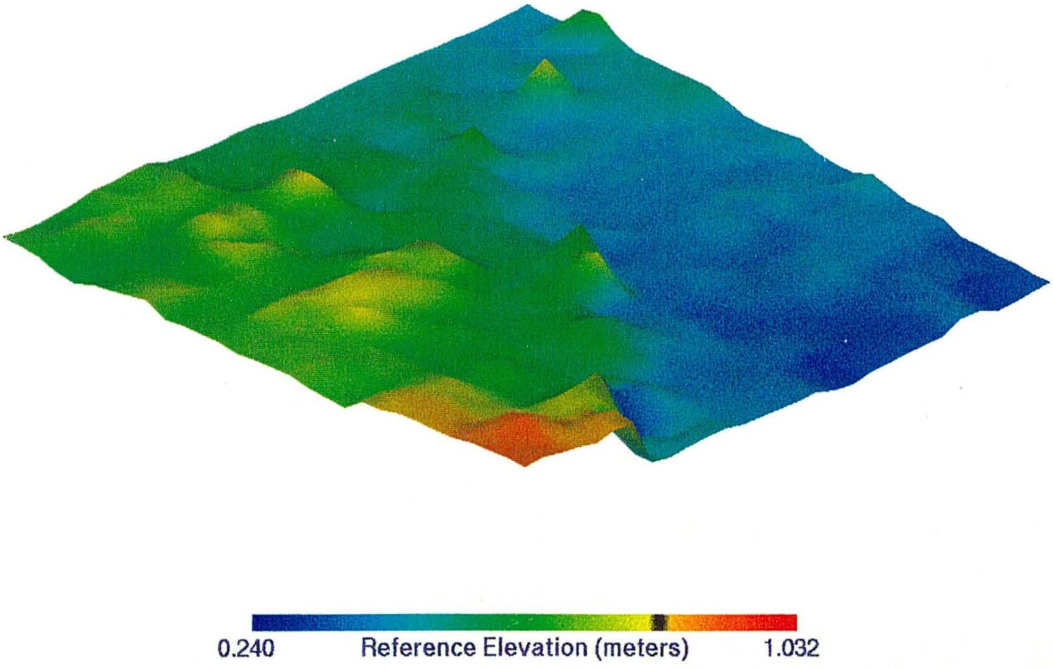

Figure 5.6. Three-dimensional view of surface topography created using AVS.

Borehole layout

The borehole layout is shown in Figure 5.7. The borehole layout was designed to examine fracture connectivity in the near surface prior to conducting an infiltration test. Because we are concerned with infiltration, we are concerned with how fluid moves in the vertical direction. Naturally, vertical flow will prefer vertical fractures, but vertical fractures are poorly sampled by vertical holes. We considered drilling horizontal holes from the cliff face, but such holes were very expensive and very difficult to instrument. We selected the alternative of drilling slant holes in order to maximize the opportunity to intersect vertical fractures. Because there is a possibility of extensive lateral gas flow when injecting into the rubble zones, several deep monitoring wells were drilled away from the center of the site, and shallow wells were drilled in the vicinity of the center of the site. All in all, 17 wells were drilled.

- There are 13 vertical wells, including:
    - 1 well (II-5), 23 m (74 ft) deep (drilled by a water-rotary method, with full core recovery).
    - 7 wells, 18.3-19.2 m (60-63 ft) deep, including 4 wells (II-2, II-3, II-7, and II-8) drilled using an air-rotary method, and 3 wells (II-1, II-4, and II-6) cored using a water rotary method.
    - 5 wells (I-1 through I-5) were drilled using an air rotary method, down to 12 m (40 ft) (except well I-5 which was drilled to 6 m (20 ft)). Three of the shallow wells were initially drilled down to 6 m (20 ft), but when the site geology became more precisely known from drilling the deep boreholes, these wells were deepened to 12 m (40 ft) to provide penetration of a rubble zone located between 10.7 and 12 m (35 and 40 ft).
- There are 4 slant wells (30° from the vertical) were cored using a water rotary system. All slant boreholes were parallel and terminated beneath the center of the site such that they lie one on top of another.

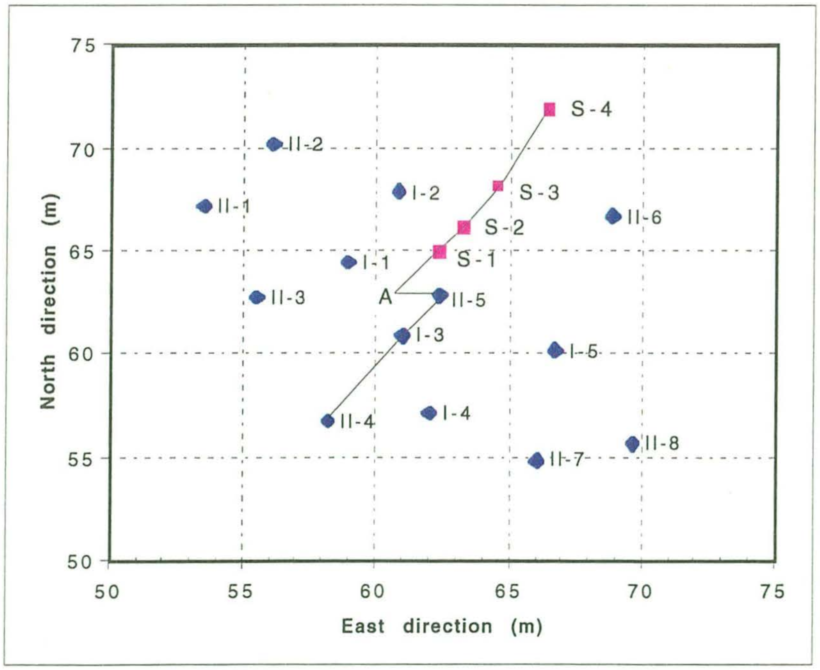

Figure 5.7. Borehole layout at the Box Canyon site. The line identifies the lithological profile shown in Figure 5.14. Slant holes as show in red.

Table 5.1 summarizes well completion depths, surface elevations, locations, and drilled diameters.

Table 5.1. Well identification, completion depths, elevation, location, and drilled diameters of the Box Canyon wells drilled in 1995. The leading number shown with the slant holes is length and the trailing number is depth below land surface.

Well ID	Depth	Elev.	East	North	Bit diam.
	m(ft)	m(ft)	m(ft)	m(ft)	(cm)
I-1	12.2(40)	1599.9(5249.0)	58.9(193.2)	64.4(211.4)	14.9 to 6.1m 14.3 to 12.2m
I-2	12.2(40)	1599.8(5248.8)	60.8(199.4)	67.9(222.9)	14.9 to 6.1m 14.3 to 12.2m
I-3	12.2(40)	1599.9(5249.0)	61.0(200.0)	61.0(200.0)	14.9 to 6.1m 14.3 to 12.2m
I-4	12.2(40)	1600.0(5249.3)	62.0(203.3)	57.2(187.5)	14.9 to 6.1m 14.3 to 6.1m
I-5	6.1(20)	1599.5(5247.8)	66.7(218.8)	60.3197.7	14.9
II-1	18.3(60)	1599.1(5246.5)	53.5(175.4)	67.3220.7	9.5
II-2	19.3(63.2)	1599.8(5248.7)	56.1(184.0)	70.1(230.1)	14.9 to 14.6m 14.3 to 19.3m
II-3	18.3(60)	1599.9(5249.0)	55.5(182.0)	62.8(205.9)	9.5
II-4	18.3(60.1)	1599.8(5248.7)	58.2(190.8)	56.8(186.4)	9.5
II-5	22.5(73.7)	1600.1(5249.7)	62.4(204.6)	62.9(206.4)	9.5
II-6	18.3(60)	1600.2(5249.9)	68.9(226.0)	66.7(218.9)	9.5
II-7	18.3(60)	1600.0(5249.4)	66.0(216.6)	54.9(180.2)	9.5
II-8	18.3(60)	1600.2(5250.0)	69.6(228.4)	55.7(182.9)	9.5
S-1	4.9/4.1(16.0/13.6)	1599.9(5248.9)	62.3(204.5)	65.0(213.1)	9.5
S-2	6.1/5.2 (20.1/17.1)	1600.0(5249.2)	63.3(207.6)	66.1(217.0)	9.5
S-3	13.5/11.5(44.4/37.7)	1600.0(5249.3)	64.6(211.9)	68.1(223.4)	9.5
S-4	21.2/17.9(69.4/58.7)	1600.0(5249.5)	66.5(218.2)	71.8(235.7)	9.5
Center of Site	N/A	1599.8(5248.6)	61.5(201.7)	63.2(207.2)	N/A

Borehole logging

The following types of borehole logs were performed:

- gamma
- caliper
- TV recording
- borehole scanner
- core description

Examples of gamma logging, caliper data, core description, and photos of cores are presented in Figures 5.8, 5.9, 5.10, and 5.11, respectively. A custom computer format for recording the drilling logs is being prepared to be compatible with the data visualization system. The core description and TV logs of the slant boreholes improved the understanding of the vertical fractures, especially the locations of joints between basalt columns. The interpretation of borehole TV and scanner data is ongoing.

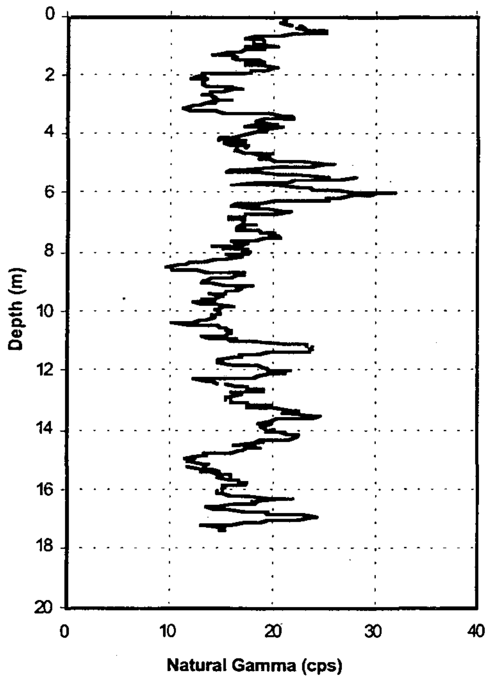

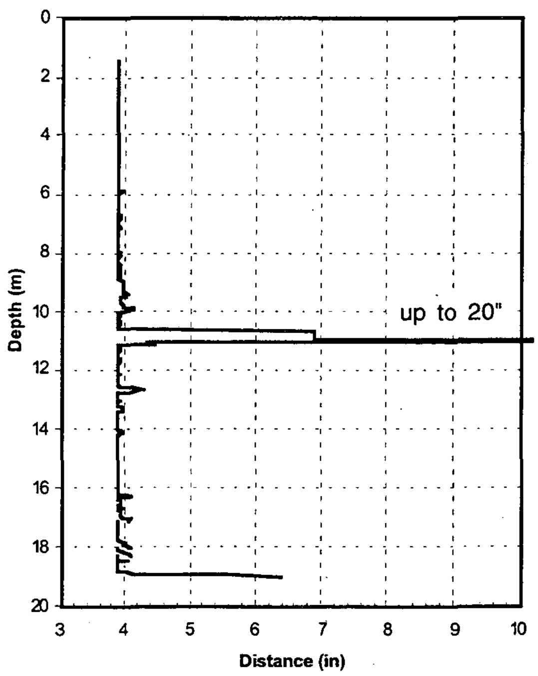

Figure 5.8. Example of gamma logging - well II-7.

Figure 5.9. Example of caliper measurements - well II-7.

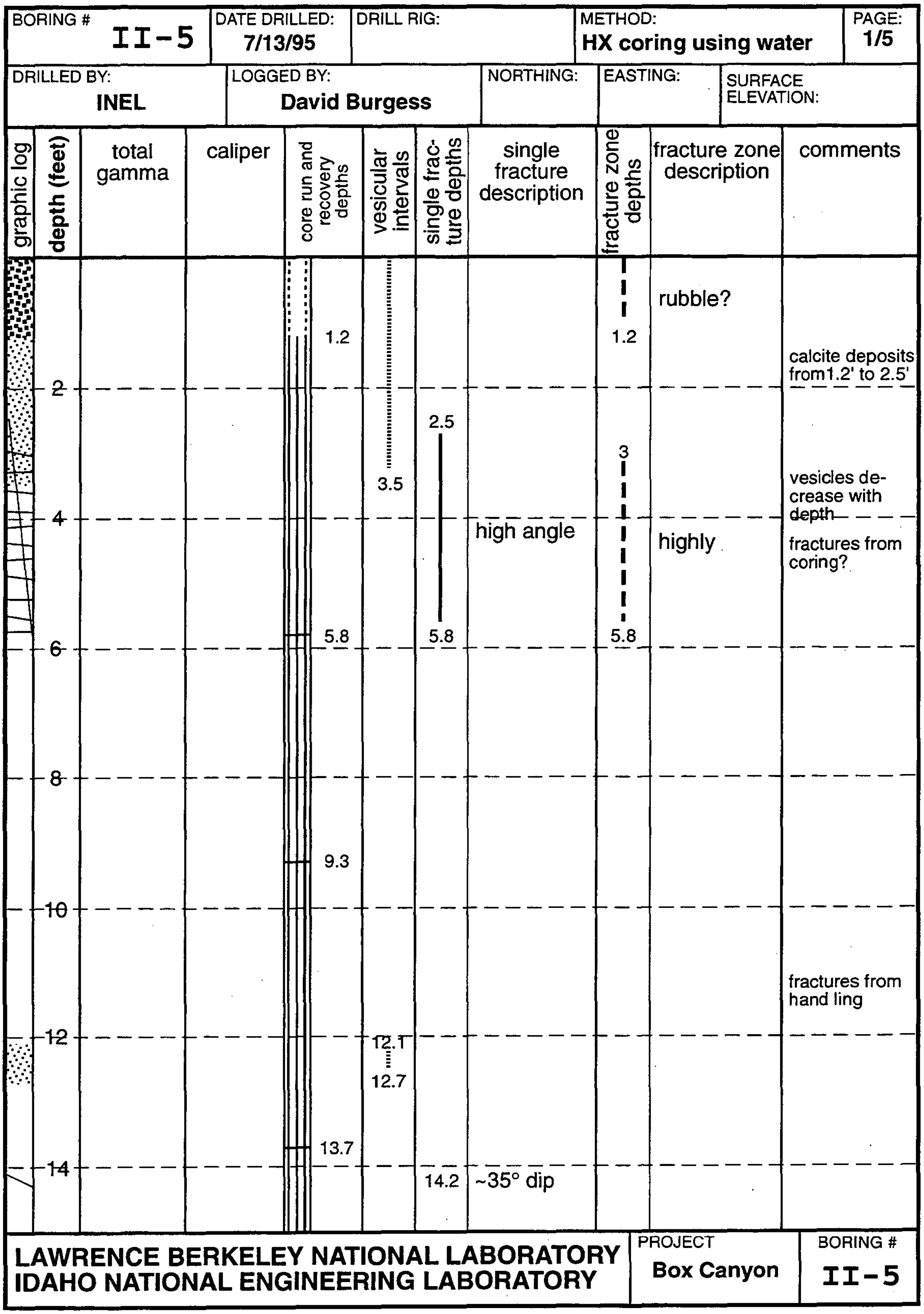

BORING # II-5	DATE DRILLED: 7/13/95	DRILL RIG:	METHOD: HX coring using water	PAGE: 1/5
DRILLED BY: INEL	LOGGED BY: David Burgess	NORTHING:	EASTING:	SURFACE ELEVATION:

graphic log	depth (feet)	total gamma	caliper	core run and recovery depths	vesicular intervals	single fracture depths	single fracture description	fracture zone depths	fracture zone description	comments
				1.2				1.2	rubble?	calcite deposits from1.2' to 2.5'
	2				3.5	2.5		3		vesicles de-crease with depth
	4			5.8		5.8	high angle	5.8	highly	fractures from coring?
	6									
	8			9.3						
	10									fractures from hand ling
	12			13.7	12.1 12.7					
	14					14.2	~35° dip			

LAWRENCE BERKELEY NATIONAL LABORATORY IDAHO NATIONAL ENGINEERING LABORATORY	PROJECT Box Canyon	BORING # II-5

Figure 5.10a. Example of core logging - well II-5.

BORING # **II-5**	DATE DRILLED: **7/13/95**	DRILL RIG:	METHOD: **HX coring using water**	PAGE: **2/5**
DRILLED BY: **INEL**	LOGGED BY: **David Burgess**	NORTHING:	EASTING:	SURFACE ELEVATION:

graphic log	depth (feet)	total gamma	caliper	core run and recovery depths	vesicular intervals	single fracture depths	single fracture description	fracture zone depths	fracture zone description	comments
	16				15.8 16.3					
						16.9	horizontal			
	18			18.7						
	20				19.4 20.4	19.6	horizontal			
	22									
	24			23.7				23.7 26	highly, high angle	
	26				26.7 28.7	27.3	high angle			slightly vesicular lost circu lation at ~28 feet
	28			28.7				28.7	highly, horizontal and high angle	

LAWRENCE BERKELEY NATIONAL LABORATORY IDAHO NATIONAL ENGINEERING LABORATORY	PROJECT **Box Canyon**	BORING # **II-5**

Figure 5.10b. Example of core logging - well II-5.

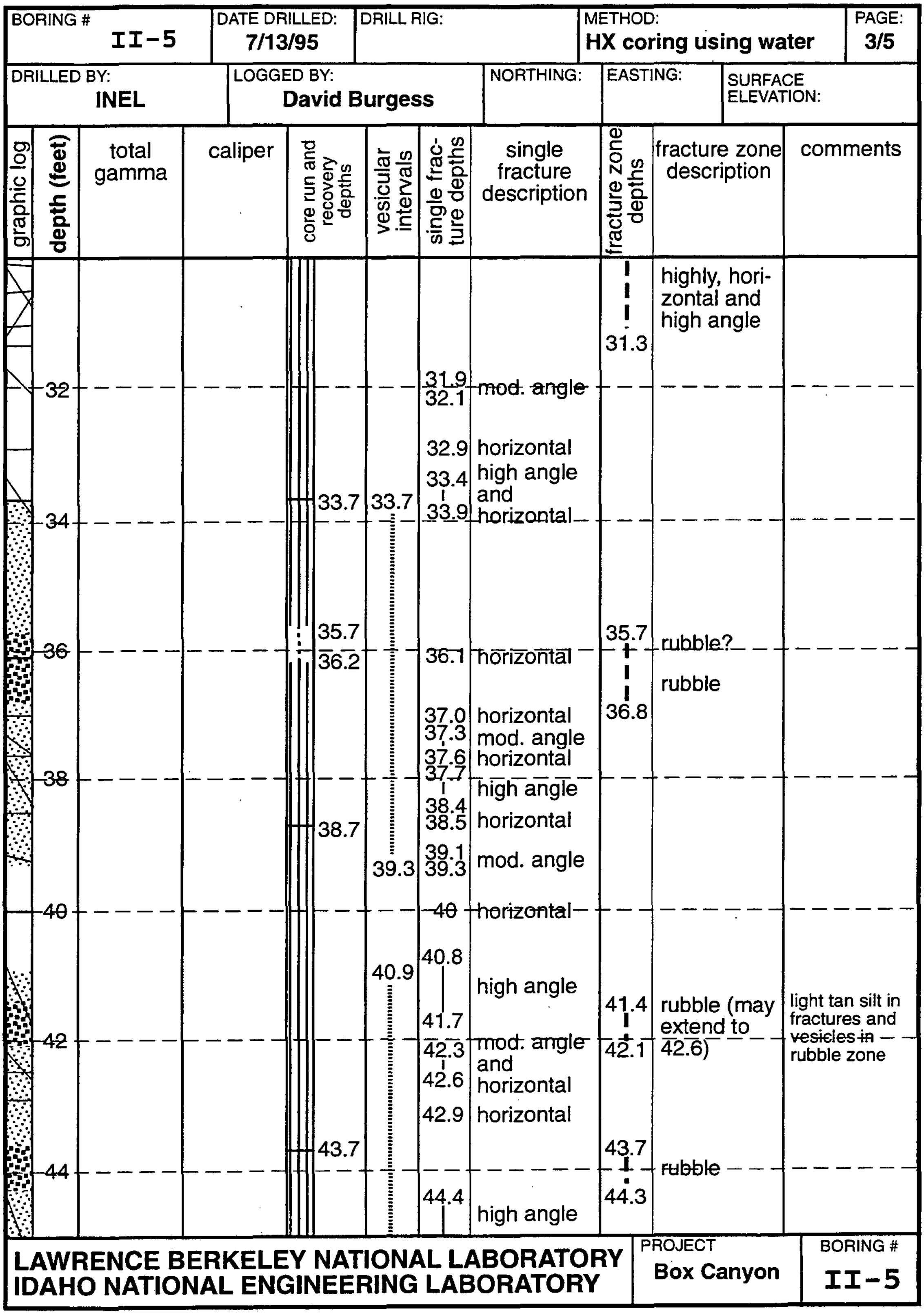

BORING # II-5	DATE DRILLED: 7/13/95	DRILL RIG:	METHOD: HX coring using water		PAGE: 3/5
DRILLED BY: INEL	LOGGED BY: David Burgess	NORTHING:	EASTING:	SURFACE ELEVATION:	

graphic log	depth (feet)	total gamma	caliper	core run and recovery depths	vesicular intervals	single fracture depths	single fracture description	fracture zone depths	fracture zone description	comments
								31.3	highly, horizontal and high angle	
	32					31.9 32.1	mod. angle			
						32.9	horizontal			
						33.4 – 33.9	high angle and horizontal			
				33.7	33.7					
	34									
				35.7				35.7	rubble?	
	36			36.2		36.1	horizontal		rubble	
						37.0	horizontal	36.8		
						37.3	mod. angle			
						37.6	horizontal			
	38					37.7 – 38.4	high angle			
						38.5	horizontal			
				38.7						
					39.3	39.1 39.3	mod. angle			
	40					40	horizontal			
					40.9	40.8 – 41.7	high angle	41.4	rubble (may extend to 42.6)	light tan silt in fractures and vesicles in rubble zone
	42					42.3 – 42.6	mod. angle and horizontal	42.1		
						42.9	horizontal			
				43.7				43.7		
	44							44.3	rubble	
						44.4	high angle			

LAWRENCE BERKELEY NATIONAL LABORATORY **IDAHO NATIONAL ENGINEERING LABORATORY**	PROJECT Box Canyon	BORING # II-5

Figure 5.10c. Example of core logging - well II-5.

BORING # **II-5**	DATE DRILLED: **7/13/95**	DRILL RIG:	METHOD: **HX coring using water**	PAGE: **4/5**

DRILLED BY: **INEL**	LOGGED BY: **David Burgess**	NORTHING:	EASTING:	SURFACE ELEVATION:

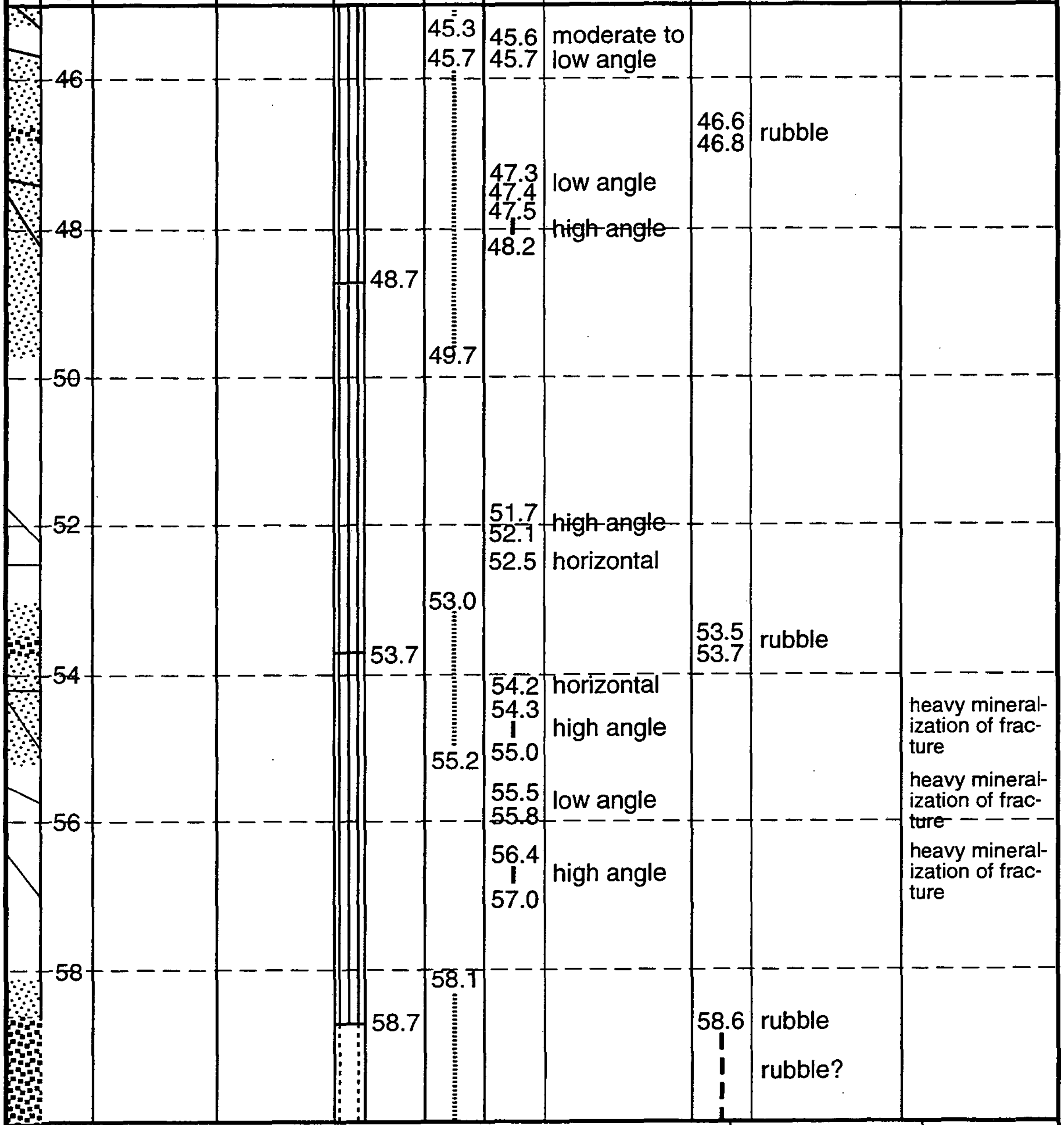

graphic log	depth (feet)	total gamma	caliper	core run and recovery depths	vesicular intervals	single fracture depths	single fracture description	fracture zone depths	fracture zone description	comments
					45.3 45.7	45.6 45.7	moderate to low angle			
	46									
								46.6 46.8	rubble	
						47.3 47.4 47.5	low angle			
	48					48.2	high angle			
				48.7						
					49.7					
	50									
	52					51.7 52.1	high angle			
						52.5	horizontal			
					53.0					
				53.7				53.5 53.7	rubble	
	54					54.2	horizontal			
						54.3 55.0	high angle			heavy mineralization of fracture
					55.2					
						55.5 55.8	low angle			heavy mineralization of fracture
	56									
						56.4 57.0	high angle			heavy mineralization of fracture
	58				58.1					
				58.7				58.6	rubble	
									rubble?	

LAWRENCE BERKELEY NATIONAL LABORATORY **IDAHO NATIONAL ENGINEERING LABORATORY**	PROJECT **Box Canyon**	BORING # **II-5**

Figure 5.10d. Example of core logging - well II-5.

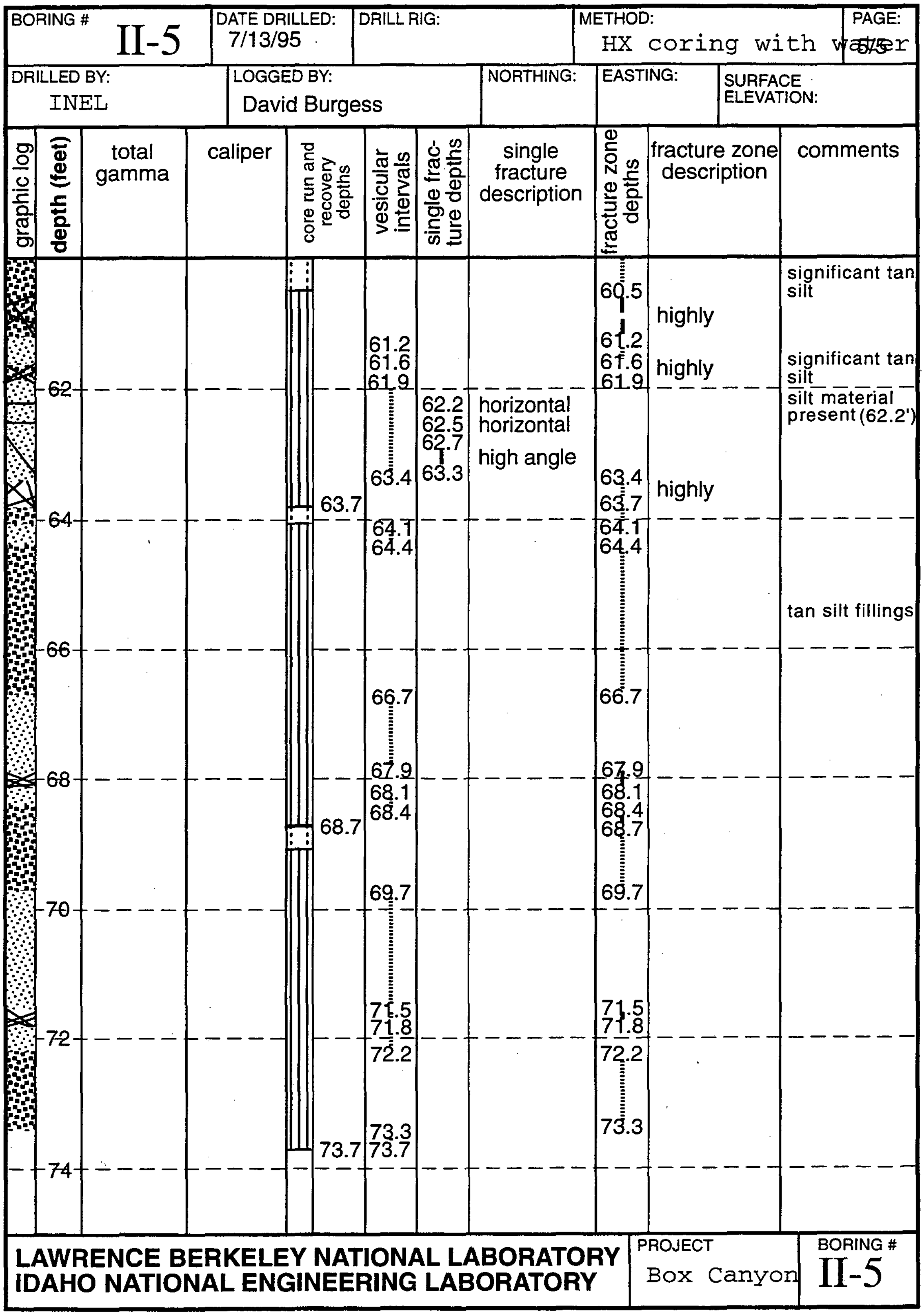

BORING # II-5
DATE DRILLED: 7/13/95
DRILL RIG:
METHOD: HX coring with water
PAGE: 5/5
DRILLED BY: INEL
LOGGED BY: David Burgess
NORTHING:
EASTING:
SURFACE ELEVATION:

graphic log	depth (feet)	total gamma	caliper	core run and recovery depths	vesicular intervals	single fracture depths	single fracture description	fracture zone depths	fracture zone description	comments
					61.2 61.6 61.9			60.5 61.2 61.6 61.9	highly highly	significant tan silt significant tan silt
	62			63.7	63.4	62.2 62.5 62.7 63.3	horizontal horizontal high angle	63.4 63.7	highly	silt material present (62.2')
	64				64.1 64.4			64.1 64.4		tan silt fillings
	66				66.7 67.9			66.7 67.9		
	68			68.7	68.1 68.4 69.7			68.1 68.4 68.7 69.7		
	70				71.5 71.8			71.5 71.8		
	72			73.7	72.2 73.3 73.7			72.2 73.3		
	74									

LAWRENCE BERKELEY NATIONAL LABORATORY
IDAHO NATIONAL ENGINEERING LABORATORY
PROJECT Box Canyon
BORING # II-5

Figure 5.10e. Example of core logging - well II-5.

Figure 5.11a. Example of core photos - well II-5.

Figure 5.11b. Example of core photos - well II-5.

Borehole Scanner

The Borehole Scanner (BSS) is a relatively new tool that provides nearly photographic quality pictures of the borehole wall. The tool consists of a probe, depth encoder, winch, controller, TV monitor and a VCR unit. *Thapa* (1994) describes the BSS in more detail and compares it to other logging tools. The water-tight probe houses a white-light source and a magnetic compass at the bottom . A mirror rotating at 3000 rpm sits directly above the lamp, and reflects light from the lamp onto the borehole wall through a glass window. The light reflected off the borehole wall is directed into a photoelectric transformer. The photoelectric transformer measures the intensity of the incoming light in the red, blue and green wavelength bands and converts the intensities into digital form. The digital data from the photoelectric transformer is passed to an azimuth gauge that marks the point in the data stream corresponding to north. The data then passes through an amplifier to the controller at the surface where it is stored on a digital tape. The entire borehole wall is scanned along a spiral path in this manner as the winch lowers the probe. The maximum vertical resolution is 0.001 mm at present. The resolution along the periphery of the borehole wall depends on the borehole size. An 89 mm diameter borehole will have a horizontal resolution of 0.28 mm.

One complete revolution of the probe's mirror picks up reflectance from all of the contiguous segments on the borehole wall at the same depth. The contiguous segments along the periphery of the borehole wall are discretized into a line of 1000 data points covering reflectance from equal angular intervals. A data point in each such line is a three-dimensional vector defining the reflectance intensity, on a scale of 0 to 255, in the red, green and blue (RGB) wavelength bands. The location of the borehole wall segment represented by each such point is defined by the depth at which the point was scanned and the rotation sequence number (1-1000), which specifies the azimuth of the data point with respect to north. Thus the entire borehole wall is represented by lines of RGB data points at successive depths. A true color unrolled image of the borehole wall can be obtained by combining the RGB components of each data point on a computer. Each data point is represented by one pixel on a computer display of the borehole wall. Figures 5.12 and 5.13 shows typical images, obtained from BSS data by this process, and Table 5.2 summarizes depth, type, dip, dip direction of discontinuities in well II-8. Table 5.3 summarizes the extent of rubble zones and vertical fractures.

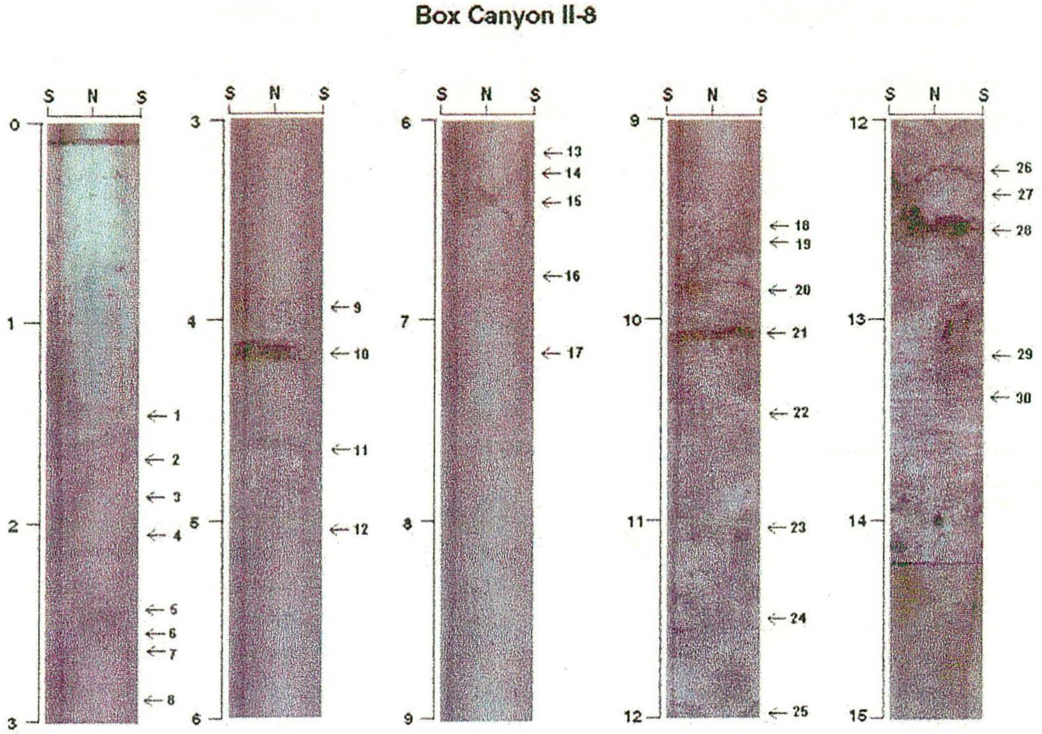

Figure 5.12. Images obtained using the BSS in well II-8 (numbers are main features summarized in Table 5.2).

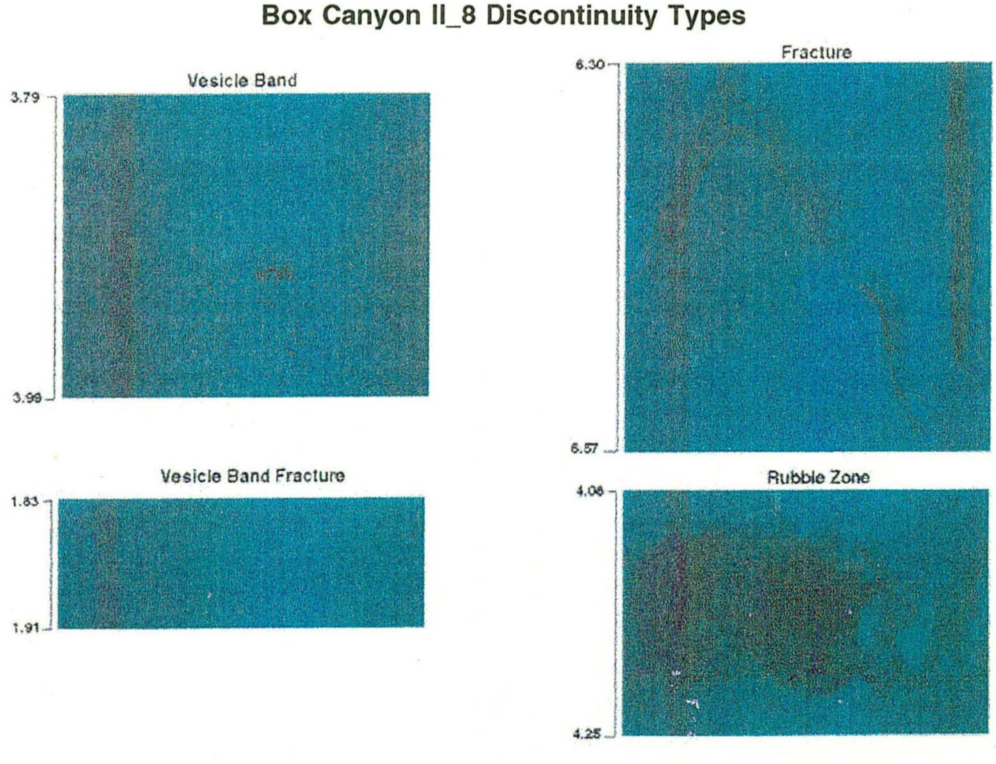

Figure 5.13. Expanded view of main types of discontinuity obtained using the BSS in well II-8.

Table 5.2. Results of the determination of depth, type, dip and dip direction of discontinuities in well II-8.

Discontinuity No.*	Discontinuity Type	Dip (degrees)	Dip Direction** (true north)	Average Depth (m)
1	fracture	39	297	1.56
2	vesicle band fracture	5	299	1.67
3	fracture	19	4	1.87
4	vesicle band fracture	12	356	2.19
5	fracture	67	227	2.50
6	fracture	5	341	2.56
7	fracture	90	152	2.56
8	fracture	5	341	2.87
9	vesicle band	21	31	3.86
10	rubble zone	1	36	4.21
11	fracture	38	197	4.65
12	fracture	5	195	5.26
13	fracture	65	25	6.23
14	fracture	90	161	6.30
15	fracture	52	133	6.44
16	fracture	35	195	6.79
17	fracture	63	20	7.30
18	fracture	34	316	9.50
19	fracture	13	317	9.68
20	fracture	28	197	9.84
21	rubble zone	14	198	10.06
22	fracture	19	273	10.50
23	rubble zone	32	205	11.07
24	fracture	12	188	11.53
25	fracture	50	38	12.00
26	fracture	35	246	12.29
27	fracture	44	342	12.38
28	rubble zone	2	7	12.57
29	fracture	35	249	13.28
30	fracture	2	292	13.41

Note: * Discontinuity numbers are shown in Figure 5.12
** True north correction: 17 degrees
*** Extent is not aperture when dip >>0.

Table 5.3. Summary of distribution of rubble zones and vertical fractures in well II-8.

Discontinuity No.*	Discontinuity Type	Start Depth (m)	End Depth (m)	Vertical Extent (cm)
10	rubble zone	4.10	4.23	12.48
21	rubble zone	10.03	10.12	9.97
23	rubble zone	11.02	11.13	11.13
28	rubble zone	12.43	12.62	19.55
7	vertical fracture	2.56	2.96	39.90
14	vertical fracture	6.14	6.51	36.70

Note: * Discontinuity numbers are shown in Figure 5.12 and Table 5.2.

Borehole geology

Site geological conditions were established on the basis of the core descriptions and photographs of the cores, as well as TV logs. The following description has to be considered as preliminary and will be updated to include new data. Figure 5.14 presents a schematic cross section through the upper flow, traversing the well field as shown in Figure 5.7. The section ends at the base of the upper flow because few wells penetrate into the lower flows, so little is known about them at this time. Elevations for the various features at the boreholes are determined from photographs of cores. Features between boreholes are inferred from knowledge of the cliff face adjacent to the well field. The central fracture zone indicated is fractured at the wells, and it is assumed that this zone is continuous away from the wells. The columns formed by joints are known to have diameters of about 1 m (from measurements on the surface and on the cliff face). It is not known at this time whether they penetrate the central zone.

In the vicinity of the wells, the upper flow is 11-12 m thick. Immediately underneath this upper flow, are several other flows (Figures 5.10 and 5.11). Discerning the boundaries of these flows is complicated, as rubble zones (generally taken to represent flow boundaries) are separated by as little as tens of cm, as in well II-5. However, there does appear to be a continuous rubble zone (*i.e.*, lower flow boundary) ranging in depth from 16-19 m below the land surface.

The central fracture zone exists in apparently vesicle-free rock, about 1 m thick, and located about 3 m above the base of the upper flow. This is probably near where the upper and lower cooling fronts met as the lava cooled as has been modeled by *Grossenbacher and McDuffie* (1995). It is important to note that this fracture zone, which appears to be continuous throughout the site, has been identified by several procedures: from the core description and photos, TV logs, and a radar survey performed in September of 1995. Preliminary analysis of the radar records indicates that the thickness and the depth of this fracture zone appear to be variable. The northern portion of the site shows the shallowest depths with increasing depth towards the south and west, which was confirmed by observations on the cliff face and borehole geology (see Figure 5.14). The deepest occurrence of this zone is toward the northwest. The depths and thicknesses as determined from the radar records correspond well with core data (see Sections 2.2.3.2).

The rubble zone at the base of the upper flow ranges in thickness from 10 cm as in well II-5 to nearly a meter, as in well II-1. This may reflect variation in roughness of the flow base at different scales. Void space within this zone ranges up to tens of centimeters vertically. Samples of core taken from this rubble zone are coated with a white to yellow material. We are currently determining whether this is alteration, sedimentary interbed material, or sediments washed down through fractures from the surface.

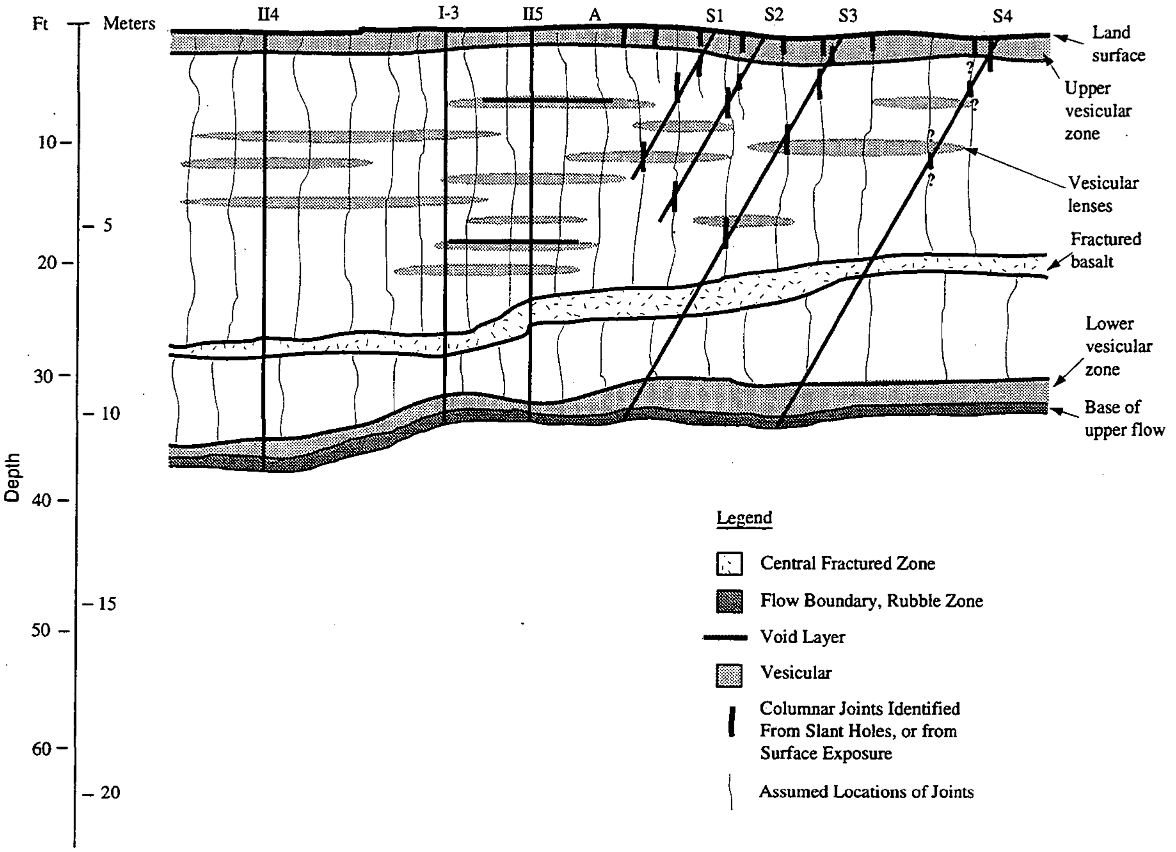

Figure 5.14. Preliminary schematic cross section showing the upper flow, traversing the well field along the line shown in Figure 5.7.

Within the upper flow, several vesicular lenses from 1 to 20 cm thick occur. Some of these are continuous from hole to hole (particularly the thicker ones), while others are not. Many of these zones have horizontal fractures within them, often near or at the base of the zone. A striking example of such features appears in wells I-1 and II-5 at a depth of about 3 meters. Here, an open void on the order of one cm exists within a band of vesicles a few centimeters thick. These fractures may be quite rough, and typically intersect many vesicles. Accordingly, they may have a very high porosity associated with them. Possibly some of these fractures are continuous from hole to hole. Some of these fractures appear to have large apertures.

Vertical fractures (presumably columnar joints) are seen in photographs of core from slant holes. Identification of these fractures is tentative at this time, as fracture orientation is unattainable from video logs. These fractures appear very smooth and have parallel sides, consistent with their interpretation as mode I (*i.e.*, pure tension) cooling cracks. This is in contrast with the horizontal fractures, which frequently have rougher and more non-parallel walls, and may intersect vesicles. It is uncertain at this time whether the vertical joints continue through the central fracture zone, or even how far they penetrate into it. Below the upper flow zone, the lithology is much more complex and difficult to extrapolate between holes. In this region, rubble zones are often stacked directly on top of one another or separated by only a few meters of rock. These probably represent intercalated flow fingers. In general, these rubble zones do not correlate in elevation from hole to hole. Apparent void spaces within these zones range up to 5 or 10 centimeters in vertical dimension, as they appear on the video logs.

Visualization of the Box Canyon Data

Visualization of data from the Box Canyon site was begun at the end of FY 95 and is a part of the activities conducted under Task 6, described in Section 2.6. The results of visualization of fracture zones within the Box Canyon test area include: fracture orientation; locations of rubble zones; fracture infilling; locations of vesicular zones; and air and hydraulic connectivity. They have been given here for clarity. The data input into the visualization system is based on analysis of data such as: photographs of cores, written descriptions of cores, drawings of cores, descriptions of the TV scanner logs, and results of field experiments (as they become available).

The overall visualization plan includes several steps or "layers" as listed below. This work will be performed in FY 96, though some examples have been incuded.

1) Plan view showing location of boreholes at the Box Canyon site.
2) Side view (section) of site to show relative depths of boreholes.
3) "Catalogue" of where core is available (the absence of intact core is presumed due to mechanical failure or due to a void or rubble zone in the rock).
4) Locations of fractures in individual wells, including information such as:
    (a) whether the fracture or fracture zone is horizontal, vertical or oblique (only dip, strike is not available),
    (b) whether the fracture or fracture zone is infilled or not,
    (c) whether fracture is associated with vesicularity.
5) Characterization of fracture zones.

Regarding (5), the thickness of the disk will show the thickness of the fracture zone, and the color will show the type of each zone, *i.e.*, rubble, void, breakout, or fracture. An example of the visualization of locations of fractures identified so far is shown in Figure 5.15. Color has been used to indicate whether the fracture is associated with vesicles. Examples of the visualization of gamma data and caliper measurements are shown in Figures 5.16 and 5.17. All of these examples were created using the Application Visualization System (AVS).

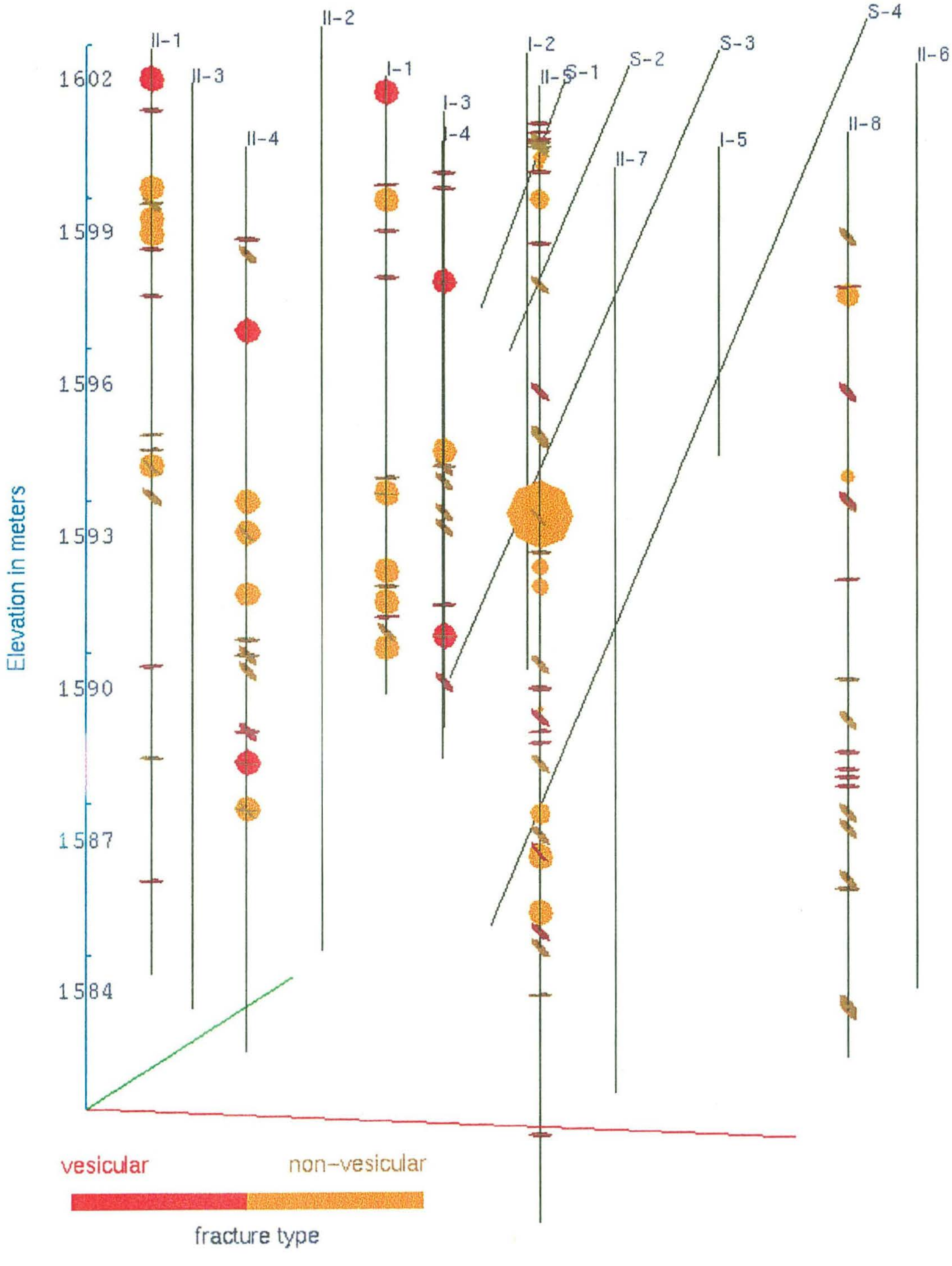

Figure 5.15. Example of visualization of fractures in wells created using AVS: red - vesicular zones, yellow - non-vesicular.

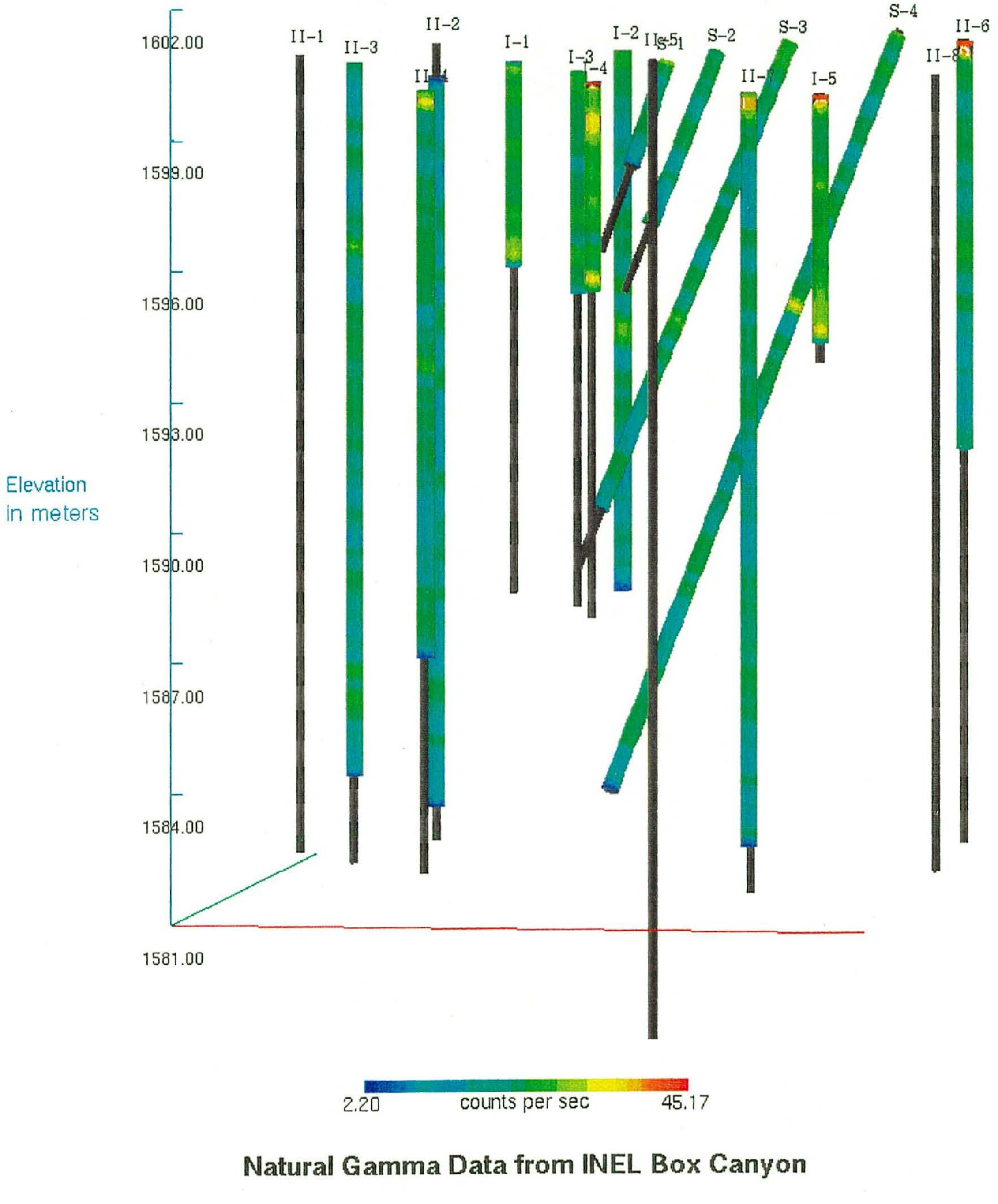

Figure 5.16. Example of visualization of gamma data in wells created using AVS.

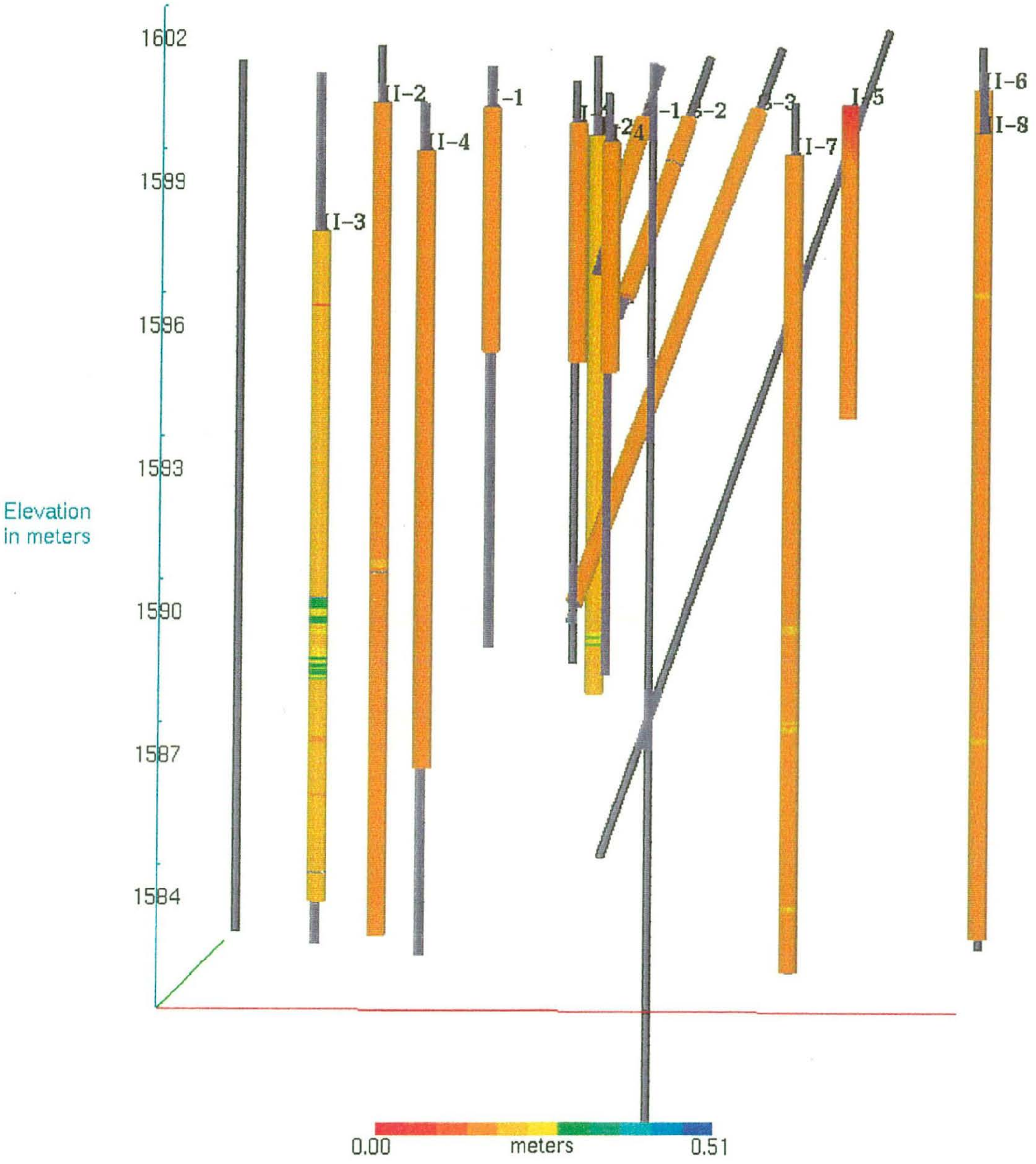

Caliper Data from INEL Box Canyon

Figure 5.17. Example of visualization of caliper measurements in wells created using AVS.

2.5.3.3. Hot Air Injection Tests

Design and Rational of the Tests

The critical problem in understanding infiltration in these rocks is to determine how vertical pathways are connected. We would like to be able to place a sensor at depth and have some assurance that infiltrating water has a connected path to the sensor. Our hypothesis was that we could inject hot air into a potential sensor installation site at depth and easily monitor where the hot air exited at the surface. Then we would know that the exit points on the surface were connected to the monitoring point. This theory depends on the fractures, particularly the vertical fractures being open and dry so that air can pass through them. Consequently, this test was designed to be used in the dry season.

In planning these tests we expected to observe both a lateral movement of hot air along the rubble zone and a vertical movement through the joints and fractures toward the land surface. Therefore, we expected to see changes in the temperature profiles in boreholes and in fractures exposed at the land surface.

Data Acquisition System

In order to handle the large volume of data collected during the FY 95 gas injection tests and the further gas injection and infiltration tests planned for FY 96, a computer data acquisition system was designed. An array of about 80 thermistors was connected to this system in order to obtain digital information. This system was used for temperature measurements in boreholes down to 23 m (74 ft) before, during, and after hot air injection tests. The Electronic Control Unit was developed using a laptop PC running Labview for Windows as the sole control and data collection instrument. An IEEE488 bus was used to interface thermistors and electronic measuring equipment with the PC. Software was coded under Labview for Windows. Electronic instruments that were coded for use in the Electronic Control Unit included Keithley 2001 Digital Multimeter, and Keithley 7001 Switch Mainframes using 7011 scan cards.

Thermistors

A thermistor is a thermally sensitive resistor whose primary function is to exhibit a change in electrical resistance with a change in body temperature. Thermistors used in the hot air tests were the NTC-DC95 (Thermometrics, New Jersey), designed for use over a range of temperatures (0°C to 70°C) with an accuracy of ±0.1°C. This type of thermistor is a ceramic semiconductor with a negative temperature coefficient of resistance (NTC), which gives decreasing resistance readings with increasing temperatures. This bead shaped thermistor has platinum alloy lead wires which are directly sintered into a ceramic body.

Each thermistor was soldered on to a 38.1 m long electric cable. To protect the thermistor from mechanical stresses in the field, each bead was housed in a stainless steel shield. To prevent moisture from seeping into the leadwires, each wire was wrapped in shrink tubing and then insulated in the steel shield with epoxy.

Each thermistor was calibrated under laboratory conditions using the procedure recommended by the manufacturer. To provide the calibration, it was assumed that the Steinhart and Hart equation (*YSI, Inc.*, 1993) is the best empirical expression for the resistance-temperature relationship of a NTC thermistor. This equation for three measurements of temperature T_i, i = 1,2,3, can be given by

$$\frac{1}{T_1} = a + b(\ln R_1) + c(\ln R_1)^3 \qquad (5.1)$$

$$\frac{1}{T_2} = a + b(\ln R_2) + c(\ln R_2)^3 \qquad (5.2)$$

$$\frac{1}{T_3} = a + b(\ln R_3) + c(\ln R_3)^3 \qquad (5.3)$$

where a, b, and c are coefficients that can be determined by solving simultaneously the system of equations (5.1)-(5.3). R_i is the thermistor resistance in ohms for temperature T_i.

To facilitate transport between and within wells, thermistors were attached to steel cables with a 1 m (3 ft) PVC pipe at the bottom end. In the longest cable used in deep boreholes, 36 thermistors were installed at 0.5 m intervals (Table 5.2). In another cable used for shallow wells, 26 thermistors also were installed in 0.5 m intervals. Three other cables contained 4-5 thermistors and were installed at 0.5 - 1.0 m intervals.

To provide temperature measurements, a cable was lowered into a well and secured at the top of the casing. Measurements were recorded at varying intervals from 10 s to 1 hr. Thermistors equilibrated in the borehole over 0.5-1 hr. It is likely that some thermistors along the cable were close to, or touching the borehole wall, while others within the rubble zone were not. For the first series of experiments (August 10 and 11, 1995), temperature measurements were made in open wells (a single continuous air column existed, which was open to the atmosphere). For the subsequent experiments, the wells were capped with 0.10 to 0.15 m thick packing foam.

IR Camera

The site was instrumented with a thermal infrared (TIR) scanner attached to a tripod and suspended approximately 10 m (30 ft) above the land surface on a tilt and pan mount to allow imaging of the area within the well field. The scanner was a MIKRON Model TH3I04 with a temperature resolution of ±0.3 K, a 273 to 573 K range, and measurement accuracy of ±1% K selected range (according to a TIP manual). The scanner was used to detect heat anomalies at the surface.

Background Conditions prior to Hot Air Injection Tests

Tensiometry measurements

Four tensiometers of a new design (described in Section 2.5.3.4) were installed in borehole II-7 at depths of 12.2, 17.7, 15.2, and 16.8 m (40, 45, 50, and 55 ft) in order to provide measurements of the hydraulic potential in the unsaturated-saturated rocks in the vicinity of the water table. Results of measurements of hydraulic pressure are shown in Figure 5.18. As can be seen from this figure, in July the two lowest tensiometers at depths of 15.2 and 16.8 m showed a positive hydraulic pressure because they were located beneath the water table. Based on tensiometery measurements in July, the water level (determined as a depth where the water pressure equals 0) was located at a depth of 14.3-14.7 m, which is consistent with direct water level measurements in the same borehole.

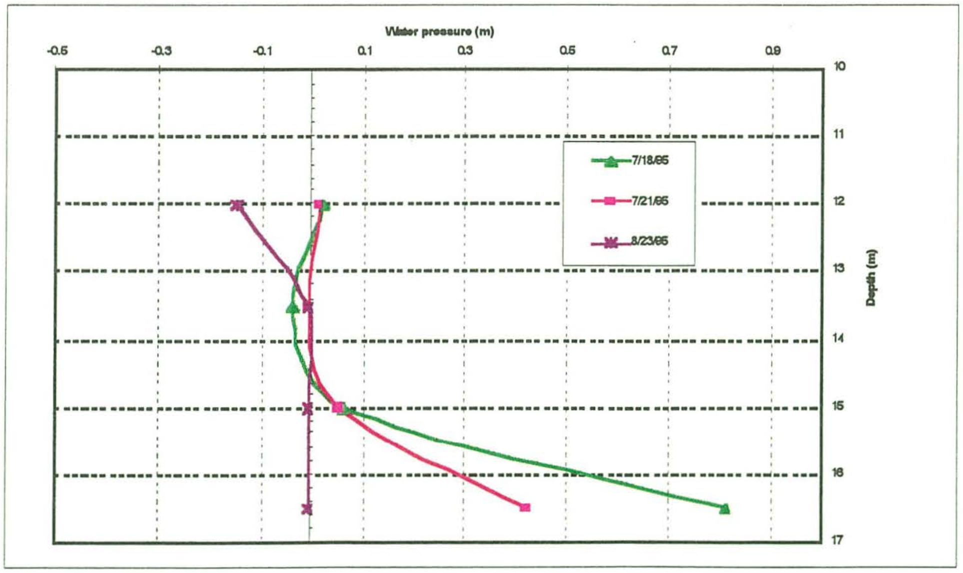

Figure 5.18. Tensiometer measurements in well II-7.

In the months of August and September, the water table declined slightly, causing a decrease in the hydraulic pressure to -(0.01-0.02) m in all four tensiometers. Such values of hydraulic potential are consistent with the observation of condensed water on the tensiometer body and the PVC pipe when it was removed from the well on September 25. Thus, tensiometery measurements have shown relatively high moisture content of the bottom part of the upper basalt flow.

Temperature Measurements

Prior to and after the air injection experiments, a series of measurements were made along profiles of wells I-3, II-7, II-8, II-2, and II-5 to determine baseline vertical gradients and temporal variations in temperature at various depths and at the surface of the site. Vertical temperature distributions recorded in two monitoring wells, a shallow well I-3 and a deep well II-5, are shown in Figures 5.19 and 5.20. Four different vertical temperature intervals can be distinguished along the vertical profile of the vadose zone.

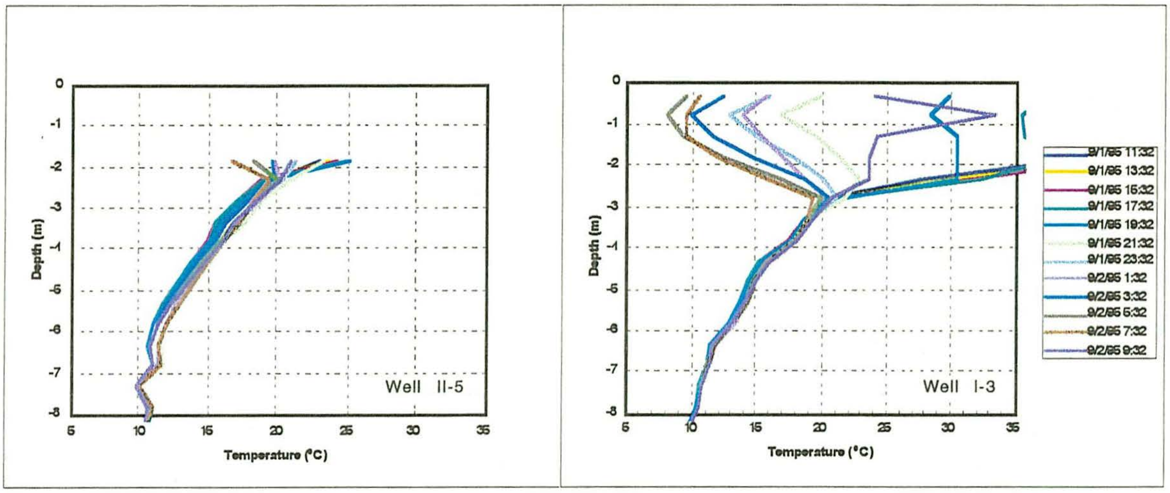

Figure 5.19. Vertical distribution of temperature in well S-3 and II-5 showing a zone of daily fluctuation of temperature.

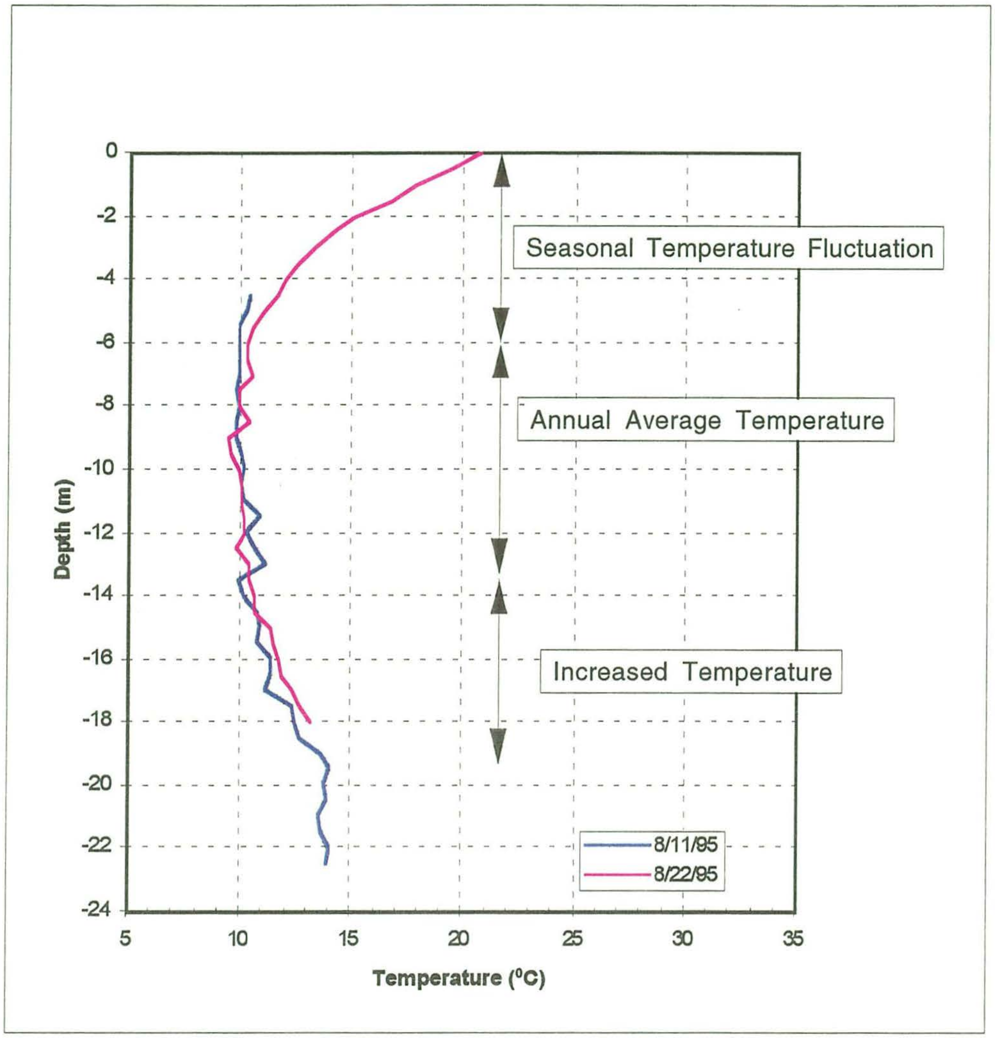

Figure 5.20. Vertical distribution of temperature in the vadose zone in well II-5 showing the following zones: seasonal fluctuation of temperature, annual average temperature, and increased temperature above the groundwater table.

The first interval is located between the land surface and a depth of about 2-2.5 m where significant daily fluctuations of temperature take place. Because these measurements were made with no backfill boreholes, they may indicate the kind of temperature changes that occur in shallow open fractures. Further monitoring of temperature in backfilled boreholes will be used to verify these results.

The second interval extends from 2.5 to 5 m, and seems to be a zone of seasonal fluctuations of temperature.

The third interval is a zone located between depths of 5 and 10 m where the temperature is practically constant (10-11°C).

The fourth interval is located below a depth of 10 m and extends down to the groundwater table at a depth of 16 m. Temperature increases downward within this interval, until it stabilizes beneath the water table in the groundwater body. Most likely, the groundwater has a limited vertical extent, and, in fact, is a perched water zone, which has been created due to recharge of water running in the adjacent Box Canyon through the rubble zone(s) beneath the upper basalt flow. During the summer, warm river water has served as a source of thermal energy for surrounding rocks. A comparison of temperature profiles in several wells located at different distances from the canyon cliff face confirmed this hypothesis.

Results of Hot Air Injection Tests

A schematic view of a packer, a pressure sensing tube, and a thermistor used for the hot air injection tests is shown in Figure 5.21. The compressor for injecting air was capable of sustaining a 3.4 m^3/min (120 scfm) flow at 80 psi (552 kPa). Flow rate was monitored using a 3 m (10 ft) section of smooth bore steel pipe with an air velocity set at 2.1 m (7 ft) from the inlet. In this configuration the flow meter has an accuracy of ± 2% of reading. Pressures at the interval of injection were estimated using a pressure transducer with a precision of ±0.01 psi connected to the injection interval by a tube inserted in the injection pipe. Temperatures were measured at the same point as pressure using a thermistor connected to the data acquisition system. In the first phase of the hot air injection test, temperature was measured in non-backfilled monitoring boreholes.

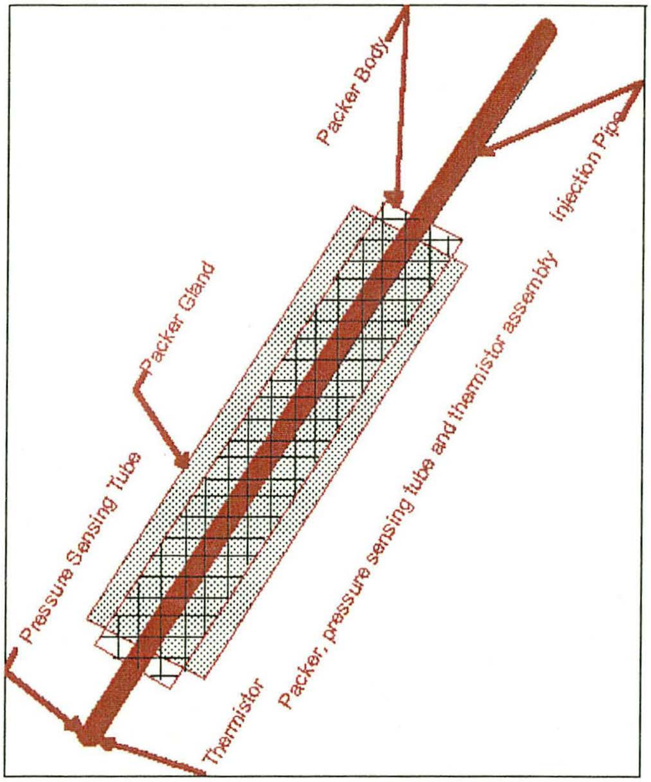

Figure 5.21. Schematic view of packer, pressure sensing tube, and thermistor used for hot air injection tests.

The following hot air injection tests were performed:

First Test: One-hour pretest of injection of ambient air into slant borehole S-1 over depths of 10 to 12 m. This test was performed on August 16, 1995 at night using injection of ambient air of slightly increased temperature (19°C) in comparison with the rock temperature (10 °C). No changes in temperature were noticed in monitoring wells II-5 and I-3 during this test.

Second test: Hot air injection of 8.5 hours duration into slant borehole S-1 within the vesicular basalt. This test was done on August 17, 1995, and it used an inflatable packer to isolate the 3.3-3.9 m (11 to 16.1 ft) below top of casing (btc) section of well S-1. Air was injected at 1.1 m^3/min

(40 scfm), 40°C, and 99.3 kPa (14.39 psig) for 8.5 hrs. After 8.5 hrs of hot air injection, the source used to heat the air flow ran out of propane, and the propane burner went out. Injection of air of ambient temperature continued at the same rate for another 0.5 hrs.

This test was performed at night when the temperature usually decreases in the upper part of the vadose zone, as can be seen in Figure 5.19, illustrating a decrease in temperature in well I-3, which was not affected by this injection. As a result of hot air injection, a practically uniform increase in temperature of 0.5-1°C was observed in well II-5 at depths between 1 and 6 m (Figure 5.22).

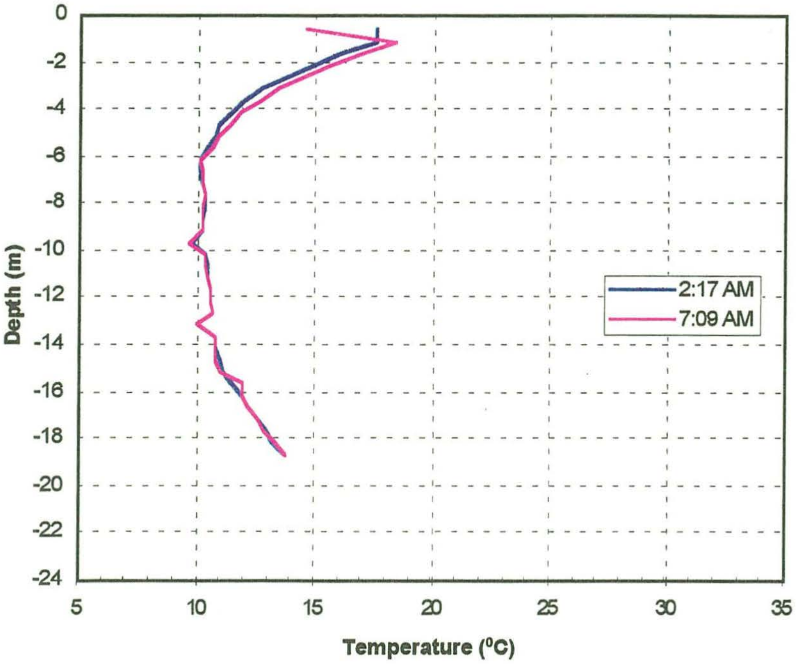

Figure 5.22. Vertical distribution of temperature in well II-5 as affected by the second hot air injection test in a slant hole.

Thermal IR images of the ground surface obtained during the injection did not show a detectable response. The lack of response was attributed to the depth, degree of sedimentary infilling and saturation of the vertical fractures. Following the injection, loose soil and drilling debris were removed from the soil surface within the well field using compressed air. While as much as one foot of material was removed it was evident that the depth and degree of wet sedimentary infilling changed little. The lack of response at the surface is explained by the observations of saturated sedimentary infilling of the exposed fractures. What was unexpected was the lack of response of thermistors placed in the nearby boreholes, but located above the zone where hot air was injected.

Third Test: Hot air injection test of 16.5 hours duration into a deep slant borehole over the 10.4-13.5 m (34 to 44.4 ft) drilled interval in borehole S-3. The test started on August 22, 1995 at 3.25 p.m. Air was injected at 3.34m^3/min (118 scfm), 90°C, and under pressure of 4.83 kPa (0.7 psi). During the test, the air compressor used to inflate the packer failed and packer pressure was lost for several hours while another pressure source was being connected to reinflate the packer. The thermistor recording the temperature of the air at the injection point stopped functioning soon after the temperature reached 90°C.

During the period when hot air was being injected into the formation, temperature changes along wells II-5, I-3, II-7, and I-4 were recorded at 15 s intervals. About one hour after the beginning of the injection, a significant increase in temperature was observed in well II-5 at depths from 11.8 through 15.3 m. Within this interval, temperature stabilized after eight hours of hot air injection (Figure 5.23). A maximum value of temperature of 29 °C was observed at the depth of 11.8 m (Figure 5.24), which coincides with the location of the rubble zone beneath the upper basalt flow. Some changes in temperature were observed above (1.5 m) and below (0.5 m) of this zone.

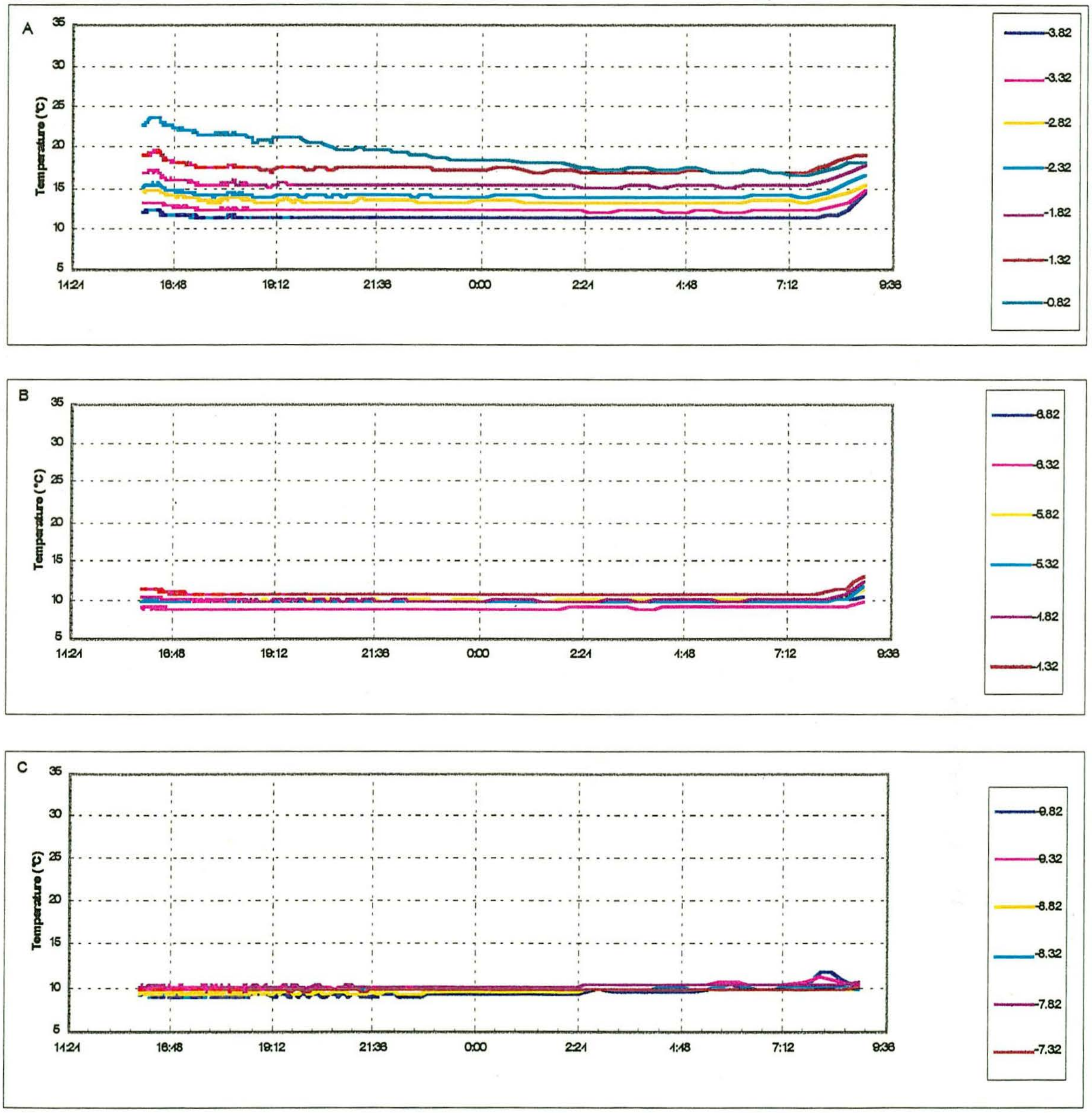

Figure 5.23a. Temporal changes in temperature in monitoring well II-5 as affected by the third hot air injection test (numbers in the key are depth in meters).

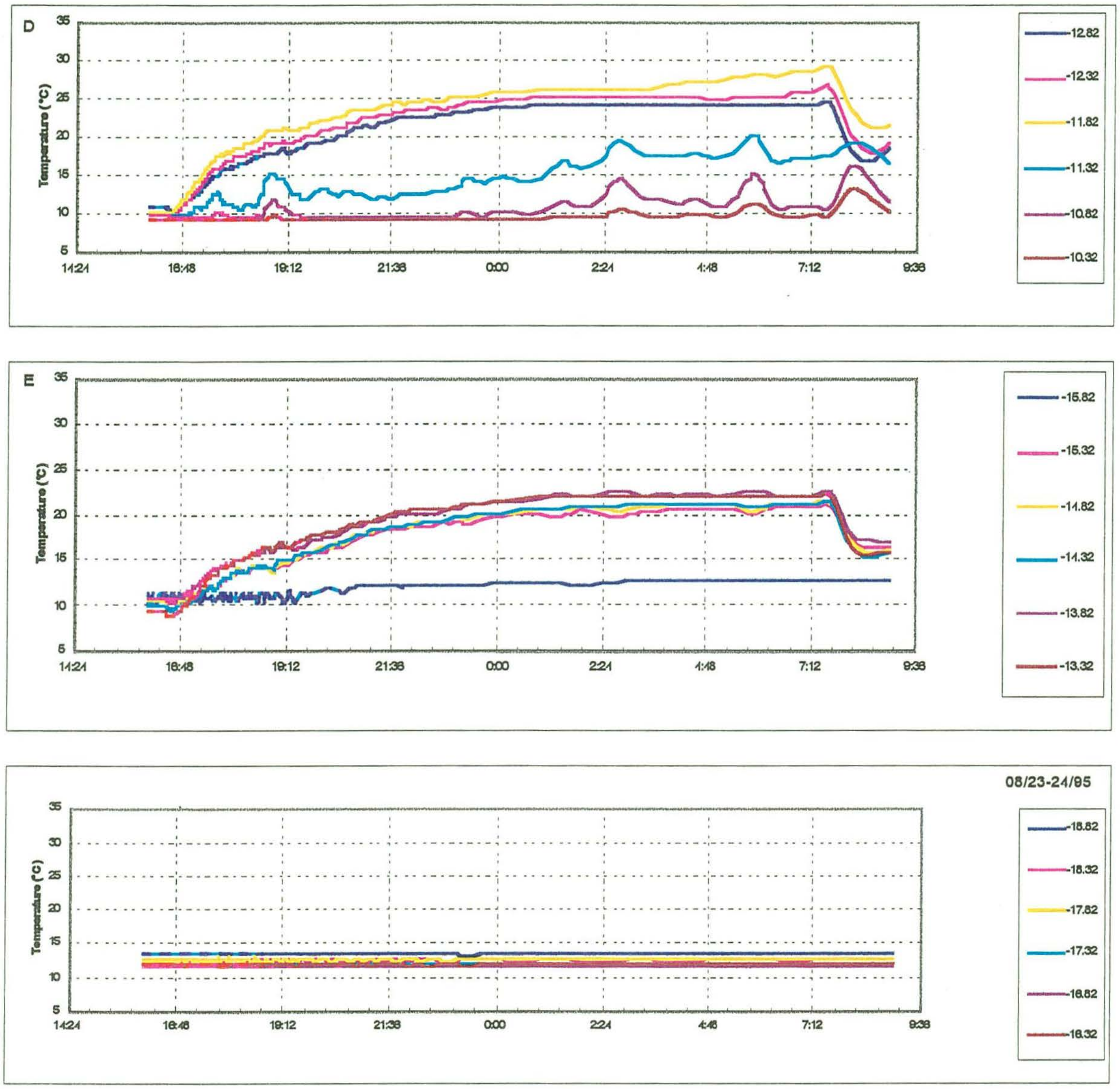

Figure 5.23b. Temporal changes in temperature in monitoring well II-5 as affected by the third hot air injection test (numbers in the key are depth in meters).

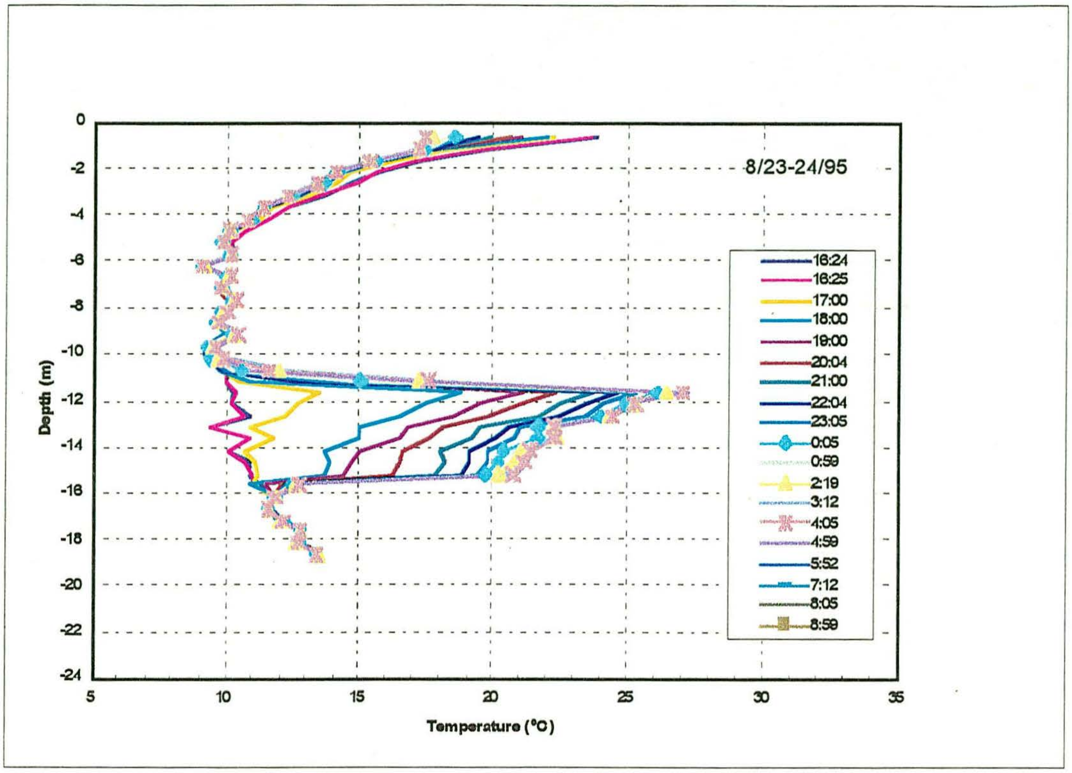

Figure 5.24. Vertical distribution of temperature in well II-5 as affected by the third hot air injection test.

A similar pattern of changes in temperature was observed in well I-3 where a zone of significant temperature increase was observed from the bottom of the borehole at 11.25 m to a depth of 9.75 m, and temperature slightly increased in a 1.5 m zone upward. The maximum temperature observed in this well was 22°C (Figures 5.25 and 5.26).

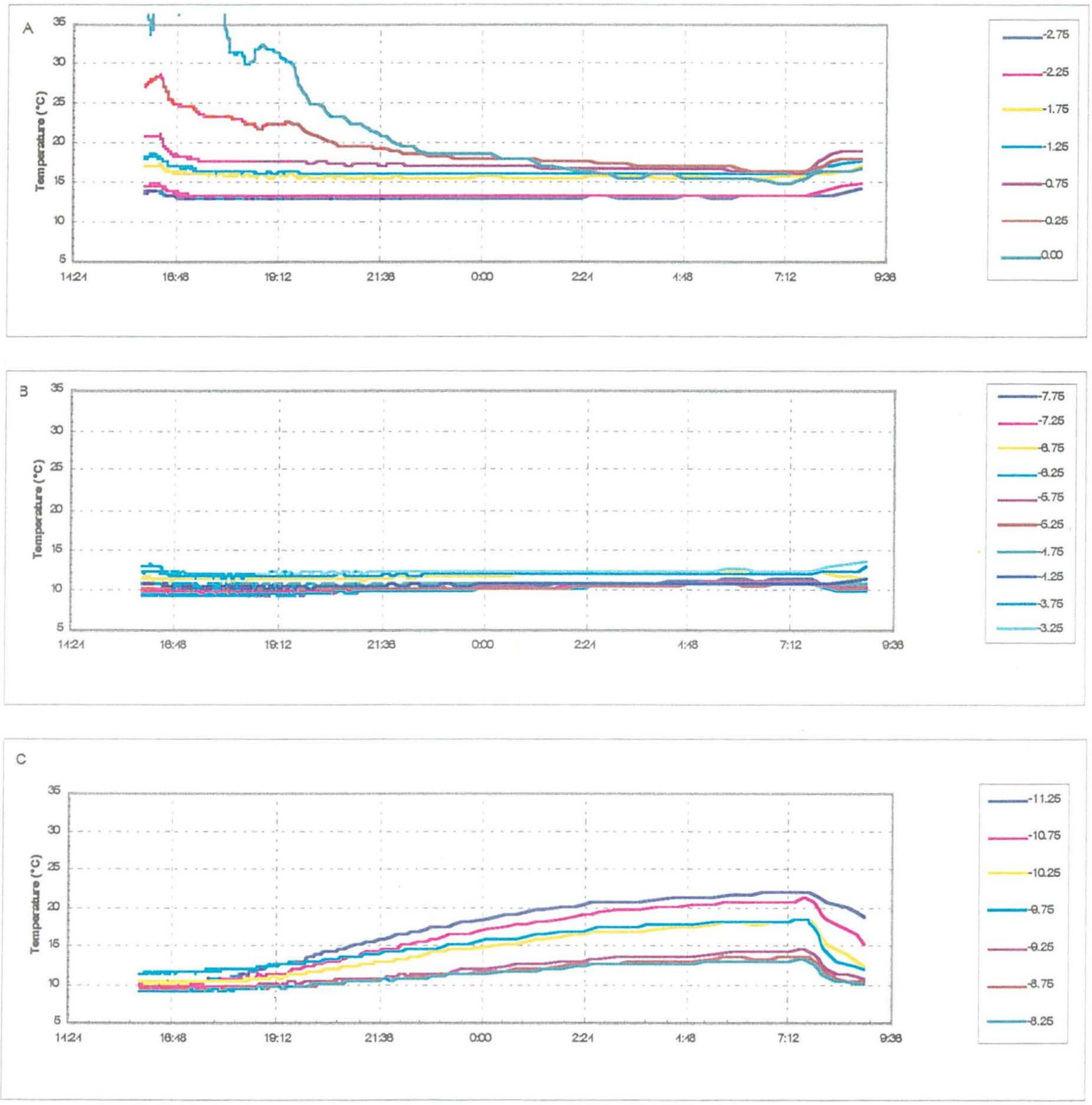

Figure 5.25. Temporal changes in temperature in monitoring well I-3 as affected by the third hot air injection test (numbers-depth in meters).

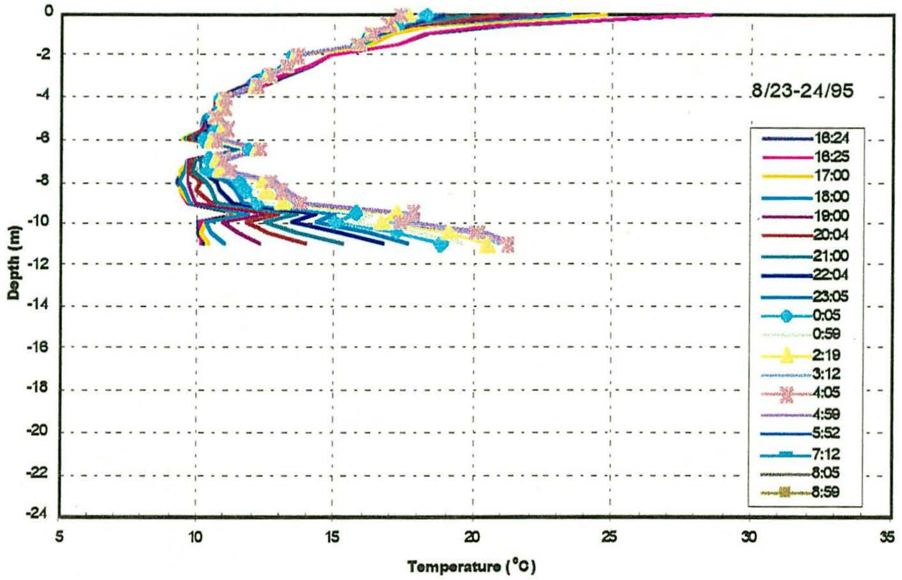

Figure 5.26. Vertical distribution of temperature in well I-3 as affected by the third hot air injection test.

Land surface temperatures obtained in real time by the TIR imaging system are shown in Figures 5.27a through 5.27d. Figure 5.27a is a two-dimensional plot of surface temperatures at 02:20 am August 18, 1995, and in general shows that the temperatures varied from 5 to 13°C. The blue cross near the center of the figure is an IR target made from galvanized sheet metal. The metal reflects the sky temperature and thus appears very cold. The diagonal lines appearing in the lower left and right hand corners of the figure were metal pipes used to support the tower suspending the TIR imagery. The patches of blue over the surface were soil that cooled at a faster rate then the exposed basalts that appear as yellow and green. The five spots shown as red and gray were open boreholes that radiated efficiently to the sky. The lack of definition between the basalts and soil is due to the fact that thermal infrared radiation is a surface phenomena and small amounts of dust on the basalts changes its radiation pattern dramatically. The surface was cleaned by blowing air over it and removing as much as a foot of soil. However, the dust remained on the surface. It is interesting to note that every feature shown on Figure 5.27a was found on the surface during visual inspections.

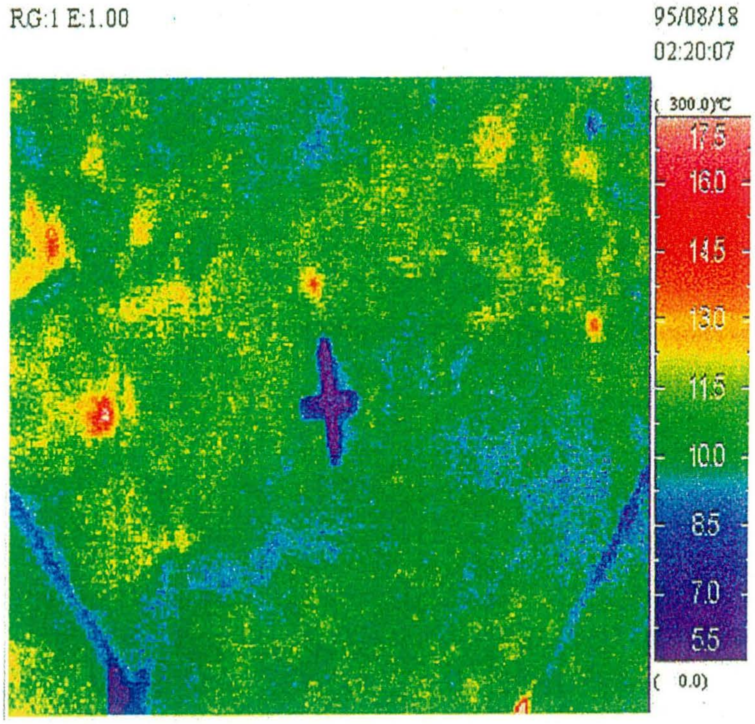

Figure 5.27a. Images from infrared camera during second hot air injection test. This frame shows temperatures at the start of the test (2:20 am). The well just above the center of the site (blue cross) is I-3, well II-5 is to the left of the cross, and well S-1, into which hot air was injected, is in the lower left corner.

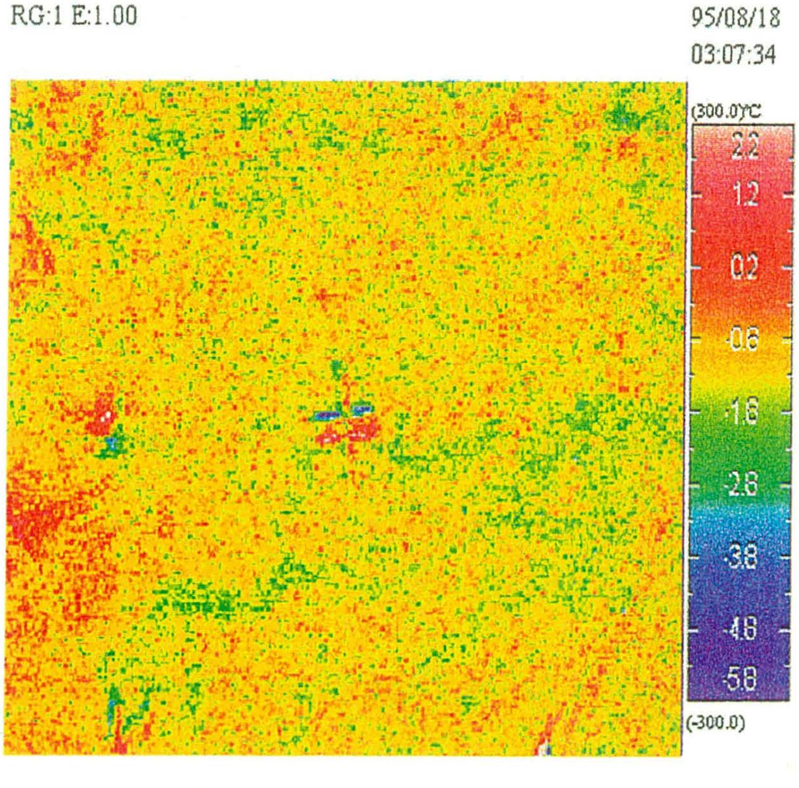

Figure 5.27b. Changes in the TiR image between 2:20 am and 3:07 am on August 8, 1995.

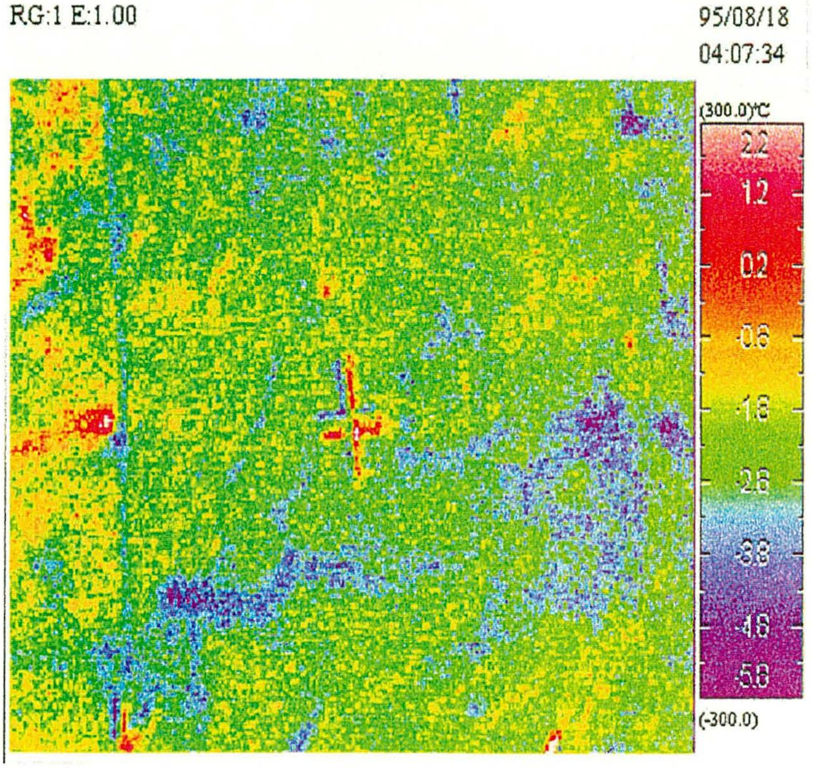

Figure 5.27c. Changes in the TIR image between 2:20 am and 4:07 am on August 8, 1995.

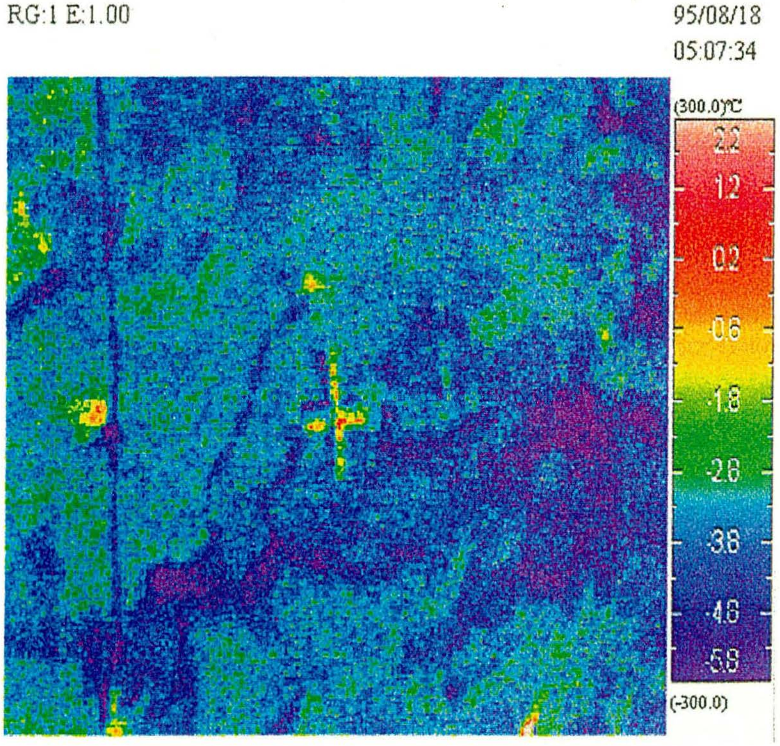

Figure 5.27d. Changes in the TIR image between 2:20 am and 5:07 am on August 8, 1995.

Figure 5.27b was obtained by taking the differences between the temperatures obtained at 2:20 am and 3:07 am and indicates that there the temperature of the soils cooled slightly faster than basalt surfaces and that the entire surface had cooled approximately 2 °C. The three blue spots resulted from wind loading on the 30 foot high tower that shifted the images slightly.

Figure 5.27c displays the temperature changes that took place between 2:20 am to 4:07 am and shows that the metal target warmed over this time interval. Recall that the target reflects the sky temperature, which changed due to clouds forming. The blue line that appears in the left quarter of the image resulted from electronic cables extended to well I-1 (see Figure 5.7).

Figure 5.27d is the image obtained by taking the differences between the temperatures found at 2:20 am and 5:07 am. Again the areas covered by soil show more pronounced cooling than the basalts. The wells are quite visible and show little if any temperature change over the time interval. The process of the temperature recovery after this hot air injection test was observed for more than 10 days.

The figures do not clearly indicate any temperature anomaly due to heated air being transported from the point of injection to the land surface. This indicates that the heated air was transported largely in the horizontal plane away from the point of injection. A major contributing factor to the lack of vertical movement was the degree of fracture sealing from natural sediments found at this site. The sealing was sufficient to cause horizontal transport even after the removal of as much as one foot of soil from the fractures found at the land surface.

Further analysis of infrared images will include comparison with a similar time series of images taken when no hot air injection test was underway, to see if the subtle temperature changes noted were due in part to hot air injection.

In the analysis of the results of this test, it is important to note that despite temperature measurements being performed in open boreholes that might serve as conduits for hot air movement, the zone of influence of hot air injection has a limited vertical extent around the rubble zone. It appears that due to high air permeability and the connectivity of the rubble zone, by far most of the air injected was distributed along this zone, while massive basalt located above the lower vesicular zone, as well as columnar joints and fractures infilled with moist sediments were relatively air impermeable. This means that vertical connectivity of the rubble zone with joints and fractures is rather limited in terms of air migration. Another factor that most likely affected the results of the test was the adsorption of heat by rocks and moist sediments that infilled void spaces in and between basalt columns.

Numerical Modeling

A simplified numerical model of the subsurface adjacent to Box Canyon was created and used to model the third hot air injection test, in order to help interpret the results of that experiment and to help design future experiments. The results of the modeling studies are not expected to be exactly representative of the field experiments, because local material properties are not well enough known. However, they are expected to provide a general picture on the important processes taking place.

The numerical simulator TOUGH2 (*Pruess*, 1989, *Pruess*, 1992), developed at LBL for multiphase, multicomponent fluid flow and heat transport, was used for the calculations. The model is axisymmetric and centered on well S-3, into which hot air was injected at depths of 8.5 to 12 m for a period of 16 hours. The upper boundary of the model is the ground surface and the lower boundary is the local water table at a depth of 20 m. The model includes layers that represent a vesicular zone, a fracture zone, and a rubble zone, which were identified by examination of borehole cores, logs, and televiewer, as described above. Figure 5.28 shows the central portion of the calculational grid, which extends a total of 4 km from well S-3. The vertical spacing was chosen based on the lithology. The radial spacing generally increases away from the injection well, but several zones are finely discretized in order to allow the inclusion of thin vertical fractures, which might provide fast paths for fluid or heat flow to the ground surface. Such fractures are considered plausible based on the conceptual model of the site, as shown in Figure 5.14. Table 5.4 shows the material properties used in the model; it should be noted that most of the values used are rough estimates.

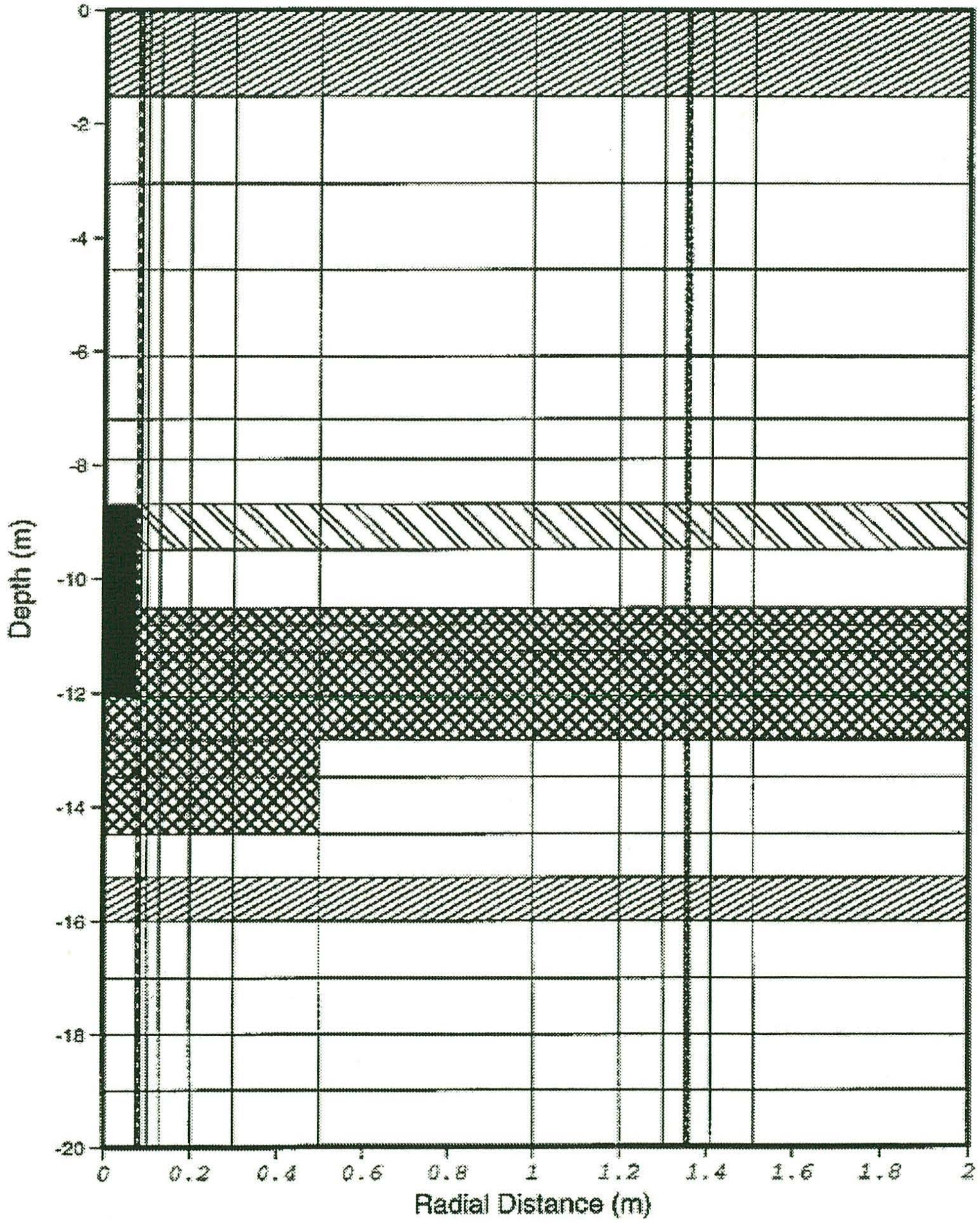

Figure 5.28a. Central portion of the axisymmetric grid used for the numerical simulation of the third hot air injection test. Shading: uniform diagonal stripes: vesicular zone; paired diagonal stripes: fracture; cross-hatching: rubble zone; solid black: injection interval. (**a**) shows the inner 2 m of the grid.

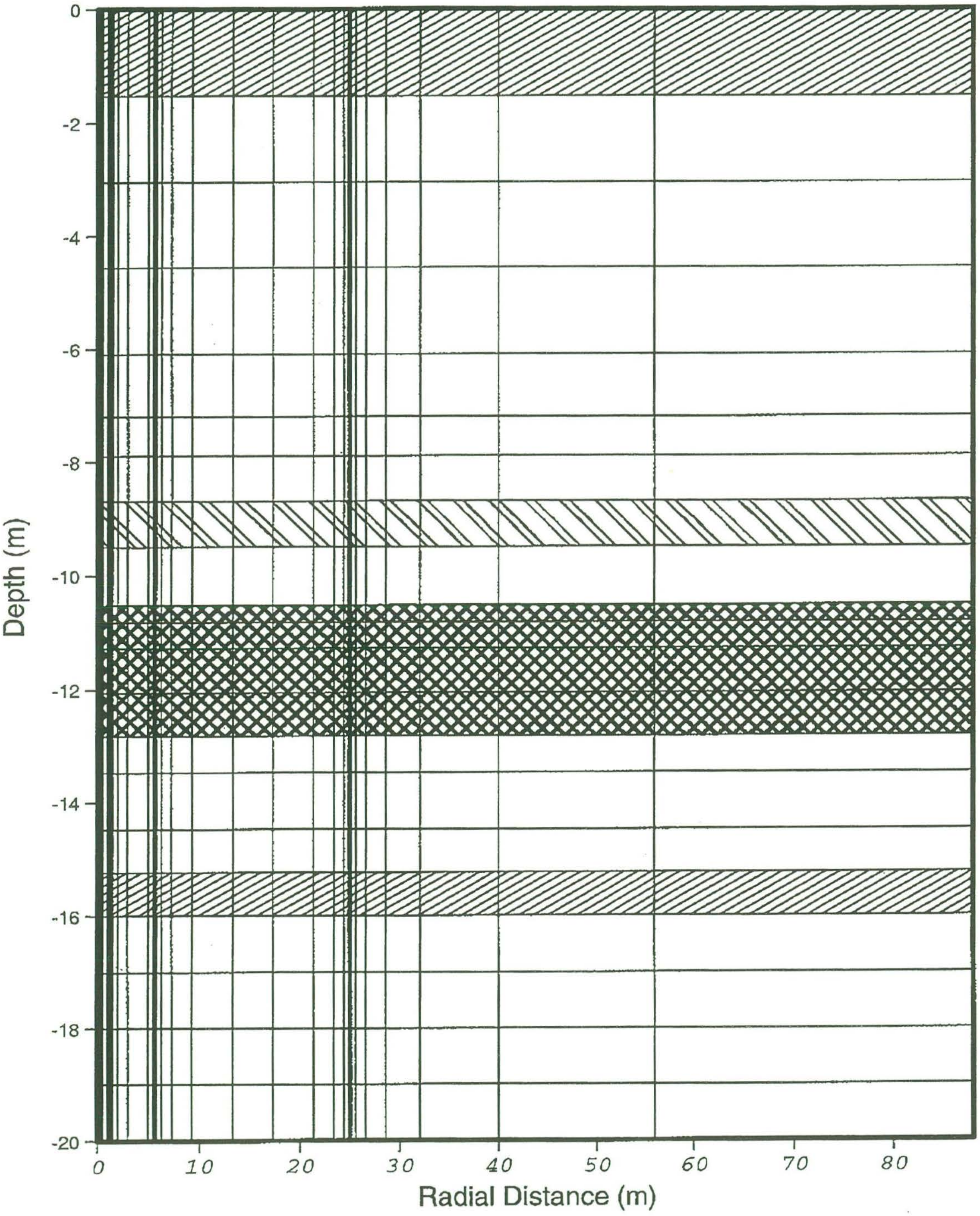

Figure 5.28b. Central portion of the axisymmetric grid used for the numerical simulation of the third hot air injection test. Shading: uniform diagonal stripes: vesicular zone; paired diagonal stripes: fracture; cross-hatching: rubble zone; solid black: injection interval. (**b**) shows the inner 88 m of the grid. The entire grid extends to 4 km.

Table 5.4. Material properties* used for the numerical simulation of the August 1995 hot air injection test into well S-3.

Material	Porosity	Permeability (m^2)	Reference
Intact Basalt	0.05	0.5 E-15	
Vesicular Zone	0.20	1.0 E-12	*Bishop*, 1991
Rubble Zone	0.50	1.0 E-09	**
Fractures	0.35	500. e-15	*Knutson et al.*, 1992

* Thermal properties for all layers: thermal conductivity 1.67 W/m °C, heat capacity 880 J/kg °C, density 2860 kg/m^3.

** Estimated from pressures and flow rates measured during hot air injection test.

Physical Processes

Heat transfer occurs due to convection and conduction; fluid (air, liquid water, and water vapor) flows in response to pressure gradients and gravity; and water can change phase via vaporization and condensation. Darcy's law is used to describe fluid flow, with relative permeability functions to describe the interference between the liquid and gas phase. For the present calculations, because no site-specific information is available, both phases are assumed to be mobile, with the relative permeability of each phase a linear function of the saturation of that phase, and capillary pressure is taken as a linear function of liquid saturation.

Initial conditions: The temperature-depth profile measured in well II-5 prior to the start of the experiment (Figure 5.20) is used for the initial temperatures for the entire grid, along with the corresponding gas-static pressure profile. Gas saturation values were estimated to be 30% for the shallowest 1.5 m of the grid, 20% between depths of 1.5 m and 10.5 m, and 10% below depths of 10.5 m.

Boundary Conditions

The boundary conditions are chosen to approximate, as accurately as possible, the conditions of the third hot air injection test. Above the ground surface, the atmosphere is represented as a constant temperature (20.5 °C), constant pressure (100 kPa) boundary, with a gas saturation of one, a relative humidity of 20%, and zero strength capillary pressure. The water table is represented as a constant temperature (13.5 °C), constant pressure (100.2 kPa) boundary, with a liquid saturation of one. The outermost block in each layer of the grid is specified as a constant-temperature, constant pressure boundary (so they maintain their initial conditions), but they are located so far from the injection well that they are not expected to have much of an effect on the calculation. At the injection interval, a constant mass injection rate is specified, corresponding to a volumetric flow rate of 4 cubic meters per minute. The injected fluid is a combination of air and water vapor at 90°C. The amount of water vapor actually injected during the field experiment is unknown, but is estimated to correspond to a 60% relative humidity at 20.5 °C (injecting dry air would result in approximately a 20% lower injection enthalpy).

Results

Figure 5.29a shows the calculated temperature distribution after 16 hours of hot air injection. The model results suggest that the region of rock around the injection interval that is heated up is relatively small, and heat would not be expected to reach the ground surface. The gas saturation distribution calculated by the model is strongly dependent on the initial distribution of gas saturation and the functional forms assumed for the characteristic curves (relative permeabilities and capillary pressure as a function of saturation), neither of which are known for the Box Canyon site. Therefore, the calculated gas saturation distribution, shown in Figure 5.29b, must be viewed as speculative. Figure 5.29a shows the gas saturation distribution after 16 hours of hot air injection; Figure 5.29b shows the gas saturation distribution after 16 hours with no injection, just the evolution of the system from the specified initial conditions. Both frames show a decrease in gas saturation in the lower portion of the rubble zone (depths from 12 to 14 m), which occurs because liquid infiltrates through the high-permeability rubble zone faster than through the underlying layer. Similarly, enhanced flow through the high-permeability vertical fractures located at radial distances of 0.02, 1.5, 5, and 26 m is also similar in both frames. The gas saturations differ at depths between 11 and 12 m (the upper portion of the rubble zone), where the hot air injection increases gas saturation for distances up to 60 m from the injection well. Note that the change in gas saturation is relatively small, approximately from 0.14 to 0.24. A choice of different characteristic curves would be likely to change the magnitude of the gas saturation changes, but the general conclusion that the spatial extent of gas saturation changes is much greater than the spatial extent of temperature changes will probably remain valid.

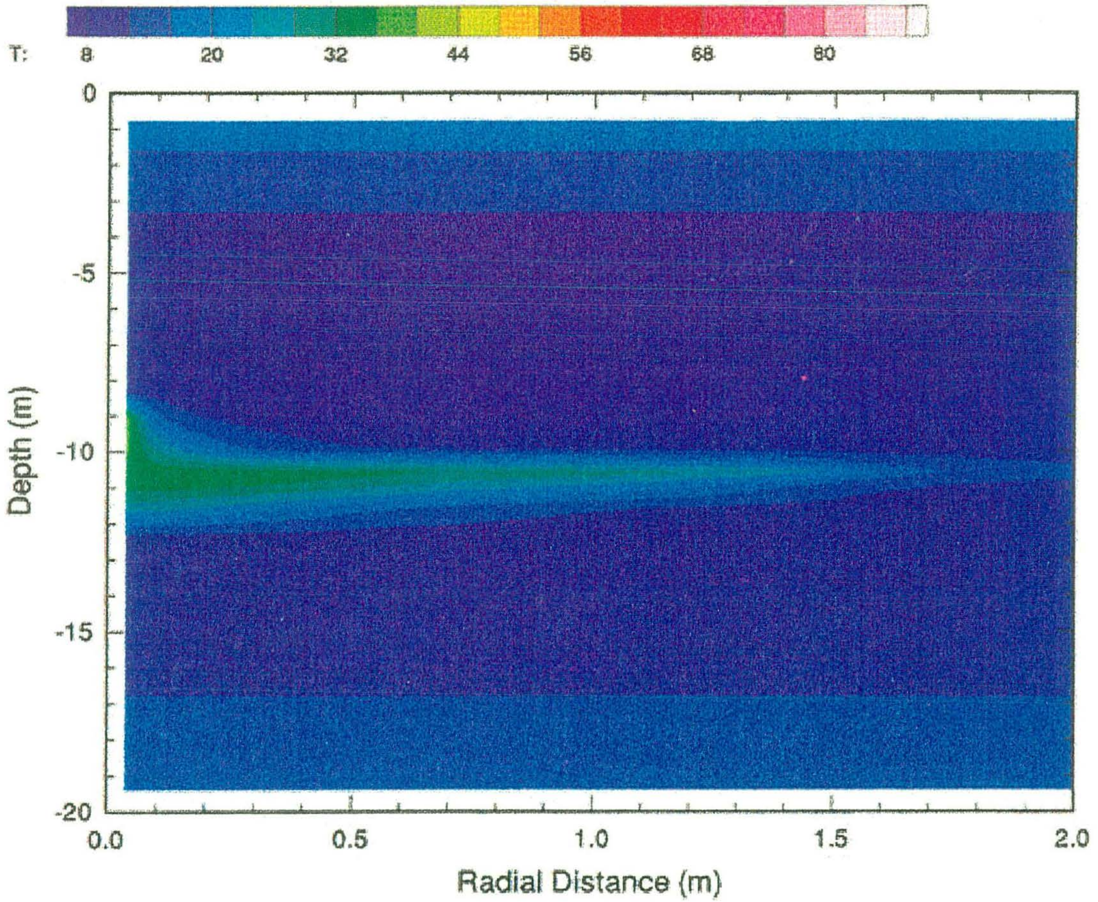

Figure 5.29a. Temperature distribution after 16 hours of hot air injection. The injection depth is 9-12 m; there is a fracture zone at 9 m depth and a rubble zone at 11-13 m.

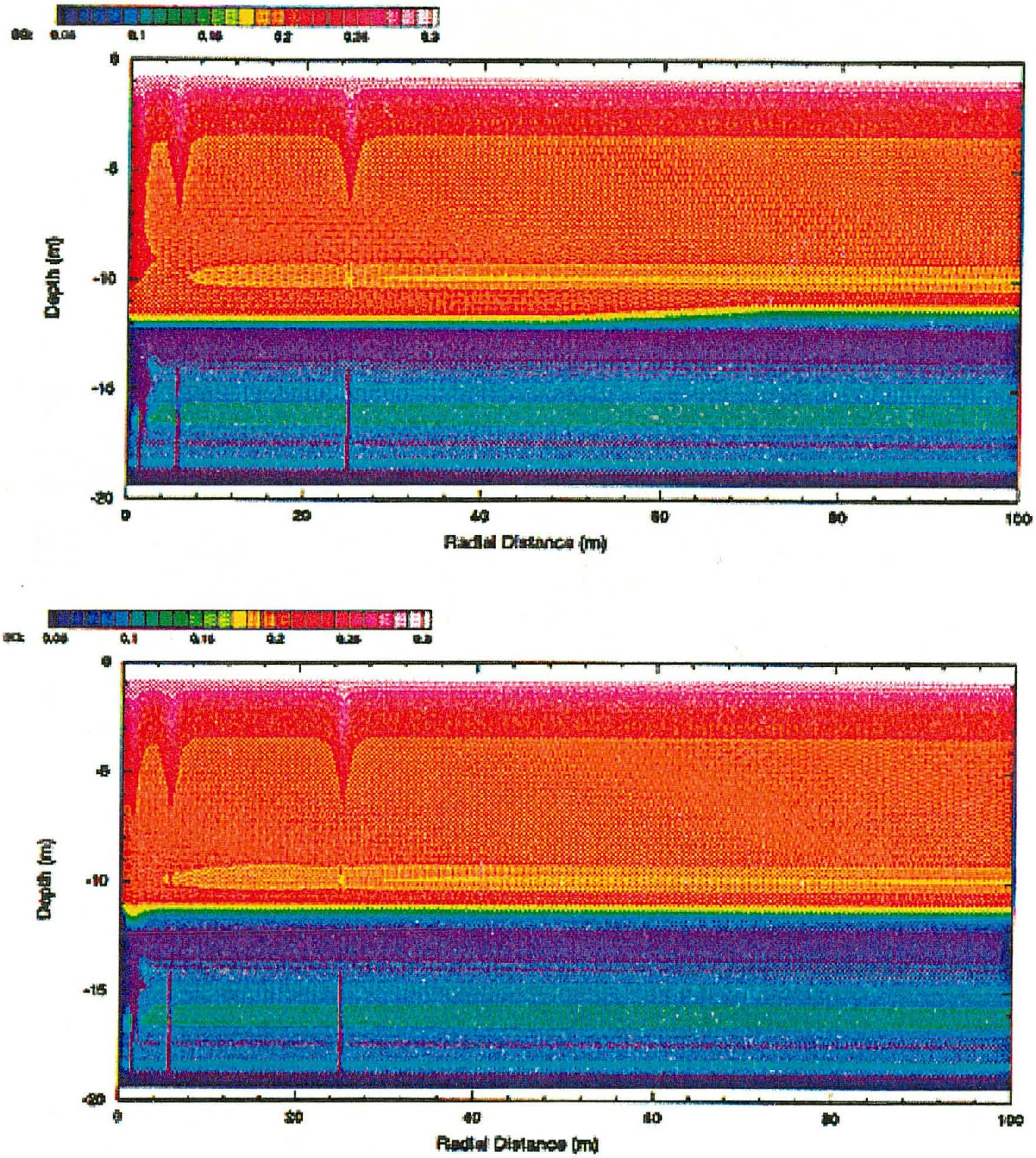

Figure 5.29b. Gas saturation distributions after 16 hours of hot air injection (upper frame) and no injection (lower frame).

Some alternate cases were considered. Because the winter of 1994-1995 was unusually wet, leading to unusually high subsurface moisture content at the time of the hot air injection test, it is useful to explore how the system might behave under drier conditions. As a limiting case a calculation was done with completely dry initial conditions (all gas saturations equal to one), to see how big the hot plume would be if none of the injected heat were used to heat up liquid water, which has a very large heat capacity. The temperature distribution after 16 hours of hot air injection into a dry medium is shown in Figure 5.30. Although the radial extent of the hot plume does not greatly differ from the previous case, the vertical extent is greater, and the maximum temperatures in the subsurface are much higher.

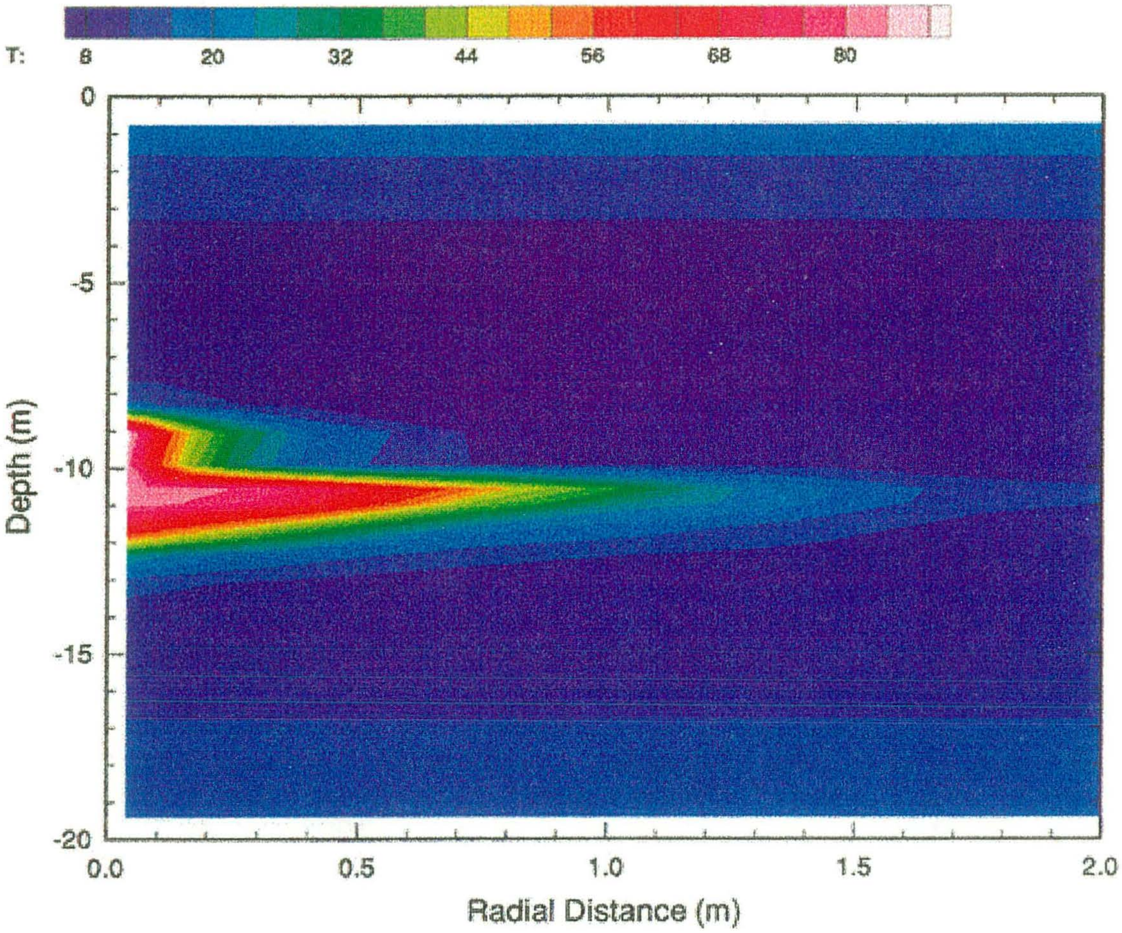

Figure 5.30. Temperature distribution after 16 hours of hot air injection into an initially dry medium.

One limitation of the August hot air injection tests is that because the moisture content of the injected air was unknown, the actual enthalpy of the injected fluid was unknown. Although the fraction of the injected fluid which was water vapor is likely to be small, its specific enthalpy is much greater than that of dry air. A calculation in which dry hot air was injected was done to bracket the effect of moisture content of the injected air. This calculation resulted in a modest decrease in the spatial extent of the hot plume, as shown in Figure 5.31. For a detailed comparison of the extent of observed and calculated hot plumes, it would be useful to know the moisture content of the injected fluid.

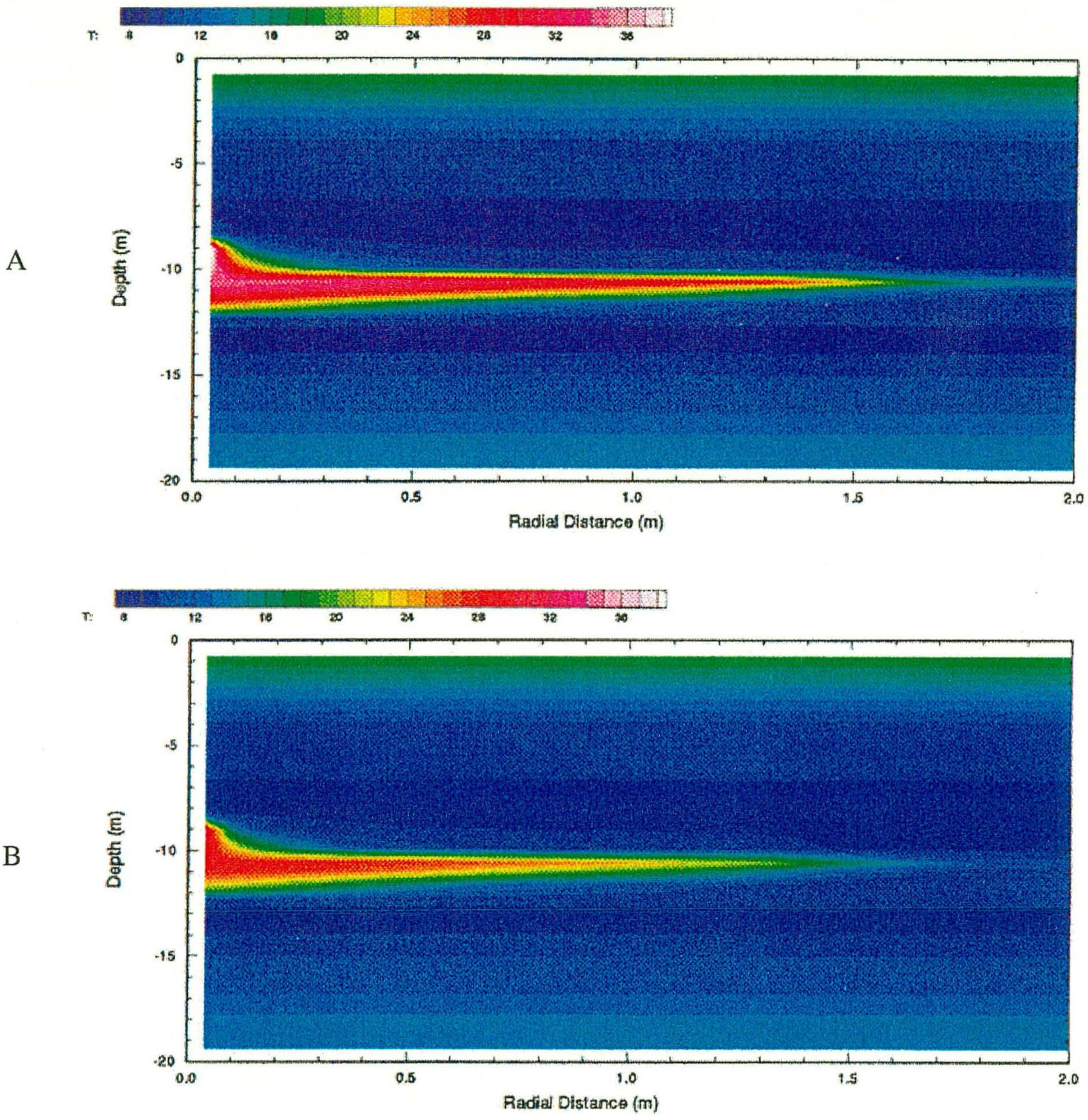

Figure 5.31. Temperature distributions after 16 hours of air and water vapor injection (A) and dry air injection (B) into an initially partially-saturated medium. Note the different temperature color scale from the previous temperature distributions, to enable subtle temperature differences to be seen.

A calculation using cold air injection produced a similar gas saturation distribution to the hot air injection case, suggesting that phase change effects are not significant for hot air injection at 90 °C. Allowing the vertical fractures to be more permeable did not affect the temperature distribution much, but did show that the simple initial gas saturation distribution assumed is inadequate to properly represent quasi-equilibrium conditions in a strongly heterogeneous medium.

Conclusions from Field Data and Numerical Modeling

The initial analyses of field data and numerical simulations have corroborated the finding from the August field experiment that hot air injected into the high-permeability rubble zone does not reach the ground surface. The relative importance of heat absorption by the rock matrix and advective spreading of air in the rubble zone are being evaluated as factors in limiting hot air flow to other monitored boreholes. The modeling results have also shown that gas saturation measurements may be useful in addition to temperature measurements. Furthermore, the modeling studies have pointed out the need for a realistic representation of the relative permeability and moisture retention (capillary pressure) relations for the different components of the subsurface.

2.5.3.4 Development of Instrumentation for Infiltration Experiments

General Characteristics

The instrument array that will be used in the FY 96 infiltration experiment, will include:

(1) a psychrometer to measure water potentials below 1 bar, which may be measured in the upper part of the vadose zone before the infiltration test;

(2) a tensiometer to monitor water front movement and measure water potential in relatively wetted rocks (The tensiometer will be fitted with a porous tip of high hydraulic conductivity [special ceramic or metal porous stainless steel tube] with a bubbling pressure from 200-250 mbar to 1 bar. Special care will be taken to assure good contact between tensiometer and rock.);

(3) a suction lysimeter to collect water samples;

(4) a probe for gas pressure measurements and gas sampling;

(5) an improved TDR system which will consist of several pairs of electrodes installed parallel to each other at the same horizontal level. (TDR electrodes are currently being tested under laboratory conditions.)

Borehole Tensiometer Design

Observations at Box Canyon Site

A tensiometer has been designed to measure water pressure in deep vadose zones [*Faybishenko*, 1986]. At the Box Canyon site, these tensiometers were attached to the 1/2" PVC pipe that was lowered into the hole. Two-inch OD ceramic cups used in these tensiometers partly touch the wall surface. The principle behind this type of installation is that equilibrium is established between the vapor phase and the liquid water in the rock, and hydraulic potential is measured in the vapor phase. Each tensiometer includes a two-cell transducer that maintains a nearly constant water level in the lower cell (Figure 5.32). Readings of water pressure are measured at the surface in nanometers. Results of using these tensiometers were presented in Section 2.5.3.2.

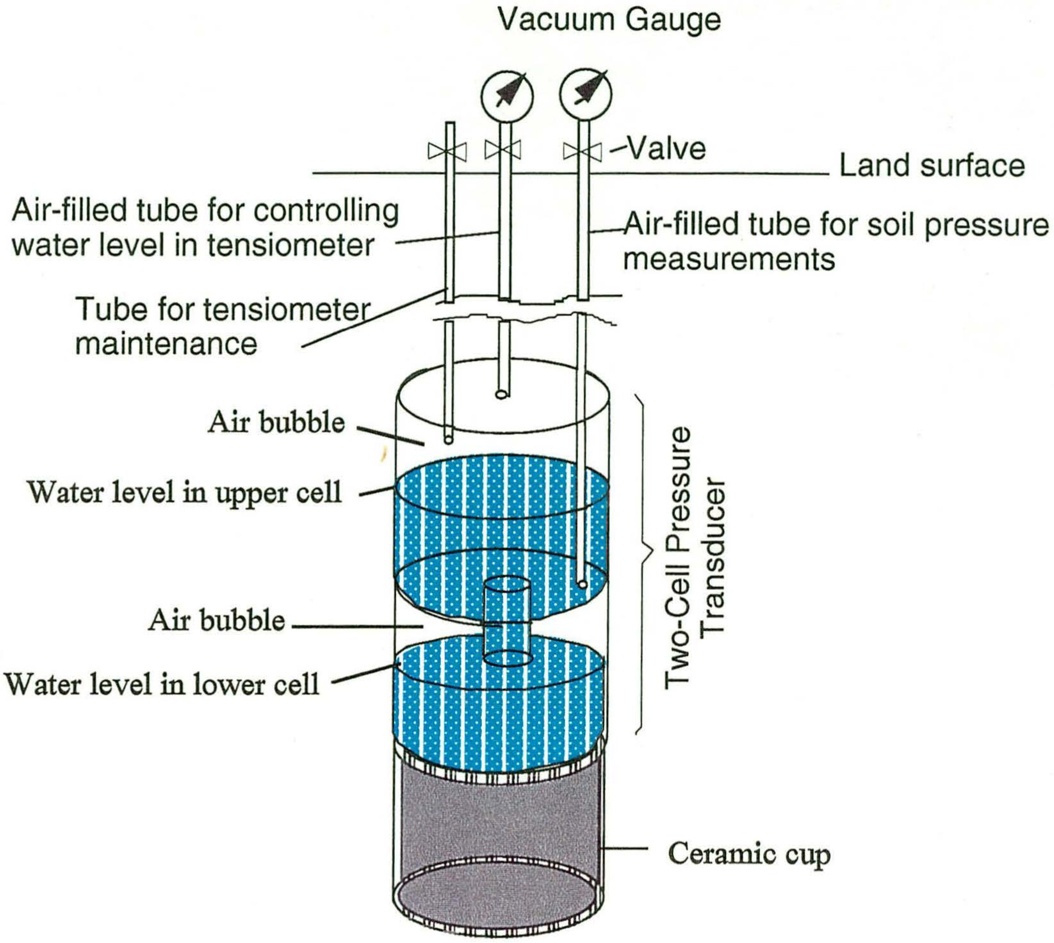

Figure 5.32. Scheme of deep tensiometer with two-cell transducer.

In addition, two tensiometers designed at INEL were installed in boreholes at the Idaho Research Complex (IRC) Test Site. The tensiometers consisted of a porous cup connected to a pressure transducer through a short water column. The pressure transducer was designed to be removable from the tensiometer for calibration in the field. One tensiometer was fixed to a 1-1/2 in PVC pipe and stood on the bottom of a 15 m (50 ft) well, the second tensiometer was suspended in the borehole at the 11 m (35 ft) depth. An electronic barometer also was installed in the borehole. Data collected from the tensiometers and barometer are shown plotted against time in Figure 5.33. The soil water pressures were unexpectedly high indicating nearly saturated basalt. We initially thought the basalt was too dry to obtain reliable tensiometer responses. The barometric data shown on Figure 5.33 is actually 867 cm - barometric pressure expressed in cm of water to allow improved visualization of the data. The correlation between the water tension and barometric pressure was quantified using linear regression with barometric pressure as the independent variable and tension as the dependent variable. The regression results are shown in Figure 5.34 where the solid lines are the regression lines. The r-square value for the regressions was approximately 0.9 indicating that 90 percent of the variation found in water tension could be attributed to barometric changes. The slope of the two regression lines was -0.89 for both lines. Currently it is believed that the barometric effects are due to changes in pressure experienced by the reference port and are not fluctuations in water tension. Further experiments are under way to verify this hypothesizes. A slight hysteresis was observed as the barometer went through highs and lows. The hysteresis effect could be due to air entrapped in the tensiometer requiring water to move into and out of the porous cup in response to barometric pressure changes. It is interesting to note here that barometric effects are not normally seen in water tension data. Tensiometers installed at the land surface experience large changes in temperature, and the temperature effects produce fluctuations in water tension that mask barometric effects.

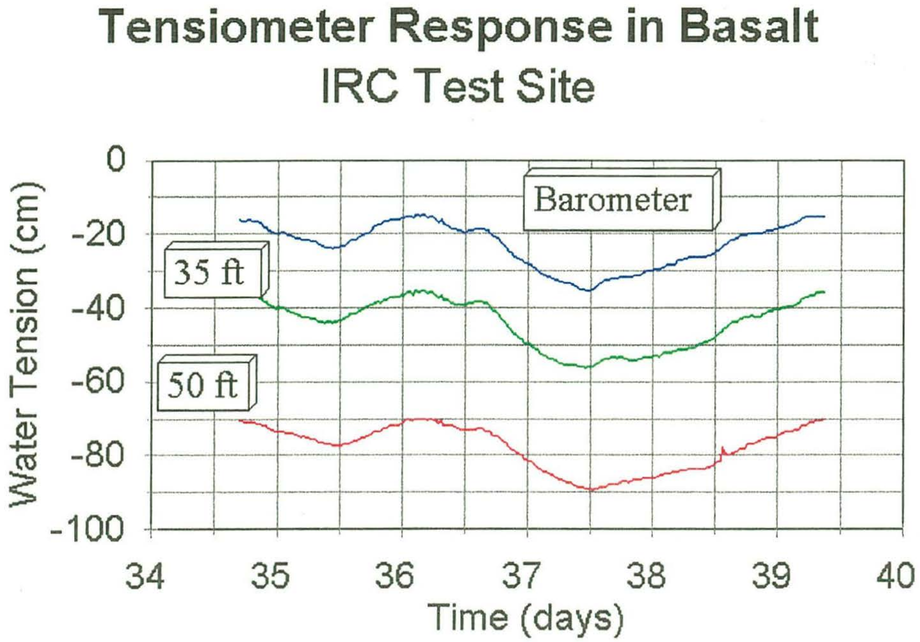

Figure 5.33. Tensiometer and barometer data measured at the IRC test site.

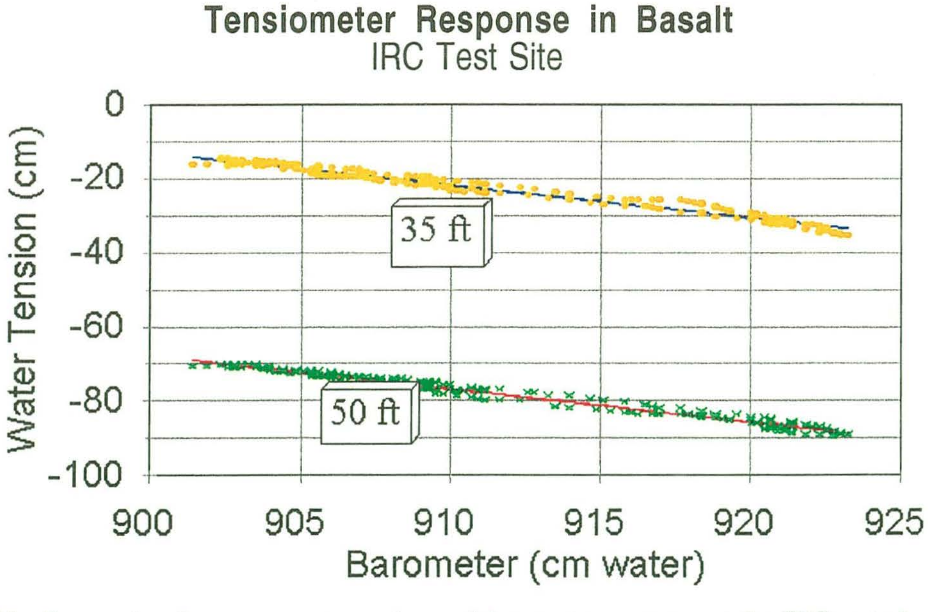

Figure 5.34. Regression between water tension and barometer pressure at the IRC test site.

The results do show that installing the tensiometers below the land surface reduces the effect of diurnal temperature effects to acceptable levels. Burial of the tensiometer has another positive effect in that the tensiometers do not require servicing to flush gas accumulations. Tensiometers installed at the land surface usually require flushing 1 to 2 times per week. The yensiometers also were designed to allow removal of the pressure transducer and be operable as vacuum lysimeters capable of obtaining water for analysis of tracer concentrations.

The tensiometers designed at the INEL have been found reliable and easy to calibrate in the field. Thus, reliable water pressure measurements can be made in fractured basalt and water samples for the tracer studies will be obtainable.

2.5.3.5 General Conclusions

The combined studies have allowed us to obtain an initial understanding of the three-dimensional structure of the fracture system of the Box Canyon site. Of key interest from the vadose zone hydrology point of view are the rubble zones between basalt flows, columnar joints, vesicularity, individual horizontal and oblique fractures, and the central fractured zone. The central fractured zone does appear to exist throughout the site. Hydraulic properties of the central fractured zone and rubble zones may be critical in controlling water and reactive chemical transport in the vadose zone.

Hot air flow tests have been successful in evaluating the horizontal connectivity within the rubble zone on a local scale, but were not able to identify vertical fractures and joints dictributed between the land surface and the rubble zone(s). Further analysis should be performed to understand the extent to which hot air injection tests may be useful in evaluating the processes of advective and diffusive transport and adsorption in fractured basalt.

A detailed analysis of the geological and geophysical information is underway to improve the understanding of main characteristics of the fracture system, and a more sophisticated plan of field investigations for FY 96 has been prepared.

2.5.4 FY 96 Activities

A series of air injection tests has been planned to determine fracture connectivity between boreholes. Air will be injected in individual fractures and the fracture zone in the slanted boreholes, with careful monitoring of air pressure in vertical and other slanted boreholes and near surface gas sampling ports. In these tests, pneumatic testing equipment that has been developed to obtain hydraulic transport parameters in boreholes will be used. The equipment was designed to have great flexibility for conducting gas injection, gas withdrawal, as well as tracer transport testing in both single and multiple borehole configurations. In addition, the system could be used for gas phase or liquid phase testing. The system was designed around pneumatic packers built specifically for making high quality seals demanded by gas testing. All monitoring and control functions are controlled by a single laptop PC. The instrumentation interface and software control allows the user to rapidly reconfigure the system in the field for conducting a varied testing program. This system has been tested at Arizona and Nevada field sites.

Investigations are underway to develop a borehole sleeve that will serve to seal and support the borehole and provide access for geophysical logging, such as neutron, gamma, and radar. The same or similar design also may be used to emplace instruments up against the borehole wall, while minimizing backfill. Several materials have been identified as likely candidates. Materials will be tested in the laboratory prior to field testing.

Conceptual model development and three-dimensional visualizations of fractures from field test data will continue to be updated as new data become available. With a 3-D visualization of connected fractures in hand, selected fractures and fracture zones will be instrumented with TDR probes and neutron access tubes for soil moisture content, tensiometers for water tension measurements, and lysimeters for obtaining soil water samples.

Subsequent infiltration tests will evaluate gas injection tests as a viable method for estimating vertical and horizontal connectivity. If this method works, the hydrologic instruments will then have a much better chance of intersecting infiltrating fluid. Also, much may be learned about infiltration potential directly from a gas injection test. If so, the gas test could be performed quickly and inexpensively at contaminated sites to predict infiltration behavior.

The final test of the conceptual model will be to conduct an infiltration test design based on and its results predicted from the hot air/gas tracer test results. If this infiltration can be predicted, then the hypothesis that gas tests are useful indicators of infiltration behavior will be supported.

2.5.5 Significance

Sensitivity studies of input parameters used for numerical simulations of the movement of radioactive contaminants through the vadose zone beneath the RWMC, indicate that one of the most critical factors driving uncertainty in performance assessments is the rate of infiltration. Movement of water through fractured rock under variably saturated conditions is poorly understood, particularly in the Snake River Basalts because of the wide variation in fracture patterns, the lack of adequate characterization/monitoring technologies and a lack of methods for identifying rapid flow paths. Successful development of an understanding of flow at Box Canyon will provide the framework for characterization at waste disposal sites like the RWMC, for the construction of performance assessments and risk assessments and the planning of remediation and containment strategies.

If we can successfully understand infiltration at Box Canyon, then we can recommend characterization and monitoring strategies, develop appropriate ways to construct performance assessment evaluations and provide a framework for planning isolation strategies at contaminated sites where fractures or other preferential flow paths are a concern.

2.6 Task 6. Database/Visualization

2.6.1 Background

Scientific visualization of 3-D field data provides researchers with the opportunity to look at large amounts of different kinds of data that are spatially distributed. For example, borehole data such as lithology, caliper data, location and orientation of fractures, and neutron data may all be combined and displayed in a single visualization. The researcher sitting at a graphics workstation may easily change the viewpoint by rotating, translating or magnifying the display image and may use different visualization techniques to examine spatial correlations for one type of data or correlations between different types of data.

Generally, visualizing field data requires manipulation of the data into a format required by the visualization software. This takes time and results in the propagation of derived data files. A preferred alternative is to store all field data in a database management system (DBMS), the benefits of which include safe and controlled data storage, easy access to the data, and the ability to query the data for specified attributes. Examples of data queries include asking the DBMS to return the location of all rubble zones present in a selected group of boreholes or the locations of all depths in boreholes for which a certain kind of data (*e.g.,* neutron) exceeded a specified threshold value.

In addition to demonstrating the value of scientific visualization in analyzing field data, another achievement of this task is the development of a prototype system that interfaces a commercial DBMS and visualization software. Using such a system, the researcher may formulate a query and visualize the results of the query without having either to prepare intermediate data files or without having to learn how to program with the visualization software. The researcher may concentrate on analyzing the data and extracting salient data from the DBMS using easy-to-use query menus.

Scientific visualization and earth sciences modeling software used by researchers on Task 6 include the Application Visualization System (AVS) by Advanced Visual Systems Inc. and the Lynx Geological Modeling System by Lynx Geosciences Inc. The database management system used was the Illustra object-relational database management system from Illustra Information Technologies, Inc. All software was used on an (upgraded) Iris Indigo R4000 graphics workstation from Silicon Graphics Inc.

2.6.2 Performer

INEL provided the data from the Large Scale Infiltration Test (LSIT) as a prototype dataset for this task, which involved analysis of the dataset both from the point of view of data management and scientific visualization.

The development of the prototype database management/visualization system, described under FY 95 Activities, was a collaboration between the Earth Sciences Division at LBL and ESEA, a small business operating in the Bay Area. The work was jointly funded by EM 50 and a DOD-funded CRADA. The LSIT dataset was used to prototype the database management/visualization system.

Dr. Debasis Mitra, a professor of Computer Science at Jackson State University, used the data from the LSIT as a sample dataset for his research in temporal sequences in earth sciences databases. Dr. Mitra was a guest researcher in the Information and Computing Sciences Division at LBL during the summer of 1995 and worked with Arie Shoshani.

2.6.3 FY 95 Activities

2.6.3.1 Scientific Visualization of Field Data from the INEL Large Scale Infiltration Test

This section describes the scientific visualization of several types of field data collected as part of the Large Scale Infiltration Test (LSIT) conducted by INEL in July 1994. *Burgess* (1995) describes the LSIT including the system of monitoring wells and instrumentation, how the LSIT was conducted, and analyses of the data collected. INEL provided the Berkeley Lab with geologic data from the test site in the summer of 1994. Other data from the LSIT were provided between January and July of 1995.

The following types of three-dimensional field data from the LSIT were visualized using AVS:

- lithology
- tracer
- hydrograph
- neutron data

In addition, Lynx GMS was used to create a "layer" model of the lithology showing different basalt flows. Visualizations of each type of data are described in subsections below.

In the figures in this section, boreholes are represented either as cylindrical tubes or as straight lines. In most views, the well names appear near the top of the wells. Some figures include a circle that represents the perimeter of the infiltration pond. Figure 2.1 provides a plan view of the monitoring well network at LSIT.

Full size versions of all figures in Section 2.6.3 have been included at the end of Section 2.6.

The visualization work described in this subsection was presented at the Technologies for Characterization Forum as part of ER '95 (*Jacobsen, Horsman, and Holland,* 1995). Development of the geological model for the LSIT was presented at AVS '95 (*Horsman and Bethel,* 1995).

Lithology

Figure 6.1 shows a visualization of lithologic data for 44 wells for the LSIT. Though over 60 wells were installed as part of the LSIT, detailed lithologic data for only 44 wells were available. The data consist of identification of different basalt flows together with thin layers of interbed material.

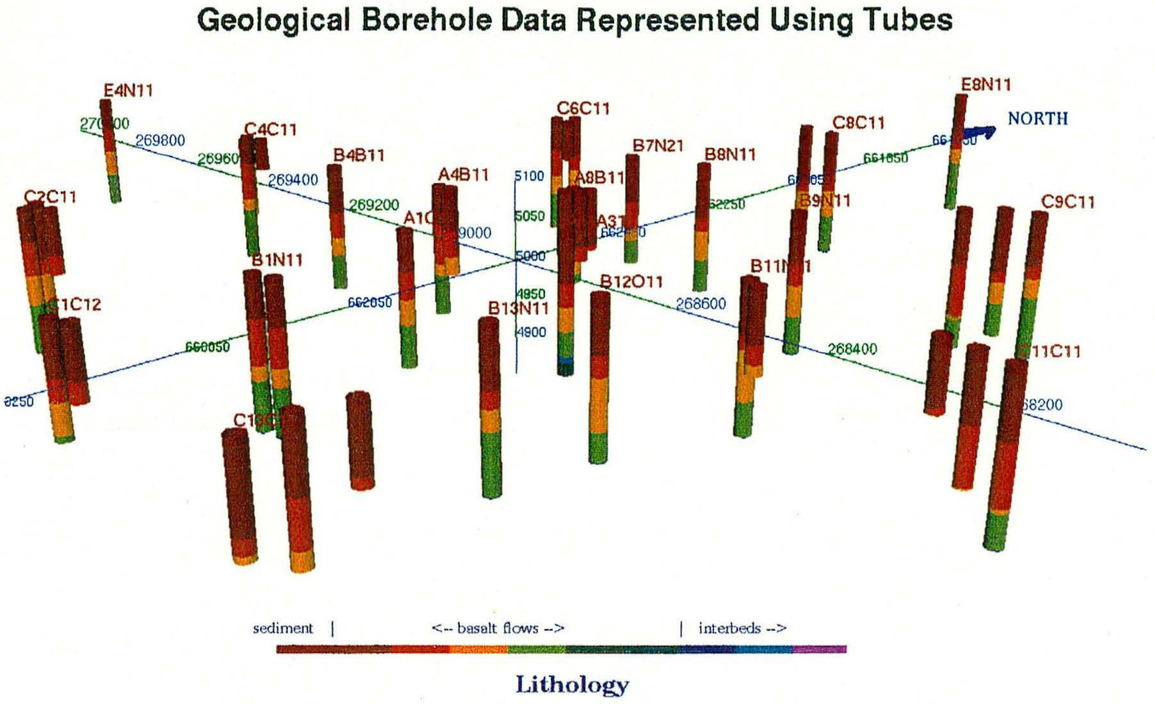

Figure 6.1. Visualization of geological data of monitoring wells at the INEL Large-Scale Infiltration Test site.

In Fig. 6.1 different basalt and interbed layers are represented using different colors. Few of the wells shown in Fig. 6.1, however, intersect the interbed located at about 55 meters below the ground surface. Fig. 6.1 clearly shows a sequence of basalt flows.

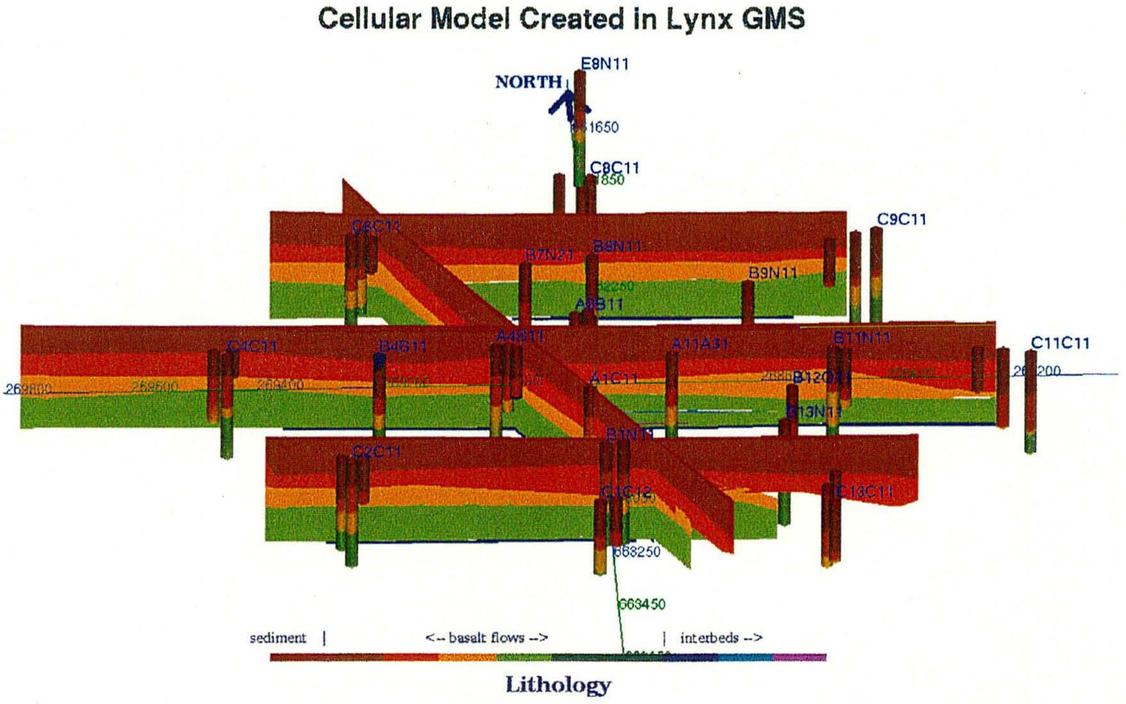

Figure 6.2. Fence diagram of geological model of INEL Large-Scale Infiltration Test site.

Whereas the visualization of the different lithologic layers shown in Fig. 6.1 is a display of field data and does not include any *interpretation*, the visualization shown in Fig. 6.2 is a result of constructing a simple geological modeling using the Lynx GMS.

Figure 6.2 shows a fence diagram based on the Lynx GMS model. Once the geologic model was created using Lynx GMS, it was visualized using AVS. AVS provides the capability to slice an object at arbitrary angles and to create fence diagrams. Figure 6.2 shows that not all basalt layers are of uniform thickness.

Tracer Data

Tracer data for 22 wells were provided by INEL. Though tracer experiments were conducted using selenium^{75}, strontium^{85}, and terbium^{160}, there were significant nonzero data only for selenium^{75}. Tracer concentrations were measured either by lysimeters or else in water samples taken from the bottom of wells. All wells at which tracer concentrations were measured have been included in the visualizations as gray tubes, though data at locations with few nonzero data values were not included in the visualizations. Included are tracer data from 23 locations in a total of sixteen wells. Of those sixteen wells, tracer data from only three of them consist of lysimeter readings; the rest of the data are from bottom hole measurements.

The three tracers were added to the infiltration pond on July 31, six days after water was first added to the infiltration pond. Concentrations of selenium^{75} were measured between August 3 to September 19, 1994. Visualizations of the tracer data for each day in this interval were performed as described below. The result is an animation showing the change in selenium^{75} with time. Visualizations for only two times have been included in this section.

One difficulty in visualizing the tracer data resulted from the time scale on which the data were collected. For some boreholes, tracer concentrations were measured more than once a day. In this case, the data were averaged to give a single tracer concentration for the day. For other boreholes, tracer measurements were made at irregular time intervals. In this case, the tracer concentrations were linearly interpolated in time

Figure 6.3 shows the tracer concentrations on August 14, the day at which the tracer concentration peaked at the most shallow lysimeter location (8.23 m) in well A11B11. Note, however, that tracer concentrations for the other lysimeter locations in A11B11 do not decrease monitonically with depth.

Figure 6.4 shows the tracer concentrations ten days later, on August 24. Note the change in concentration at different depths in well A11B11. Compared to the values shown in Fig. 6.3, the concentration at the most shallow lysimeter location (8.23 m) has decreased, whereas the concentrations at the next two lysimeter locations (14.6 m and 21.3 m) have increased. The concentration at the next lysimeter location (31.7 m) has decreased. Note also, the increase in bottom hole concentration for wells B06N11, B08N11, and C06C11 (all on the left side of the figure), and the decrease in bottom hole concentration for well B13N11 (on the far right-hand side).

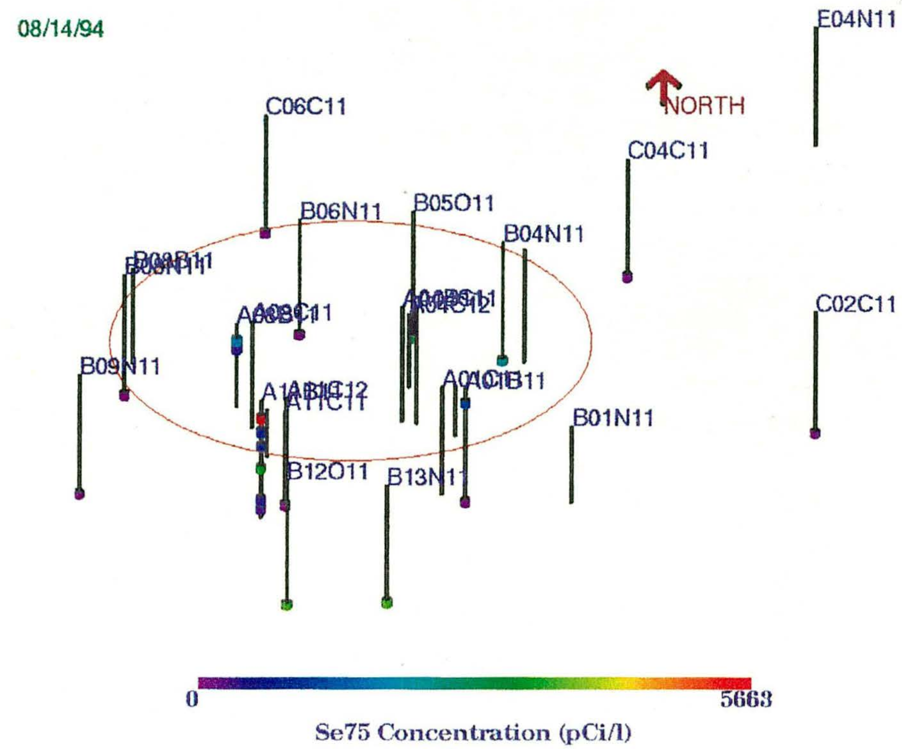

Figure 6.3. Concentrations of selenium75 measured by lysimeters or from bottom hole, water sample measurements. The concentrations are shown on August 14, 1994.

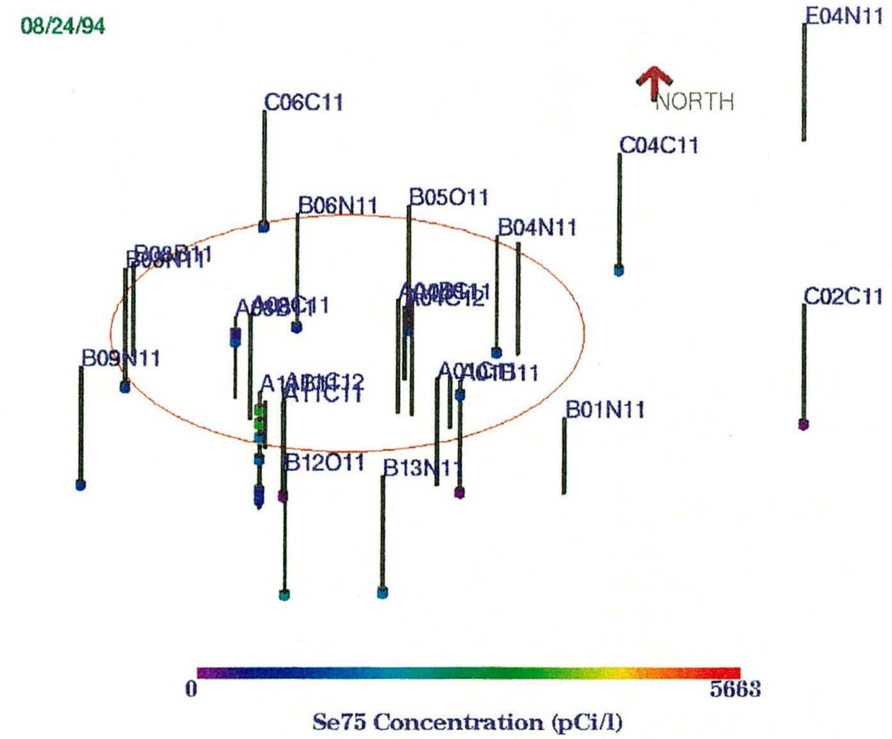

Figure 6.4. Concentrations of selenium75 measured by lysimeters or from bottom hole, water sample measurements. The concentrations are shown on August 24, 1994.

These figures, together with visualizations of the tracer data at other days during the period of August 3 to September 19 (not included in this report) strongly indicate the presence of multiple non-uniform flow paths for water and tracer movement.

Neutron Data

Neutron data taken were taken with two different strength sources: "near" neutron data were collected using a 50 mCi source, and "far" neutron data were collected using a 1 Ci source. The stronger source gives a measure of the change in moisture content farther from the edge of the borehole. In some boreholes, both near and far neutron data were collected. The letters 'N' and 'F' are used to distinguish between the two types of sources in Figs. 6.5 and 6.6. The data shown in the visualizations have been normalized by subtracting the data from background measurements made before the LSIT began. Only neutron that could be normalized and were significantly greater than zero were included in the visualizations; data for ten wells have been included.

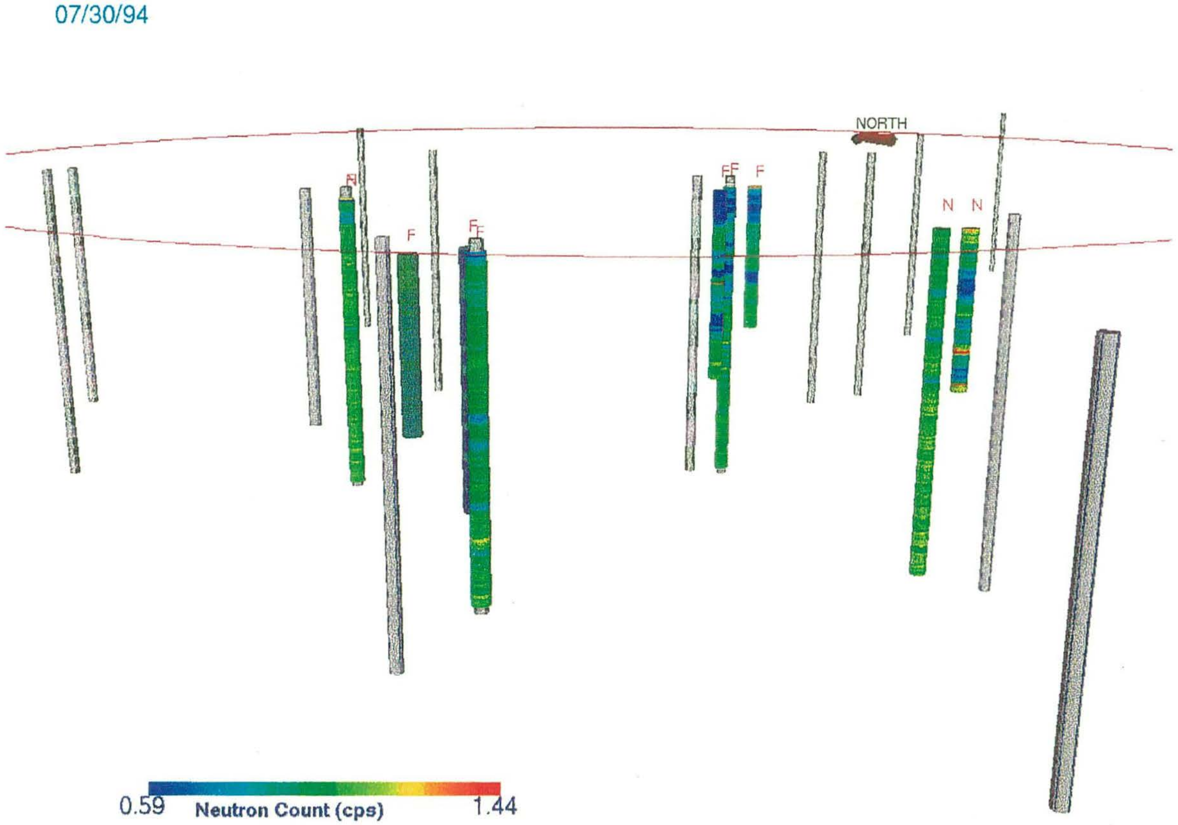

Figure 6.5. Shown are both far (1 Ci, labeled "F") and near (50 mCi, labeled "N") source neutron data collected on July 30, 1994. The neutron data have been normalized against background data collected before the LSIT began.

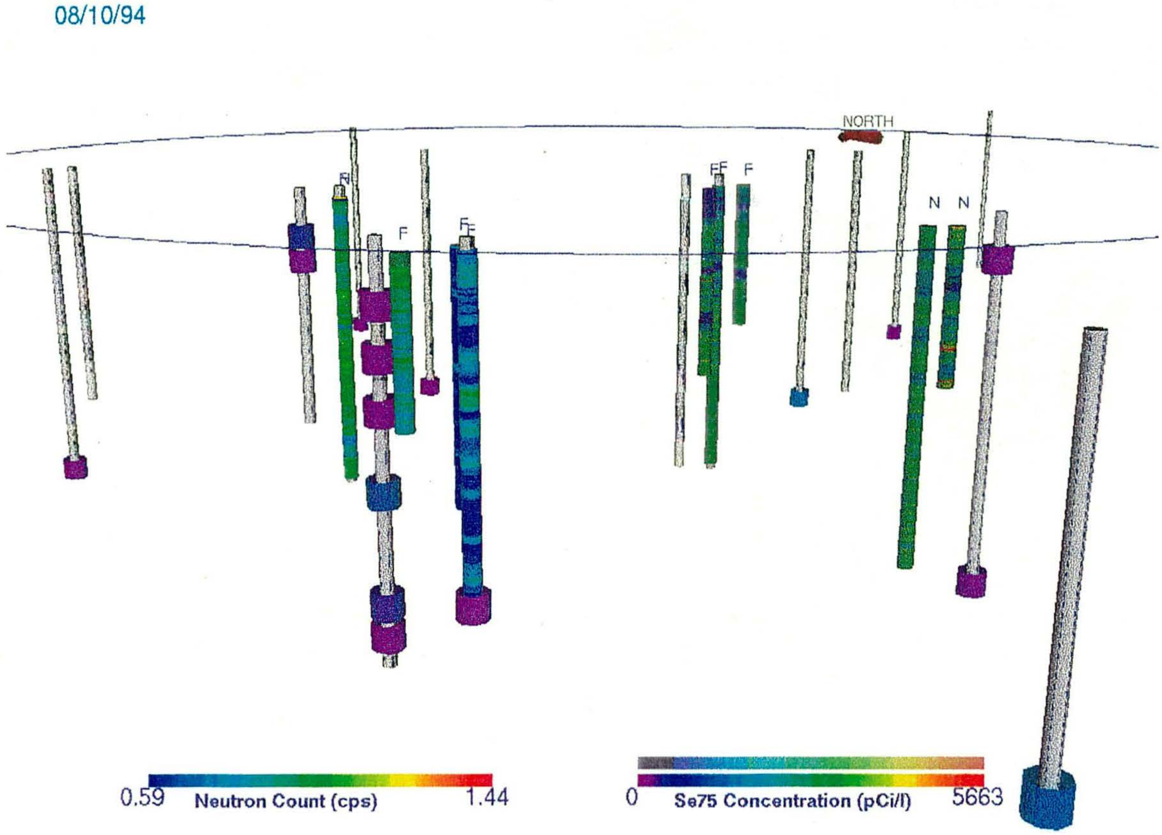

Figure 6.6. Shown are both far (1 Ci, labeled "F") and near (50 mCi, labeled "N") source neutron data collected on August 10, 1994. The neutron data have been normalized against background data collected before the LSIT began.

The neutron data were collected between July 30 and August 29, 1994. On a time scale, however, both the near and far neutron data are somewhat scarce. For only two days in the time period were data collected for more than three wells. Figs. 6.5 and 6.6 show both near and far neutron data collected on July 30th and August 10th.

Figures 6.5 and 6.6 show how the neutron data are displayed. In Fig. 6.6, the color saturation for wells for which there was no data collection on that day has been reduced (top legend). Comparing the far neutron data for the two figures for wells A08C11 and A11C11, shows a general decrease in counts per second for both wells, though the decrease is more significant in A11C11.

Hydrograph Data

The water levels in the bottom of seventeen boreholes were measured from August 9 through October 5, 1994. (Recall that water was first added to the infiltration pond on July 25.) Figure 6.7 shows the hydrograph data together with tracer data on September 6. This time was chosen because the water level in several of the wells peaked around this time. The water levels are shown in the visualization as blue cylinders, which have been slightly offset in order to not obscure the tracer data. As an indication of scale, the water level in C04C11 is about 1.5 m.

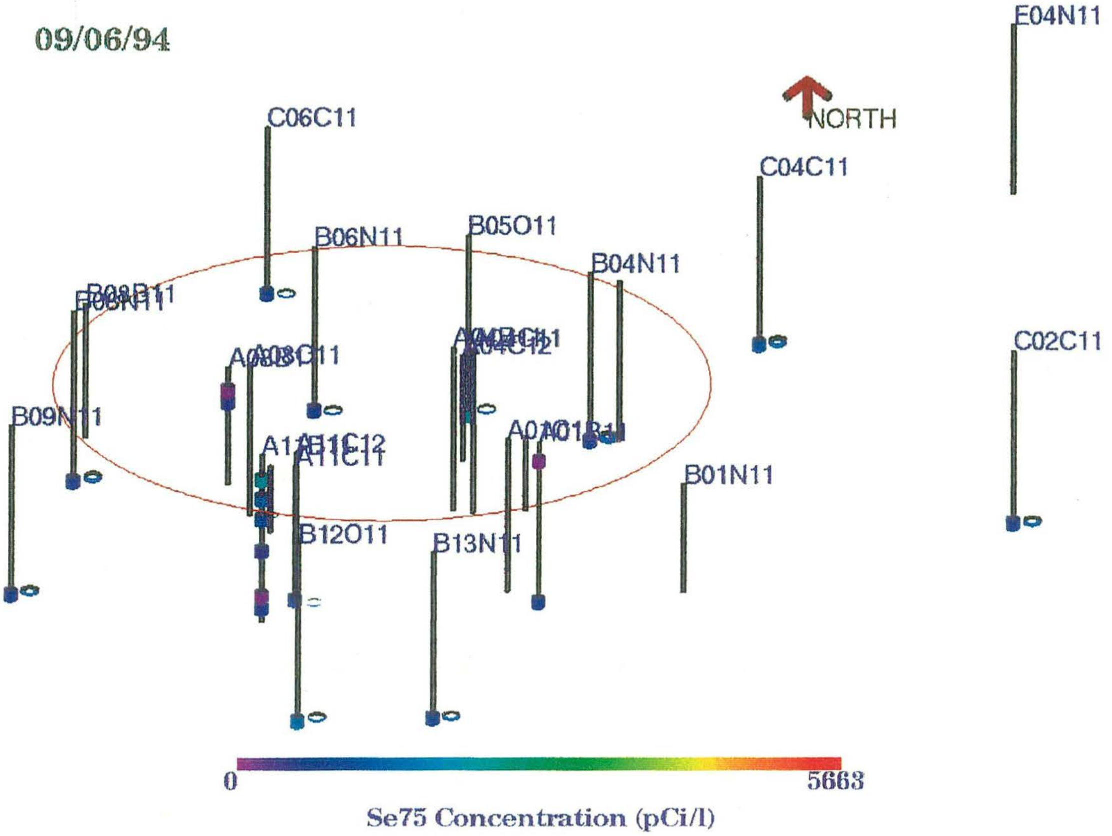

Figure 6.7. Water levels and selenium 75 concentration in open wells as measured on September 6, 1994. See text for explanation of presentation of water levels.

2.6.3.2 Scientific Visualization of Field Data from the Box Canyon Site

Visualization of field data from the Box Canyon site was begun at the end of FY 95 as geological data were becoming available. AVS (visualization) networks developed to visualize the LSIT data were modified to use with the Box Canyon data, and thus the experience gained working with the LSIT data resulted in being able to produce visualizations of the Box Canyon data faster and with less effort. Visualization of field data from the Box Canyon site was described in more detail in Section 2.5.

2.6.3.3 Development of a Linked Prototype System to Link Database Management with Scientific Visualization

In collaboration with another project in the Earth Sciences Division at the Berkeley Lab, a prototype system was developed that links an object-relational database management system (from Illustra Technologies, Inc.) with scientific visualization software (from Advanced Visual Systems). Linking or interfacing Illustra and AVS required the following:

- a database design;
- an understanding of how the prototype system would be used, specifically, how would the data in the database management system be queried and how should the data be displayed;
- software development.

Researchers involved in this task were involved in the database design and in providing guidance on how the system could be used. No software development was performed as part of this task.

For the purposes of prototyping the database management/visualization system, only geologic data (lithology, fracture data, and vesicularity), instrument locations, and matric potential data (calculated from heat dissipation measurements) were entered into DBMS. The data organization is shown in Tables 6.1a and 6.1b. Query menus were designed to allow the user to easily indicate what data was to be retrieved and visualized. Note that in the prototype system, the data are visualized as they are retrieved. This is a significant improvement over standard practice, in which the user first queries the DBMS, writes the result of the query to a file, exits the DBMS, formats the data file into a format acceptable to the visualization system, initiates the visualization system, reads the data file into the visualization system, and at last begins visualization of the data. Use of the prototype system significantly speeds up the process of analyzing field data because interface barriers between the DBMS and the visualization system have been removed.

Shown in Fig. 6.8, are two dialogue boxes to access the data stored in the DBMS. The top box allows the user to specify what kinds of geological data (lithology, fracturing, and vesicular) to select, and the second box allows the user to specify a value for the percent daily change in the heat dissipation (matric potential) data for a range of times. In this example, the user has asked to see all well segments for which the fracturing has been characterized as "very close," "breccia," or "rubble," and in addition, all locations at which a percent daily change in the heat dissipation data of at least 18% has been observed.

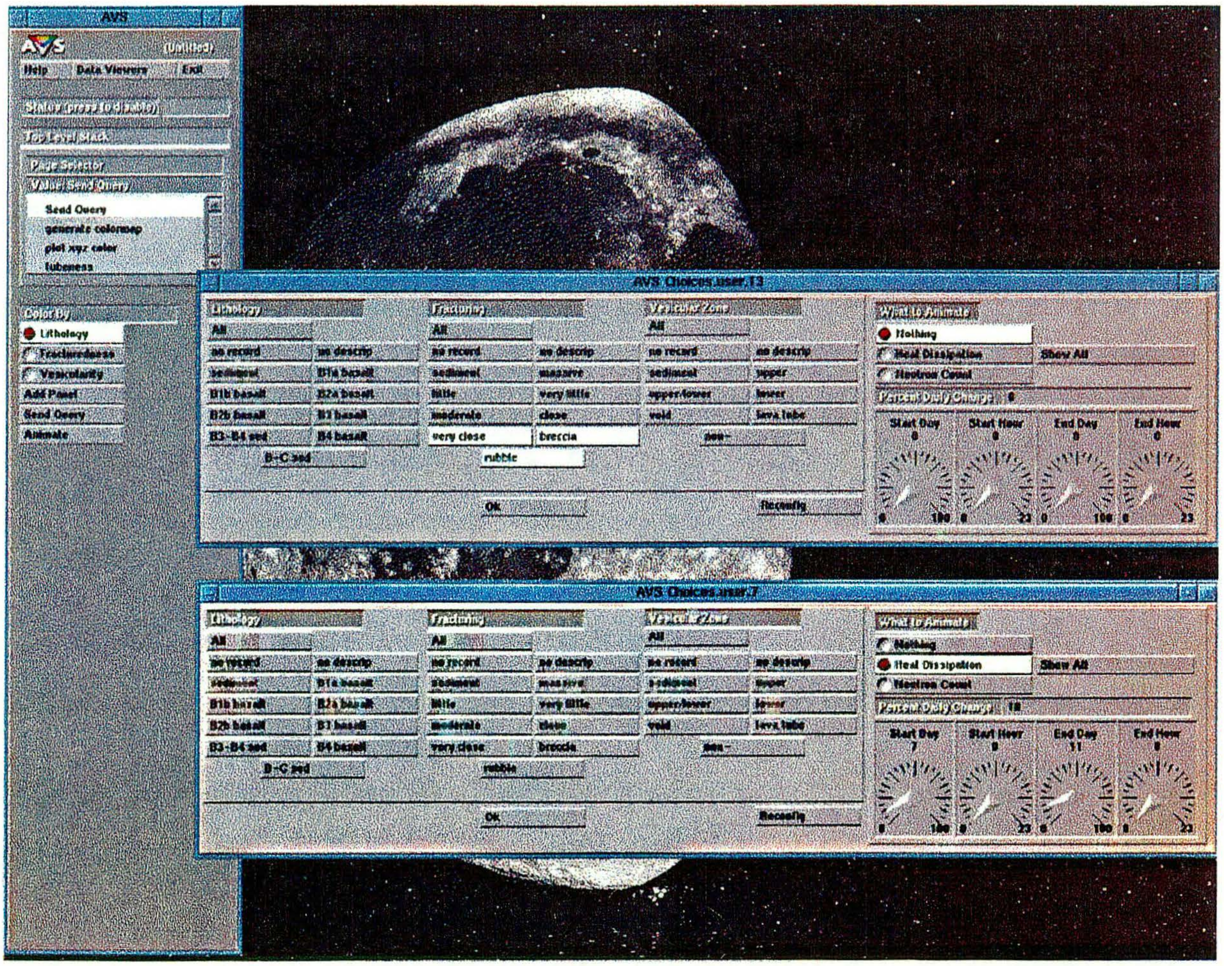

AVS Choices.user.13: Fracturing: very close, breccia, rubble; What to Animate: Nothing; Percent Daily Change 0; Start Day 0, Start Hour 0, End Day 0, End Hour 0

AVS Choices.user.7: What to Animate: Heat Dissipation; Percent Daily Change 18; Start Day 7, Start Hour 0, End Day 11, End Hour 0

Figure 6.8 Shown are dialogue boxes that allow the user to query the Illustra database management system.

The result of the queries is shown in Fig. 6.9 for a single time, nine days, nineteen hours from the start of the experiment. (A user sitting at the graphics workstation would be able to see all times in the specified range of times.) The wells are shown as tubes if they possess one of the selected attributes; otherwise they are shown as lines. The white spheres are the locations of the heat dissipation instruments, and the colored spheres show where the heat dissipation data exceeded the threshold value of a percent daily change of 18%. The colored well segments show the lithologic units in which there is fracturing possessing the desired attributes of "very close," "breccia," or "rubble." The value of this set of queries is that the user may determine for which lithologic units in which wells did a high degree of fracturing correspond to a percent daily change of 18% or greater in the heat dissipation data.

An extended abstract describing characterization of temporal sequences in geological databases has been submitted for presentation at the International Statistical and Database Conference in 1996 (*Shoshani et al.*, 1995).

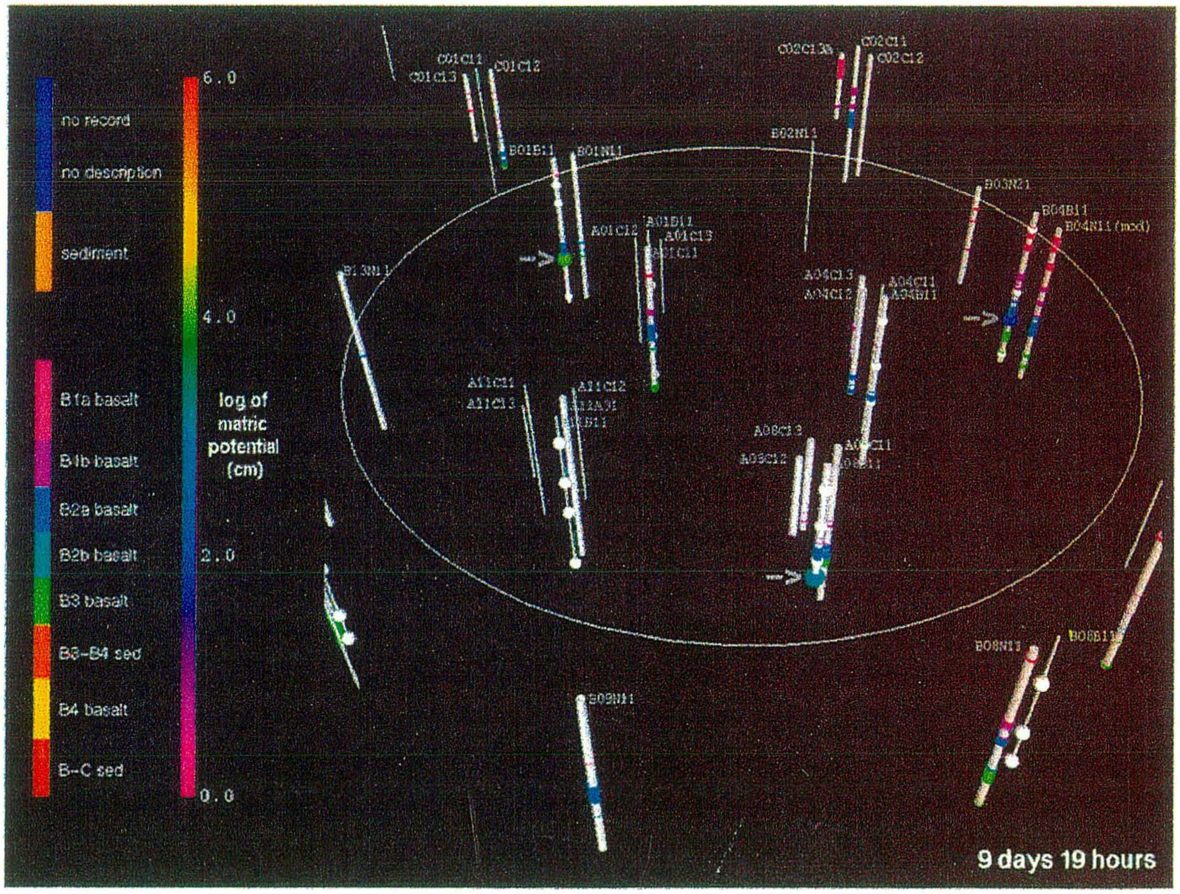

Figure 6.9 Shown are the results of the query shown in Fig. 6.8. See text for explanation.

2.6.4 FY 96 Activities

Efforts in FY 96 will be focused on data management and visualization of field data from the Box Canyon Site.

2.6.5 Significance

The value of this project has been in demonstrating the value of 3-D visualization of field data compared to traditional ways of looking at the same data. Only 3-D visualization techniques provide a way of looking at different types of data from all areas of a field site simultaneously. Traditionally, researchers have analyzed field data curve by curve, where each curve represents the measurement of one kind of data made at a single location over time (*e.g.*, tracer concentrations measured at a lysimeter) or measurements down a borehole at a single time (*e.g.*, neutron probe measurements). Each 3-D visualization presented in this section contains not only the equivalent of many "curves" of measured data, but also provides the spatial relationship of one dataset to another. In addition, time-dependent data may be "animated"; each frame in an animation shows the data collected at a given time.

Though not completely implemented for the LSIT, researchers on this task participated in the design and development of a prototype data management/visualization system, which provides all of the advantages of a DBMS with 3-D visualization. In such a system, the user may easily query data stored in the DBMS, and the results are visualized without the researcher needing to learn how to use the visualization software. This provides an easy-to-use, yet powerful interface to large and complex datasets so that the user may quickly and easily answer specific questions that he or she may have about certain types of data, how they vary in time, their correlation with other types of data or with depth, *etc.*

From a quality control point of view, the DBMS provides safe and controlled storage and a means to track data, from raw data to calibrated data to interpreted data. Interfacing the DBMS with 3-D visualization provides the capability to communicate information about site characterization and field test results through color images such as the ones included in this section.

Borehole Table

Wellname		*string*
elevation of top of well		*number*
x-coord.		*number*
y-coord.		*number*
type of backfill or open		*string*
casing info:	type of casing	*string*
	slotted?	*char*
	perforated?	*char*
	screened?	*char*
diameter		*number*
bottom depth of well		*number*
well completion:	top depth	*number*
	bottom depth	*number*
	material	*number*
lithology data available?		*char*
fracturing data available?		*char*
vesiculation data available?		*char*
tracer data available?		*char*
neutron data available?		*char*
gamma data available?		*char*
caliper data available?		*char*

Lithology Table

Wellname	*string*
source of data	*string*
date data collected	*date*
collector's name	*string (personal name)*
interpretor's name	*string (personal name)*
top depth	*number*
bottom depth	*number*
lithology type	*string*

Fracture Data Table

Wellname	*string*
source of data	*string*
date data collected	*date*
collector's name	*string (personal name)*
interpretor's name	*string (personal name)*
top depth	*number*
bottom depth	*number*
type (ves. or non-ves.)	*number*
orientation (dip)	*number*
type of infilling	*string*
aperture	*number*

Vesiculation Data Table

Wellname	*string*
source of data	*string*
date data collected	*date*
collector's name	*string (personal name)*
interpretor's name	*string (personal name)*
depth	*number*
degree of vesiculation	*number*

Table 6.1a. Design of data tables for LSIT: well information and geological information.

Heat Dissipation Table

Wellname	*string*	
source of data	*string*	
collector's name	*string (personal name)*	
interpretor's name	*string (personal name)*	
depth	date	*number*
	time	*number*
	measurement	*number*

Instrument Locations

Wellname	*string*
x-coord.	*number*
y-coord.	*number*
z-coord.	*number*

Table 6.1b. Design of data tables for LSIT: heat dissipation data and instrument locations.

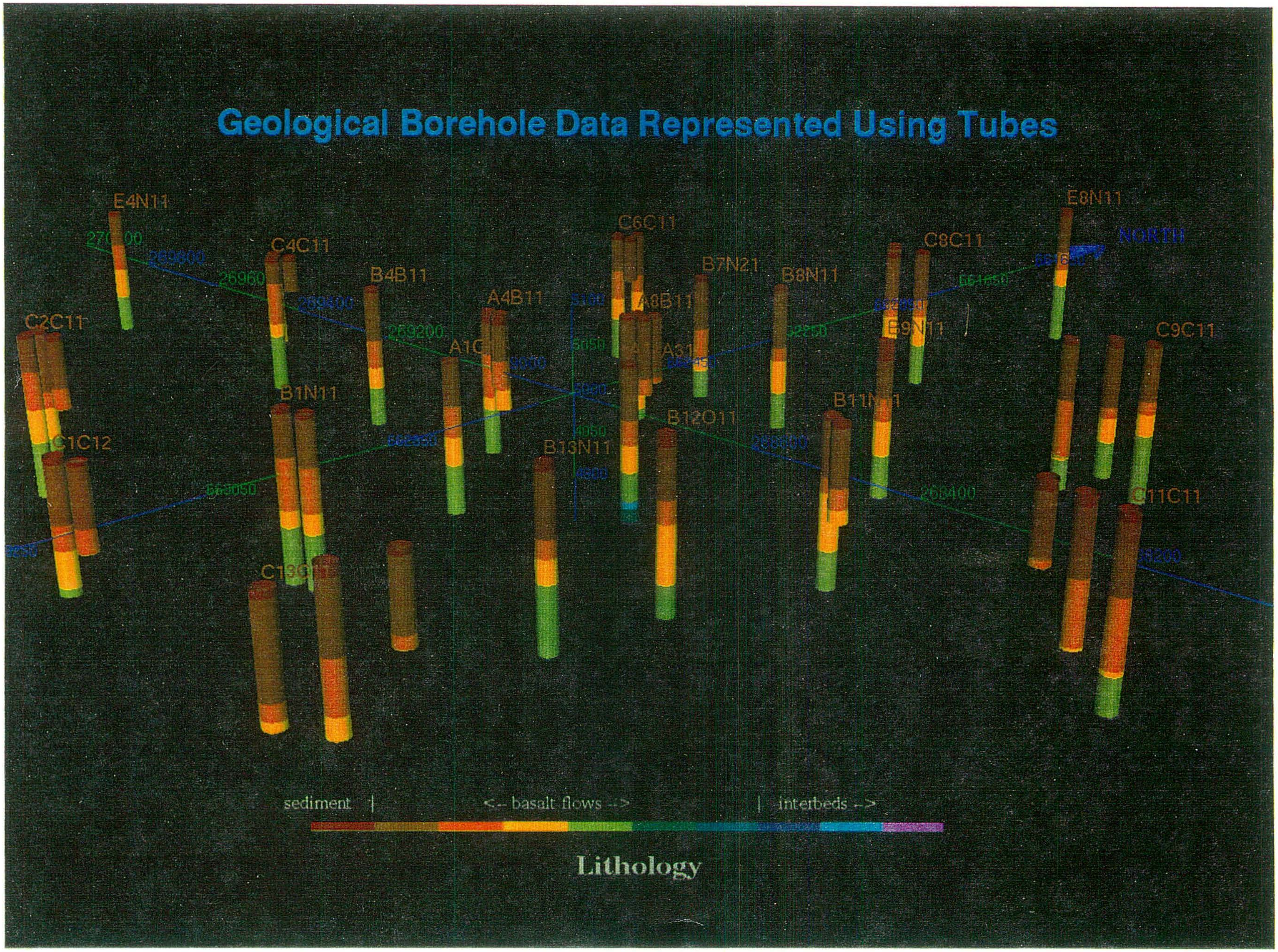
Geological Borehole Data Represented Using Tubes
E4N11
C4C11
B4B11
A4B11
C6C11
B7N21
B8N11
C8C11
E8N11
NORTH
C2C11
A1C11
A8B11
A31
E9N11
C9C11
B1N11
B11N11
B12O11
B13N11
C1C12
C13C11
C11C11
sediment |
<-- basalt flows -->
| interbeds -->
Lithology

Figure 6.1

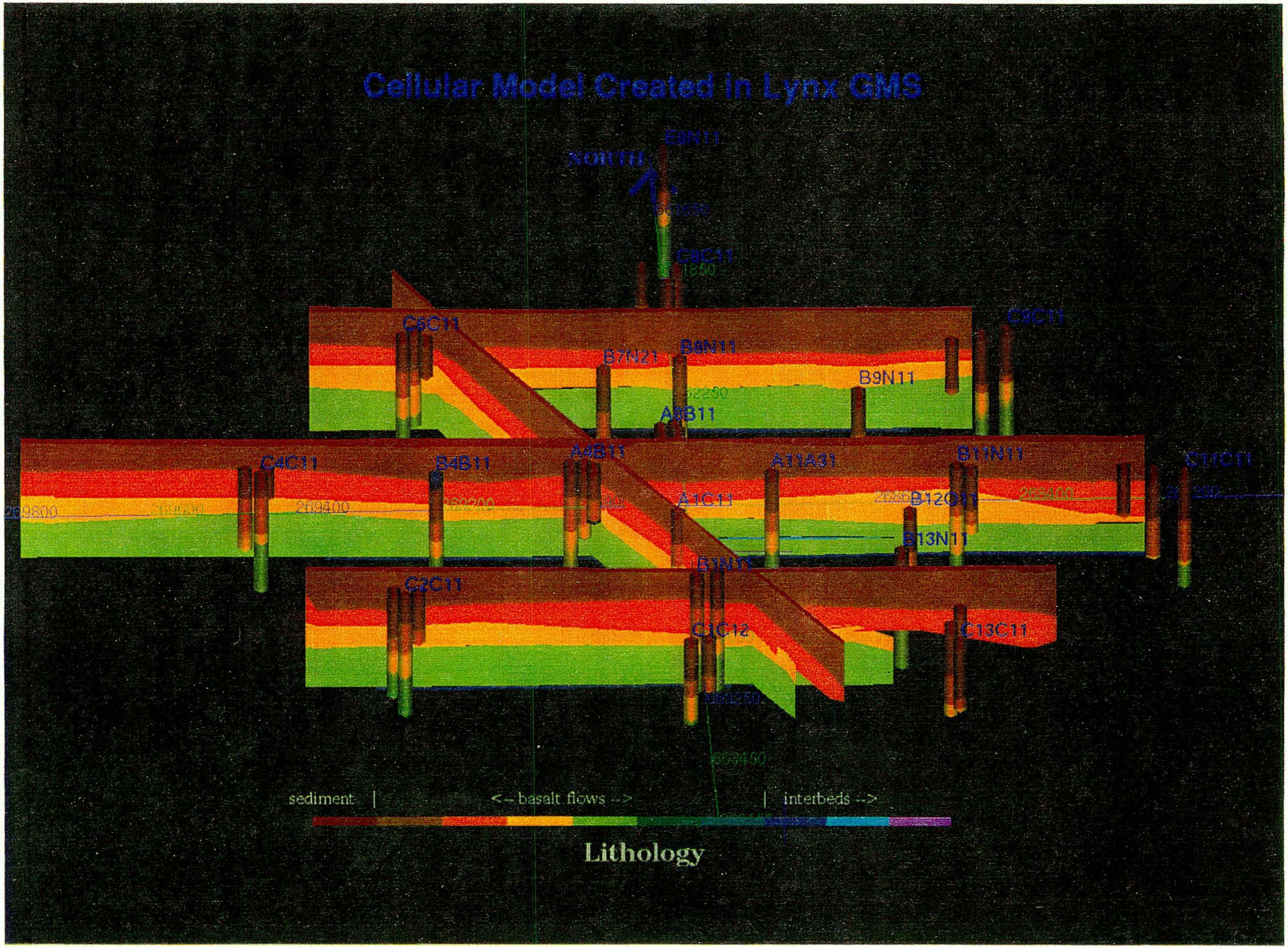
Cellular Model Created in Lynx GMS
E8N11
NORTH
C8C11
1850
C6C11
B7N21
B8N11
2250
A8B11
B9N11
C9C11
C4C11
B4B11
A4B11
A11A31
B11N11
C11C11
269800
269400
269200
A1C11
B12O11
268400
B13N11
B1N11
C2C11
C1C12
C13C11
sediment |
<-- basalt flows -->
| interbeds -->
Lithology

Figure 6.2

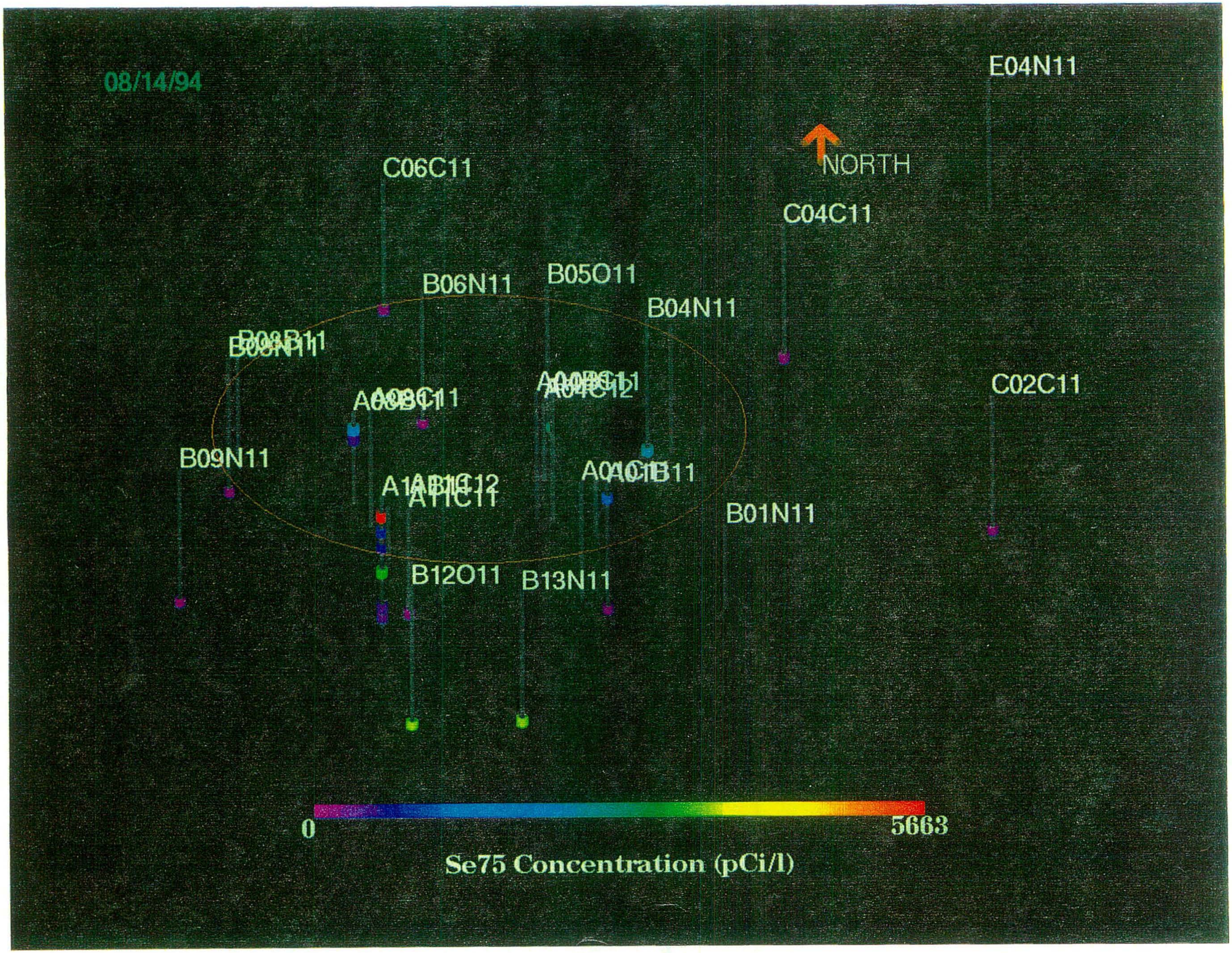
08/14/94
E04N11
NORTH
C06C11
C04C11
B06N11
B05O11
B04N11
B09N11
A11C11
A01C11
B01N11
C02C11
B12O11
B13N11
0
5663
Se75 Concentration (pCi/l)

Figure 6.3

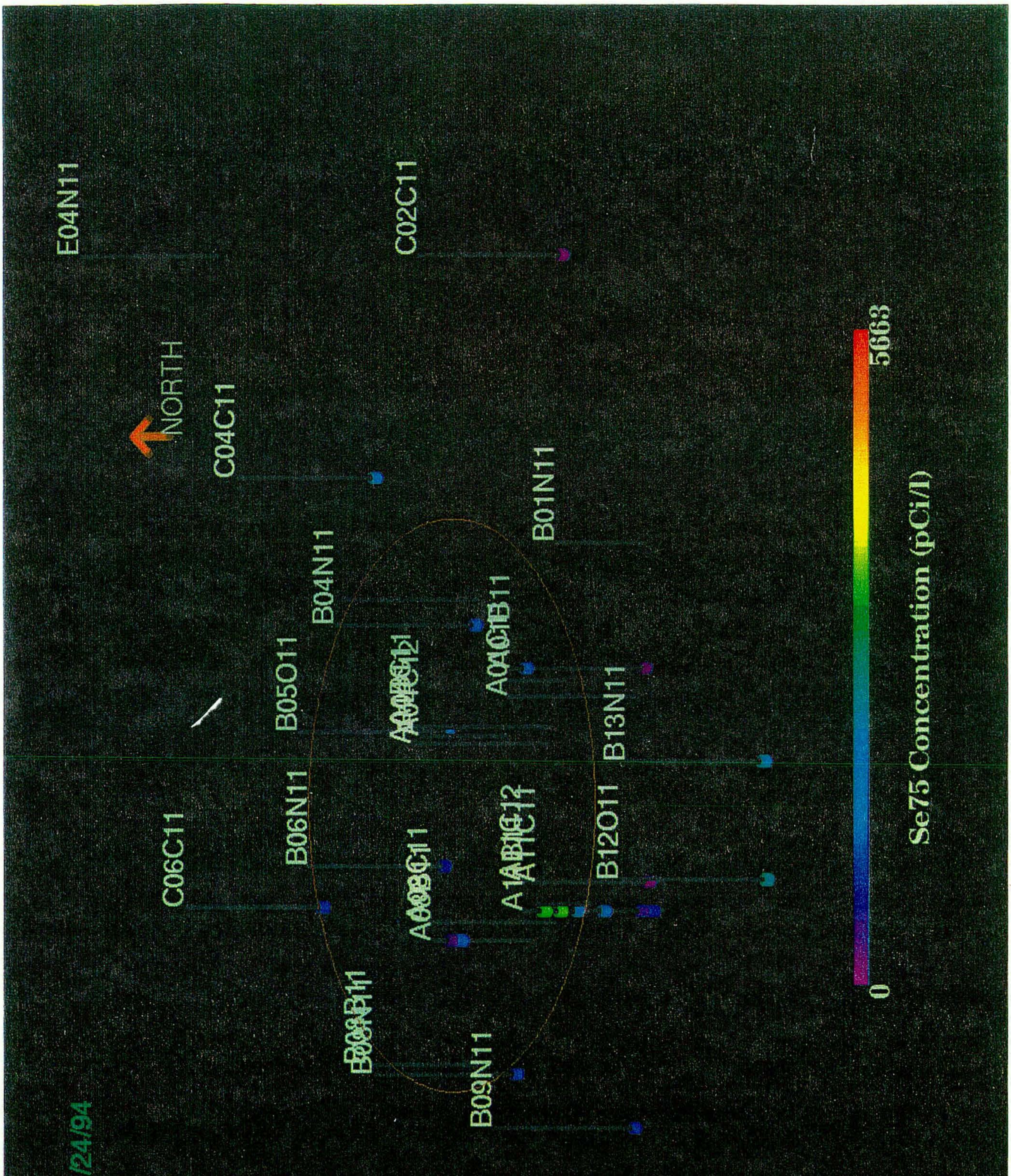
08/24/94
E04N11
C02C11
NORTH
C04C11
B01N11
B04N11
B05O11
B13N11
B06N11
C06C11
B12O11
B09N11
0
5663
Se75 Concentration (pCi/l)

Figure 6.4

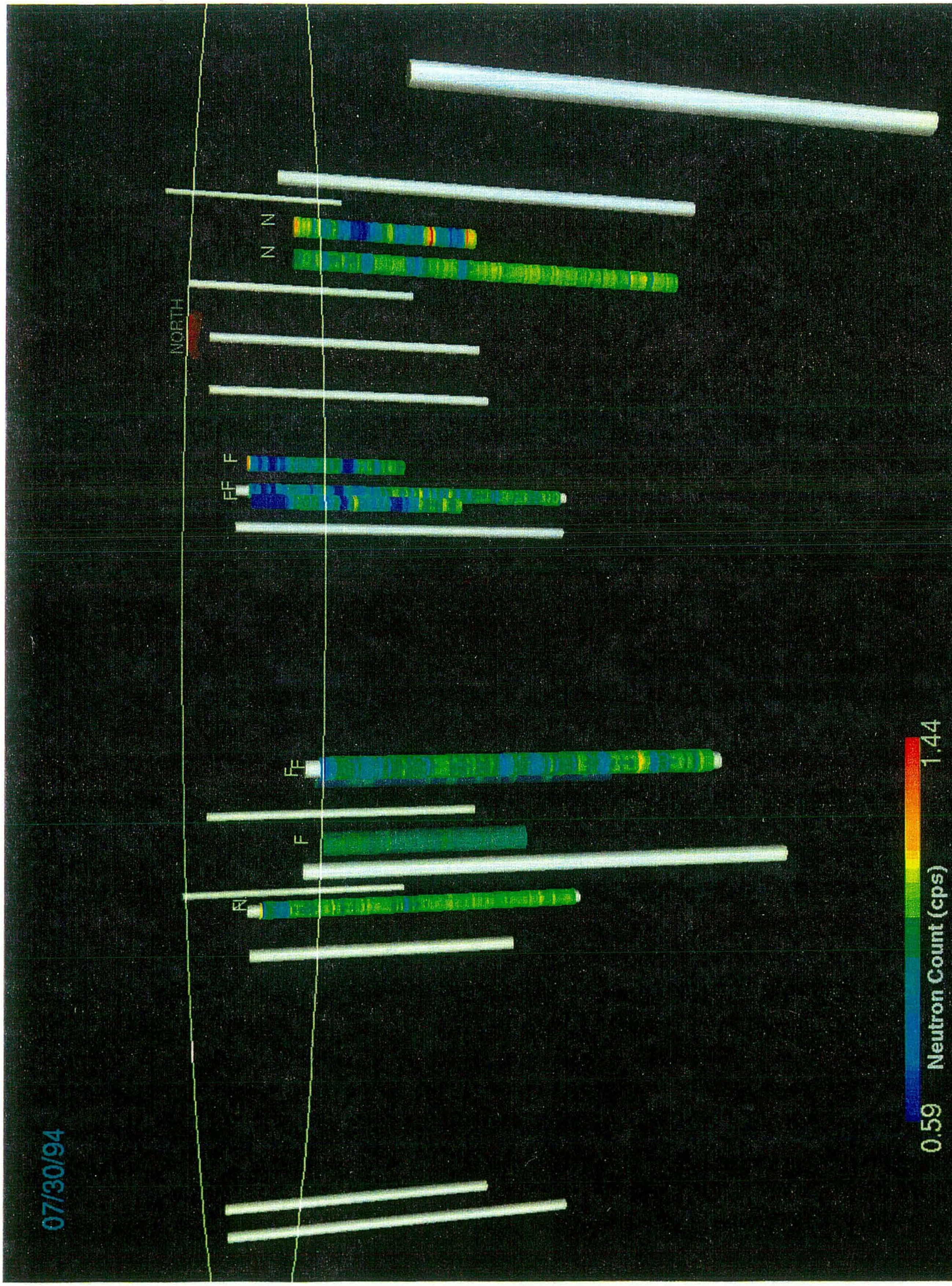

Figure 6.5

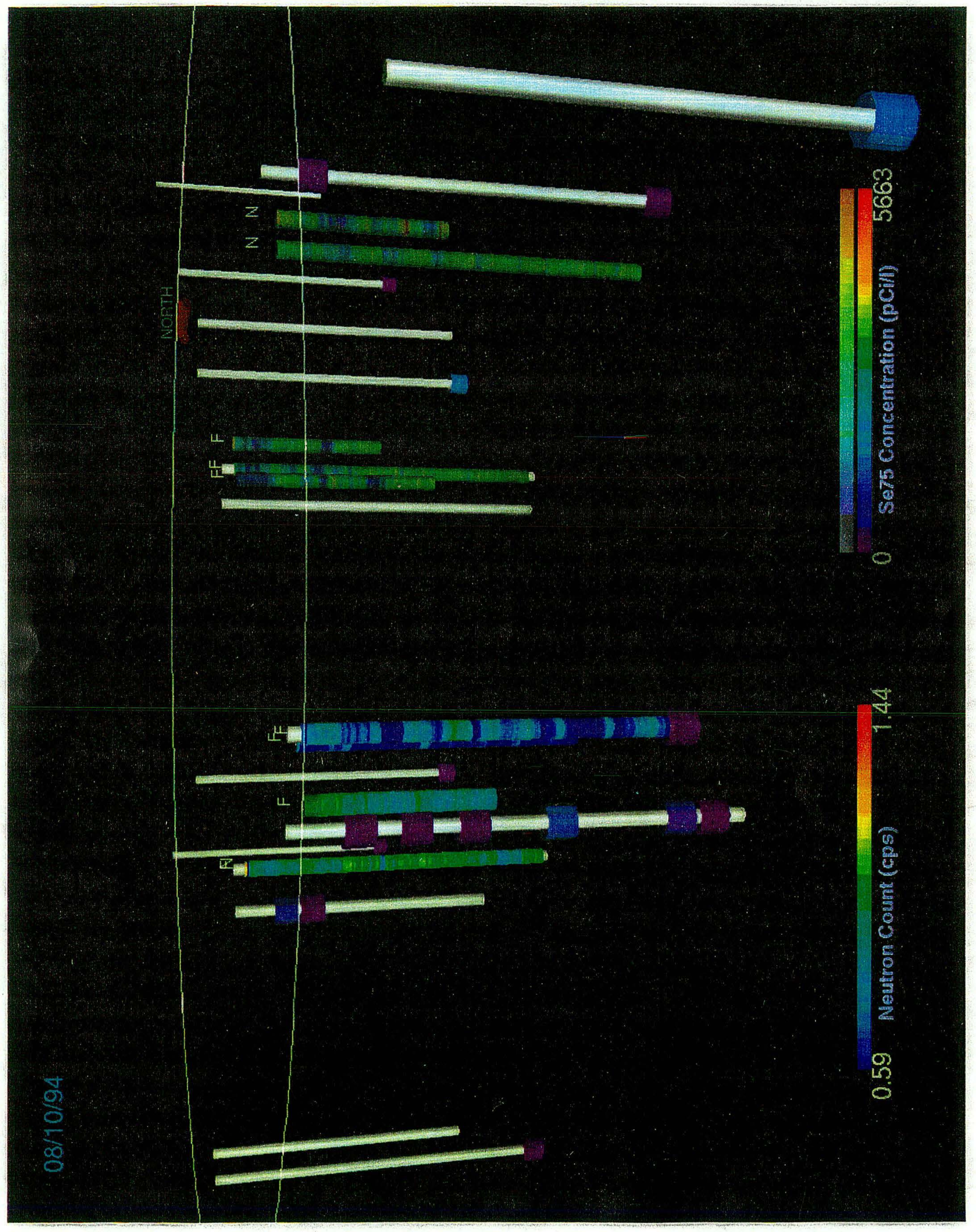
08/10/94
NORTH
N
N
F
FF
F
F
FF
R
0.59
Neutron Count (cps)
1.44
0
Se75 Concentration (pCi/l)
5663

Figure 6.6

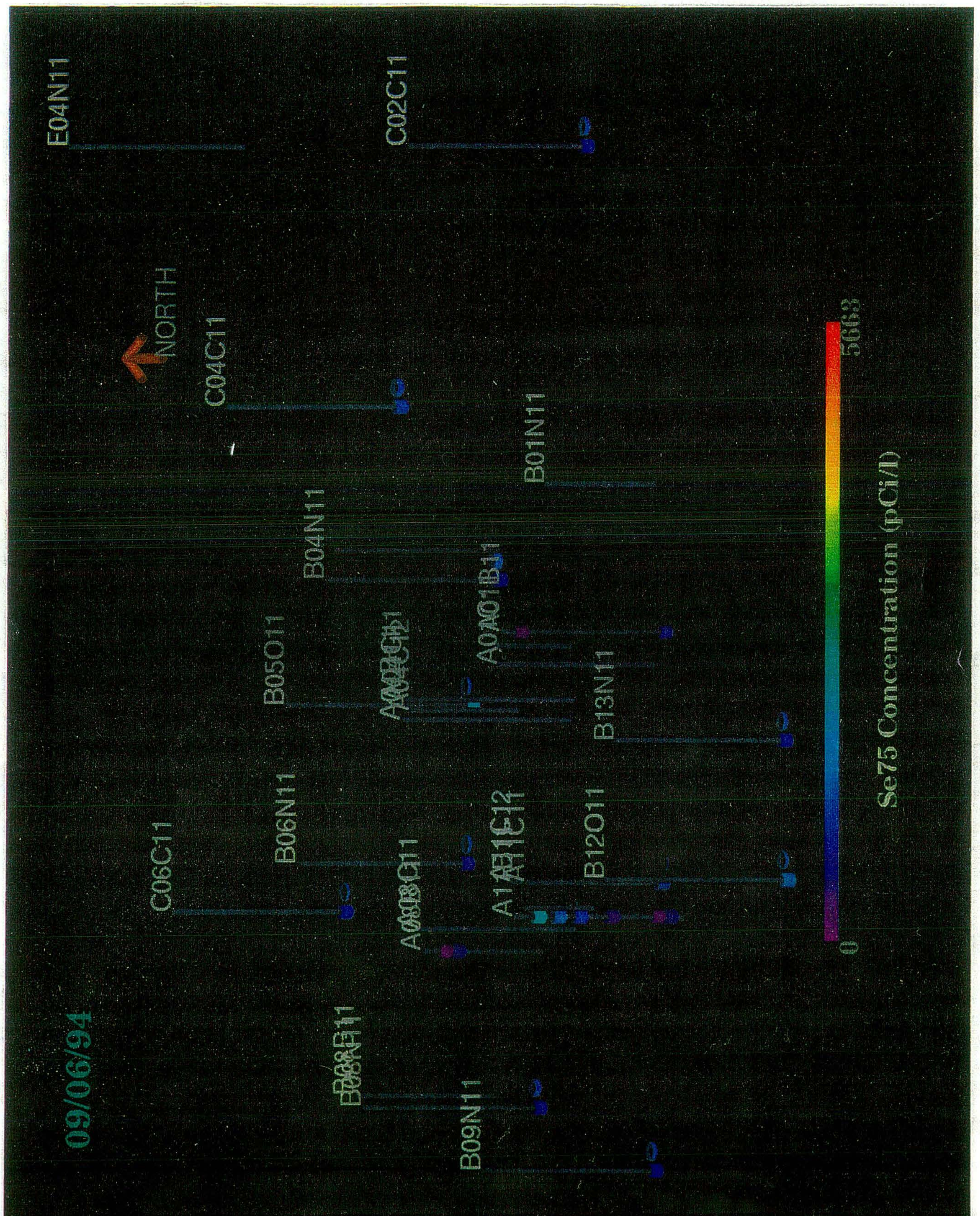
09/06/94
NORTH
E04N11
C02C11
C04C11
B01N11
B04N11
B05O11
B13N11
B06N11
C06C11
A11C12
A11C11
B12O11
B08N11
B09N11
0
5668
Se75 Concentration (pCi/l)

Figure 6.7

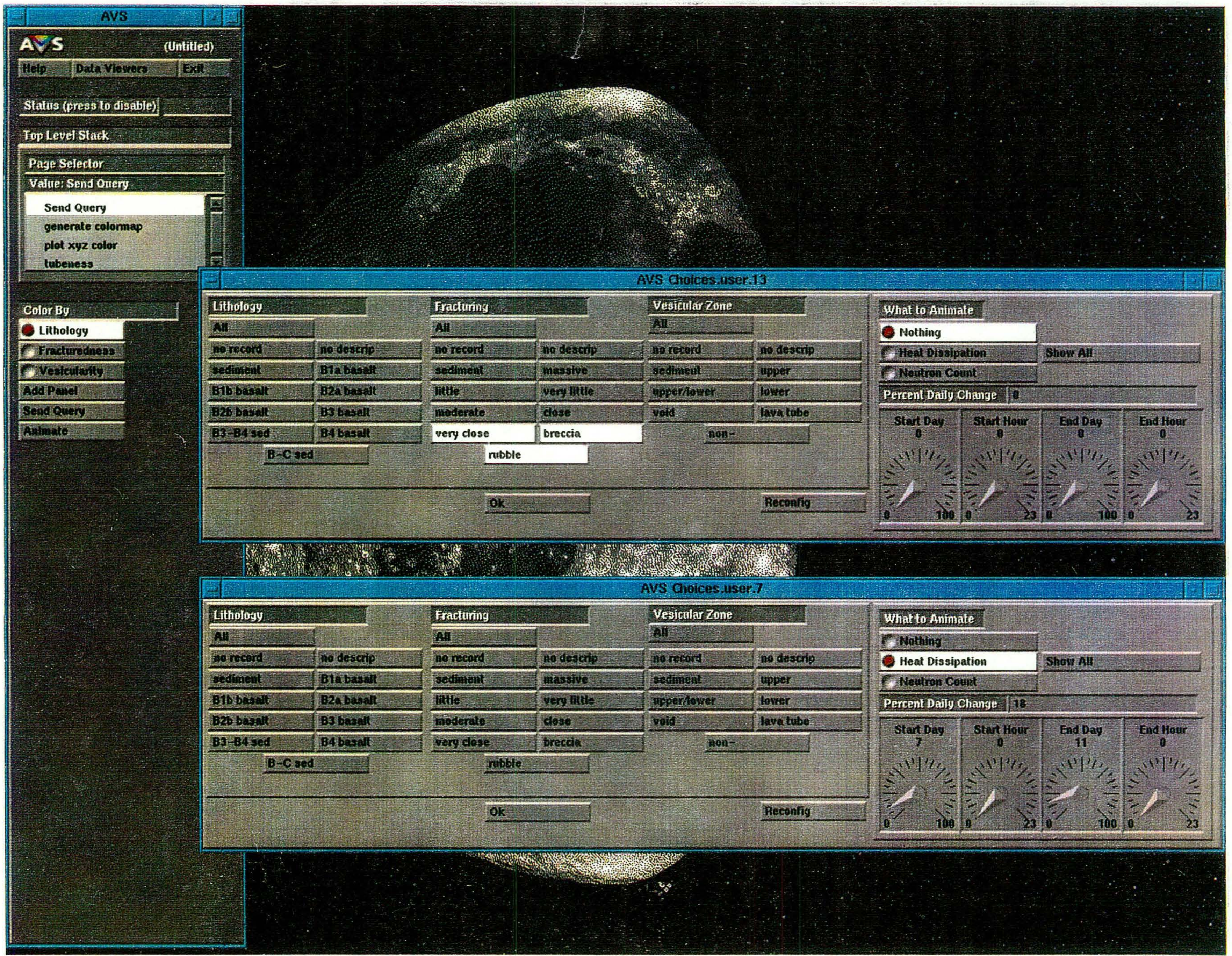

Value: Send Query

Color By: ● Lithology

AVS Choices.user.13: What to Animate: ● Nothing; Percent Daily Change 0; Start Day 0; Start Hour 0; End Day 0; End Hour 0

AVS Choices.user.7: What to Animate: ● Heat Dissipation; Percent Daily Change 18; Start Day 7; Start Hour 0; End Day 11; End Hour 0

Figure 6.8

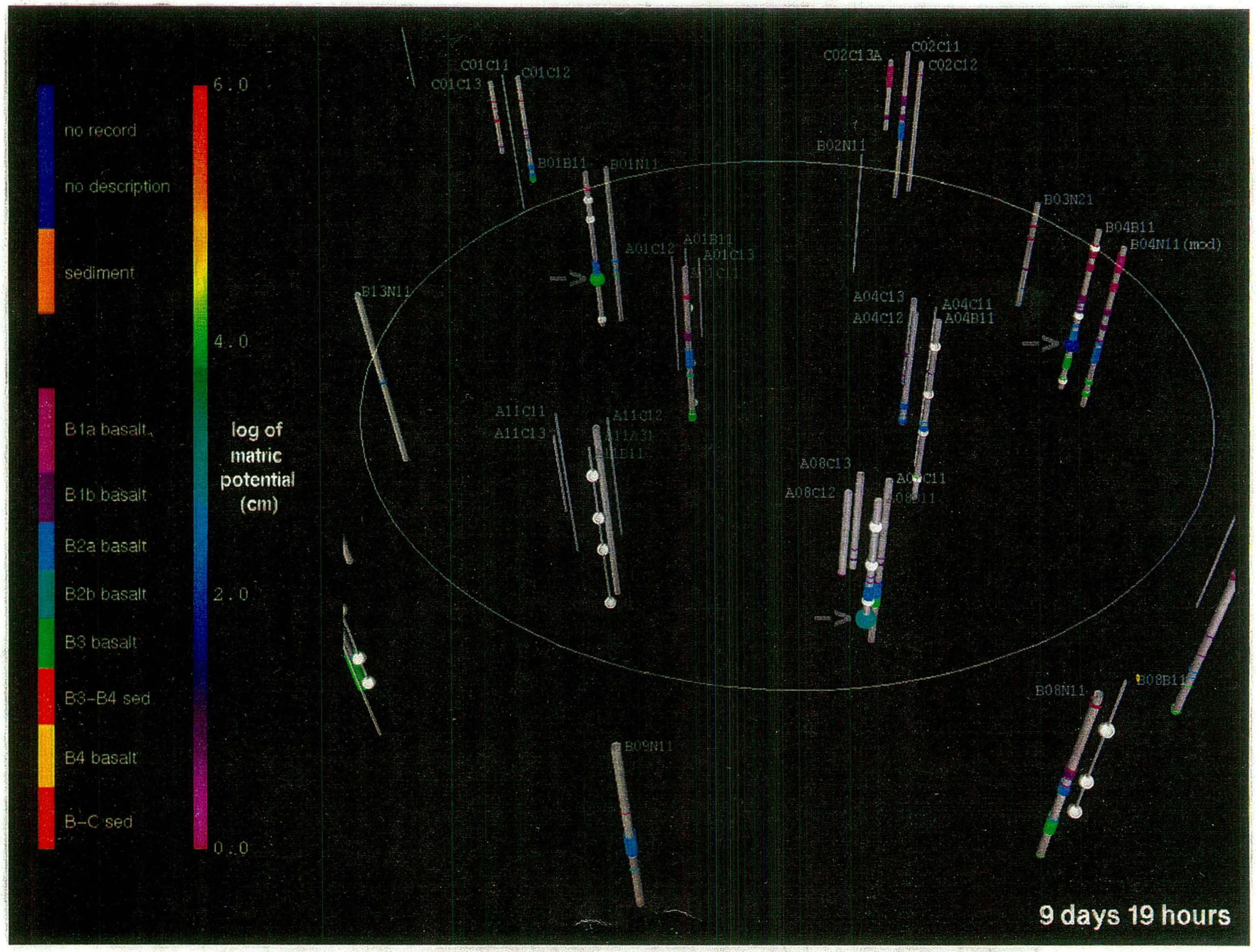
no record
no description
sediment
B1a basalt
B1b basalt
B2a basalt
B2b basalt
B3 basalt
B3–B4 sed
B4 basalt
B–C sed
6.0
4.0
2.0
0.0
log of matric potential (cm)
C01C11
C01C13
C01C12
B01B11
B01N11
B13N11
A01C12
A01B11
A01C13
A11C11
A11C13
A11C12
B09N11
C02C13A
C02C11
C02C12
B02N11
A04C13
A04C12
A04C11
A04B11
A08C13
A08C12
B03N21
B04B11
B04N11 (mod)
B08N11
B08B11
9 days 19 hours

Figure 6.9

2.7 Task 7. Coordination

2.7.1 Background

The coordination and integration of this project is managed through the Project Coordination Task Force. The Task Force meets regularly to plan and review experiments, monitor progress and also ensure that individual experimental plans fit into the overall objectives for site characterization.

The coordinators (Jane Long and Tom Wood) are also responsible for facilitating information sharing and coordination with the INEL customer personnel.

2.7.2 Performer

LBL and INEL organize these meetings. They are attended by other participants as required.

2.7.3 FY 95 and FY 96

A kick-off coordination meeting was held in November, 1994. Informal meetings were held frequently. Video conferences have been used as a means to reduce the amount of travel between LBL and INEL. A similar pattern is expected for FY96.

2.7.4 Significance

The ultimate goal of technology development is to configure a suite of tools, which when used together can effectively characterize the flow domain. By applying technologies from widely varying disciplines, the performance of each method can be assessed. Once the appropriate tools are developed, the goal of characterizing the flow domain with a special focus on fast-path flow can be achieved. The final assessment of the project's success hinges on the ability to predict flow processes and transport rates. Characterization tools will be used to predict the outcome of flow and transport experiments in fractured rock in order to assess the performance of these tools for characterizing important hydrologic features in similar contaminated sites.

The success of these technologies will be measured in two different ways. First, technologies will be cross-checked with each other to determine which of these give a consistent picture of the nature of fluid flow in this fractured rock. Secondly, the project will include the performance of a series of validating experiments. PI's will be expected to predict the outcome of these experiments *a priori* whenever appropriate. The comparison of prediction *vs*. measurement will be viewed as the performance criteria for the technologies. Particular attention will be paid to testing the effectiveness of technologies designed to locate and characterize fast flow paths. This process will be managed by the Task Force.

3.0 SUMMARY AND CONCLUSIONS

This report represents the conclusion of the first year of work on the Fracture Analog Project. The project is designed to develop tools and understanding relevant to contamination behavior in the fractured basalts at the INEL site. The project initially focused on both the saturated zone and the vadose zone. We have completed two pilot studies in the saturated zone. Due to funding constaints, we have continued to concentrate on the vadose zone studies.

The completed saturated zone pilot studies focused on what can happen to contaminants once they reach the Snake River Plain aquifer, which is a major resource for agriculture. If contaminants reach the groundwater system, they may enter fast flow paths that quickly move the harmful substances, possibly into regions where ground water is being pumped for irrigation. The first pilot study evaluated the concept of using numerical inversion methods on multiple well test records to characterize the connectivity of fracture system on the 100 m to 200 m scale. Although the data were very limited, this study showed clearly that connectivity was more ubiquitous in the horizontal direction than in the vertical direction. The study indicated that analysis of such well tests could be useful in understanding the nature of fracture connectivity. This work demonstrates clearly that fracture connectivity can play a strong role in controlling contaminant movement at INEL. We strongly recommend this type of testing and interpretation be done in the vicinity of waste injection sites at INEL where it is critical to know where the waste is moving through the fracture system.

The second pilot study evaluated a new possibility for determining fast flow paths on the aquifer scale through a co-inversion of hydraulic head and isotope data. Strontium isotope ratios in groundwater evolve over time toward the ratio of Sr acquired from the matrix rock. Thus, these isotope ratios are affected by the length of time that the water has been in contact with the rock (residence time). Unless there is significant mixing of different types of water, contours of Sr ratios should be roughly orthogonal to the flow paths and parallel to isopotentials (assuming isotropy). LBL has developed methods for inversion of head data, but they had been only applied to well test data as described above, not regional aquifer data. Methods recently developed at LBL enable interpretation of isotope ratios to yield flow path information, but it was not clear that there was any trend in the Snake River Plain aquifer isotope ratio data worthy of interpretation. This pilot study established that our hydrologic inversion method was applicable to the aquifer scale and examined the strontium ratio data from the Snake River Aquifer to establish that there was a trend in the strontium ratio data that was worth trying to interpret as a variation in residence time. Consequently, a proposal to develop a co-inversion was submitted to DOE/ Energy Research (ER) as part of a cooperation between DOE/ Environmental Restoration Waste Management (EM) and ER.

The major focus of this work is on the infiltration problem. The first order problem is to know how water moves downward. Does water follow vertical fractures and are these persistent through the basalt flow units? Does water only travel around the noses of the basalt flows where they consist of rubble? Where does water travel horizontally in order to get to the next vertical conductor? In other words, what are the operative hydrologic components of the fracture system that control infiltration?

A key problem encountered in the Large Scale Infiltration Test (LSIT) conducted by INEL in July 1994 was that water from the infiltration pond generally moved vertically downwards and did not spread horizontally to a large degree until it reached an interbed zone about 180 feet (60 m) below the surface. Therefore much of the monitoring effort (vertical boreholes located outside the pond radius) was ineffective. Neutron data collected during the infiltration test in a number of boreholes located directly under the infiltration pond did show increases in water content. Analysis of the tracer data, however, clearly showed the presence of multiple flow paths for water and tracer movement. In some boreholes, tracer was detected at instrument locations at greater depth before being detected at locations near the surface. So while the preferential paths for tracer movement were vertical, there was some horizontal movement of tracer in the subsurface directly below the infiltration pond. Outside of the infiltration pond, tracer was not detected. Evidently, infiltration occurs largely in discrete vertical channels, which are almost impossible to find with vertical boreholes.

Learning from this experience, we developed a strategy for finding the critical vertical pathways. First, we conducted a geological analysis of the fracture pattern at the Box Canyon site in order to analyze fracture connections. In FY 96 we will use this information to develop a stochastic process that mimics the formation of fracture conduits.

Second, we drilled slant holes that are more likely to intersect vertical fracture conduits than vertical holes are. These holes were logged and provided good information on the location of both vertical and horizontal fractures in the interior of the basalt flow. One of the new borehole imaging methods, the borehole scanner logging method, was particularly useful and provided vivid pictures of the borehole walls.

Third, we took a point at depth where we might consider emplacing an instrument to detect infiltration. We then injected air into that borehole interval within the rubble zone and monitored other boreholes to determine the pattern of connectivity was. First, we used hot air, hoping to detect a temperature change at the surface. Previous work on hot air injection provided by INEL was successful at sensing temperature changes on the cliff face. However, a significant change in temperature at the surface was not observed. The reason for this is probably that the fractures at the surface were filled with sediment and, due to an unusually wet year, these sediments were nearly saturated. Water in the sediments thus blocked the flow of hot air. Our expectation had been that the fractures would be relatively dry in August when the hot air injection tests were conducted. Also, the majority of fractures located just above the rubble zone may not be connected to a set of fractures exposed at the land surface.

Modeling studies indicated that the absence of temperature change was reasonable under the existing field conditions. More importantly, these studies also showed that although a change in temperature may not be observed at the surface, there may be a change in saturation of the infilled sediment. Since it is possible to detect even slight saturation changes, this is an idea we will return to in FY 96.

The next step was to conduct air injection tests to find patterns of connectivity below the surface. These tests were successfully carried out in October and will be analyzed and reported on in FY 96.

We also conducted cross-hole and single hole radar measurements. The images produced with these data clearly show some of the critical structures that create preferential flow paths. The interpretation of these images will be done in FY 96, and we will pursue the use of this very promising technology further. In particular, it remains to be determined whether radar imaging can detect changes in saturation during an infiltration experiment.

We began the design and testing of several key instruments for this test, including tensiometers and borehole time domain reflectometry devices to measure changes in saturation. The key plan for FY 96 is to design, predict and run an infiltration experiment at the site. The preliminary conceptual model for the site will be developed first, and the design of the test will be based on the conceptual model. The key challenges are to see if we can predict the results of this test before we conduct it, and to see if we can understand the system well enough to instrument the site appropriately.

Plans are also being made to meet with INEL program managers sometime in January or February of FY 96 to exchange information.

4.0 REFERENCES

Bishop, C.W., 1991, Hydraulic properties of vesicular basalt, M.Sc. Thesis, Dept. of Hydrology and Water Resources, University of Arizona, 117 pp.

Burgess, D., 1995, Results of the neutron and natural gamma logging, stratigraphy, and perched water data collected during a large-scale infiltration test, EDF Serial Number ER-WAG7-60, INEL File Number 95/062.

Datta-Gupta, A., D.W. Vasco, and J.C.S. Long, 1994, Detailed characterization of a fractured limestone formation using stochastic inverse approaches, SPE/DOE-27744, Presented at the SPE/DOE Ninth Symposium on Improved Oil Recovery, Tulsa, Oklahoma, 17-20 April.

Degraff, J. M. and A. Aydin, 1993, Effect of thermal regime on growth increment and spacing of contraction joints in basaltic lava, *J. Geophy. Res. 98* 6411-6430.

Degraff, J. M., P. E. Long, and A. Aydin, 1989, Use of joint growth directions and rock textures to infer thermal regimes during solidification of basaltic lava flows, *J. Volcanol. Geotherm. Res., 38* 309-324.

Doughty, C., 1995, Estimation of hydrologic properties of heterogeneous geologic media: an inverse method based on iterated function systems Ph.D. dissertation, Department of Material Science and Mineral Engineering, University of California, Berkeley, in progress.

Doughty, C., J.C.S. Long, K. Hestir, and S.M. Benson, 1994, Hydrologic characterization of heterogeneous geologic media with an inverse method based on iterated function systems, Water Resour. Res, 30, 6, 1721-1745.

Doughty, C., J.C.S. Long, K., Hestir and S.M. Benson, 1994, Hydrologic characterization of heterogeneous geologic media with an inverse method based on iterated function systems, *Water Resour. Res.,* 30(6), 1721-1745.

Faybishenko, B.A., 1986, Water-Salt Regime of Soils under Irrigation, Moscow, Agropromizdat, 304 p.

Garabedian, S.P., 1992, Hydrology and digital simulation of the regional aquifer system, Eastern Snake River Plain, Idaho, U.S. Geological Survey Professional Paper 1408-F.

Grossenbacher, K.A. , and S.M. McDuffie, Conductive cooling of lava: Columnar joint diameter and stria width as functions of cooling rate and thermal gradient. In print at *Journal of Volcanology and Geothermal Sciences.*

Horsman, J. and W. Bethel, 1995, Methods of Constructing a 3D Geological Model from Scatter Data, presented at AVS '95, April 19-21, Boston, Massachusetts.

Jacobsen, J., J. Horsman and P. Holland, 1995, 3-D Visualization of Data from the INEL Large Scale Infiltration Test, presented at the Technologies for Characterization Forum Workshop, August 17, 1995, Denver, Colorado.

Johnson, T.M. and D.J. DePaolo, 1994, Interpretation of isotope ratios in groundwater systems: Model development and application to Sr isotope data from Yucca Mountain, *Water Resour. Res.*, 30, 1571-1587.

Karasaki, K., 1987, A new advection-dispersion code for calculating transport in fracture networks, in Earth Sciences Division 1986 Annual Report, Rep. LBL-22090, pp. 55-58, Lawrence Berkeley Laboratory, Berkeley, California.

Knutson, C.F., K.A. McCormick, J.C. Crocker, M.A. Glenn, and M.L. Fishel, 1992, 3D RWMC vadose zone modeling (including FY-89 to FY-90 basalt characterization results), Rep. EGG-RD-10246, Idaho National Engineering Laboratory, Idaho Falls, Idaho.

Knutson, C.F., and T.R. Wood, 1994, Proof of concept - geophysical methods for characterization and monitoring of buried waste, Interim Report, Idaho National Engineering Laboratory, Idaho Falls, Idaho.

McCarthy, J.M., R.C. Arnett, R.M. Neupauer, M.J. Rohe, and C. Smith, 1995, Development of a regional groundwater flow model for the area of the Idaho National Engineering Laboratory, Eastern Snake River Plain aquifer, INEL-95/0169, Idaho National Engineering Laboratory, Idaho Falls, Idaho.

Olsson, O. (Editor), 1992, Site Characterization and Validation - Final Report, STRIPA Project 92-22. Swedish Nuclear Fuel and Waste Management Company, Sweden.

Pruess, K., 1987, TOUGH user's guide, Rep. LBL-20700, Lawrence Berkeley Laboratory, Berkeley, California.

Pruess, K., 1991, TOUGH2 - A general-purpose numerical simulator for multiphase fluid and heat flow, Rep. LBL-29400, Lawrence Berkeley Laboratory, Berkeley, California.

Shoshani, A., P. Holland, J. Jacobsen and D. Mitra, 1995, Characterization of temporal sequences in geophysical databases. Submitted to the International Statistical and Scientific Database Conference, to be held in Sweden, 1996.

Thapa, B.B., 1994, Analysis of in situ joint strength using digital borehole scanner images, Ph.D. Thesis, University of California, Berkeley.

Theis, C.V., 1935, The relation between the lowering of the piezometric surface and the rate and duration of discharge of a well using ground-water storage, Trans. Amer. Geophys. Union, 16, 519-524.

Wylie, A.H., J.M. McCarthy, E. Neher, and B.D. Higgs, 1995, Large-scale aquifer pumping test results, Rep. INEL-95/012, Idaho National Engineering Laboratory, ER-WAG7-56, Idaho Falls, Idaho.

YSI, Inc., 1993, Temperature Sensors and Probes, Yellow Springs, Ohio.

BERKELEY LAB

ERNEST ORLANDO LAWRENCE BERKELEY NATIONAL LABORATORY
TECHNICAL AND ELECTRONIC INFORMATION DEPARTMENT
UNIVERSITY OF CALIFORNIA | BERKELEY, CALIFORNIA 94720